Aerodynamic interaction effects of circular and square ducted propellers

H. F. Mourão Bento

Technische Universiteit Delft

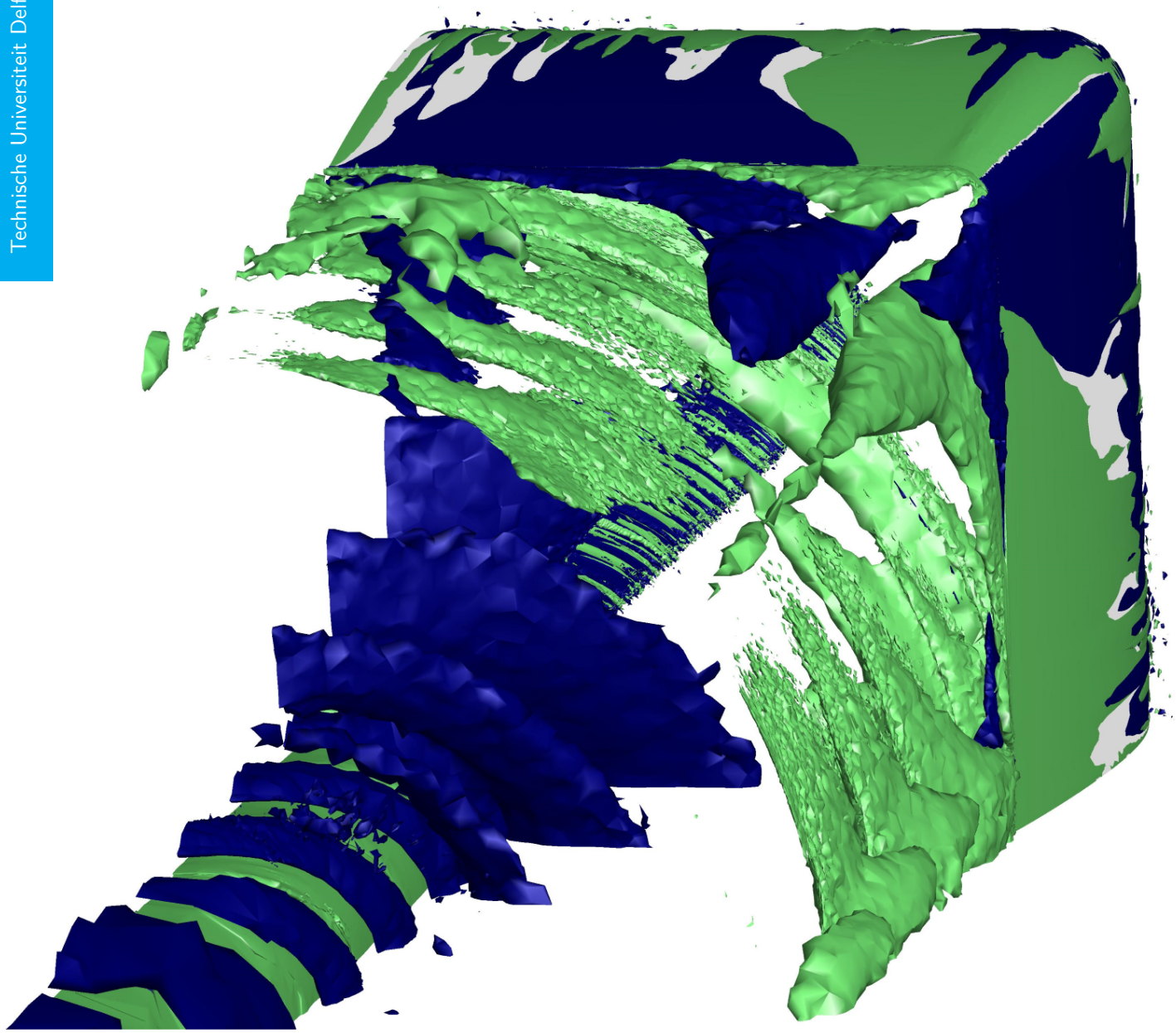

TU Delft Delft University of Technology

Challenge the future

Aerodynamic interaction effects of circular and square ducted propellers

by

H. F. Mourão Bento

to obtain the degree of Master of Science
at the Delft University of Technology,
to be defended publicly on Friday May 3, 2019 at 14:00 PM.

Student number:	4514750	
Project duration:	September, 2017 – April, 2019	
Thesis committee:	Ir. R. de Vries,	TU Delft, supervisor
	Prof. dr. ir. L.L.M. Veldhuis,	TU Delft, supervisor
	Prof. dr. ing. G. Eitelberg,	TU Delft
	Dr. F. Avallone,	TU Delft

An electronic version of this thesis is available at http://repository.tudelft.nl/.

TU Delft

PREFACE

Studying in Delft has been an amazing experience, both personally and academically.

I would like to give a special thanks to Reynard, who was always available to help me and who has followed my work closely. Besides the important feedback, our discussions always made me question my understanding of every problem with high detail. The motivation he always gave me was very important as well.

I would like to thank Professor Veldhuis for the very interesting and challenging thesis topic, and for providing me important guidance. I would also like to thank all the participants of the propeller meetings. With these meetings, my learning curve on the thesis topic grew considerably faster, and my interest was also motivated.

The continuous help from Nando and Tom was essential for this project. I would like to thank them for the advices given during all the stages of the CFD simulations, whenever I got stuck. I would also like to thank Tomas for providing me with the wind tunnel data on the performance of the Xprop, as well as with his MATLAB tool for running XROTOR.

Doing the thesis project was a lot of fun, but had its difficult moments, specially when ANSYS decided to be moody. For me to overcome these moments, the company from everyone who has worked in room 6.01 was very important. The coffee and lunch breaks, the discussions and the help with the project have made whole thesis easier. I also want to thank everyone for always being nice towards square ducts.

Besides, it was also incredible to face the courses at TU with my friends from class. Saga, Cristina, Jaydeep, Jona, Jóhn (the accent is important), Juan, Kaushik, Marco, I hope we can join the whole group again soon.

For me to decide taking this adventure abroad, the initial planning with Bruno and Diogo was very important and motivating. The time spent in the Netherlands has certainly been easier and more enjoyable with all my Portuguese friends who have lived here or visited me in the last years. I was very lucky to have them around.

Last but not least, I would like to thank my parents and my family for always supporting me.

H. F. Mourão Bento
Delft, April 2019

CONTENTS

List of Figures

List of Tables

NOMENCLATURE

LATIN SYMBOLS

Symbol	Definition	Units
A	area	[m^2]
$A_{\text{d, exit}}$	area of the duct at its trailing edge	[m^2]
$A_{\text{d, prop}}$	area of the duct at the propeller location	[m^2]
A_{in}	area of the propeller streamtube far upstream	[m^2]
A_{out}	area of the propeller streamtube far downstream	[m^2]
A_{p}	area of the propeller disk	[m^2]
AR	aspect ratio	[-]
B	number of blades	[blades]
b	wing's span	[m]
C_D	drag coefficient $C_D = \frac{D}{1/2\rho V_\infty^2 S_{\text{ref}}}$	[-]
C_d	section drag coefficient $C_d = \frac{C_d}{1/2\rho V_\infty^2 S_{\text{ref}}}$	[-]
C_{D_0}	zero-lift drag coefficient $C_{D_0} = \frac{D_0}{1/2\rho V_\infty^2 S_{\text{ref}}}$	[-]
C_{D_i}	$C_{D_i} = \frac{D_i}{1/2\rho V_\infty^2 S_{\text{ref}}}$	[-]
C_f	Skin friction coefficient $C_f = \frac{\tau_w}{q_\infty}$	[-]
C_L	lift coefficient $C_L = \frac{L}{1/2\rho V_\infty^2 S_{\text{ref}}}$	[-]
$C_{L_{\text{duct}}}$	duct lift coefficient $C_{L_{\text{duct}}} = \frac{L_{\text{duct}}}{1/2\rho V_\infty^2 S_{\text{ref}}}$	[-]
C_{L_α}	lift curve slope $C_{L_\alpha} = \frac{dC_L}{d\alpha}$	[/°]
C_p	pressure coefficient $C_p = \frac{p - p_\infty}{q_\infty}$	[-]
C_{p_t}	total pressure coefficient $C_{p_t} = \frac{p_t - p_\infty}{q_\infty}$	[-]
C_ω	vorticity coefficient $C_\omega = \frac{\omega}{2\Omega}$	[-]
c	chord	[m]
D	diameter	[m]
D	drag force	[N]
D_0	zero-lift drag force	[N]
D_i	lift-induced drag force	[N]
$\mathrm{d}r$	infinitesimal radial distance	[m]
e	Oswald factor	[-]
F	force	[N]
F_{loss}	propeller loss factor	[-]

f	parameter used for the definition of a propeller loss	[-]
f_{hub}	parameter related to the propeller loss near the hub	[-]
f_{tip}	parameter related to the propeller tips loss	[-]
g	acceleration of gravity	[m/s^2]
h	height	[m]
J	advance ratio $J = \frac{V_\infty}{nD}$	[-]
k	Turbulent kinetic energy	[m^2/s^2]
L	Lift force	[N]
L_F	duct length (equal to its chord, if stagger is 0°)	[m]
M	Mach number	[-]
$\dot{m}$	mass flow rate	[kg/s]
n	angular velocity	[revolutions/s]
P	power	[J/s]
P_c	power coefficient $P_c = \frac{P}{q_\infty S_p V_\infty}$	[-]
P_{shaft}	shaft power $P_{\text{shaft}} = \Omega Q$	[J/s] = [Nm/s]
P_{AMB}	ambient pressure (static)	[Pa]
p	pressure	[Pa] = [N/m^2]
p_{dwn}	pressure immediately downstream of the propeller	[Pa]
p_s	static pressure	[Pa]
p_t	total pressure	[Pa]
p_{up}	pressure immediately upstream of the propeller	[Pa]
Q	torque	[Nm]
Q_c	torque coefficient $Q_c = \frac{Q}{q_\infty S_p R_p}$	[-]
q	dynamic pressure $q = 1/2\rho V^2$ (incompressible eq.)	[Pa]
r_h	radius of the hub	[m]
R	radius of the propeller	[m]
r	radial position	[m]
S	surface area	[m^2]
S_{duct}	duct projected area $S_{duct} = Dc$	[m^2]
S_{ref}	reference area	[m^2]
T	thrust	[N]
T_c	thrust coefficient $T_c = \frac{T}{q_\infty S_p}$	[-]
T_{duct}	thrust of the duct	[N]
T_{NET}	net thrust (for a ducted propeller: $T_{\text{NET}} = T_{\text{duct}} + T_{\text{prop}}$	[N]
T_{prop}	thrust of the propeller	[N]
T_{system}	thrust of the propulsion system	[N]
U	axial velocity	[m/s]
U_∞	free-stream axial velocity	[m/s]
V	velocity	[m/s]
V_a	axial induced velocity by the propeller, at its location	[m/s]
V_a	axial flow velocity	[m/s]
V_{eff}	effective velocity	[m/s]
V_{F}	induced axial velocity by the ring wing	[m/s]
V_t	induced tangential velocity by the propeller	[m/s]

V_∞	free-stream velocity	[m/s]

GREEK SYMBOLS

Symbol	Definition	Units
α	angle of attack	[°]
α_0	zero-lift angle of attack	[°]
β	blade section pitch angle	[°]
$\beta_{3/4}$	blade section pitch angle at 3/4 radius	[°]
Γ	circulation	[m^2/s]
ΔP_t	total pressure jump	[Pa]
δ	increment in axial velocity due to the airfoil ring	[-]
δ_0	increment in axial velocity due to the isolated airfoil ring	[-]
δ_1	increment in axial velocity due to the airfoil ring's interference with the propeller slipstream	[-]
δ_h	horizontal vane's control surface deflection	[°]
δ_tip	gap between blade tip and duct, or tip clearance	[-]
ζ_w	Weissinger's section-lift reduction factor	[-]
η_prop	propeller efficiency $\eta_\mathrm{prop} = \frac{V_\infty T}{P_\mathrm{shaft}}$	[-]
η_F	froude efficiency	[-]
θ	azimuthal location	[°]
Λ	stagger angle	[-]
λ_i	internal advance ratio	[-]
μ	dynamic viscosity	[$Pa \cdot s$]
ν_t	eddy viscosity	[m^2/s]
ρ	density	[kg/ m^3]
ρ_0	reference density	[kg/ m^3]
τ_w	skin friction	[Pa]
φ	local inflow angle	[°]
ϕ	propeller phase angle	[°]
ϕ	spanwise location $\phi \equiv l_p/(p_{duct}/4)$	[-]
Ω	angular velocity	[rad/s]
ω	vorticity	[1/s]
ω	specific dissipation rate	[1/s]

ABBREVIATIONS

2D	two-dimensional
3D	three-dimensional
AD	actuator disk
AVL	Athena Vortex Lattice program
BC	boundary condition
BE	blade element theory
BEM	blade element and momentum theory
BHP	brake horsepower

BL	boundary layer
CAD	Computer-aided design
CFD	Computational Fluid Dynamics
DNS	Direct numerical simulation
DUUC	Delft University Unconventional Concept
FPS	feet per second
GCI	Guide convergence index
HWA	Hot wire Anemometry
LES	Large Eddy simulation
LDV	Laser Doppler Velocimetry
LPD	Large propeller domain
MRF	Multiple reference frame
OEI	one engine inoperative
OR	open rotor
OJF	Open jet facility
OTW	over the wing
PIV	particle image velocimetry
RANS	Reynolds-averaged Navier-Stokes
Re	Reynolds number
RPM	rotations per minute
SCEPTOR	NASA's Scalable Convergent Electric Propulsion Technology Operations Research
sPD	small propeller domain
SST	Shear stress transport
TU Delft	Delft University of Technology
UAV	unmanned aerial vehicle
UDF	user defined function
URANS	Unsteady RANS
VTOL	vertical take-off and landing

SUMMARY

Propellers were the first means of propulsion for aircraft. However, their development was abandoned in the 1950s due to the growth of interest in jet propulsion. In the 70s, the oil crisis renewed the importance of propeller propulsion. This was due to the high efficiency of these propulsion systems. In more recent years, both the motivation to reduce aircraft's fuel costs and the willingness to decrease the environmental footprint of air travel have raised the importance of propeller research.

With the goal of further increasing propellers efficiency, ducts emerge as an appealing option. Indeed, these were found to be able to increase the thrust to power ratio of a propeller system by both producing thrust and/or lowering the tip losses of propellers. Literature indicates that the advantages of ducting a propeller are most noticeable at low free-stream Mach numbers, when the propeller is able to cause a stronger slipstream contraction. Furthermore, ducts can increase the safety and decrease noise emissions of propellers. With all their advantages, ducted propeller systems have also been appealing for rather unconventional aircraft designs. One example is the Delft University Unconventional Concept (DUUC), in which two ducted propellers are present at the aft fuselage, and are also integrated with a control and stability system. For control and stability of the aircraft, it could be beneficial if the duct could have a shape different than the usual circular shape (e.g. square). However, the studies found in literature only refer to circular ducts, reason for which it would have been difficult to estimate the impact of such a modification in the propulsive performance of the system. Furthermore, also distributed propulsion systems using propellers have gained interest in the past years. Distributed propeller propulsion systems could also benefit from having a square duct around each propeller, instead of a circular duct around each propeller. This could reduce both the weight and the wetted area of the system.

With the aim of understanding the possible impacts of modifying a propeller duct shape from a circular to a square geometry, RANS CFD simulations were used to compute the flowfields of the different configurations tested. Firstly, the isolated circular and square ducts were simulated, as well as the isolated propeller, in order to characterize their isolated performance. Besides simulating the propeller with a conventional (radially large) propeller domain, this component was also studied with radially smaller propeller domain, in order to evaluate if this unconventional domain could be used in full blade model ducted simulations, inside the duct. Afterwards, the installed configurations were considered. Each duct was first tested with an AD model simulating the performance of the propeller, for which the inputs obtained from the isolated propeller configurations were used. The steady AD simulations were used to understand the impact caused by the propulsor on each duct, at different power settings. Afterwards, each installed duct system was simulated using the full blade model of the propeller, with an unsteady simulation. Due to the high computational costs of the unsteady ducted full blade model simulations, only one operating condition was tested, characterised by the propeller's advance ratio $J = 0.7$.

The results obtained from the isolated ducts simulation showed differences in the drag of the two components. The larger wetted area of the isolated square duct was found to be the dominant contributor for this difference in drag. Nevertheless, the results also indicate that separation occurs at the corner of the square duct, near the trailing edge. This phenomenon also contributes towards the increase in pressure drag of the component. Besides, the boundary layer at the square duct's corner was found to be considerably thicker than at other spanwise locations, which indicates that the square duct's BL is more prone to separation at the corner. Literature relative to corner flows also indicates a that the BL height is expected to be larger at geometry corners. Moreover, the simulation of the isolated ducts also suggested that there should be differences in the performance of the propeller inside each duct. Firstly, the axial flow velocity at the propeller disk location was found to be higher inside the circular duct. Secondly, the axial velocity of the flow was found to be uniform inside the circular duct (in the azimuthal direction), but was found to vary inside the square duct. Therefore, the results of the isolated ducts indicated that the propeller could be able to produce more thrust inside the square duct, but that the loading on the blades would vary in time for this configuration.

The results of the isolated propeller simulations also led to interesting conclusions. Firstly, the results obtained with the conventional propeller domain were verified and validated. Afterwards, the results obtained with the small propeller domain were analysed, which led to the conclusion that this unconventional domain is inappropriate for the calculation of a propeller flowfield with the steady MRF approach. Nevertheless, the sliding mesh unsteady calculations performed with both domains showed good agreement, which led to the conclusion that the sPD could still be used for unsteady calculations of the ducted systems' performance.

After characterizing the isolated components performance, the installed configurations were considered. The AD steady simulations indicate that the circular duct considered is able to produce more thrust than the square duct. Firstly, the results indicate that the square duct corner sections, which are further away from the AD, feel a lower change in effective angle of attack, which is the main reason for the production of thrust by a propeller duct. Secondly, a relatively large region of reversed flow was found at the ducts corner, with axial separation starting at 30% duct chord. Finally, the square duct was found to generate strong vortices at its corner, which also lead to a decrease in performance.

The results obtained from the simulation of the circular and square ducts with the full blade propeller model are in agreement with the hypothesis formed by analysing the AD simulations, that using a square duct leads to a decrease in propulsive performance. Nevertheless, since the performance of the propeller is also influenced by the duct's flowfield, the estimated differences in performance between the two ducted systems were smaller for the full blade model simulations. The thrust of the propeller inside the circular duct was indeed found to be lower than inside the square duct, due to the differences in axial inflow velocities. Moreover, the thrust of the propeller was found to vary depending on the blade's azimuthal location, as suggested by the analyse of the isolated duct results. Besides the variation of axial inflow velocity during the blade's rotation, the variation of tip clearance was also confirmed to affect the thrust produced by the blades at each azimuthal location, inside the square duct. Overall, the efficiency of the square ducted propeller was estimated to be 4.5% lower than the efficiency of the circular ducted propeller, at $J = 0.7$ and 30m/s. At this operating condition, both systems were estimated to be producing a similar thrust, since the thrust calculated for the circular duct was only 0.4% lower than the thrust of the square duct system.

The present study has contributed towards a better understanding of the performance of unconventional square duct designs. The results indicate several disadvantages of the square duct tested with respect to the conventional circular duct. Nevertheless, future study should still be performed in the topic. At higher Mach numbers, when slipstream contraction caused by propellers is lower, unconventional aircraft featuring distributed propulsion systems could still benefit from the usage of square (or rectangular) ducts instead of a circular duct around each propeller. At an operating condition where the ducts produce drag instead of thrust, decreasing the wetted area of the ducted system can still help improving the aerodynamic performance of the aircraft. The present study indicates that the duct corners of such a configuration should be carefully designed, in order to minimise separation and the strength of the corner vortices.

I

BACKGROUND

1

INTRODUCTION

The first aircraft built made use of propellers as a propulsion mechanism. However, the need for faster aircraft, and, with it, more powerful engines, made the aerospace industry turn its major investments and research into the development for jet engines in the 50s. Recent greater concern for the climate effects caused by aviation, combined with the need for lowering fuel consumption since the oil crisis in the 70s, have since then driven the sector into the investigation of more efficient means of propulsion. For this reason, propellers have again been largely studied worldwide for the past decades. Still with the lowering fuel consumption goal in mind, ducts appear as a mean of increasing the efficiency of propellers. Indeed, there are several examples of recent usage of ducted propellers that justify its deeper understanding and an investment in its research. Some of these are for maritime applications (studied e.g. by Oosterveld [40]), unmanned aircraft vehicles (UAVs) [27], distributed propulsion concepts such as the Lilium Jet [54], or even 'propulsive empennage' projects such as the Delft University Unconventional Concept (DUUC, shown in Figure 1.1) [22]. Further than increasing the propulsive efficiency of the system, other commonly referred advantages of shrouded propellers are the shielding of the propeller for protection, and noise reduction [15]. In this report, the terms duct and shroud are used with the same meaning.

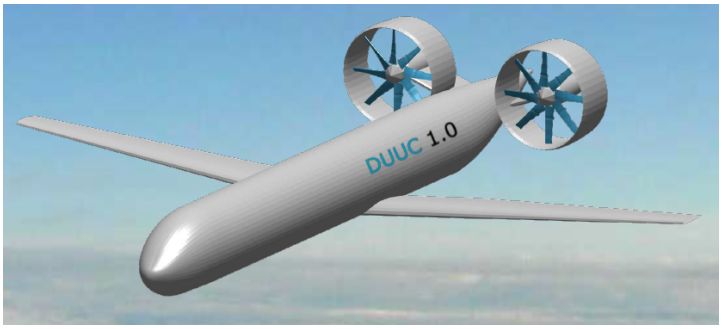

Figure 1.1: DUUC aircraft with ducted propellers for propulsion, control and stability [58].

1.1. HISTORY OF DUCTED PROPELLERS

In the history of aviation, the ducted propeller concept is considerably old. Hitchens traced these back to 1910, when the Bertrand Monoplane was built [13]. This aircraft made use of both a tractor and a pusher propellers inside a single duct. In 1933, there was already clear evidence of the potential of increasing propeller efficiency with a shroud. Popular Science magazine [12] referred that the "speed of an airplane may be increased from thirty-nine to 140 percent by putting a ring around the propeller". This improvement in the propulsive efficiency, however, seems to be excessively optimistic. If it is considered that the drag of an aircraft varies approximately proportionally to the square of its velocity (in the subsonic regime), a 100 percent increase in velocity would result in 4 times the drag, reason for which a 4 times greater thrust would also be required. Another interesting fact of this invention patented by Carl E. Hall, was that it also included vanes

inside the duct which could be shifted to increase the airplane's drag during landing (see Figure 1.2).

In the 1950s, a vertical take-off and landing (VTOL) vehicle making use of ducted propellers also appeared. This was the Hiller 1031 flying platform (Figure 1.3). Using counter-rotating propellers for propulsion, it also relied on the duct to produce 40% of the total thrust [15]. This was mainly possible due to the shape of the lip of the duct. In this region the air sucked by the system would be further accelerated to produce a region of lower pressure, which contributed to the total trust of the aircraft. The Hiller flying platform was, however, excessively stable. For this reason, horizontal travel was difficult, and the project was eventually abandoned. Nevertheless, recent duct designs still make use of thrust produced at its inlet, due to generated lower pressures. One example is the shroud optimised for the UAV MOSUPS [27]. However, this increase in thrust at the duct is dependent on the slipstream contraction caused by the propeller. For this reason, it is specially beneficial at static conditions, losing relevance at higher free-stream Mach numbers. Indeed, at greater velocities the slipstream contraction is lower.

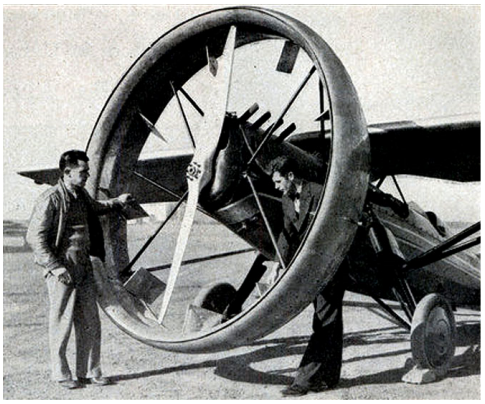

Figure 1.2: Aircraft propeller cowling patented by C. E. Hall [12].

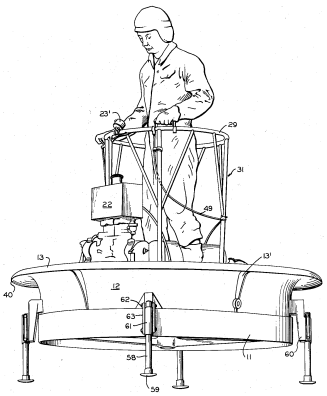

Figure 1.3: Hiller 1031 Flying platform [47].

Nowadays, intensive research regarding shrouded propellers is being conducted. For instance, the DUUC model developed at TU Delft is powered by two ducted propellers at the aft end of the fuselage. This way, it is possible to incorporate control surfaces in the duct, so that an horizontal and vertical tail are unnecessary [22]. In the scaled model already tested, control surfaces are located inside the duct, aft of the propeller, as shown in Figure 1.4. However, the future plans for the model include modifying this characteristic. It is intended to test the aircraft with control surfaces integrated in the duct surface, as can be seen in Figure 1.5. This control system, therefore, would benefit from the use of a quadrangular duct, for greater efficiency of the control surfaces. Furthermore, N. van den Dungen has estimated that DUUC's 'propulsive empennage' would not be favourable when compared to a conventional tail design [58]. The reason given for this was the excessive weight caused by the aft propulsive system, which would result in a large shift of the aircraft's centre of gravity. Therefore, the interest in understanding the aerodynamic implications of using a quadrangular duct is increased. In case this unconventional duct could be used without a large negative impact on propulsive performance, the potential benefits for control and stability of the aircraft, including a decrease in its complexity, could result in a reduction of duct's weight. The importance of studying unconventional propeller shrouds is again justified.

Propeller duct systems have also gained the interest of distributed propulsion projects. One example of this is the Lilium jet aircraft, which can be seen in Figure 1.6. However, this aircraft makes use of a circular shroud around each propeller system, resulting in added weight. Therefore, for projects of this nature, it would also be beneficial to understand how the propellers would interact with an unconventional duct shape. Distributed square ducts, or a large rectangular duct enclosing all the propellers, would be interesting design alternatives to the solution found by Lilium jet.

Even though considering propfans is out of the scope of this thesis, it is important to refer that the applications of shrouds also extend to the design of these state-of-the-art advanced turboprop systems. One example is the NK-93 (Figure 1.7), a shrouded propfan developed by the Kuznetsov Design Bureau.

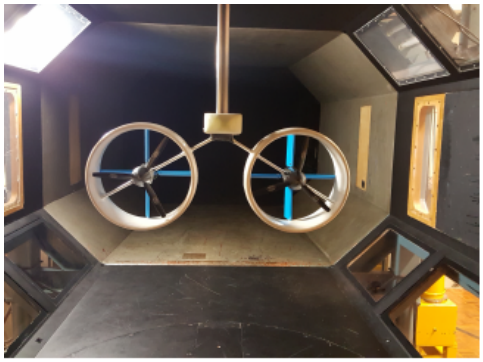

Figure 1.4: Propulsive system of the DUUC, with control surfaces inside the duct [22]

Figure 1.5: DUUC shroud with the control surfaces (shown in blue) incorporated at its surface. Adapted from [57].

Figure 1.6: Lilium jet distributed propulsion concept [54].

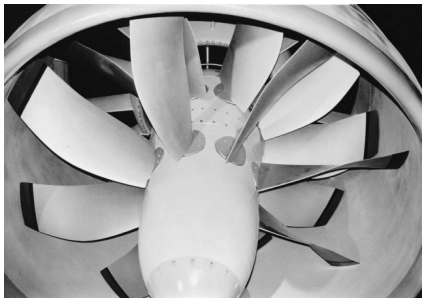

Figure 1.7: NK-93 advanced turboprop [53].

1.2. RESEARCH PLAN

One interesting fact found in literature, is that usually it is opted for shielding the propeller with a circular ring. Indeed, this has the obvious advantage of enabling the decreasing of the gap between the propeller and duct, this way lowering the tip vortices on the propeller and further increasing propulsive efficiency. However, there are cases when other duct shapes could be beneficial. For example, on aircrafts with a 'propulsive empennage', a quadrangular duct could be used to improve the control surfaces' efficiency. On distributed propulsion concepts, a rectangular duct could be used to cover several ducts, this way saving the weight of having a duct around each propeller. However, unconventional propeller duct shapes have not been widely studied, causing a barrier to its implementation on new aeronautical projects. For this reason, it is considered relevant to investigate the performance of ducts with a shape different than the common circular one. Therefore, an opportunity for a Masters thesis project arose within this topic.

The thesis was outlined with the aim of contributing to the fundamental understanding of the aerodynamic implications of different duct designs. In this way, the project focused on the aerodynamic differences between a conventional circular ducted propeller and a square ducted propeller systems. Using computational fluid dynamics, the flow around both ducts was simulated in an isolated case, and also for power on conditions. Even though it is expected that a circular shape of the shroud would result in higher thrust to power ratio of the system than unconventional ducts, a deeper understanding of their differences can still help deciding upon the use of a less efficient duct. In that case, a trade off would have to be made between the estimated loss in propulsive efficiency and other advantages of the unconventional shroud design.

Based on the previously explained motivation, a research objective was defined:

> *The aim of the thesis project is to achieve a deeper understanding of the fundamental aerodynamic effects present in an unconventional propeller duct design (square), by performing CFD simulations.*

Based on this objective, a research question was elaborated, along with several sub-questions. The main research question is:

> *How does the performance of square duct designs, for single-propeller concepts, compare with the conventional circular duct?*

The research work was organised based on following research questions:

- How does the aerodynamic performance of an isolated square duct compare to the performance of a conventional circular duct?
  - How can the main differences in the drag of both designs be justified?
  - How does each duct affect the flowfield at the propeller location, inside the shroud?
- How does the performance of a propeller in a square duct compare with a circular duct system?
  - Which steady aerodynamic effects affect the performance of the quadrangular ducted propeller system?
  - Which aerodynamic interference effects are dominant between the propeller and the quadrangular duct, considering the unsteady effects caused by the rotation of the blades?
  - How does the overall performance of the different propulsive systems compare at the specific operating conditions tested, considering the isolated propeller, the circular ducted propeller and the square ducted propeller?
- How well do the numerical methods used perform in terms of accurately predicting the aerodynamic characteristics of the different flowfields?
  - How well does the turbulence model used represent the aerodynamic characteristics of the flowfield?
  - How well do the results from the two different domains used to model the isolated full blade propeller model compare, considering both steady and unsteady simulations?
  - How does the estimated performance of each installed system modelled with an actuator disk compare to the performance estimated with a complete propeller model?

1.3. THESIS OUTLINE

The project started with a literature review under the topics aerodynamics of propellers and ducted fans. Based on the literature review, the thesis research questions were elaborated, along with the methodology to be followed. The approach consisted on successively performing CFD simulations on the different test cases. For each case, the computational domain was created, the mesh was generated, the simulation was run in the solver, and the results were preliminarily post-processed, before moving to the next test case. The thesis test matrix consisted of different geometries, with different levels of complexity. Therefore, the simulations were ordered from simplest to the most challenging ones. This had two advantages: the flowfield and aerodynamic phenomena obtained from each simulation was easier to be understood, and the complexity of the simulations followed the author's learning curve. Exemplifying, the first test case referred to a 2D steady axisymmetric simulation of the circular duct, and the last case referred to a 3D unsteady simulation of the propeller shrouded by the square duct. The final post-processing of the results was performed in parallel to the report and comparison of the findings.

In this report, the main findings from the literature study are presented in chapter 2. Chapter 2 also intends to provide the reader with the necessary theoretical background to understand the project work. Afterwards, Part II of the report explains the project's methodology. Chapter 3 relates to the numerical modelling of the flow with CFD. This chapter explains why the thesis was based on CFD simulations. This justification is

then followed by a discussion of the main choices regarding how the flowfields were modelled with CFD (e.g. choice of the governing equations). Chapter 4 provides a more detailed overview of the approach followed. The chapter specifies the test matrix followed, and discusses how the numerical methods chosen in the previous chapter were applied.

In Part III, the thesis' results are shown and discussed. Chapter 6 presents the results relative to the isolated configurations. Subsequently, Chapter 7 analyses the results obtained with the simulation of the installed configurations. Finally, Part IV shows the main conclusions of the research, along with the recommendations for future study.

2

AERODYNAMIC BACKGROUND

In this chapter, it is intended provide theoretical background on the aerodynamics of propellers (section 2.1) and ducts (section 2.2). Also, several definitions are given, such as aerodynamic coefficients or performance indicators. These definitions are used throughout the report as defined in this chapter.

2.1. AERODYNAMICS OF PROPELLERS

In this section is explained how propellers produce thrust, and the main aerodynamic phenomenon that occur. Also, studied interference effects regarding propellers are explained. First, it is important to introduce some of the main variables and coefficients for characterizing propellers.

The thrust, torque and power coefficients are defined as:

$$T_c = \frac{T}{q_\infty S_p} \quad , \tag{2.1}$$

$$Q_c = \frac{Q}{q_\infty S_p R_p} \quad , \tag{2.2}$$

and:

$$P_c = \frac{P}{q_\infty S_p V_\infty} \quad , \tag{2.3}$$

where q_∞ is the free-stream dynamic pressure, S_p is the propeller disk area, R_p is the propeller radius, T is the thrust of the propeller, Q is the propeller's torque, and P is the Power. The shaft power delivered to the propeller is given by:

$$P_{shaft} = \Omega Q \quad , \tag{2.4}$$

where Ω is the rotational speed of the propeller in radians per second. Based on the later definition, it is possible to calculate the efficiency of a propeller:

$$\eta_{prop} = \frac{V_\infty T}{P_{shaft}} \quad , \tag{2.5}$$

where V_∞ is the free-stream velocity. Another important parameter for the analysis of propellers is the advance ratio, J, which relates the free-stream velocity and the tangential velocity at the propeller tip. It is defined as:

$$J = \frac{V_\infty}{nD} \quad , \tag{2.6}$$

where n the rotational speed of the propeller in revolutions per second and D the propeller diameter.

2.1.1. MOMENTUM THEORY

With momentum theory, it is possible to calculate the thrust produced by a propeller using the momentum given to the fluid by the propeller. Considering a closed control surface S, a force ($\boldsymbol{F}$) acting on a fluid can be calculated from the momentum theorem [60]:

$$\boldsymbol{F} = \int_S (p\boldsymbol{n} + \rho \boldsymbol{n} \cdot \boldsymbol{v}\, \boldsymbol{v}) dS \quad , \tag{2.7}$$

assuming steady flow. In this equation, p stands for pressure, $\boldsymbol{n}$ is the unit vector normal to the surface S, directed outwards, and $\boldsymbol{v}$ is the velocity at S. In momentum theory, it is considered a control volume which encloses the propeller streamtube. This region can be visualized in 2D in Figure 2.1, where the propeller is represented as an actuator disk. The streamwise limits of this control volume are set when the inflow velocity is equal to the free-stream velocity (upstream limit) and when the slipstream static pressure is equal to the free-stream static pressure (downstream limit). This way, it is possible to simplify the previous equation to:

$$F = \rho A_{out} V_{out} (V_{out} - V_\infty) \quad , \tag{2.8}$$

where V_{out} is the velocity in the slipstream far from the propeller, where the static pressure has already equalled the free-stream static pressure. A_{out} is the area of the slipstream at the same location. Since the force acting on a fluid in this representation is indeed the thrust force, T, it can be written:

$$T = \rho A_{out} V_{out} (V_{out} - V_\infty) \quad . \tag{2.9}$$

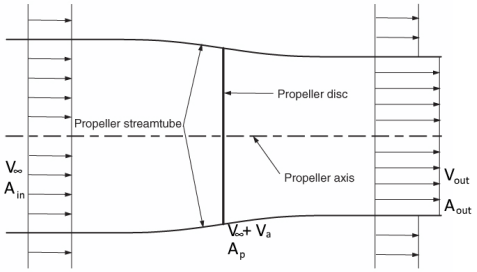

Figure 2.1: Representation of the propeller inflow and slipstream. Adapted from [38].

The propeller slipstream contraction seen in Figure 2.1 is present due to the fact that there has to be conservation of mass in the stream-tube, while the velocity is increasing. Therefore, at any location in the stream tube, its area times the velocity has to be constant:

$$\rho AV = constant = \dot{m} \quad . \tag{2.10}$$

where $\dot{m}$ is the mass flow rate. Furthermore, the conservation of mass implies that the increase in velocity at the actuator disk (AD) has to be 0, assuming that ρ stays constant. If a control surface is chosen with streamwise limits directly upstream and downstream of the AD, i.e. with an infinitesimal width, equation 2.7 simplifies to:

$$F = (p_{dwn} - p_{up}) A_p \quad , \tag{2.11}$$

and therefore:

$$T = (p_{dwn} - p_{up}) A_p \quad , \tag{2.12}$$

where p_{dwn} and p_{up} are the pressures immediately downstream and upstream of the propeller, respectively, and A_p is the prop disk area. This means that the propeller can be represented as a static pressure jump in the fluid, which causes the fluid to accelerate before and after the propeller. For a more accurate representation of a fan by an actuator disk, the jump in tangential velocity (V_t) caused by the propeller may also be included in the model.

2.1.2. BLADE ELEMENT THEORY

In this section, the main aspects of the blade element (BE) theory are presented. This simplified model can give a valuable understanding on how propellers operate. BE theory is also extremely useful for early stages of propeller design, specially when combined with momentum theory. Examples of its application can be found for aircraft propellers [30], maritime props [2] and wind turbines [24].

The blade element theory is based on using various annular stream-tube control volumes. At the propeller, these divide the blades into several sections of width dr, which have an airfoil shape. Then, for each of these elements, the incoming velocity components are estimated and the 2D lift and drag are calculated, based on the airfoil properties. Within this estimation, the induced velocities, V_a and V_t, have to be iteratively predicted at each blade element. Indeed, these velocities influence the aerodynamic forces at the airfoil, but also depend on them. For this calculation of the induced velocities, blade element theory is combined with the momentum theory. After calculating the lift (L) and drag (D) of the element, it is possible to find the thrust (T) and torque (Q) components of the resultant force at the element. For a better understanding, the induced velocities, the free-stream velocity (V_∞), the section rotational velocity (Ωr) at the element radial location (r), the effective velocity (V_{eff}) and the referred forces are plotted in Figure 2.2. The local inflow angle (φ), the element angle of attack (α) and the blade section pitch angle (β) are also shown.

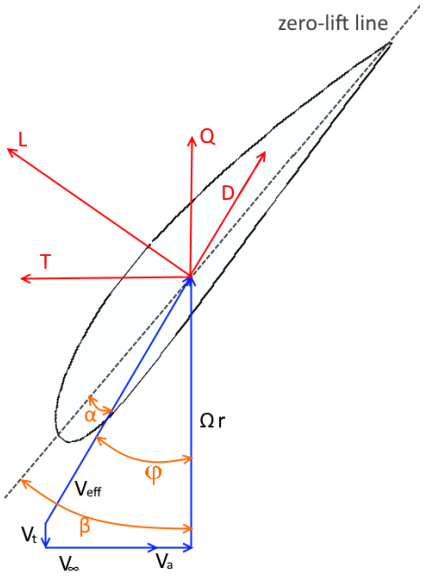

Figure 2.2: Blade element velocities, angles and forces.

From a trigonometric analysis of the later figure, it is possible to calculate the inflow angle, φ, using:

$$\tan\varphi = \frac{V_\infty + V_a}{\Omega r - V_t} \quad , \tag{2.13}$$

The thrust and torque of each element (respectively dT and dQ) of with dr are then calculated from:

$$dT = (dL\cos\varphi - dD\sin\varphi)dr \quad , \tag{2.14}$$

and:

$$dQ = (dL\sin\varphi + dD\cos\varphi)r\,dr \quad . \tag{2.15}$$

Or, from the circulation at the element, the thrust and torque can be calculated from [60]:

$$dT = \rho\Gamma(\Omega r - V_t)dr \tag{2.16}$$

and:

$$dQ = \rho\Gamma(V_\infty + V_a)r\,dr \quad . \tag{2.17}$$

Having estimated the thrust and torque for each element, it is possible to calculate the overall T and Q of the propeller from:

$$T = B\int_{r_h}^{R} dT\,dr \tag{2.18}$$

and:

$$Q = B\int_{r_h}^{R} dQ\,dr \quad , \tag{2.19}$$

where r_h is the radius at the hub, R is the radius of the blade at the tip, and B is the number of blades.

Even though the blade element theory can provide a valuable estimation of propeller characteristics, it also has its own limitations. These include neglecting radial flow over the propeller, disregarding mutual interference between blade elements as well as losses at the blade tips and at low radial positions, near the hub. However, these losses can be modelled with a relevant accuracy by adding loss factors to the blade element theory.

LOSS FACTOR

In this sub-section, the loss factors which can be incorporated into the blade element method are discussed. Near the tip of the blades, there is a loss in circulation due to the finite effects. This is similar to a finite wing, where, near the tip, the air flows from the region of higher pressure (lower surface) to the region of lower pressure (upper surface). This generates a vortex, loss of lift near the tip, and induced drag for the wing. To model this effect on propellers, the tip-loss correction factor initially developed by Prandtl can be used [45]. This translates in a loss in circulation that depends on the radial position of the element that is being considered, on its 2D aerodynamic characteristics (lift and drag polars) and on the effective incoming velocity. As the circulation also affects the induced velocity at each element, an iterative approach is required. The loss factor (F_{loss}) can be defined as [45]:

$$F_{\text{loss}} = \frac{2}{\pi}\arccos e^{-f_{\text{tip}}} \quad , \tag{2.20}$$

where f_{tip} is:

$$f_{\text{tip}} = \frac{B}{2}\frac{R-r}{r\sin\varphi} \quad , \tag{2.21}$$

R is the prop radius, and φ is the local inflow angle. This tip-loss however, can be considerable attenuated. Similarly to the effect of winglets on wings, which lower the lift induced drag and the vortex generation near the tips, a duct around a propeller can lower the flow of fluid from the pressure side of the blade to the suction side. This effect increases the loading near the blade tips, raising the effective disk area of the propeller. For this effect, the gap between the duct and the propeller tips is extremely relevant. Larger gaps result in an approximation of the system to the unducted prop case, with greater tip losses [36].

Besides the tip losses, a decrease in circulation also occurs at low radial locations, due to the proximity to the hub. Indeed, the vortex shed from the hub results in a decrease in circulation of the nearby blade sections. This effect can be modelled similarly to the tip-loss, if, in equation 2.20, f_{tip} is substituted by:

$$f_{\text{hub}} = \frac{B}{2}\frac{r-r_{\text{hub}}}{r\sin\varphi} \quad , \tag{2.22}$$

where r_{hub} is the hub's radius.

2.1.3. SLIPSTREAM

In this subsection, greater insight is given into the slipstream of propellers. In section 2.1.1 it was already referred that a propeller causes a static pressure jump on the flow, therefore causing an acceleration of the flow upstream and downstream of the propeller. The increase in velocity is associated with a contraction of the stream-tube, as there has to be conservation of the mass flow. The static pressure jump represents a total pressure jump of equal value, since there is no change in flow velocity at the propeller. Upstream

and downstream of the propeller, where the total pressure remains constant, Bernoulli's equation has to be satisfied:

$$p + 1/2\rho v^2 + \rho g h = \text{constant} \quad , \tag{2.23}$$

where p is the static pressure, v is the fluid velocity, g is the acceleration of gravity and h is the height, relating to a reference plane. The term $\rho g h$, however, can be neglected for the analysis of propeller slipstreams, where it usually experiences very small variations.

This way, the change in pressure and in axial velocity along a propeller streamtube can be represented as shown in Figure 2.3. From this Figure, it should also be noticed that the increase in axial velocity is V_a at the propeller, and $2V_a$ far downstream, where the static pressure equals the freestream static pressure. In the following Figure (2.4), it can be seen that the induced velocities at the propeller, V_a and V_t, vary with radial position. The value at each radial location greatly depends on the circulation over that element. Similarly, the jump in static and, therefore, total pressures at the propeller is non-uniform.

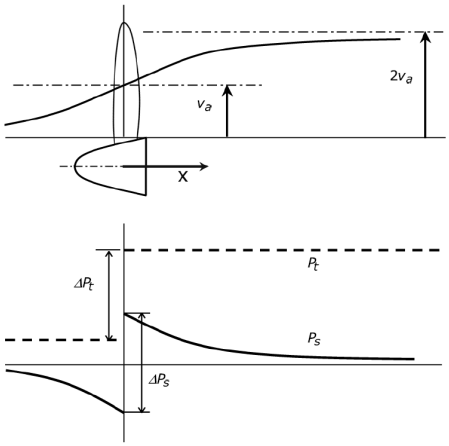

Figure 2.3: Increase in flow velocity, static and total pressure across the stream-tube [59].

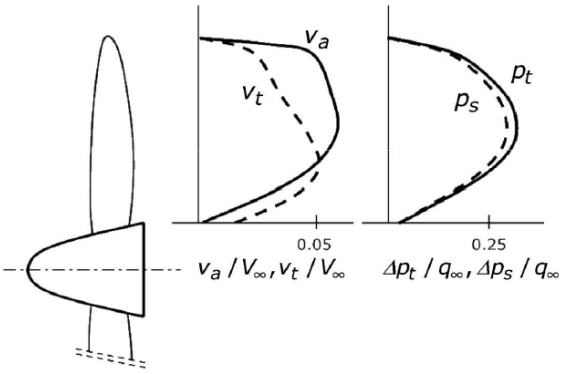

Figure 2.4: Schematic representation of the increased axial flow velocity, v_a, tangential flow velocity, v_t, static pressure, Δp_s, and total pressure, Δp_t, at the propeller location depending on radial position [59]. The propeller is represented on the left. v_a and v_t are respresented with respect to the free-stream velocity, V_∞, and Δp_s and Δp_t are represented with respect to the free-stream dynamic pressure q_∞.

Furthermore, the slipstream of a propeller also has periodic unsteady characteristics. This is due to the fact that the flow aft of the propeller varies depending on the instantaneous tangential distance to the blades, which are rotating. However, in the limit situation of a propeller with an infinite number of blades, the slipstream can then be assumed to be axisymmetric. This is the case of a fan modelled as an actuator disk, which causes a steady axisymmetric stream-tube, unless there is interference with other components. Li et al. studied the differences between the flow of a full propeller and an actuator disk model of the same propeller, in order to validate their AD model [3]. The AD was modelled with a blade element and momentum theory method (BEM) for determining induced velocities at the disk, as well as the corresponding pressure jump. The results of the research indicated that the flow of the full blade simulation resembles the AD's axisymmetric flow from $1R$ downstream of the propeller [3]. However, this value might vary for different propellers, inflow conditions, and power settings.

In this research, it is considered what is defined in [15] as a shrouded propeller: a propeller inside a shroud of length lower or equal to the propeller diameter, in contrast to a longer duct or a fan entirely buried inside the aircraft's structure. This is also the case of, for example, the DUUC's ducted propeller [22]. For this reason, it was foreseen that the propeller's unsteady slipstream would be present at a relatively large percentage of the duct's length. Therefore, it was expected that a full blade simulation of a propeller inside a shroud would give more accurate results than an AD simulation.

VORTICITY IN THE SLIPSTREAM

The slipstream of a propeller is also characterized by the vortices it contains. Vorticity can be defined as:

$$\omega = \nabla \times V = \begin{pmatrix} \omega_x \\ \omega_y \\ \omega_z \end{pmatrix}. \tag{2.24}$$

Even though the vorticity generated by the propeller is an unsteady phenomenon, the vorticity pattern in the slipstream is expected to be repeated periodically. This is due to the periodic nature of the propeller blades' rotation. In Figure 2.5, the axial components of vorticity in the slipstream of a 4-bladed propeller are shown. Firstly, it is clear that the vorticity in the x direction is the only axis-symmetric component. Secondly, the three vorticity components were found to have relatively similar magnitudes [59]. For a ducted propeller, the characteristics of the vortices generated by the propeller were also expected to have an impact on the performance of the system.

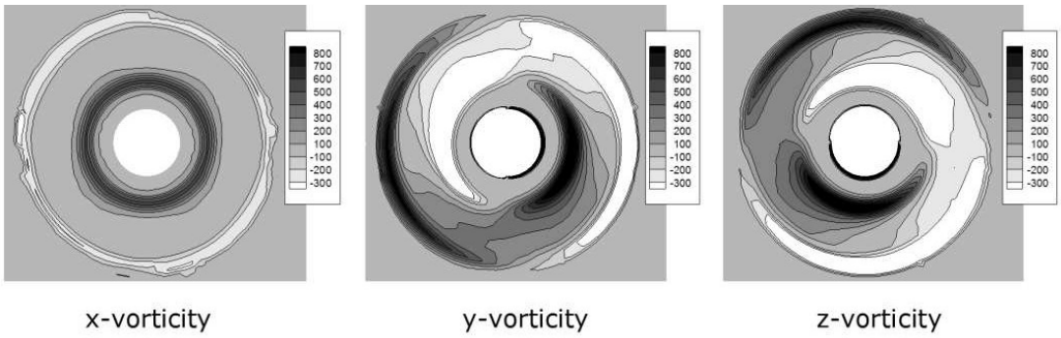

Figure 2.5: Distributions of ω_x, ω_y and ω_z immediately aft of a 4-bladed propeller [59].

2.1.4. PROPELLER EFFICIENCY

This subsection aims at providing a better understanding of the propeller's efficiency as a performance evaluation parameter. It is also compared with the thrust to power ratio, in order to understand which parameter would be more relevant to the comparison of different systems, or distinct operating conditions.

The efficiency of a propeller was defined as the ratio between the useful power and the power provided by the shaft (equation 2.5). It is also possible to calculate the Froude efficiency (η_F) of a propeller propulsion system as the ratio between the useful power and the rate of increase in axial kinetic energy in the far downstream slipstream [6]:

$$\eta_F = \frac{TV_\infty}{T(V_\infty + V_a)} = \frac{1}{1 + \frac{V_a}{V_\infty}} \quad . \tag{2.25}$$

Since, for propellers:

$$V_{out} = V_\infty + 2V_a \quad , \tag{2.26}$$

the Froude efficiency is given by:

$$\eta_F = \frac{2}{1 + \frac{V_{out}}{V_\infty}} \quad . \tag{2.27}$$

From this Froude efficiency equation, it is possible to understand why it is assumed that a propulsive system which produces thrust by giving a lower increase in velocity to a larger mass of fluid is more efficient. Indeed, this is the reason why propeller systems are more efficient in their optimum operating conditions (i.e. subsonic regime) than, for example, jet engines. Nevertheless, it is assumed by the author of this study that efficiency as defined in equation 2.5 is more adequate to compare the performance of different prop systems than the Froude efficiency, since it considers the actual power required from the engine, which is greater than the power assumed in Froude's efficiency equation due to losses (e.g. energy lost in increasing V_t). However, equation 2.5 can only be used if the rotational velocity and torque of the propeller are known.

2.2. DUCT AERODYNAMIC EFFECTS

In this section, the aerodynamic impact of having a shroud around a propeller is assessed. This was done based on the studies available in literature. However, the information found only refers to conventional circular ducts. Indeed, propeller ducts are widely defined as annular wings or circular airfoil rings (e.g. [6], [15]). This further justifies the study of unconventional ducts. These can have structural and, in the case of a propulsive empennage, control and stability benefits for an aircraft. However, it is expected that non circular ducts would have a worse aerodynamic performance than conventional shrouds. An obvious reason for this is the greater wetted area of a non-circular duct (e.g. square), when compared to a circular duct which perfectly fits the fan. A larger wetted area necessarily results in more viscous drag.

2.2.1. AIRFOIL RING

To understand the aerodynamics of ducts, first the isolated airfoil ring is considered. This has been vastly investigated, not only motivated by ducted propeller applications, but also by the possibility of using it as a primary lift generator for aircraft. The Bell X-22 aircraft combined both of these possible functions for annular wings (Figure 2.6).

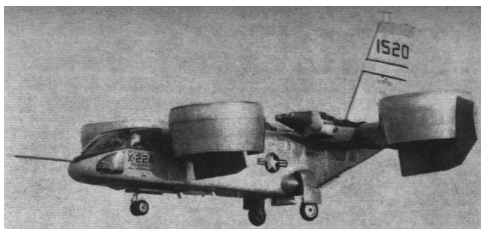

Figure 2.6: Bell X-22 aircraft, which uses ring wings as propeller ducts, as well as primary lifting surfaces during cruise [11].

Ribner [20] studied the behaviour of the annular wing at an angle of attack. For this, lifting-line theory was used. The results obtained were compared to the equivalent for a wing with a span (b) equal to the diameter (D) of the duct, with one quarter of the ring's area and with an elliptical lift distribution. It is interesting to notice that the lift of the annular wing is the double of the lift of the flat wing, for equivalent inflow conditions.

Moreover, ring wings have also been studied experimentally, as it is the case of Fletcher's experimental campaign [19]. This campaign consisted of testing several circular ring wings with the same projected area ($S_{duct} = Dc$). These had, however, different aspect ratios, AR, ranging from 1/3 to 3. For ring wings, the aspect ratio is defined as the ratio between the duct's diameter (D) and its chord (c):

$$AR = D/c \quad . \tag{2.28}$$

One relevant conclusion made from Fletcher's experiments was that the lift curve slope (C_{L_α}) obtained for the ducts was the double of the equivalent planar wing's C_{L_α} [19]. This matches with Ribner's [20] theoretical predictions. Furthermore, it was realised that the induced drag coefficient (C_{D_i}) of the annular wings was approximately:

$$C_{D_i} = \frac{C_L^2}{2\pi AR} \quad , \tag{2.29}$$

which had been estimated previously by another author, according to Fletcher [19]. This increase in induced drag with C_L is half of the increase for a planar wing with the same aspect ratio and with an elliptic lift distribution. This is the optimum lift distribution for planar wings. Therefore, it indicates an advantage of annular wings with respect to conventional planar wings. However, ring wings with the same projected area as a planar wing are expected to provide a greater zero-lift drag (C_{D_0}), due to the larger wetted area. Indeed, the greater C_{D_0} of annular wings as been found to greatly offset their improvement in induced drag [35]. Traub also refers that the Oswald factor (e) calculated from the performed experiments at low Reynolds number was lower than the expected inviscid value ($e = 2$), but still greater than 1 [35]. The Oswald factor is extracted from the equation for the lift induced drag:

$$C_{D_i} = \frac{C_L^2}{\pi e AR} \quad . \tag{2.30}$$

For this reason, Traub's conclusions also suggest that an annular wing is more aerodynamically efficient than a planar wing. However, Wan [61] also studied the lift and drag polars of an annular wing, reaching a different conclusion. Wan considered the obtained e to be low when compared to flat wings, as the calculated value was $e = 0.4899$.

After investigating the possible reasons for this divergence in results found in literature, it was understood that the reference area considered on each study had a great influence. Indeed, most of the studies consider the annular wing's projected area for the lift and drag coefficients (such as Fletcher [19] and Traub [35]). In turn, Wan [61] considers the wing surface area, which is π times larger. This difference invariable results in very different calculated Oswald factors.

As an example, two rectangular wings are considered (wing A and wing B). These have the same symmetrical airfoils, the same aspect ratio and wing B has an area 2 times larger than wing A. If differences due to the Reynolds number are neglected, wing B produces the double of the lift produced by wing A, while generating the double of the zero-lift drag, the double of the lift induced drag and, therefore, the double of the total drag:

$$2L_A = L_B \quad , \qquad 2D_{0_A} = D_{0_B} \quad , \tag{2.31}$$

$$2D_{i_A} = D_{i_B} \quad , \qquad 2D_{total_A} = D_{total_B} \quad , \tag{2.32}$$

considering an equal angle of attack and remaining inflow conditions. The same relations would be obtained for the non-dimentional coefficients of these physical quantities, as long as each wing's area is used for the calculation of its coefficients:

$$C_{L_A} = \frac{L_A}{q_\infty S_A} \quad = \quad C_{L_B} = \frac{L_B}{q_\infty S_B} \quad , \tag{2.33}$$

$$C_{D_A} = \frac{L_A}{q_\infty S_A} \quad = \quad C_{L_B} = \frac{L_B}{q_\infty S_B} \quad , \tag{2.34}$$

where q_∞ is the free-stream dynamic pressure ($q_\infty = 1/2\rho V_\infty^2$). In this case, the lift coefficient curve slope (C_{L_α}) of each wing is also equal for both wings:

$$C_{L_{\alpha_A}} = C_{L_{\alpha_B}} \quad . \tag{2.35}$$

The equation for the lift induced drag:

$$C_{D_{i_A}} = \frac{C_{L_A}^2}{\pi e_A AR} \quad = \quad C_{D_{i_B}} = \frac{C_{L_B}^2}{\pi e_B AR} \tag{2.36}$$

also indicates that the Oswald factor is the same for the two wings ($e_A = e_B$).

In a second case, all these aerodynamic coefficients are non-dimensionalised with the reference area equal to the area of wing A ($S_{ref} = S_A$). In this situation, the lift and drag coefficients of wing B will have double the value of wing A's coefficients:

$$C_{L_A} = \frac{L_A}{q_\infty S_A} \quad , \qquad C_{L_B} = \frac{L_B}{q_\infty S_A} \quad , \tag{2.37}$$

$$C_{D_A} = \frac{L_A}{q_\infty S_A} \quad , \qquad C_{L_B} = \frac{L_B}{q_\infty S_A} \quad , \tag{2.38}$$

and, therefore:

$$2C_{L_A} = C_{L_B} \quad , \qquad 2C_{D_A} = C_{D_B} \quad , \tag{2.39}$$

$$2C_{D_{0_A}} = C_{D_{0_B}} \quad , \qquad 2C_{D_{i_A}} = C_{D_{i_B}} \quad . \tag{2.40}$$

Furthermore, the induced drag of wing B could be calculated from:

$$C_{D_{i_B}} = \frac{C_{L_B}^2}{\pi e_B AR} \quad <=> \quad C_{D_{i_B}} = \frac{(2C_{L_A})^2}{\pi e_B AR} \quad , \tag{2.41}$$

therefore:

$$2C_{D_{i_A}} = C_{D_{i_B}} \quad <=> \quad 2\frac{C_{L_A}^2}{\pi e_A AR} = 4\frac{C_{L_A}^2}{\pi e_B AR} \quad <=> \tag{2.42}$$

$$2e_A = e_B \quad , \tag{2.43}$$

indicating that the larger wing (B) would have a superior aerodynamic efficiency, as the Oswald factor calculated is double the Oswald factor for wing A. If wings with elliptical lift distribution were considered, wing A would have $e_A = 1$ and wing B $e_B = 2$. This large e_B is similar to the values estimated by other authors for circular wings, when considering the wing's projected area for the aerodynamic coefficients calculation. However, it should not be assumed that the larger wing (B) has a superior aerodynamic performance than the smaller wing A, just because of the Oswald factor determined. Moreover, with this reference area, the lift coefficient curve slope would also be the double for wing B:

$$2C_{L_{\alpha_A}} = C_{L_{\alpha_B}} \quad . \tag{2.44}$$

In summary, the latter case with $S_{ref} = S_A$ resulted in the double zero-lift drag coefficient for wing B, in a double Oswald factor for wing B, and in a double lift coefficient curve slope for wing B. However, none of the small wing (A) or the large wing (B) is better than the other, aerodynamically. It can only be said that one wing is more suitable for a specific operating condition, when its lift to drag ratio is larger.

Similarly, from studies such as Fletcher's [19] and Traub's [35] it was estimated a largely superior C_{D_0}, a greater Oswald factor and higher lift coefficient curve slope for the annular wing when compared to a flat wing with the same projected area, which was used as a reference area. Therefore, it should not be assumed that the aerodynamic performance of an annular wing is superior to that of a flat wing, just because a higher estimated Oswald factor indicates a lower lift induced drag of the annular wing. As it was demonstrated, the Oswald factor calculation greatly depends on the reference area assumed. Indeed, Traub has considered the larger zero-lift drag to greatly counteract the superior Oswald factor calculated. And, as it was referred, Wan [61] concluded that the lift induced drag of circular wings was worst than for planar wings based on the low Oswald factor obtained. This estimation was carried out considering the wing's surface area as reference, which is larger than the projected area.

2.2.2. FLOW INSIDE THE DUCT

For the performance of the propeller, it is relevant to understand how its inflow conditions inside a shroud are different from the free-stream. These have been assumed to vary with the propeller location with respect to the duct chord [15]. At the inlet of the duct, the flow is usually more similar to the free-stream conditions. It is also expected to have a greater radial velocity variation due to the duct's influence on the flow. On the other side, if the propeller is located at half of the duct's chord, it is expected to experience a more uniform inflow [15].

The nature of the flow experienced by a propeller inside a circular airfoil ring was discussed by Kuchemann and Weber as well [6]. Limited importance was given to the radial variation of velocity due to the isolated duct. However, the increment in axial velocity caused by the ring due to interference with the propeller was found to vary largely with radial position. A non-dimensional parameter was defined:

$$\delta = \frac{V_F}{V_\infty} \quad , \tag{2.45}$$

where V_F is the axial velocity increase inside the annular wing. This parameter was then divided into two components:

$$\delta = \delta_0 + \delta_1 \quad , \tag{2.46}$$

where δ_0 reflects the axial velocity variation due to the annular wing alone, and δ_1 is associated with the variation in axial velocity due to the duct in the propeller flow. δ_1 was found to vary proportionally to the ratio between the axial induced velocity by the propeller at the prop disk and the free-stream velocity:

$$\delta_1 \propto \frac{V_a}{V_\infty} \quad . \tag{2.47}$$

This parameter also depends on the propeller position inside the duct. For this reason, it was estimated for different prop locations: duct's inlet, half chord and at the exit of the duct. The results are shown in Figure 2.7. It is interesting to notice that δ_1 is radially more constant towards the ducts exit. When the fan is at a central position, δ_1 is already almost uniform for the duct with a length (L_F) equal to half the diameter (aspect ratio of 2). For the duct with an higher aspect ratio of 4, δ_1 is shown to vary more, radially.

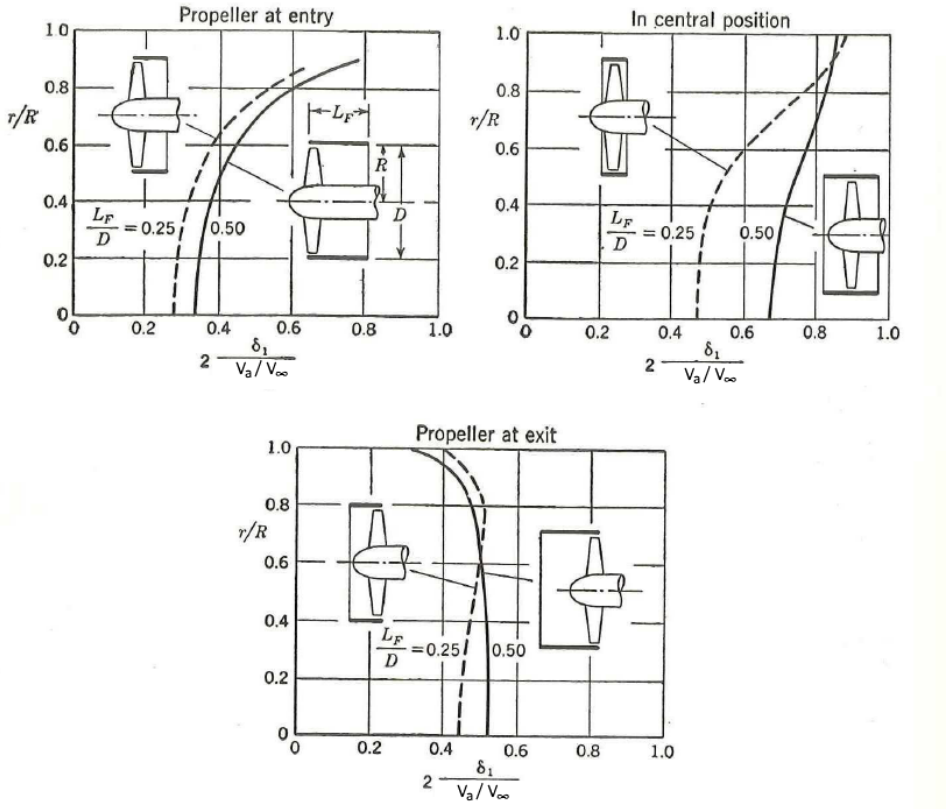

Figure 2.7: Axial velocity increase at the duct ($2\frac{\delta_1}{V_a/V_\infty}$) with respect to radial position (r/R), for 3 different propeller positions. These are the inlet (top-left), half duct chord (top-right) and at the duct's exit (bottom) [6]. The results are shown for two ducts, with aspect ratios of 2 ($L_F/D = 0.5$) and 4 ($L_F/D = 0.25$). The image was modified to include variables defined in this report, namely V_a and V_∞.

2.2.3. TIP LOSS REDUCTION

A very important phenomenon in ducted propellers is the end plate effect. This is caused by the shroud on the blades, as long as the gap between both components is small enough. The end plate effect has a great potential in improving the efficiency of propellers, thus it has been greatly studied (e.g. [36], [42], [7]). This effect causes the circulation over the blades to not decrease towards the tips, or at least allows this loss to be lowered. The blade tip vortices, associated with the lift-induced drag component, are also reduced due to this effect. Similarly, the winglets on aircraft wings cause the wingtip vortices to be weaker, and the lift induced drag to be lower.

Williams et al. performed estimations of ducted propellers based on a three-dimensional (3D) lifting-surface method [36]. During the validation process, it was concluded that their static performance calculations gave similar results to those of a 3D Euler method, which is computationally more expensive. In Figure 2.8 the calculated radial thrust distributions along the blade can be seen. The cases presented are for an unducted propeller, ducted propeller with 0 gap, propeller with a tip device (also 0 gap) and a ducted prop

with a gap equal to 0.02 R, or 1% of the fan diameter. The tip device is basically a truncated duct, with only a short duct portion left, the panels adjacent to the blade tips. Since the results for the duct with 0 gap and for the tip device case were similar, it was concluded that the major influence of the duct on the blades is due to duct's most nearby components. Therefore, the rest of the shroud has a small influence on the blade's loading. Comparing with the isolated propeller case, it can be understood that the duct provokes a large increase in the blades' circulation, but only near the tips. Indeed, this effect is only significant for $r > 0.75$. For the $0.02R$ gap case, the increase in thrust towards the tip is also present, even though this effect is considerably lower than for the 0 gap shrouded prop. Thus, the results indicate that the tip loss reduction effectiveness decreases rapidly with increasing blade - duct gap. The authors also refer that the usual gap for ducted propellers is about $0.15\%D$, however this value could have let to inaccurate results with the used method [36].

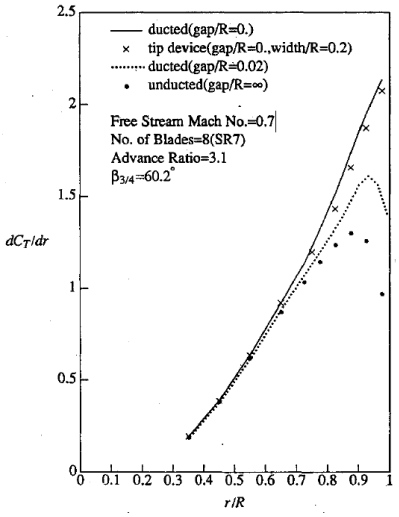

Figure 2.8: Sectional thrust coefficient radial distribution for an unducted propeller, a ducted prop with a blade tip to duct surface gap of 0.02 R, a ducted prop without a gap and a propeller with a tip device [36]. The propeller considered had 8 blades, a pitch angle of 60.2° and was operating at 0.7 Mach number and at $J = 3.1$.

With unconventional duct shapes, such as a square case, it was quite uncertain how the end plate effect would affect the system's performance. Due to the shape of this shroud, each blade sees great periodical tip clearance variations. Near the duct's corner, the gap between blade and duct is at a maximum, whereas at the midpoint of each side of the square, the gap to the propeller disk is minimum. This is illustrated in Figure 2.9. In Figure 2.10 it is represented a circular duct, where the propeller-duct gap is constant along the propeller disk.

2.2.4. DUCT THRUST

One aerodynamic phenomenon that greatly affects the performance of shrouded propellers is the thrust produced at the duct itself. At the leading edge region, the shroud feels a lower pressure, in contrast to the higher pressure at the trailing region of the duct. The major reason for this lower pressure is the effective angle of attack (or side slip) experienced by the duct's lip. This effective angle with the flow is caused by the slipstream contraction due to the propeller. The flow contraction is different between ducted and isolated propellers, since the flow only contracts outside the duct. Due to the dependence of the duct's thrust on slipstream contraction, this thrust is usually greatest for static conditions. Indeed, the slipstream contraction for a given propeller loading is highest at $V_\infty = 0$. To reach the same contraction at larger free-stream velocities, the propeller has to operate at a greater power loading.

Black et al. investigated the thrust produced by the duct of a shrouded propeller system [7]. In the wind tunnel, the pressure was measured along a shroud in order to calculate the forces at each location of the surface. This way, it was possible to understand where the pressure thrust or drag forces are generated. The

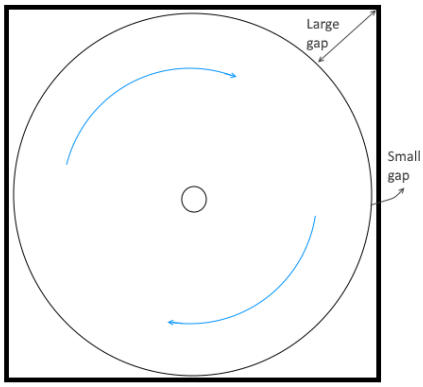

Figure 2.9: Square duct with a propeller disk. It is indicated a point of lower gap, and a location of highest gap, near the duct's corner.

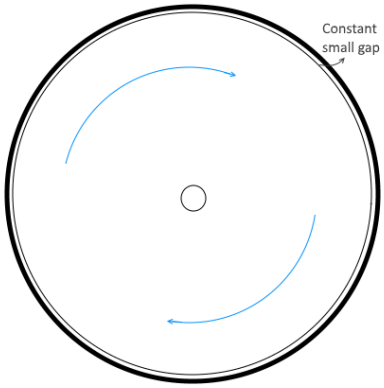

Figure 2.10: Circular duct representation. It is shown that, for this configuration, the gap between the blade tips and the duct is constant.

results can be seen in Figure 2.11. In this Figure, the magnitude and direction of the arrows represent, respectively, the absolute value of the static pressure at that location subtracted by the ambient pressure, and its sign (positive or negative). It is important to refer that this experiment was performed at a very low Mach number (M=0.05). This way, it was possible to achieve a large slipstream contraction and, therefore, a considerable thrust at the duct. As it can be seen, most thrust is produced at locations I and II of the duct (near the leading edge), whereas a pressure drag was obtained at III. For comparison, the viscous drag was also estimated during this experiment. The value obtained was 5% of the duct thrust calculated at these conditions [7].

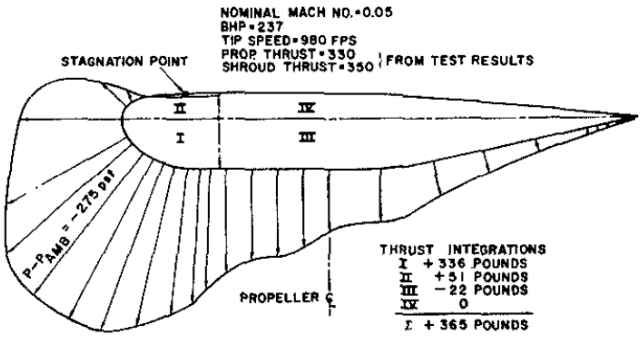

Figure 2.11: Pressure distribution along a duct's section, with area ratio of 1.3 [7].

Furthermore, Black et al. also concluded that the most critical parameter for the design of ducted propellers is the ratio between the cross sectional area of the duct at the trailing edge and the cross sectional area of the duct at the propeller location [7]. Black et al. found that larger area ratios are desired for situations in which the slipstream contraction is larger, in order to maximise the thrust produced by the duct. However, at higher Mach numbers, when slipstream contraction is low, the performance of the propulsion system is better for ducts with lower area ratios. As an example, at $M = 0.5$ the duct with $A_{d,exit}/A_{d,prop} = 1.3$ showed a decrease in thrust of 50% when compared to the duct with $A_{d,exit}/A_{d,prop} = 1.1$ [7].

2.2.5. CORNER FLOW

When considering quadrangular ducts, it is expected that aerodynamic effects typical of corner flows are going to be encountered. These were studied, for example, by Rubin and Grossman [44] with a numerical approach. In a corner region, the boundary layer of the flow has 3D characteristics, and therefore differs from what can be calculated with 2D boundary layer theory [43]. The two regions, of 3D flow and approximately 2D flow near a corner, are represented in Figure 2.12. Figure 2.13 shows the lines of constant axial velocity in the vicinity of a corner. Since near the corner these are further away from the surface, it can be concluded

that the boundary layer (BL) thickness in larger when one moves closer to the corner. This phenomenon is also expected to happen for the corners of a square duct.

Moreover, the skin friction near a corner was also estimated by Rubin and Grossman [44]. Along with a higher boundary layer thickness, it was calculated a lower skin friction at the corner layer. In fact, this was used to differentiate the corner layer from the 2D boundary layer. It was defined that the corner layer extended until the skin friction reaches 99% of the value for a two-dimensional BL. The secondary flows near a corner were also represented (Figure 2.15). In this image sketched accordingly to the numerical solution, it is interesting to notice that there is a "swirling flow in the corner but a closed vortical pattern is not established" [44]. During this thesis, the results were also evaluated in order to understand if a similar flow pattern was present near the corners of the square duct, for the different simulations.

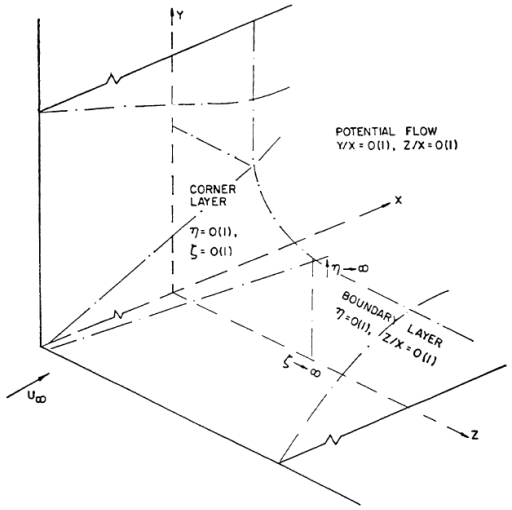

Figure 2.12: Representation of the region with a corner layer (3D flow) and with a 2D boundary layer [44].

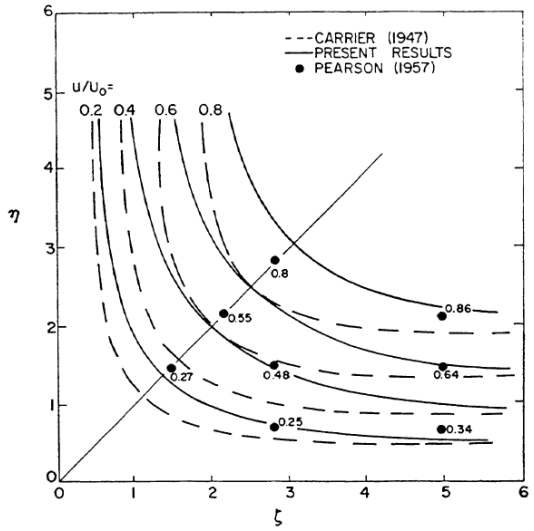

Figure 2.13: Representation of the lines of constant axial velocity in the vicinity of the corner. In this image, U/U_0 is the ratio of axial velocity to free-stream axial velocity [44].

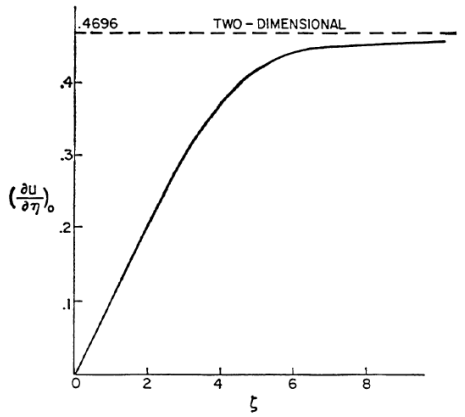

Figure 2.14: Skin friction ($(\delta U/\delta\eta)_0$) at the corner layer versus distance to the corner ζ [44].

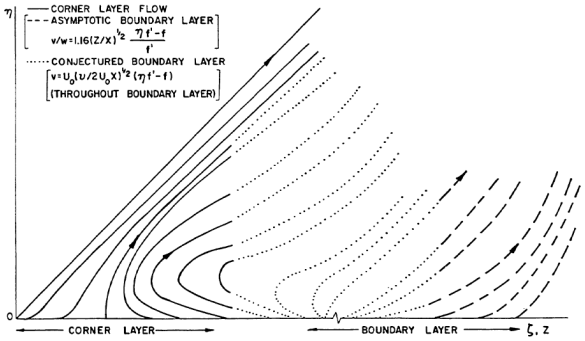

Figure 2.15: Qualitative representation of the secondary flows near a corner [44].

2.3. SUMMARY

In this chapter, it was provided the necessary theoretical background to understand the relevant aerodynamic phenomena that occur in isolated or ducted fans. Moreover, several aerodynamic advantages of propeller shrouds were identified:

- Shielding of the propeller from unfavourable exterior flow conditions. As discussed in section 2.2.2, the flow inside the duct tends to get oriented with the duct's central axis. In this way, the effective angle of attack of the flow inside a duct is expected to be lower, in module, than the angle of attack of the duct. This phenomenon can also protect the performance of the fan, when the propulsive system is operating under the influence of wind gusts.
- Propeller tip loss reduction, discussed in section 2.2.3. Ducts were found to lower the vortices generated at the propeller tips, this way increasing the thrust production by the blade sections at relatively high radius.
- Production of thrust at the duct, discussed in section 2.2.4. At high slipstream contractions, it was found that propeller shrouds are capable of producing thrust. This is due to a change of the effective angle of attack of the duct sections, which results in very low pressures at the duct's lip. However, at high Mach number it is difficult for a fan to provoke a high slipstream contraction of the flow. Therefore, at high Mach number it is expected that the duct produces drag instead of thrust.

Besides, it can also identified which phenomena should be expected to cause differences between a conventional circular ducted propeller and a fan shielded by a square shroud:

- Differences in axial velocity of the flow at the fan location. If one of the ducts causes the velocity at the fan location to be higher, this would cause the effective α of the blade sections to be lower (see image 2.2). The blade sections would then produce a lower thrust.
- The propeller tip loss reduction was also expected to be different for both ducts. This is due to the fact that this effect greatly depends on the tip clearance of the blades. As it was previously discussed, the tip clearance sees large variations in a square duct.
- The production of thrust at the duct's lip could also be different for each shroud. Indeed, the capabilities of the square duct to produce thrust were quite uncertain, even for high slipstream contractions.
- Effect of the corner flow at the corners of the square duct. The corners of the unconventional duct were expected to develop a flow characteristic of corner layers (discussed in section 2.2.5). However, it was uncertain how this effect would influence the overall performance of the system.

II

Methodology

3

NUMERICAL MODELLING

In this chapter, the numerical method used for this thesis' simulations is introduced. In this way, it is firstly explained why computational fluid dynamics was used in the research (section 3.1). Secondly, the choice of the governing equations is discussed (section 3.2). Since the Reynolds-averaged Navier-Stokes (RANS) equations were used, it was also necessary to choose an appropriate turbulence model (section 3.3). Afterwards, the boundary conditions used are also explained (section 4.4). Moreover, the actuator disk model used is introduced as well (section 3.5).

3.1. WHY COMPUTATIONAL FLUID DYNAMICS?

For the choice of the aerodynamic analyses method, it was intended to allow the investigation to capture several phenomenon. These include viscous effects, interference between components, and unsteady phenomena as well. Therefore, simpler computational methods than CFD such as panel methods, simple BEM theory or vortex lattice methods (as used by AVL program) are unable to capture all the expected phenomena. As an example, the comparison done in [36], between Euler computations and 3D lifting-surface method estimations, shows that low order methods (both inviscid in this case) can give different results when simulating ducted propellers. Therefore, the study from Williams et al. [36] suggests that a higher order analyse could be beneficial for this thesis. Viscous simulations are possible with CFD.

Successful examples of the use of CFD for the study of propellers or ducts are numerous. For instance, in [56], [52] or [50], this can be seen for propellers. Cases of ducts simulated in CFD without a propeller can be seen in [29], [21], or [48]. Moreover, full ducted propeller models have been investigated in [9] (ducted prop-fan) or [46]. Furthermore, Hameeteman [21] also simulated ducted propellers with the propeller represented as an actuator disk. Using an AD to simplify the problem allows for a great saving in computational costs. However, the performance of the propeller itself is independent of the operating conditions or any interference effects, if modelled as a simple actuator disk.

The simulations which were performed in this thesis could also be carried out with experiments in a wind tunnel. However, this research is a very fundamental study on the aerodynamic effects which occur on the different ducted systems. Therefore, it was intended to capture the characteristics of the flow on a very wide range of locations. These include the flow over the blades, over the duct sections, secondary flows inside the duct, and also on several planes (perpendicular to the free-stream velocity) upstream and downstream of the propeller. Capturing all of the aerodynamic phenomena which was obtained with CFD could be very difficult with experiments. Even though state-of-the-art flow measurement methods such as particle image velocimetry (PIV) can also provide accurate and complete data, it would still be difficult to capture all the phenomena which occurs inside the ducts. Indeed, one of the drawbacks of PIV is the need for optical access to the measurement location. Similarly, it would be difficult to capture the flowfield inside the duct with Laser Doppler Velocimetry (LDV) measurements, due to the challenging optical access. On the other hand, pressure measurements or hot wire anemometry (HWA) could be used to obtain the velocity field inside the duct. However, these two measurement techniques have the disadvantage of being intrusive, and could alter the characteristics of the flow inside the shroud. Still, based on the results of the CFD simulations, it would be

interesting to validate them with an experimental campaign. Simple balance measurements would already provide important data for validation.

3.2. GOVERNING EQUATIONS

The CFD simulations performed during this research were based on the solution of Reynolds-averaged Navier–Stokes (RANS) equations. For the choice of the governing flow equations, it was taken into consideration the fact that viscous effects should be present in the simulations. Indeed, the characteristics of boundary layers (BL) of the different geometries were expected to have an impact on the overall performance of each shrouded propeller configuration. In particular, each duct boundary layer was expected to have a direct impact on the viscous drag of the duct, and also an influence over the propeller's loading distribution. This is due to the fact that the blade tips, when shrouded, rotate through the duct's boundary layer (in the configurations considered). As an example, Black et al. [7] attributed an unexpected trend in ducted propeller performance, for varying blade tip clearance, to "interaction between the shroud boundary layer and the propeller blade tips". Black et. al studied ducted propellers experimentally. In this way, it is clear that it is advantageous to use RANS equations for investigating ducted propellers, in comparison to Euler equations (inviscid).

In CFD, there are also more accurate methods for calculating viscous flows than RANS. Examples are Large Eddy Simulations (LES) and Direct Numerical Simulations (DNS). However, these methods would have been too expensive (computationally) for the present research. The large number of cell elements required by these two methods causes a great increase in computational time. As an example, Krajnović and Davidson [31] studied a simplified car model with LES. From their study, it was understood that the use of LES to estimate drag or lift on a ground vehicle was not yet possible, due to the large amount of cells needed near the walls [31].

Moreover, the flow (air) was assumed to be an ideal gas during the research. In this way, compressibility effects were taken into account in the simulations. Assuming air the be an ideal gas, the following relation applies to the fluid:

$$p = \rho R T \quad , \tag{3.1}$$

where p is static pressure, R is the specific gas constant and T is the static temperature.

3.3. TURBULENCE MODELLING

When using RANS equations to describe the flow, it is necessary to choose an appropriate turbulence model. During this research, the two equation $k-\omega$ shear-stress transport (SST) model was used. The eddy-viscosity $k-\omega$ SST model was developed by Menter [16], combining advantages of what were considered to be the best eddy-viscosity models: $k-\omega$ and $k-\epsilon$. In these models, k stands for the turbulent kinetic energy, ω is the specific dissipation rate, and ϵ is the rate of dissipation of turbulent kinetic energy. However, Menter's model works with the $k-\epsilon$ model in a $k-\omega$ formulation. In this way, the $k-\omega$ SST model uses the $k-\omega$ model in the inner layer of boundary layers, and the $k-\epsilon$ in the outer wake region of boundary layers. The inner layer includes the viscous sub-layer (closer to the wall) and the log-law layer, extending until 10% of the boundary layer hight [56]. Far from no-slip boundaries, in free-shear layers, the $k-\omega$ SST model also uses the $k-\epsilon$ original model. Furthermore, Menter's model features a shear stress correction, assuming that the shear stress is proportional to k in boundary layers. This results in a different formulation of the eddy-viscosity near no-slip walls, whereas outside boundary layers the original $k-\omega$ model's expression to calculate eddy viscosity is used:

$$\nu_t = \frac{k}{\omega}, \tag{3.2}$$

where ν_t is the eddy-viscosity.

In this way, the $k-\omega$ SST model has a series of advantages with respect to the original $k-\omega$ and $k-\epsilon$ models [16]:

- The boundary layer flow is captured with the accuracy of the $k-\omega$ model, where it is superior to the $k-\epsilon$. In this thesis, since it was expected that the propeller blades would pass through the BL of the

ducts, it was concluded that it would be important to have an accurate simulation of the boundary layers.

- The flow in the boundary layer and in free shear layers has a relatively low dependence on the free-stream values of k and ω chosen (k_∞ and ω_∞). In fact, the high dependence on the k_∞ and ω_∞ values is a strong disadvantage of the $k-\omega$ model with respect to $k-\epsilon$.

- With the shear stress transport correction in boundary layers, the $k-\omega$ SST model performs well when calculating flows with a strong adverse pressure gradient. This causes improvements in predicting separation due to adverse pressure gradients and also the resulting flowfield. For the simulations of this thesis, is was intended to capture accurately the flowfield around the ducts, in spite of the strong pressure jump that occurs inside the ducts due to the propeller. Indeed, strong adverse pressure gradients were captured at the duct surfaces due to the presence of the propeller.

Besides the expected advantages of the $k-\omega$ SST model with respect to other eddy-viscosity models, it is also important to consider its applicability to propeller simulations. Indeed, the turbulence model has already been used in several propeller research studies [4, 14, 34, 39]. Moreover, Menter's model has been used for studying ducted propeller systems, with the propeller modelled as a pressure jump [32]. Bardina also compared several eddy-viscosity models in a validation study [26]: $k-\epsilon$, $k-\omega$, $k-\omega$ SST, and the Spalart-Allmaras (SA) one equation model. These models were compared for a series of test cases, including simple free-shear flows, and also complex flows where flow separation should be predicted. From this study, Menter's SST model was concluded to be the most accurate overall, mainly due to the better prediction of separation in complex flows [26]. However, Bardina also refers that none of these turbulence models is capable of predicting reattachment flows accurately. Moreover, Stokkermans also did a validation study comparing the SA model with the $k-\omega$ SST model for propeller flows [51]. Over one propeller diameter downstream of the fan, it was found a higher numerical diffusion in the vortex cores for the $k-\omega$ SST model, indicating that the SA model was superior in this aspect. In the study, it was also concluded that the SA model predicted separation better on a wing downstream of the propeller. Therefore, even though Menter's SST model is often indicated (e.g. by [16, 26]) as the most appropriate eddy-viscosity model for a wide variety of flows, it should be kept in mind that the $k-\omega$ SST model also has its own limitations.

3.4. BOUNDARY CONDITIONS

In this section, the boundary conditions (BC) used for the simulations are described. The free-stream values imposed at these boundaries are also justified, in subsection 4.6. For a clear indication of the location where each boundary condition was applied, section 4.4 should be consulted. In this thesis, several types of BC were used:

- The inlet boundaries of the different domains were defined as pressure-inlets. In this way, a gauge total pressure, a total temperature, a gauge static pressure, and the values of k and ω were set [17]. Moreover, the direction of the flow was also fixed to be the axial direction, since the free-stream angle of attack of the flow was kept at 0°. The conditions set at the inlets pose a limitation to the characterization of the flowfield. Indeed, in subsonic flows there is an influence of the bodies in the upstream flow, meaning that the static pressure and direction of the flow should be slightly different from the free-stream values at the defined location of the inlets. To reduce the influence of this condition in the calculated flowfield, the inlets are located relatively far upstream from the bodies.

- The far-field boundaries were defined as pressure far-fields. Therefore, the gauge static pressure, the Mach number, the static temperature and the flow direction were fixed [17]. Therefore, similarly to the inlets, the far-field boundaries had to be placed far from the bodies. Otherwise, the propeller or duct being simulated would suffer from a blockage effect, identically to what happens in closed wind tunnel experiments.

- The outlets were defined to be pressure-outlets. At these boundaries, a gauge static pressure and backflow conditions are set [17]. Thus, the outlets have to be located sufficiently downstream, so that the static pressure of the flow has returned to the free-stream values. The backflow conditions were set to be the free-stream values of the required quantities. However, since in none of the simulations the flow had a reversed direction at the outlet, these conditions did not influence the obtained solutions.

- In the 2D axisymmetric simulation of the circular duct (also called ring wing), the flow was defined to be axisymmetric with respect to the central axis of the duct. This condition impedes the flow to have tangential gradients. For the isolated ring wing at $\alpha = 0°$, it was expected that the spanwise movement of the flow would be very low. For this reason, the assumption of axisymmetry was considered to be appropriate. However, this condition would not hold for a different angle of attack of the duct.

- Symmetry boundary conditions where used on the simulation of the isolated circular and square ducts. In this way, it was possible to run simulations with one quarter of each duct only. Thus, the overall size of the domain and mesh were also reduced to one quarter, decreasing the computational cost of the simulations. In the symmetry planes, the solver enforces the normal velocity component to be zero, as well as the normal gradients of the variables calculated [17]. As an example, Werle [37] also used symmetry boundary conditions for the CFD simulation of ring wing ducts.

- Periodic boundary conditions were used on the simulations involving a propeller or actuator disk. Similarly to the symmetry condition, the periodic boundaries were used to reduce the domain to one quarter of the full domain, saving computational costs. Indeed, it was possible to simulate a 4 bladed propeller using only one blade. At a periodic boundary, the solver assumes its cells to be adjacent to the cells at the other corresponding periodic boundary [17].

- No-slip wall boundary conditions were applied in most body surfaces. These include the propeller blade, spinner and duct surfaces. In this way, velocity components are assumed to be zero at the walls, and a boundary layer is formed.

- Free-slip wall boundary conditions were also used. The condition was defined by setting the shear at the walls to zero. A free-slip wall implies that the flow velocity normal to the wall is zero, while no restriction is made to the tangential components of velocity. With a free-slip wall, no boundary layer is formed at the specific surface.

Besides the above boundary conditions, it is also important to refer that the propeller was modelled in a different domain than the stationary components, in the same simulation. On the contact surface between two domains, interface boundary conditions were applied. In this way, two different methods were used to model the movement of the blades, with respect to the stationary frame of reference:

- Multiple reference frame (MRF) method. The MRF method was used in the steady simulations of the propeller. With this method, the flow in the propeller domain is considered to be rotating, and the fan blades are considered to be stationary with respect to a rotating frame of reference. The MRF method was used to simulate the isolated propeller, and also to obtain an initial solution for the propeller unsteady simulations. The usage of the MRF method results in large savings in terms of computational time.

- Sliding mesh method. The sliding mesh method was used to perform unsteady simulations with the rotating propeller. This method is capable of capturing the unsteady interaction between moving and stationary components more accurately than the MRF method, with the drawback of resulting in much higher computational costs [18].

3.5. ACTUATOR DISK MODEL

An actuator disk model was used to simulate the propeller with lower computational costs, before the final full blade model simulations. The actuator disk model used was developed by Tom Stokkermans, at TU Delft, to be used as a user defined function in ANSYS Fluent. The AD model has been previously subject to a validation study by Stokkermans et al. [51], for a wingtip mounted propeller set-up. The model requires the input of the radial thrust ($T'(r)$) and torque ($Q'(r)$) distributions over a propeller blade, along with the number of blades. The distributions were obtained previously from isolated propeller simulations. Therefore, this approach has the disadvantage that the AD does not depend on the specific flow conditions where it is inserted, in this case on the flowfield inside each duct. With the thrust and torque distributions, the model calculates the momentum and energy sources which should be added to the flow at each cell. The sources depend on the cell's radial position, since thrust and torque vary along the blade's radius, and also in the axial position. The sources vary in the disk's axial direction according to a Gaussian distribution, which is adjusted to the specific

cell size of the mesh at the AD location. In this way, the momentum and energy source terms can be defined as [51]:

$$\begin{aligned} \vec{F}(x,r) &= \eta_x(x)\eta_\theta(r)\left(T'\vec{n}_T + \frac{Q'}{r}\vec{n}_Q\right) \\ S(x,r) &= \eta_x(x)\eta_\theta(r)\vec{F}\cdot\vec{V}\,, \end{aligned} \tag{3.3}$$

being $\vec{F}$ the momentum source term vector, per unit volume, and S is the energy source term, per unit time and volume. $\vec{V}$ is the local velocity vector. $\vec{n}_T$ is a unit vector normal to the disk plane, in the direction opposite to the thrust direction. $\vec{n}_Q$ is a unit vector in the actuator disk plane, with the direction of the external product between the radial unit vector ($\vec{e}_r$) and torque ($\vec{Q}$): $\vec{e}_r \times \vec{Q}$. Furthermore, η_x is the regularization function which distributes the sources in the axial direction, according to a Gaussian distribution [51]:

$$\eta_x(x) = \frac{1}{\epsilon\sqrt{\pi}} e^{-\left(\frac{|x|}{\epsilon}\right)^2}\,, \tag{3.4}$$

where ϵ is a constant which is used to adjust the distribution of sources in the axial direction to the local cell size. η_θ is a function which takes into account the number of blades (B) and the perimeter of the AD at each radial position (r) [51]:

$$\eta_\theta(r) = \frac{B}{2\pi r}\,. \tag{3.5}$$

Figure 3.1 gives a more clear representation of the variables involved in the modelling of the actuator disk. Besides the variables referred above, Θ_b and θ are also shown, which are the azimuthal location of a blade, and the azimuthal location of a given cell, respectively.

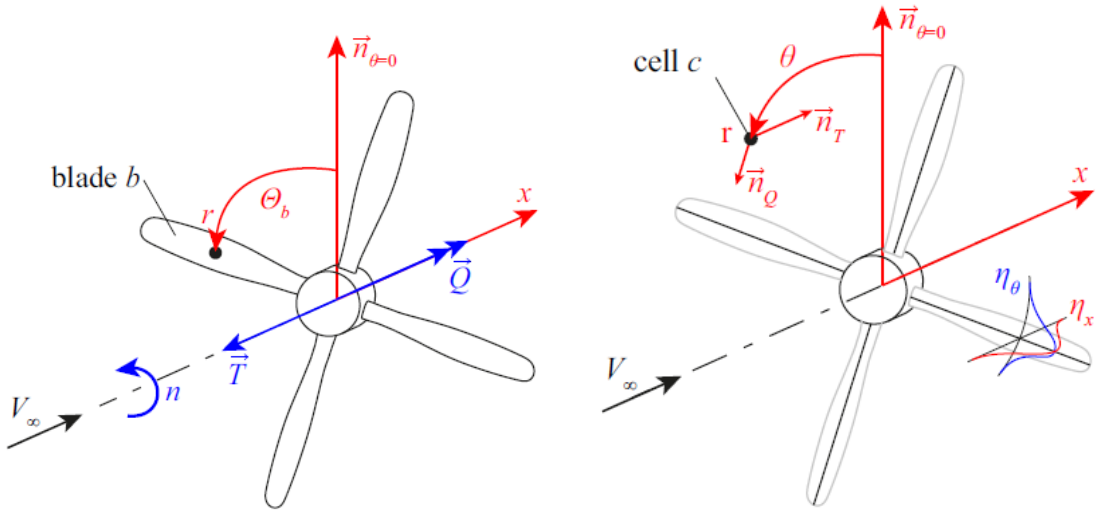

(a) Propeller representation

(b) Actuator disk representation.

Figure 3.1: Representation of the variables used in the modelling of the actuator disk [51].

3.6. DISCUSSION

The aerodynamic simulations carried out during the thesis attempted to perform flowfield estimations with high accuracy. However, these simulations also bear several limitations. The finite computational power available lead to a need for a trade-off between accuracy and computational costs of the different simulations. Examples of the approximations made in the CFD simulations are the use of RANS equations to describe the flowfield, the characterization of boundary layers by the turbulence model, the flow conditions imposed at the boundaries, and the actuator disk model used to model the effect of the propeller in the flowfield. Moreover, there are also sources of numerical error in CFD simulations, which further decrease the accuracy of the calculations. The numerical error present in the thesis's simulations is discussed in the next chapter, along with further details on the specific approach that was taken to make the best use of CFD in the research.

4

COMPUTATIONAL APPROACH

With this chapter, it is intended to explain the specific approach that was taken for the numerical study of ducted propellers in this thesis. Thus, it is first stated which software packages were used (section 4.1). It is considered that the computational process starts with the definition and creation of the geometries (discussed in section 4.2), before the delineation of the test matrix (section 4.3). Then, the work moves to the creation of the computational domains (shown in section 4.4), and then to the generation of the grids, whose main features are discussed in section 4.5. The operating conditions defined in the simulations' setup are explained in section 4.6. It is also important to access the numerical error of the calculations, how the approach taken can influence this error, and how it was quantified. The different sources of numerical error in the simulations are examined in section 4.7.

4.1. SOFTWARE

Throughout the thesis, several software packages were used with the purpose of preparing, running, and analysing CFD simulations. The first task in a CFD study is to define the geometry and computational domain to be used in the simulations. For each new geometry, this step was performed using SolidWorks, a computer-aided design (CAD) software, and ANSYS DesignModeler. Afterwards, it is necessary to generate the mesh over the computational domain. This step was performed with ANSYS Meshing. This software had been previously used to generate meshes for propeller simulations at TU Delft (e.g. [56], [51]). Subsequently, each mesh was imported to the solver ANSYS Fluent. When choosing the CFD solver, it was taken into account the fact that an actuator disk (AD) model had already been developed in TU Delft for ANSYS Fluent. The actuator disk model is described with more detail in section 3.5. The simulation results were then post-processed with ANSYS CFD-Post and Tecplot 360.

4.2. GEOMETRIES

In this section, it is given a description of the different bodies simulated in CFD. The main decisions involved in the design of the geometries are also discussed. As it was previously referred, the geometries were edited with SolidWorks CAD software and ANSYS DesignModeler.

4.2.1. CIRCULAR DUCT

The circular duct is the reference duct geometry studied in this thesis. A circular duct is often called ring wing in literature (e.g. by [37]). This is due to the fact that a ring wing is simply a wing airfoil revolved 360° around the center of the ring, even though more complex ring wing designs can involve a varying airfoil shape (e.g. as studied in [40]). In this way, there were two main design choices which had to be made with respect to the geometry of the circular duct: the airfoil shape and the duct's aspect ratio (defined as diameter to chord ratio). Since this duct was meant to be studied as a reference case, it was decided that a relatively simple geometry should be used. Furthermore, it should be a case already studied in literature, so that the results can be validated. In this way, it was decided to use a NACA0012 airfoil shape on the ring wing. This is a symmetric airfoil, with 12% thickness to chord ratio. The thickest point of the airfoil is at 30% of the chord. Information

about the aerodynamic performance of the NACA0012 airfoil has been available in literature for a long time (e.g. in [10]). Moreover, it was chosen an aspect ratio of 2 for the duct. This AR is within the range of aspect ratios tested by, for example, Black et al. [7] in a ducted propellers performance investigation. Furthermore, the specific case of an isolated NACA0012 ring wing with $AR = 2$ has been studied previously by Traub [35] (experimental study) and Kanoria and Damodaran [28] (numerical study). Additionally, the DUUC aircraft (shown in figure 1.1) also uses a NACA0012 ring wing with $AR = 2$ [22]. Thus, the results from this thesis can also be used to gain further understanding on DUUC's propulsive system.

Besides defining the duct's airfoil and AR, it was also necessary to specify its chord. The duct's chord was calculated in order to result in the desired tip clearance between the blade tips and the duct surface. The tip clearance, or gap between blade tips and duct, was chosen to be 0.3% of the fan's radius. This is an usual tip clearance in shrouded propellers [36]. The propeller's radius was kept the same as the original radius of a propeller geometry available - the Xprop (which is further discussed in section 4.2.3). In this way, the duct's chord was calculated to be $c_{duct} = 0.216956m$. With an aspect ratio of 2, the diameter of the duct was determined to be: $d = AR \times c_{duct} = 0.433912m$. It is important to refer that the diameter of the duct was defined at the ring wing's leading edge, being therefore slightly smaller than the outer diameter of the duct at its thickest point. The final CAD model of the conventional circular duct can be visualised in Figure 4.1.

(a) Circular duct - front view.

(b) Circular duct - isometric view.

Figure 4.1: Images of the (conventional) circular duct CAD model.

4.2.2. SQUARE DUCT

The square (or quadrangular) duct is the unconventional shroud geometry studied in this thesis. For a better understanding of the aerodynamic phenomena caused by this shroud (either isolated or by interference with other components), it was designed as close as possible to the model of the reference circular duct. In this way, the square duct is also an extrusion of the NACA0012 airfoil, and has an aspect ratio of 2. For the quadrangular duct, the aspect ratio (AR_q) is defined as the side of the square (L) divided by its chord:

$$AR_q = \frac{L}{c_{duct}} . \tag{4.1}$$

Similarly to the definition of diameter for the circular duct, the side of the square duct was measured at the leading edge of the geometry. In this way, the minimum tip clearance of the propeller inside the square duct is also 0.3% of the propeller's radius.

The final CAD model of the square duct can be seen in Figure 4.2. It can be seen that the corners of the duct are slightly rounded. The corners were rounded to allow for easier computation of the flow at this location, by the solver. If, instead, the angle between each side of the duct was exactly 90°, it would be more difficult to achieve convergence of the CFD simulations. The corners were rounded so that the lowest radius of curvature at the corner would be 1% of the propeller radius. As it can be seen in Figure 4.2b, the lowest curvature of the corners happens at the point of higher thickness of the airfoil section (at 30% chord), at the duct's inner surface.

(a) Square duct - front view.

(b) Square duct - isometric view.

Figure 4.2: Images of the (unconventional) square duct CAD model.

4.2.3. PROPELLER

For the choice of the propeller geometry, firstly the main requirements were set. These requirements were similar to those defined for the choice of the circular ducts' geometry: the aerodynamic performance of the isolated propeller should have been studied before, so that the simulations could be validated; and the flow around the isolated propeller should be simple enough that it does not overcomplicate the understanding of the interaction effects between propeller and the different ducts. Moreover, a CAD model of the propeller should be available, so that the validation process could be done with lower differences between the model investigated in this thesis, and the previously studied model. In this way, it was decided to use the propeller Xprop, which had been previously studied experimentally at TU Delft. The Xprop was preferred to the propeller PROWIM, studied e.g. in [8, 51], since the PROWIM usually has a separated flow region near the root of the blades. This separated flow would in fact make the propeller flowfield more complex than it would be desired.

However, the final propeller CAD model had a major difference with respect to the original Xprop geometry. Whereas the original Xprop had 6 blades, the number of blades was reduced to 4, for this thesis. The reason behind this modification has to do with the periodic boundary conditions used in CFD simulations with the propeller. With periodic boundary conditions, it is possible to reduce the propeller CFD domain, so that it includes only 1 blade. If a 6 bladed propeller is used, this means that a 60° domain can be used, instead of a 360° domain. If a 4 bladed propeller is used, it is possible to simulate the propeller with a 90° domain. Since it was intended to simulate the propeller inside two different ducts, it is also necessary to take into account the constraints imposed by the ducts. Whereas the circular duct can be simulated with any angle between the periodic boundaries, the computational domain of the square duct can only be effectively reduced with periodic boundaries if the angle between periodic BC is either 90° or 180°. Therefore, a simulation of a 6 bladed propeller inside a square duct would have to be made in a 180° domain, which would include 3 blades and half the duct. This domain and mesh would be significantly larger than the 90° domain used in this thesis to simulate one quarter of the square duct with one propeller blade. The main drawback of this modification in number of blades was that the validation process for the isolated propeller simulations became more complicated. The uncertainty relative to the validation also increased. This validation process is further discussed in section 6.1.4.

The 4 bladed version of the Xprop's CAD model can be seen in Figure 4.3. It is also important to refer that the propeller's radius is $R_p = 0.2032m$ ($R_p \approx 0.94 c_{duct}$), and that the pitch of the blade section at $0.7R_p$ is 30°, in this CAD model. The pitch of the propeller was kept constant throughout the thesis.

4.2.4. INSTALLED PROPELLER CONFIGURATIONS

In this section, the CAD models relative to the installed configurations are shown (Figure 4.4). The circular ducted configuration is shown in Figures 4.4a and 4.4b, whereas the quadrangular duct can be seen in Figures 4.4c and 4.4d. As it was previously referred, the ducts were designed so that the minimum tip clearance between propeller and ducts would be 0.3% of the Xprop radius. It was considered that the propeller's axial position would be at 30% duct chord (at the shroud's thickest point). Examining Figures 4.4a and 4.4c of the front view of the ducted systems, it becomes once again clear that the tip clearance is constant for the circular

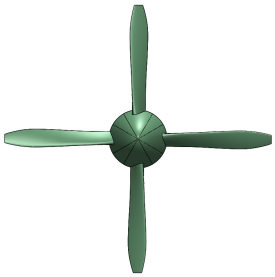

(a) Xprop - front view.

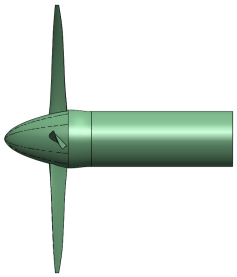

(b) Xprop - side view.

Figure 4.3: Images of the 4 bladed Xprop CAD model.

duct case, but changes significantly for the square duct case. In fact, the maximum tip clearance of the blades inside the square shroud is approximately 29.6% of the propeller radius. This variation in tip clearance was already expected to influence the peformance of the system, and was one of the focus of the research. It is also important to refer that the simulations of the two ducts with the actuator disk model included the nacelle of the propeller, which is seen in Figure 4.4, even though the propeller blades were not modelled. The differences between the computational domains of the AD and propeller installed configurations are further discussed in section 4.4.

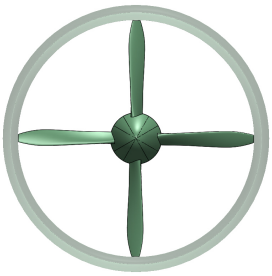

(a) Circular ducted Xprop - front view.

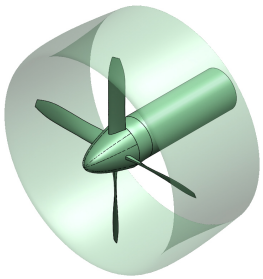

(b) Circular ducted Xprop - isometric view.

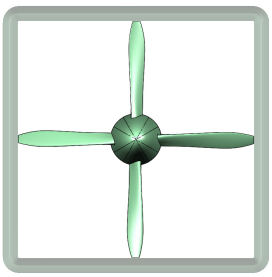

(c) Square ducted Xprop - front view.

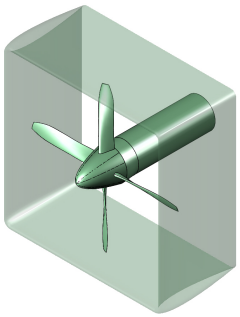

(d) Square ducted Xprop - isometric view.

Figure 4.4: Images of the 4 bladed Xprop CAD model.

4.3. TEST MATRIX

After having described the different geometries studied in the thesis, it is relevant to discuss the steps taken for the investigation of their aerodynamic performance. Each step consisted of a series of CFD simulations. For ordering the different case studies, it was taken into account the fact that the complexity of the simulations should grow with the author's learning curve, in terms of CFD application. Moreover, simulating the simplest cases first, also makes it easier to understand the calculated flowfields as their complexity grows (in terms of superimposed or interacting aerodynamic phenomena). Beside these considerations, the only major constraint in therms of ordering the computations was the fact that the isolated propeller simulations had

to be done before the simulations with the actuator disk model. As it was previously discussed (section 3.5), the AD model requires the input of the radial thrust and torque distributions for the propeller blades, which were obtained from the isolated Xprop simulations.

With the above considerations in mind, it was decided to start the numerical research with the simulation of the isolated configurations. Firstly, the circular duct was simulated in a 2D domain. Since the ring wing used is an axisymmetric revolution of an airfoil, it was possible to simulate this component with 2D axisymmetric boundary conditions. For this case, it was performed a mesh convergence study to access the discretization error of the simulations. Secondly, the circular duct was again simulated in a 3D domain. For this case, it was intended to simulate the duct with a mesh similar to what could be used in the installed configurations, with the circular duct. Moreover, a mesh convergence study was performed for the 3D simulation of the circular duct as well. The square duct geometry, since it is not axisymmetric, could not be simulated with a 2D domain. In this way, the quadrangular duct was simulated with a 3D domain only. Several meshes with different refinements were made to simulate the square duct as well, so that a convergence study could be performed.

After simulating the isolated ducts, the isolated propeller was studied. The Xprop was simulated with two different domains. Initially, the isolated Xprop was simulated in a conventional way, meaning that the propeller domain had a radius considerably larger than the propeller radius. For the test case with a large propeller domain, a mesh convergence study was performed. Moreover, the operating condition of the isolated propeller was also varied in this case, by varying the rotational speed of the fan (in order to vary the advance ratio). The range of advance ratios tested was: $J = 0.7$, $J = 0.8$ and $J = 0.9$. The simulation of the isolated propeller at different J had two main purposes. Firstly, it would provide more data for the validation of the isolated propeller simulations. Secondly, it would compute more thrust and torque distributions to be used with the actuator disk model. Furthermore, the isolated Xprop was also simulated in an unsteady case, with the large propeller domain, for the highest advance ratio tested. Since it was intended to simulate the shrouded propeller cases with unsteady computations, it was found to be beneficial to simulate the isolated Xprop with an unsteady computation as well, to access the accuracy of the results. It is relevant to point out that the unsteady simulations performed in this thesis were always initialized with a steady MRF computation, in order to decrease the computational time. Indeed, unsteady simulations are significantly more costly.

However, the radially large propeller domain could not have been used in a shrouded configuration, since the gap between blade tips and duct is very short, and the ducts had to be placed outside the propeller domain. Therefore, the propeller was also simulated with a radially smaller propeller domain, which could fit inside the ducts for the installed simulations. With the smaller propeller domain, it was performed a steady and an unsteady simulation at $J = 0.7$. With this unconventional domain, it was found that the accuracy of the steady simulation was very poor (this topic is further discussed in section 6.2). This is the main reason why the steady grid refinement study and the investigation of the effect of varying J were performed with the case with a large propeller domain, instead of the unconventional propeller domain. Another advantage of using the conventional isolated propeller domain is that a lower grid refinement is needed, and the cost of the simulations is lower.

After simulating the isolated geometries, the installed configurations were analysed. First, the ducts were studied with the actuator disk model. To reduce the differences between actuator disk and full blade simulations, the Xprop nacelle was also included in the AD disk computations. Furthermore, the blockage effect caused by the propeller nacelle on the ducts was also accessed independently, therefore without the AD. With the AD, the power setting was varied between the 3 advance ratios used on the isolated propeller simulations. The next and final step was to simulate the ducted propeller configurations with the full blade propeller model and with unsteady conditions. In these simulations, the radially small propeller domain had to be used. The propeller domain is used to simulate the rotating components (blade and spinner), with a MRF approach for steady simulations and with a sliding mesh technique for unsteady cases (these two methods were previously discussed in section 3.4). Since the ducts are stationary components (in their own reference frame), these were placed in the outer domain. However, the circular duct could have been placed in the propeller domain as well, since it is axisymmetric and Fluent allows for the specification of a different rotational velocity for each component. Still, since the square duct had to be placed outside the propeller domain, the circular duct was placed in the outer domain as well, to increase consistency in the comparison of the dif-

ferent cases. In this way, the circular ducted Xprop and the square ducted Xprop were investigated with an unsteady simulation each, at a high thrust setting ($J = 0.7$). The reason why a high advance ratio was used, in these simulations, has to do with the fact that it was intended to study the effect of slipstream contraction on the performance of the systems. Indeed, slipstream contraction increases with the fan's power setting. It would also have been interesting to simulate the ducted propeller configurations at different advance ratios. However, the large amount of cells used in these simulations resulted in too large computational costs for the unsteady simulations, meaning that it would be unfeasible to perform many simulations.

The test matrix described in the above lines is summarised in table 4.1. The different test cases are referred (first column), and it is specified: for which cases a mesh convergence study was made (second column); for which cases the advance ratio was varied (third column); and which cases involved unsteady simulations (last column).

	Test case	Grid Convergence study	Varying J	Unsteady
Isolated configurations	2D - Circular duct	X	-	-
	3D - Circular duct	X	-	-
	Square duct	X	-	-
	Xprop - large propeller domain	X	X	X
	Xprop - short propeller domain	-	-	X
Installed configurations	Duct + Nacelle	-	-	-
	Duct + Nacelle + AD	-	X	-
	Duct + Xprop	-	-	X

Table 4.1: Test matrix for the project. For each case (first column), it is specified whether a mesh convergence study was performed (second column), whether the advance ratio (J) was varied (third column) and if an unsteady simulation was run (last column). "X" stands for was performed, and "-" stands for was not performed.

4.4. DOMAINS AND BOUNDARIES

In this section, the different domains used in the computations are discussed. It is also pointed out where each boundary condition was applied. Subsection 4.4.1 refers to the domains used to simulate the isolated ducts, subsection 4.4.2 refers to the isolated propeller domains, and subsection 4.4.3 is relative to the simulation of the installed configurations. The specific constraints which were applied at each boundary condition were explained previously, in section 3.4.

4.4.1. ISOLATED DUCTS

Three different domains were used for the simulation of isolated ducts, as shown in Figures 4.5 and 4.6. In Figure 4.5, the domain used for the 2D simulation of the ring wing is shown. The BC used were a pressure-inlet, a pressure far-field, a pressure outlet and an axis boundary. The inlet and far-field were placed 10 duct chords away from the geometry, whereas the outlet was placed 20 duct chords downstream of the ring wing's leading edge. In this way, the total length of the domain in the axial direction corresponds to $30c_{duct}$. The axis boundary was placed at the centerline of the ring wing. For the 3D simulations of the isolated circular and square ducts, the inlet, far-field and outlet boundaries were placed at the same distance from the geometries as for the 2D case. The boundaries can be seen in Figures 4.6a and 4.6b, respectively. Moreover, the 3D domains were reduced to 90° domains by using symmetry BC. Since no propeller or AD was used in these simulations, it was possible to use symmetry conditions to reduce the domain to one quarter, instead of periodic boundaries. Periodic boundaries have the disadvantage of (possibly) resulting in interpolation errors, in case the cells in each of the periodic faces do not exactly match. For each of the 3 domains shown in Figure 4.6, a grid convergence study was performed. Moreover, the isolated ducts were always simulated

with steady computations. The only inherently unsteady aerodynamic effect present in these simulations was the separation of the boundary layer, at the trailing edge of each duct. It was considered that the steady calculation of the flowfield would provide sufficient accuracy to the estimation of the forces at the duct, and of the flow at the propeller location.

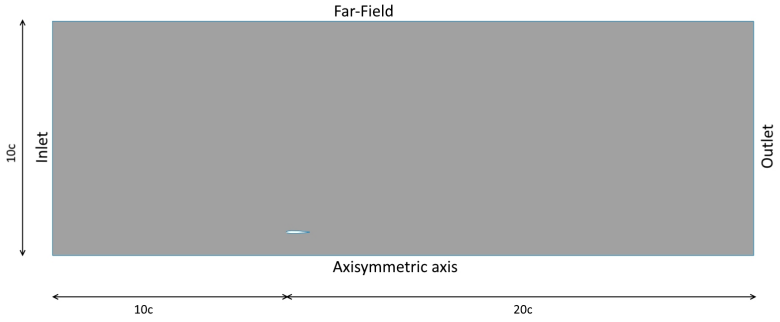

Figure 4.5: Domain and boundary conditions used for the simulation of the isolated ring wing in 2D. The location and shape of the ring wing section can be seen 10 duct chords downstream of the inlet, and 1 duct chord above the axisymmetric axis.

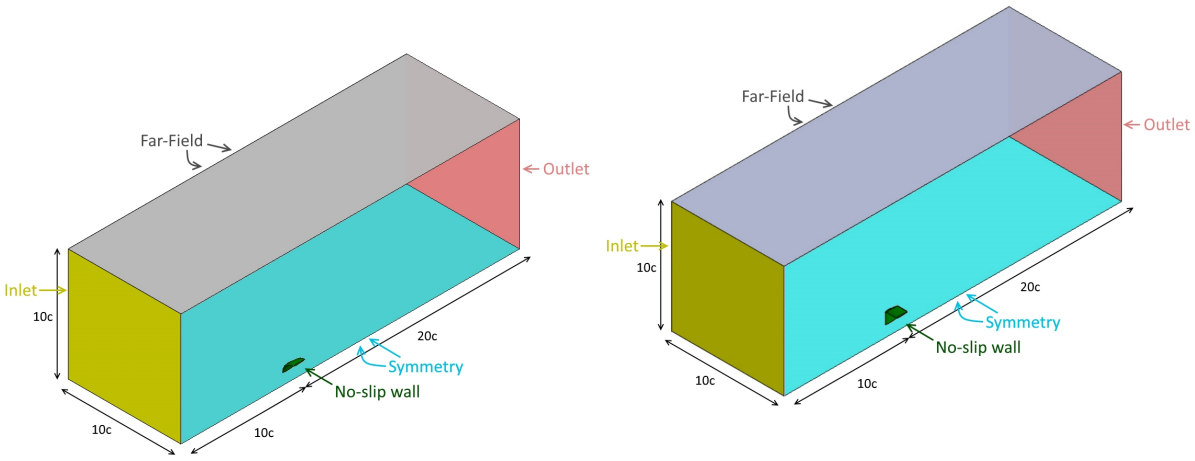

(a) Circular duct domain - isometric view.

(b) Square duct domain - isometric view.

Figure 4.6: Domains and boundary conditions used for the simulation of the isolated ducts.

4.4.2. ISOLATED PROPELLER

As it was previously referred, the isolated propeller was simulated with two different domains (seen in Figure 4.7). For both cases, the inlet, far-field and outlet boundaries had the same dimensions as the ones used for the simulation of the isolated ducts. Furthermore, the domains were reduced from 360° to 90° by applying periodic boundary conditions, already discussed in section 3.4. This means that only one of the four propeller blades was directly modelled in the simulations. Moreover, it is also interesting to notice that the nacelle was extended until the outlet. This modification of the original geometry was done to simplify the problem, by avoiding flow separation at the trailing edge of the nacelle. It is also important to refer that, while the blade and spinner where modelled with no-slip BC, the remaining part of the nacelle was modelled as a free-slip boundary. This was also done to simplify the problem. Modelling the spinner as a free-slip boundary would

simplify the simulation even further, but this was not done since the spinner's boundary layer has a more direct influence in the propeller loading, mainly at low radial positions.

The conventional Xprop simulation had a propeller domain with a radius considerably larger than the Xprop radius (Figures 4.7a and 4.7b). More specifically, it was approximately 25% larger than the propeller radius. On the other side, the second computational domain used for the simulation of the isolated Xprop had a propeller domain with a radius only 0.13% larger than the fan radius (Figures 4.7c and 4.7d). This is the same propeller domain which was used in the ducted propeller simulations, since it "fits" inside the shrouds. The computations of the isolated propeller included both steady and unsteady cases. The solutions of the steady simulations were used as initial flowfields for the unsteady calculations. Moreover, the unsteady results were obtained with a time step equivalent to 1° of blade rotation.

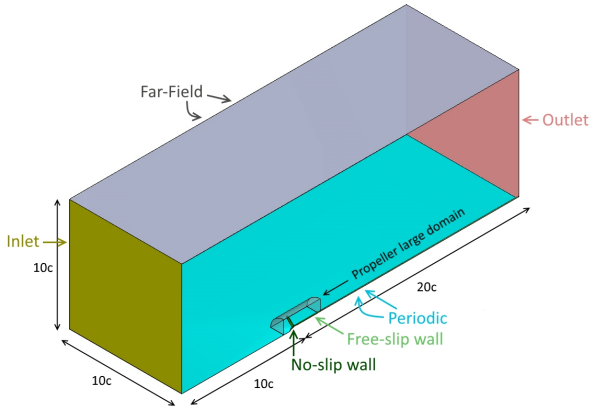

(a) Xprop conventional simulation - isometric view of the domains.

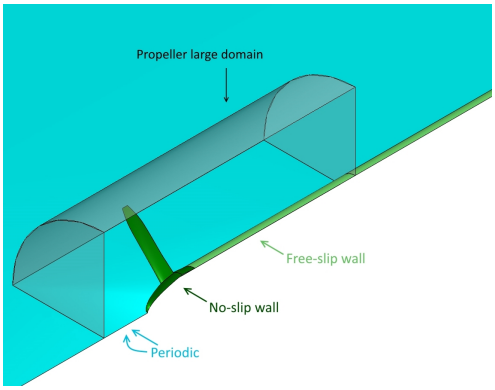

(b) Xprop conventional simulation- zoom at the propeller domain.

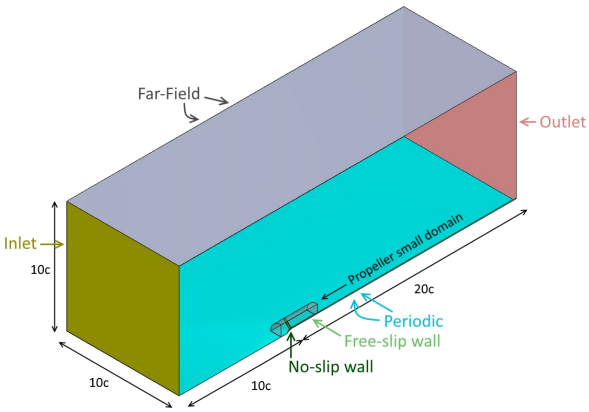

(c) Xprop simulation with a small moving domain - isometric view of the domains.

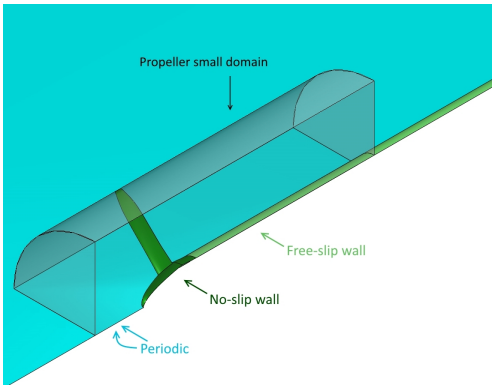

(d) Xprop simulation with a small moving domain - zoom at the propeller domain.

Figure 4.7: Domains and boundary conditions used for the simulation of the isolated propeller.

4.4.3. INSTALLED CONFIGURATIONS

The installed configurations consisted of the shrouds with an AD, or with the full blade propeller model. As it was previously referred, the simulations with a duct and AD also included the nacelle of the propeller, as it can be seen in Figure 4.8. Thus, the blockage effect that is caused by this component was taken into account in the AD simulations. Similarly to the isolated propeller simulations, the nacelle also extend until the outlet for the shrouded AD simulations. However, in the AD computations, the full nacelle and spinner were modelled as a free-slip boundary. In the AD cases, the outlet was also located 20 duct chords downstream of the duct's

leading edge, and 30 duct chords downstream of the inlet. The far-field boundaries were positioned at a distance of $10c_{duct}$ from the center of the shroud. For the AD simulations, the domain was also reduced to one quarter (90°) by applying periodic boundary conditions. From Figure 4.8, it can also be seen that there is a smaller domain surrounding each of the ducts. This separate domain was only used to define the AD model. In this way, the AD domain was used to make sure that there would be no error in the AD user defined function (UDF). Otherwise, it was possible that the UDF would place momentum or energy sources in the flow far from the AD location. These poorly located sources could be very difficult to find in the solution. The actuator disk position was defined in the UDF, and was equivalent to the position of the propeller in the full blade model simulations: at 30% duct chord, i.e. at the duct's thickest point. It is also important to refer that the power-off computations of each duct with the nacelle were done with the exact same domains as the simulations of the ducts with nacelle and AD (power-on). As it was previously discussed, the AD were simulated only with steady calculations.

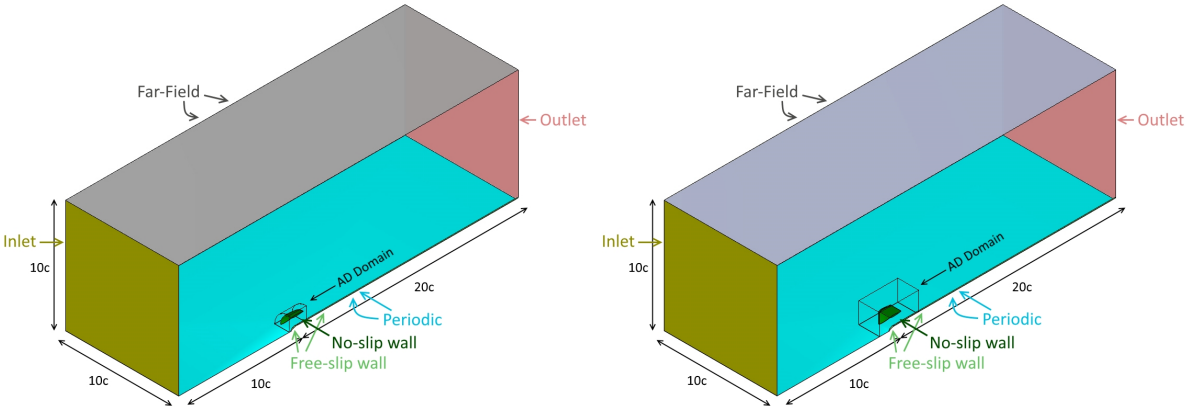

(a) Domains used for the simulation of the circular duct with AD - isometric view.

(b) Domains used for the simulation of the square duct with AD - isometric view.

Figure 4.8: Domains and boundary conditions used for the simulation of both ducts with the actuator disk model.

The final simulations of this thesis were performed to estimate the flowfield around the two ducted propeller systems. The domains used in these simulations are identical, and can be seen in Figure 4.9. Similarly to the previous simulations, the inlet was placed 10 duct chords upstream of the duct's leading edge, the outlet was placed 20 duct chords downstream of the shroud's leading edge, and the far-field boundaries were placed 10 duct chords away from the center of the shroud. Once again, the domains were reduced to 90° using periodic BC. Moreover, these simulations included both no-slip and free-slip boundaries. The shrouds, propeller blades and spinner were considered as no-slip boundaries, whereas the remaining part of the nacelle (from the spinner until the outlet) was modelled as a free-slip boundary. For both circular ducted and square ducted propeller simulations, the solution was initialized with a steady calculation. The results of for the case with the circular duct were then obtained for a time step equivalent to 1° of propeller rotation (the same was used for the isolated propeller simulations). However, when the same time step was used for the square ducted propeller simulations, the simulation diverged. For this reason, the unsteady calculation with the square duct was performed with a time step equivalent to 0.5° of propeller rotation. The justification for the need of a lower time step in the later simulation lies in the fact that the temporal gradients of the calculated quantities are greater for the square ducted propeller simulation, specially when the modelled propeller blade tip is close to the duct surface, and the blade tip clearance sees relatively fast variations, in percentage.

4.5. MESH

Following the analyses of the different domains used for the CFD simulations, it is important to discuss the meshing techniques used. In this way, this section provides a description of the main characteristics of the meshes used. Furthermore, it is given an explanation on how the mesh was generated in the most critical areas (e.g. boundary layers, regions of interference between components). Thus, the most problematic areas of the final grids are discussed as well. With this section, it is intended to give a clear idea of how the different

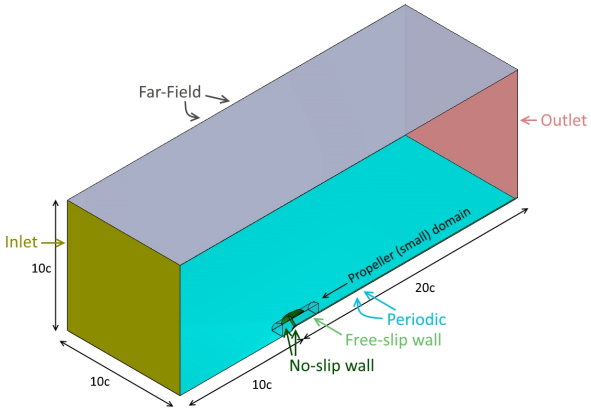

(a) Circular ducted Xprop simulation domains - isometric view.

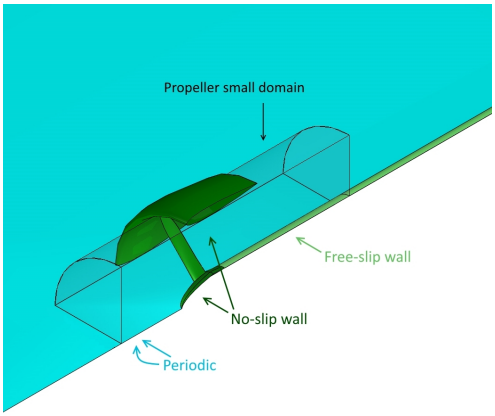

(b) Circular ducted Xprop simulation domains - zoom at the propeller domain.

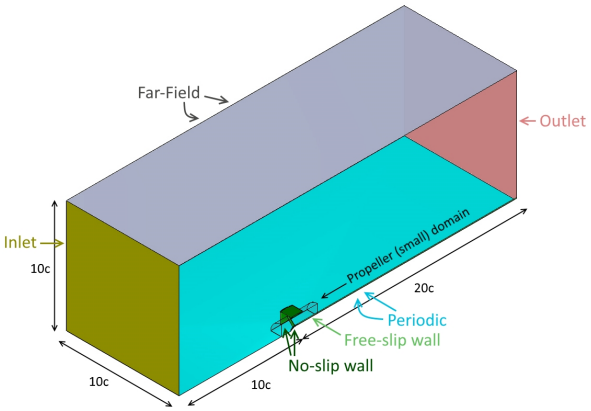

(c) Square ducted Xprop simulation domains - isometric view.

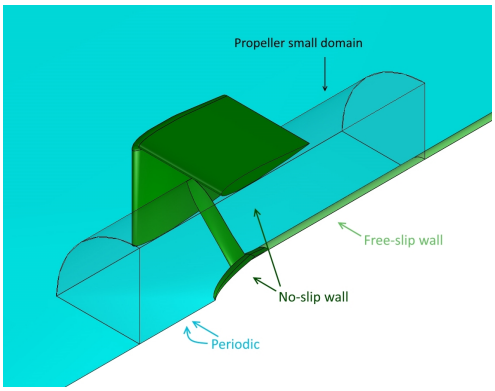

(d) Square ducted Xprop simulation domains - zoom at the propeller domain.

Figure 4.9: Domains and boundary conditions used for the simulation of both ducts with the Xprop.

mesh settings were used in order to solve each flowfield accurately, and also to examine the regions where the quality of the grids is not ideal, in order to access their possible impact on the calculations.

Firstly, it should be pointed out that each mesh used was generated with ANSYS Meshing software. With ANSYS Meshing, it were generated unstructured meshes in most of the domain regions. In the unstructured mesh regions, the average cell size was specified considering the expected gradients of the flow in each specific region. As an example, the unstructured mesh was more refined in the ducts' wake or inside the propeller streamtube than in far stream regions. Furthermore, the mesh was also more refined downstream of the propeller than upstream, since there are higher gradients of the flow quantities in the propeller slipstream. However, in boundary layer regions, a mesh that resembles a structured mesh was used, even though the solver Fluent always reads each mesh as if it was fully unstructured. This type of structured mesh is named inflation mesh. There are three main advantages which justify the use of structured like inflation layers in boundary layer regions. Firstly, these layers are usually generated with cells parallel to the main direction of the flow in the boundary layer region, which makes it easier for the solver to calculate the flow more accurately [25]. Secondly, using inflation layers it is easier to refine the mesh in regions around the bodies where the flow gradients are higher (e.g. at the leading and trailing edge of the propeller blade). Finally, using inflation layers it is easier to generate a mesh with a very short layer of cells (in height) close to the no-slip boundaries. The height of the cell layers was then gradually increased until the last inflation layer, with the prescribed growth

rate. It is important to have a small layer of cells near no-slip boundaries, and an appropriate growth rate for the following layers, so that boundary layer flows can be properly estimated. In this way, the first layer height was always set so that the center of its cells are in the viscous sub-layer of the boundary layer. More specifically, the first layer height was estimated so that the maximum y^+ in the first layer would be approximately 1. The y^+ is a non-dimensional distance to the nearest no-slip wall, and it is defined as [17]:

$$y^+ \equiv \frac{\rho u_\tau y}{\mu}, \tag{4.2}$$

where y is the distance to the wall, ρ is the density, μ is the molecular viscosity, and u_τ is the friction velocity:

$$u_\tau = \frac{\tau_w}{\rho}, \tag{4.3}$$

being τ_w the wall shear stress. The estimation of the required first layer height (Δs) to achieve a $y^+ \approx 1$ at the wall was made for each component, based on flat plate theory:

$$\Delta s = \frac{y^+ \mu}{u_\tau}. \tag{4.4}$$

For the estimation of friction velocity with equation (4.3), the wall shear stress was calculated by:

$$\tau_w = \frac{C_f \rho U_\infty^2}{2}, \tag{4.5}$$

where the skin friction C_f was estimated from:

$$C_f = \frac{0.026}{Re_L^{1/7}}. \tag{4.6}$$

The Reynolds Number, Re_L, was calculated for each component, with its reference length L:

$$Re_L = \frac{\rho U_\infty L}{\mu}. \tag{4.7}$$

Moreover, it was also desired that the total height of each inflation mesh would be larger than the corresponding boundary layer height. For this reason, an initial guess for each BL height (at the trailing edge) was done with Blasius' approximation for the boundary layer thickness of a turbulent flat plate (δ_{t_L}) of length L:

$$\delta_{t_L} = \frac{0.37L}{Re_L^{1/5}}. \tag{4.8}$$

In Figure 4.10, it can be seen the 2D mesh used for the axisymmetric simulation of the isolated circular duct. It is evident that the majority of the domain area is covered by unstructured elements. In Figure 4.10b, the structured like cells of the inflation mesh can be seen.

However, there are regions where the inflation mesh can not reach the specified height. These could be, for example, regions of close proximity between two different geometries. In this thesis the first case where the inflation mesh had to be shrunk was the isolated Xprop in the unconventional domain, i.e. in the propeller domain with a radius just slightly larger than the propeller radius. This domain was described previously in section 4.7. In this case, since the prescribed inflation layer height at the tip is larger than the distance to the outer domain, the inflation layer of the blade tip has to shrink, in order to fit inside the propeller domain. The differences in blade tip inflation mesh between the cases of the Xprop in a large propeller domain and the Xprop in a small domain can be visualized in Figure 4.11. The other cases where inflation layers had to be shrunk were the meshes around the duct for the installed configurations, with the propeller. Similarly to the previous case, the inflation of the ducts' inner surface had to shrink in order to fit in the outer domain, due to the proximity of the propeller domain. This can be visualized in Figure 4.12, for the square shroud case. In these domains, the shrinking of the inflation layers was unavoidable (with the meshing tools available in ANSYS Meshing), however, it can result in a lower accuracy of the simulations in these zones. Indeed, it is expected that the discretization error would increase due to a lower mesh quality. The problem was mitigated by refining the unstructured mesh in zones where there should be an inflation mesh. However, too large refinements were not possible due to the associated increase in computational costs of the simulation.

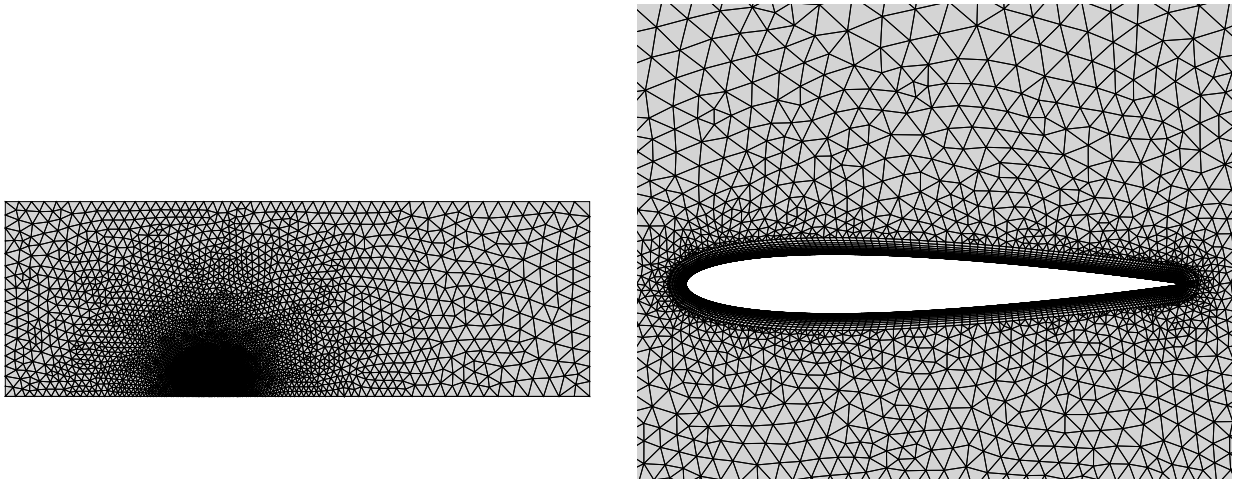

(a) 2D axisymmetric ring wing mesh - view of the whole domain.

(b) 2D axisymmetric ring wing mesh - zoom at the inflation layers.

Figure 4.10: Mesh used for the 2D axisymmetric simulation of the ring wing.

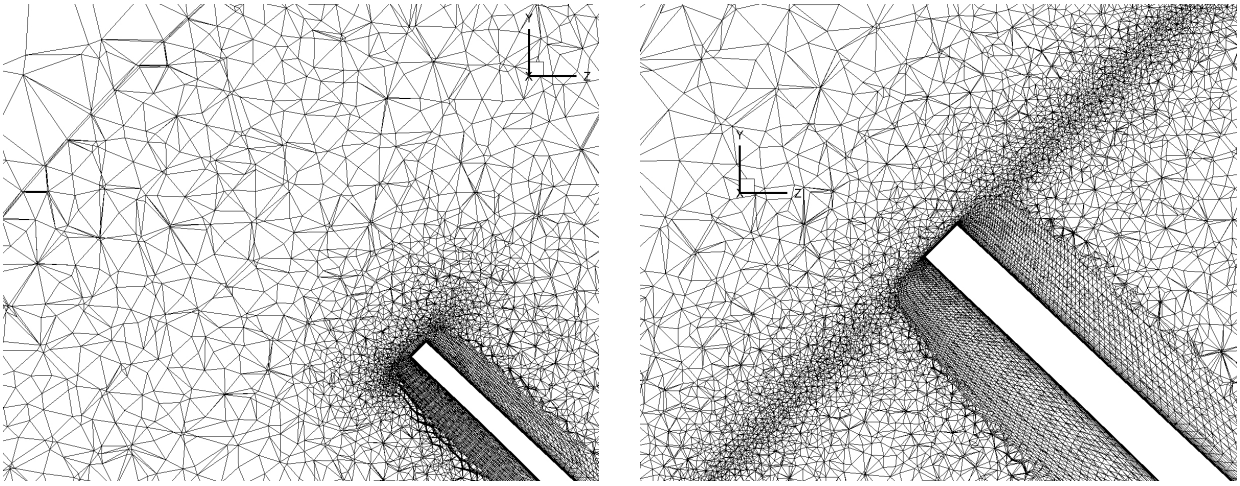

(a)

(b)

Figure 4.11: Inflation mesh at the isolated Xprop blade tip: for the simulation with the conventional propeller domain (a), and for the radially small propeller domain (b). The grid cuts were made parallel to the inlet and outlet boundaries, at the propeller location. Zoom at the blade tip.

Besides using inflation layers, the mesh at the surface of the ducts and propeller blades was also meshed with a structured liked approach. Using the mapped-mesh feature in ANSYS meshing, it was easier to specify the number and location of chordwise and spanwise divisions of the mesh, in the surface of the components. Therefore, this approach helped refining the mesh in critical areas, while not increasing the number of elements excessively. The mapped-mesh for the surfaces of the circular duct and propeller blade can be seen in Figure 4.13, as and example.

There were, however, also surfaces where mapped-meshes could not be used. An example is the corner mesh of the square duct, at the inner surface. In this surface, prescribing a fixed number of spanwise divisions would lead to too small elements where the thickness of the airfoil is larger, since the corner inner surface is too narrow in this region. Therefore, it was opted for using an unstructured surface mesh at the inner corner of the square duct, for every case which included this shroud. The unstructured mesh at the corner of the square duct can be visualised in Figure 4.14. Nevertheless, there are disadvantages related to the use of unstructured mesh at the corner of the quadrangular duct. Firstly, the generated elements are less oriented with the flow direction, which, as explained before, is not ideal. Secondly, the number of elements used increases

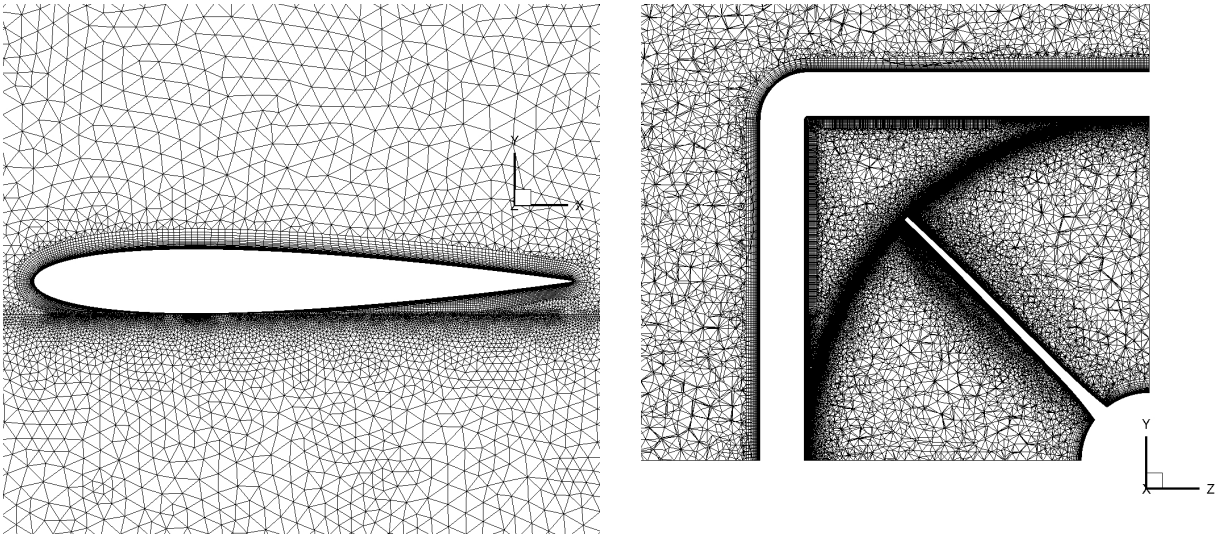

(a) (b)

Figure 4.12: Inflation mesh of the square duct in the installed configuration, with the propeller. Image (a) corresponds to a view of the grid at a periodic boundary. Image (b) corresponds a grid cut parallel to the inlet and outlet boundaries, at the propeller location.

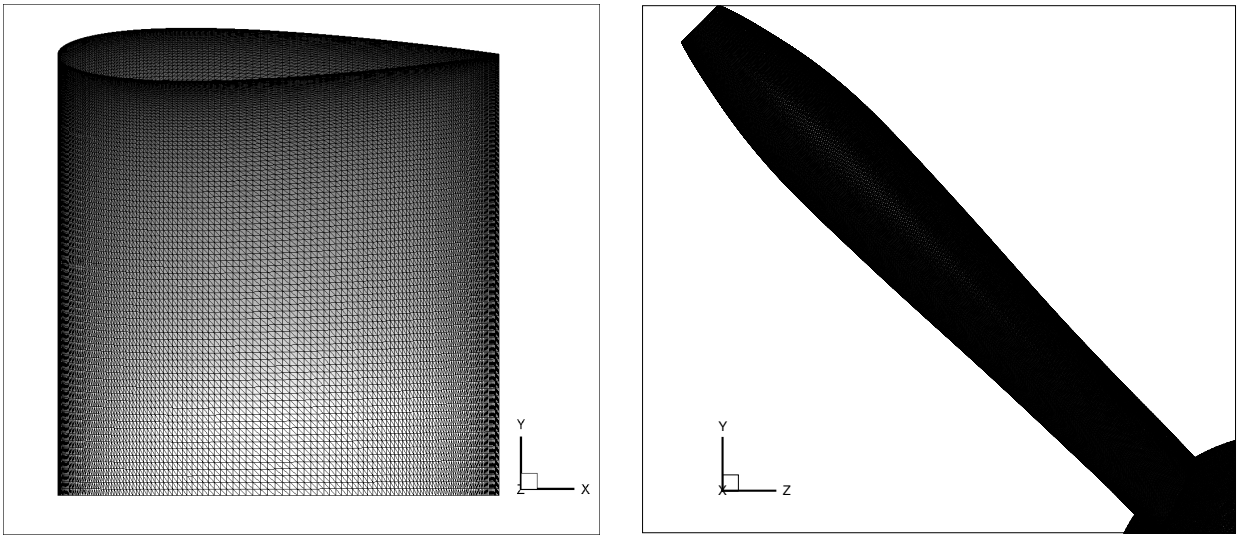

(a) (b)

Figure 4.13: Mapped mesh at the isolated ring wing (a) and isolated Xprop (b) surfaces. The mesh of the isolated Xprop corresponds to the case with the unconventional propeller domain.

considerably, in order to keep the necessary mesh refinement with an unstructured surface grid.

Furthermore, the mapped-mesh setting was also used at the interfaces between propeller and outer domain, when the Xprop was simulated. At the interfaces, when the mesh of adjacent faces of different domains does not match, the flow quantities have to be interpolated between different cells. This can result in an interpolation error, and in convergence difficulties for the solver. Therefore, to mitigate this problem, a mapped mesh was used to force the meshes of adjacent faces (of different domains) to be similar. Furthermore, another problem that comes with the unsteady simulation of a propeller using the sliding mesh technique is that the mesh in the propeller domain also rotates, along with the fan's rotation. For this reason, the mapped mesh at the interfaces for the isolated Xprop simulations was made with 90 division in the tangential direction. In this way, if the propeller domain's mesh rotates 1° or a multiple of 1°, the mesh would again be matched with the mesh of the outer domain. Indeed, the time step used for the unsteady simulations of

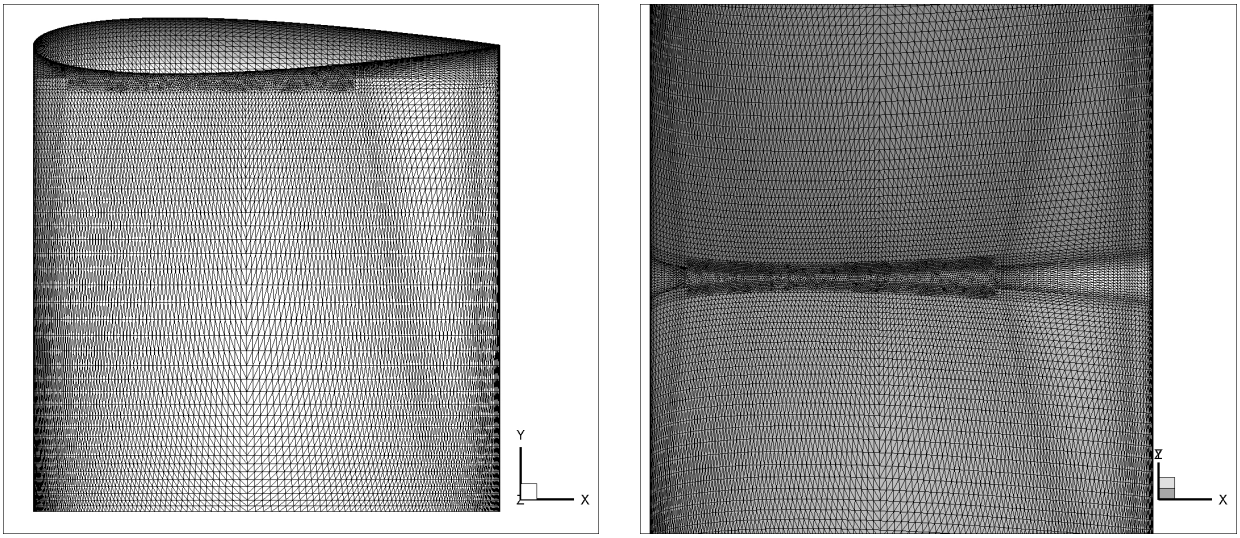

(a) (b)

Figure 4.14: Unstructured mesh at the square duct's corner: side view of the duct (a), and zoom at the inner corner (b).

the isolated propeller was equivalent to 1° rotation of the propeller. The mapped mesh at the interfaces between the two domains of the conventional isolated propeller simulation can be seen in Figure 4.15. For the unconventional simulation of the isolated Xprop (the simulation with a small propeller domain), the same approach was used to mesh the interfaces between domains. However, at the propeller location, a stripe of very fine unstructured elements was used to mesh the interfaces. This was done due to the close proximity of the interfaces to the propeller blade tip, where high gradients in the flow quantities are generated. However, it results in a large increase in the computational costs of the simulation. In Figure 4.16, the mesh at the interfaces for the unconventional domain of the isolated Xprop can be seen. In the simulations of the ducted Xprop, the same approach was used to mesh interfaces, i.e. most of the interfaces' area was covered with a mapped mesh, and only at the propeller axial location an unstructured mesh was generated. However, in the shrouded propeller simulations the resulting flowfieds are more complex. Thus, it were used 180 tangential divisions in the interfaces, instead of 90 divisions. The number of radial divisions was increased as well. The interface mesh used for the shrouded propeller simulation (with the square shroud) can be seen in Figure 4.17.

The spatial discretization error in CFD simulations depends directly on the grid refinement level, and on the precision with which grid is refined (i.e. refining the mesh in areas of higher flow gradients is a more effective way of decreasing the discretization error). However, increasing the number of elements in a simulation also leads to higher computational costs. Therefore, mesh convergence studies were performed for the simulations of the isolated components, in order to access the discretization errors of the different grids. The approach used to generate the different grids of each convergence study is discussed in section 4.5.1.

4.5.1. MESH CONVERGENCE STUDY

As previously referred, it was performed a mesh convergence study to access the discretization error in several case studies. These cases were the 2D axisymmetric simulation of the ring wing, the 3D simulation of the circular duct, the simulation of the square duct, and the simulation of the isolated Xprop with the conventional (large) propeller domain. The remaining cases were not subject to a convergence study, due to their high computational costs. The results from the convergence studies performed for the isolated components are taken as an indicator of the discretization error for the remaining simulations, since the mesh settings used are similar. However, the uncertainty in the discretization error is considerably larger in the cases for which a grid dependency study was not performed.

In the cases for which a convergence study was done, first the mesh with the considered medium refinement was generated. Afterwards, a set of grids were generated. The various mesh settings were modified with the aim of keeping the meshes geometrically similar (within the same set), as was done e.g. by Eça and

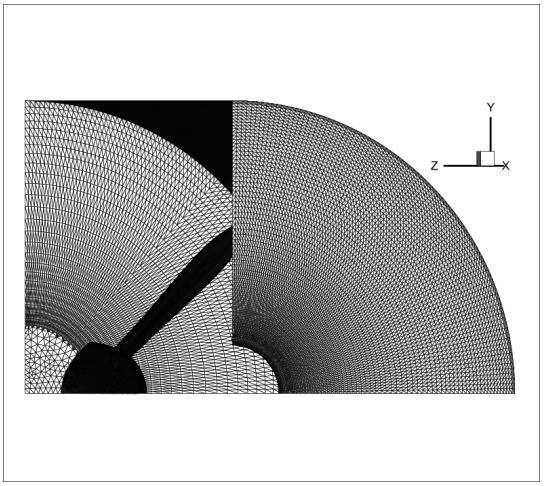

Figure 4.15: Mapped mesh at the interface between the propeller and outer domains, for the conventional Xprop simulation.

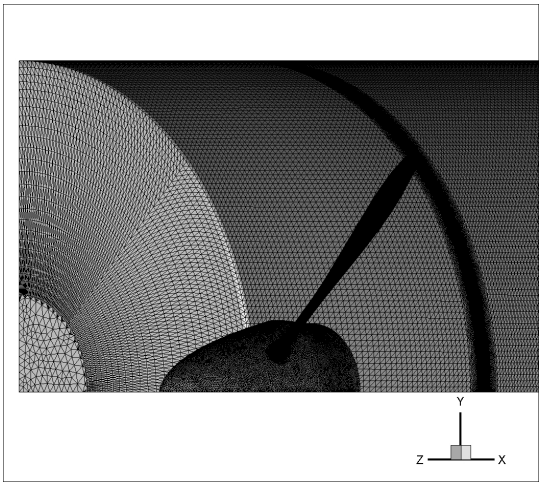

Figure 4.16: Mesh at the interface between the propeller and outer domains, for the unconventional Xprop simulation. While most of the mesh is a mapped mesh, there can be seen a stripe of unstructured elements at the propeller location.

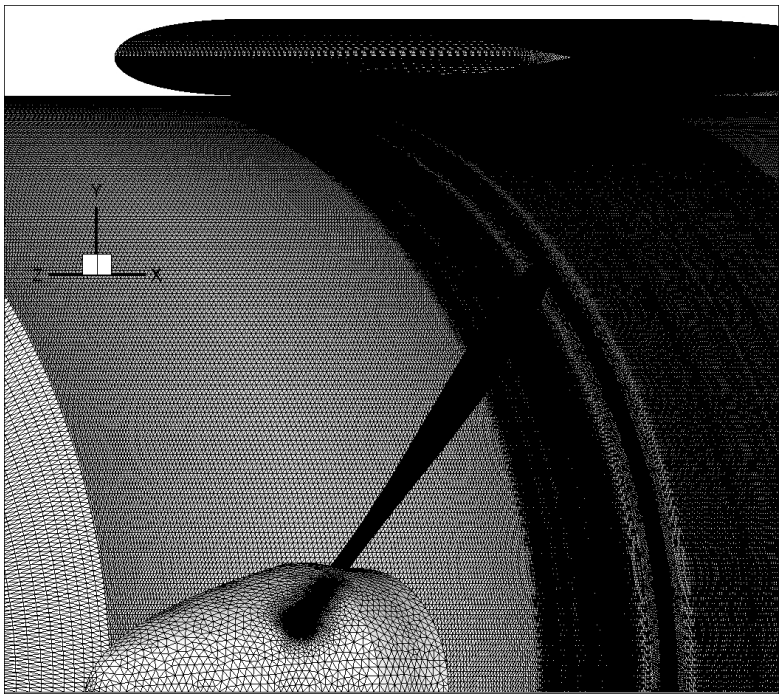

Figure 4.17: Mesh at the interface between the propeller and outer domains, for the square ducted Xprop simulation. The interface mapped mesh was made with 180 tangential divisions.

Hoekstra [33]. In this way, each finer or coarser mesh was generated, by modifying each cell sizing setting, according to the following methodology:

- For the mesh settings which specify the average cell size in a given zone (either the zone was a volume or an area), the cell size was divided or multiplied by 1.3, for setting up a finer or a coarser mesh respectively.
- For the mesh settings which specify the number of divisions in a given edge, the number of divisions was multiplied or divided by 1.3 (and rounded to unit), for setting up a finer or a coarser mesh, respectively.

- The number of layers in each inflation mesh was multiplied or divided by 1.3 (and rounded to unit), for setting up a finer or a coarser mesh, respectively. In order to keep the same total inflation height, the growth rate of the layers was adjusted. The height of the first layer was kept constant, in order to keep the same wall y^+.

- The remaining prescribed growth rates were kept constant, in volumes and areas with unstructured meshes.

Due to the associated lower computational costs, the 2D axisymmetric circular shroud case was the one for which more meshes were generated. Thus, it is also the case with a greater ratio of cell size between the finest and coarsest grids. The parameter used to quantify the refinement of each mesh was the ratio between the average cell height of the given mesh (h_i), and the average cell height of the finest mesh (h_F):

$$\frac{h_i}{h_F} = \sqrt[d]{\frac{n_{cells_i}}{n_{cells_F}}}, \tag{4.9}$$

where n_{cells_i} is the number of cells in a domain i, n_{cells_F} is the number of cells in the finest domain, and d is the domain's number of spatial dimensions. Thus, d is 2 for meshes relative to the 2D axisymmetric simulation and 3 for the remaining domains, which are 3D. In Figure 4.18, the finest and the coarsest meshes of the 2D convergence study are shown. Their refinement ratio is, respectively, $h_0/h_F = 1$ and $h_5/h_F = 2.89$. The results obtained from the convergence studies are presented in sections 5.1.1, 5.2.1, 5.3.1 and 6.1.1, for the isolated cases of the 2D ring wing, 3D ring wing, square duct and Xprop in the conventional domain, respectively.

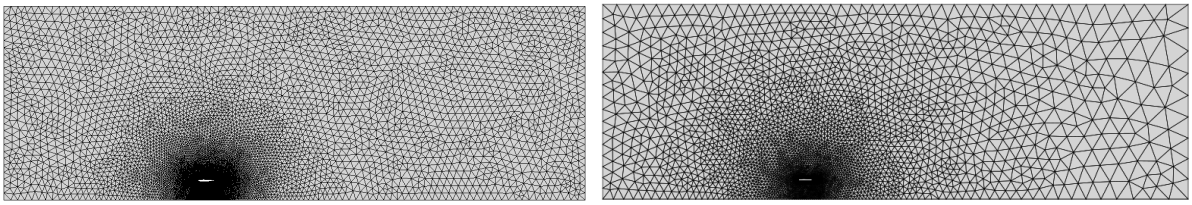

(a) (b)

Figure 4.18: Finest (a) and coarsest (b) meshes of the convergence study for the 2D axisymmetric case.

4.6. SETUP - OPERATING CONDITIONS

For each CFD simulation, after creating the computational domain and generating the grid, it was necessary to prepare the setup for the calculation. A CFD setup involves the selection of the governing equations, for example, and also the definition of the different flow quantities at the boundaries. It was previously referred, in section 3.4, which boundary conditions imposed in the simulations require the input of flow free-stream values. In order to choose the operating conditions for the simulations, several major considerations were taken into account:

- The conditions tested should be comparable to the available data for validation.

- The operating conditions should be possible to recreate in a wind tunnel, in case it is intended to do an analogous experimental study, in the future.

- The free-stream values should be such that strong compressibility effects are avoided (e.g. shock waves). Substantial compressibility effects would make the resulting flowfield more complex. Therefore, it would be more difficult to isolate and understand the fundamental aerodynamic differences between the configurations studied. It was also taken into account that the Mach number at the tip of the propellers is considerably higher than the free-stream, due to their rotational velocity.

- For the choice of the ambient values of turbulent kinetic energy and specific dissipation rate, the recommendations from Spalart and Rumsey were followed [41].

With the above restrictions in mind, it was decided to perform the simulations at ambient sea-level conditions and with a free-stream velocity of 30 m/s. These conditions are often used for wind tunnel experiments at TU Delft. Indeed, there was experimental data available for validation of the propeller Xprop's performance at these conditions, at several power settings (defined by the blade's incidence and rotational velocity). The propeller's wind tunnel data was obtained by Tomas Sinnige at TU Delft's open jet facility (OJF), and was provided by internal communication.

In this way, it was decided to use the following free-stream values for the fluid (air), which was considered to be an ideal gas:

$$\begin{aligned} V_\infty &= 30\ m/s \\ \rho_\infty &= 1.225\ kg/m^3 \\ p_{s_\infty} &= 101325\ Pa\,, \end{aligned} \tag{4.10}$$

where V_∞ is the free-stream velocity, ρ_∞ is the free-stream density, and P_{s_∞} is the free-stream static pressure. As discussed in the previous section (3.4), the boundary conditions used in ANSYS Fluent require the input of several other variables (in rounded up values):

$$\begin{aligned} T_{s_\infty} &= 288.17\ K \\ M_\infty &= 0.0882\ [-] \\ T_{0_\infty} &= 288.61\ K \\ p^G_{0_\infty} &= 552.32\ Pa\,, \end{aligned} \tag{4.11}$$

where T_{s_∞} stands for free-stream static pressure, M_∞ is the free-stream Mach number, T_{0_∞} is the free-stream total temperature, and $p^G_{0_\infty}$ is the Gauge free-stream total pressure, which corresponds to the difference between the free-stream total pressure and a reference pressure, in this case p_{s_∞}. The static temperature was calculated from the ideal gas relation:

$$T_s = \frac{p_s}{\rho R}\,, \tag{4.12}$$

where the specific gas constant was calculated from:

$$R = \frac{\hat{R}}{M'}\,, \tag{4.13}$$

being $\hat{R}$ the universal gas constant, and M' the fluid's molecular mass. The Mach number was calculated from:

$$M = \frac{V}{a}\,, \tag{4.14}$$

where V is the air velocity and a is the speed of sound:

$$a = \sqrt{\gamma R T_s}\,, \tag{4.15}$$

being γ the ratio of specific heats:

$$\gamma = \frac{C_p}{C_v}\,. \tag{4.16}$$

The specific heat, C_v, was calculated from:

$$C_v = C_p - R\,. \tag{4.17}$$

Moreover, the total temperature and pressure were determined using the equations for compressible flow:

$$\begin{aligned} \frac{T_0}{T_s} &= 1 + \frac{\gamma - 1}{2} M^2 \\ \frac{p_0}{p_s} &= \left(1 + \frac{\gamma - 1}{2} M^2\right)^{\frac{\gamma}{\gamma - 1}}\,. \end{aligned} \tag{4.18}$$

TURBULENCE FREE-STREAM QUANTITIES

As it was previously referred, the free-stream values of turbulent kinetic energy, k, and specific dissipation rate, ω, were calculated according to the recommendations from Spalart and Rumsey [41]. These recommendations were followed with the intend of having the desired values of eddy-viscosity, ν_t, in the upstream vicinity of the geometries. The desired ν_t was obtained considering two main restrictions. Firstly, the eddy viscosity development in a boundary layer should have a low dependence on the ambient value. For this reason, the ambient value of ν_t should be considerably lower than the values of eddy-viscosity which are reached in the boundary layer. Secondly, the ambient value of ν_t should be low enough, so that the gap flow between different elements is well estimated. Moreover, the suggested appropriate values for ambient k and ω also take into account the intention of estimating accurately the flow at the leading edge of each element [41]. In this region, the flow should have characteristics of a laminar boundary layer.

In this way, the following equations were used to find the appropriate ambient values of turbulence kinetic energy and specific dissipation rate, respectively [41]:

$$\begin{aligned} \frac{k}{V_\infty} &= 10^{-6} \\ \frac{\omega c}{V_\infty} &= 5\,, \end{aligned} \tag{4.19}$$

where c is a reference chord length. In this thesis, the duct's chord was used as reference. However, it should be noticed that, when using the $k-\omega$ SST model, there is a decay of k and ω from the domain boundaries until the flow reaches the geometries. This poses a problem, since it would make the k and ω values lower than desired, in the upstream vicinity of the geometries. To solve this decay problem, weak sources of k and ω can be placed everywhere in the domain [41]. The appropriate sources of k and ω which lead to the ambient values estimated from equation 4.19 where found iteratively, with a trial and error approach. In this way, the free-stream values of turbulence kinetic energy and specific dissipation rate set at the boundaries were (rounded values):

$$\begin{aligned} k_\infty &= 9\times10^{-4}\ m^2/s^2 \\ \omega_\infty &= 695\ s^{-1}, \end{aligned} \tag{4.20}$$

which, from equation 3.2, result in the free-stream value of eddy-viscosity:

$$\nu_{t_\infty} = 1.3\times10^{-6}\ m^2/s\,. \tag{4.21}$$

To avoid the decay of these values until the flow reaches the geometries, the following sources of turbulent kinetic energy and specific dissipation rate were used (in all test cases), respectively:

$$\begin{aligned} S_k &= 0.07\ kg/(s^3 m) \\ S_\omega &= 49000\ kg/(m^3 s^2)\,. \end{aligned} \tag{4.22}$$

The effect of using sources for k and ω is illustrated in figures 4.19 and 4.20, for the case of the isolated duct (or ring wing) simulated with a 2D axisymmetric domain. In the simulation where the sources were used (see figures 4.19a and 4.20a), it can be understood that the values of k and ω upstream of the ring wing are equal to the inlet values. On the contrary, in the simulation where no sources for k and ω were used (images 4.19b and 4.20b), free-decay of these quantities was allowed. Indeed, it can be understood that the value of k and ω upstream of the duct are considerably lower in this case, when compared to the values at the inlet. Moreover, it is also interesting to notice that, in the simulation without the sources, k remains at a high value in the wake of the wing, until it reaches the outlet. In the simulation with the sources, k returns to the free-stream value before the outlet. This happens due to the fact that there is a strong decay of ω in the wake, when no sources are used. Therefore, k dissipates faster in the wake, if sources of ω are present. As expected, using sources of ω results in a higher value of the specific dissipation rate in the duct's wake. It should be pointed out that the purpose of using sources for k and ω is not to have an accurate estimation of these variables in the wake. The sources are used in order to have effective ambient values (of k and ω) immediately upstream of the geometries, so that their boundary layers are well estimated, with the appropriate accuracy of the $k-\omega$

SST turbulence model.

From the simulation results, it was understood that the difference between the total drag of the duct in these two simulations was relatively small. The difference was 0.17% of the drag of the duct in the simulation where the sources were used. Therefore, it can be concluded that for this 2D mesh with these specific inflow conditions, the total drag of the ring wing is not largely affected by the introduction of sources in the domain. It is also important to refer that, for all the remaining simulations, these sources of k and ω were introduced. The comparison with a simulation without sources was only made for the 2D axisymmetric case, which was the less expensive case (computationally).

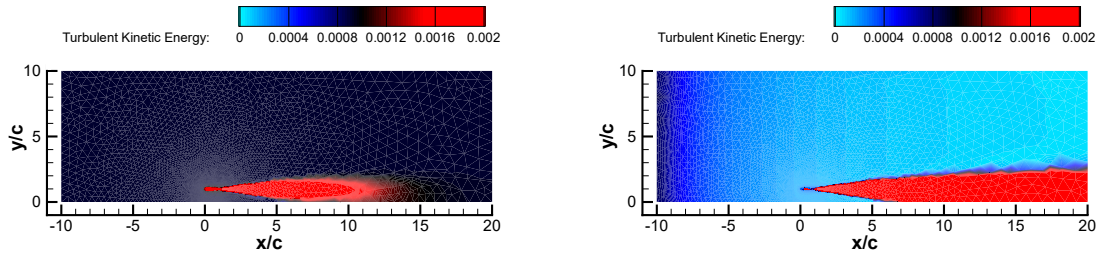

(a) Simulation with sources for k and ω over the domain. (b) Simulation without sources for k and ω.

Figure 4.19: Turbulent kinetic energy $[m^2/s^2]$ contours for two 2D axisymmetric simulations of a ring wing, over the entire domain. One simulation had weak sources for k and ω in the domain (left image), and in the second simulation free-decay of k and ω was allowed (right image). The x and y axis show the position in the domain, which was non-dimensionalised with a reference length - the ring wing's chord.

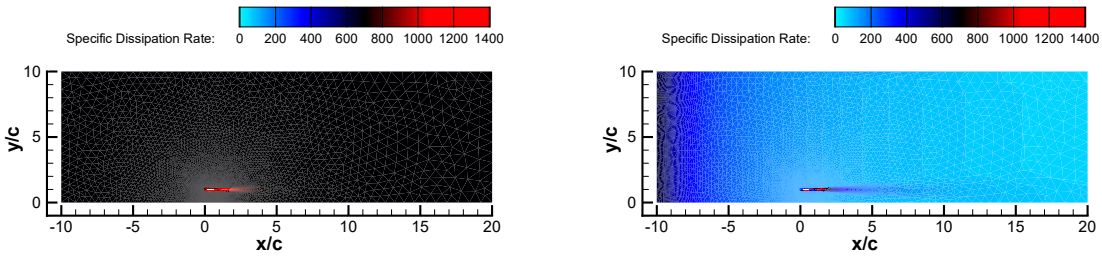

(a) Simulation with sources for k and ω over the domain. (b) Simulation without sources for k and ω.

Figure 4.20: Specific dissipation rate $[s^{-1}]$ contours for two 2D axisymmetric simulations of a ring wing, over the entire domain. One simulation had weak sources for k and ω in the domain (left contour), and in the second simulation free-decay of k and ω was allowed (right contour). The x and y axis show the position in the domain, which was non-dimensionalised with a reference length - the ring wing's chord.

4.7. SOURCES OF NUMERICAL ERROR IN THE SIMULATIONS

Until this point, it were discussed the various steps taken before performing the simulations. After running the calculations, it was necessary to post process and analyse the results. The main results are shown in the next chapters (6 and 7). When interpreting the CFD results, it should be kept in mind that the simulations' results are different from any possible exact solutions to the combination of boundary conditions and equations used. Indeed, there are numerical errors associated with the calculation of flowfields with CFD. There are different sources of numerical errors: the round-off error, the iterative error and the discretization error [33]. The round-off error is present due to the finite number of digits used by the computer, which leads to the round up of the exact values of each variables. Usually, in CFD this source of error is considerably lower than the iterative and discretization error. Therefore, the round-off error was considered to be negligible during this thesis.

The discretization error is usually the strongest source of numerical uncertainty in CFD simulations [33]. This error comes from the fact that the differential fluid mechanics equations are considered by the solver as a system of algebraic equations. In CFD simulations, the spatial discretization error can be decreased by increasing the number of cells in the domain, specially in zones were the gradients in the flow variables are high. However, increasing the number of elements has the drawback of higher computational costs. The meshes generated in the thesis, along with the mesh convergence study used to access the discretization error in the simulations are further discussed in section 4.5 of the report. In unsteady RANS simulations (URANS), there is also an error relative to the temporal discretization. The temporal discretization error can be lowered by decreasing the time interval between time-steps. In this project, even though no specific study was done to investigate the temporal error in the simulations, it was used a time step which was considered to be low enough to resolve each flowfield. For the isolated propeller case, and for the propeller ducted in a (conventional) circular duct, the time-step used in each simulation corresponds to 1° rotation of the fan blades. For the unconventional ducted propeller case, however, the time step had to be lowered to 0.5° of propeller rotation. This is due to the fact that the temporal gradients were higher in this case, and the solver could not reach a converged solution with a higher time step. These time steps are relatively lower than the time step used in [51] for unsteady propeller simulations, where a time step corresponding to 2° rotation of the fan was used. In this thesis, the close proximity between propeller and duct, which can lead to higher gradients of the flowfield variables, justifies the need for a more resolved simulation (temporally).

Ideally, the iterative error in CFD should be orders of magnitude lower than the discretization error, so that it can be neglected [33]. However, since the fluid mechanics equations used in CFD are highly non-linear, an iterative error is always present. In order to monitor the iterative error during the thesis' simulations, two main indicators were considered. Firstly, the convergence of certain quantities of interest was checked, versus the iteration number. These quantities were, for example, viscous and pressure drag at the ducts, or thrust at the propeller. Secondly, the convergence of the residuals was also checked, in each simulation. The residuals are an indicator of the imbalance of different quantities in the whole domain (e.g. mass imbalance, energy imbalance). Therefore, the residuals should be as low as possible. More precisely, the normalized residuals should be at least of the order of 10^{-3}, preferably 10^{-4} [23]. During this thesis, it were not always obtained ideally low values of the residuals, for every equation. Therefore, it can not be concluded that the iterative error is negligible in comparison to the discretization error. As an example, the scaled residuals for 4 simulations are presented in Figures 4.21 and 4.22. The 2D axisymmetric simulation of the ring wing was the case with best convergence of the residuals. On the simulation with the medium sized mesh (see Figure 4.21a), the highest remaining residual was the one relative to the turbulent kinetic energy equation, with a value of $1.8e-4$. The residuals of the remaining equations all converged to values bellow $1e-11$. However, for the 3D simulations, the remaining residuals were higher. In the steady simulation of the isolated square duct (see Figure 4.21b), the residual relative to the continuity equation was the highest ($3.7e-4$). In the steady simulation of the circular duct with the actuator disk at high thrust setting (corresponding to the propeller at an advance ratio of 0.7), the residual for the continuity equation lowered until $1.1e-3$, as it is shown in Figure 4.22a. Figure 4.22b shows the residuals' convergence for the unsteady simulation of the propeller shrouded by the unconventional square duct. Since it is an unsteady simulation, the residuals have to converge for each time step, during the inner iterations' loop. The final residuals shown in figure 4.22b correspond to the time step where the propeller completes 3.5 revolutions. For convenience, it is not shown the full residuals' convergence history, since too many time steps were computed. For this unsteady simulation, it also can be seen that the least converged residual is the one relative to the continuity equation, which converged until approximately $9e-4$ for each time step. It is important to refer that the scaled residuals were calculated by Fluent as the summation of the imbalance in every cell in the domain, for a given variable ϕ, divided by the summation of the flow rate of ϕ through the whole computational domain [17].

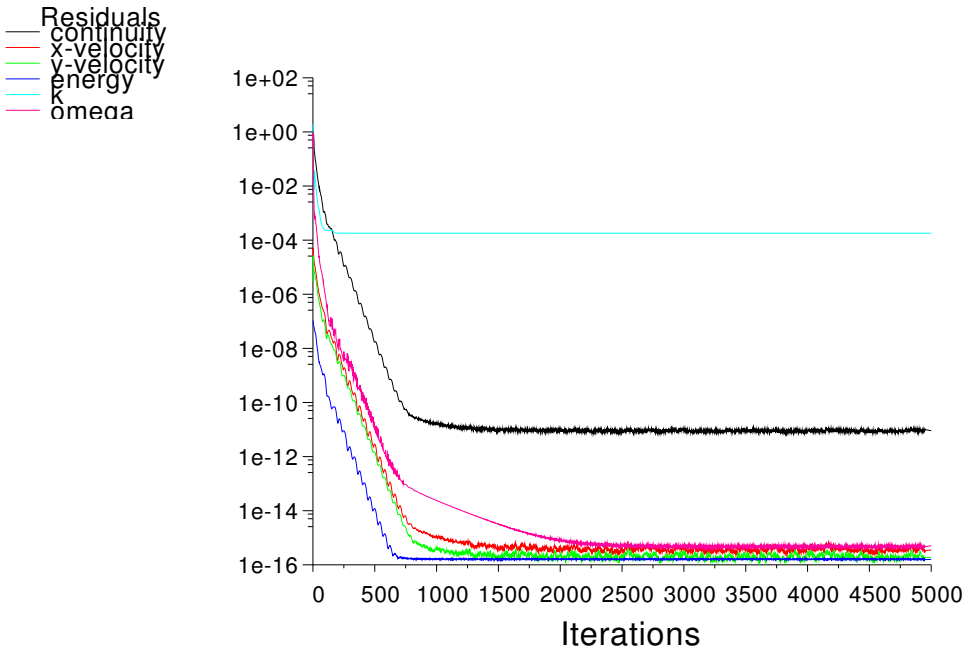

(a) 2D axisymmetric simulation of the ring wing.

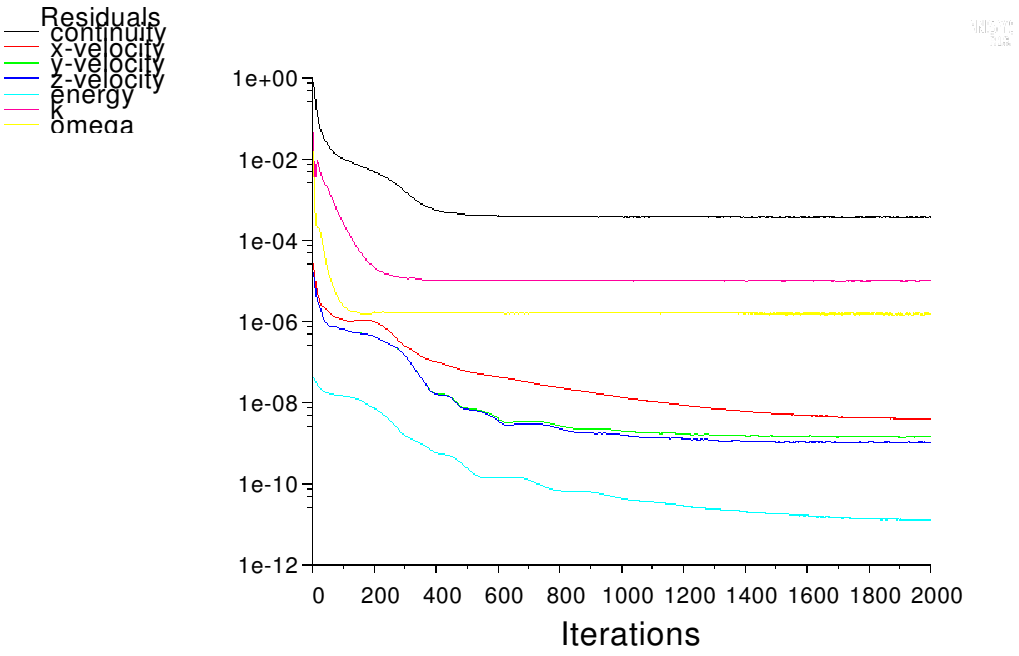

(b) Simulation of the isolated square duct.

Figure 4.21: Residuals convergence history for two simulations of isolated components. Figure (a) corresponds to the convergence history of the 2D axisymmetric simulation of the ring wing, and Figure (b) corresponds to the convergence history for the simulation of the isolated square duct. Both plots correspond to the simulations with the medium size mesh.

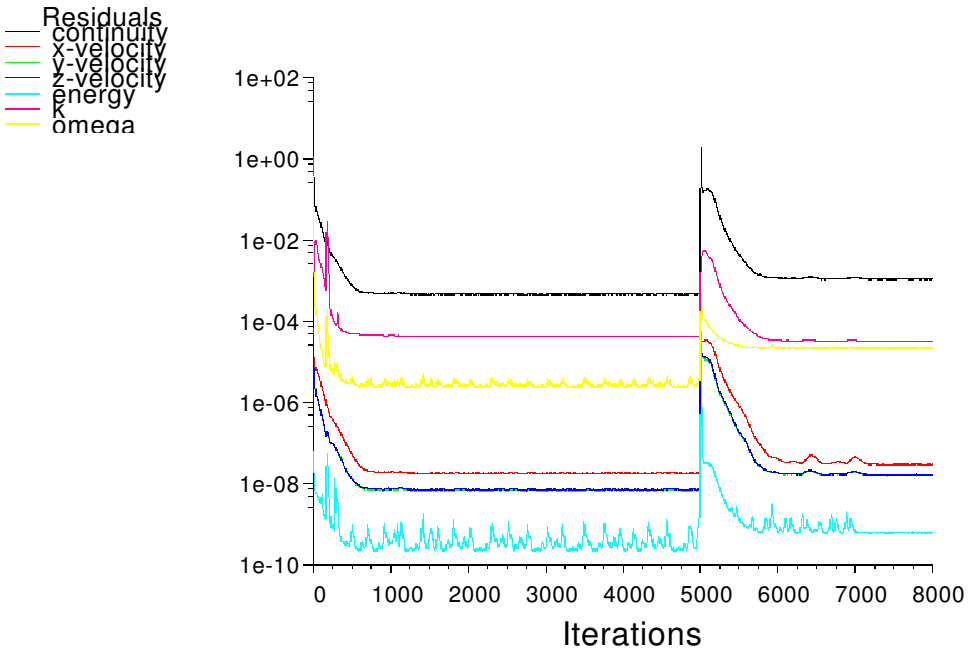

(a) Simulation of the circular duct with the actuator disk.

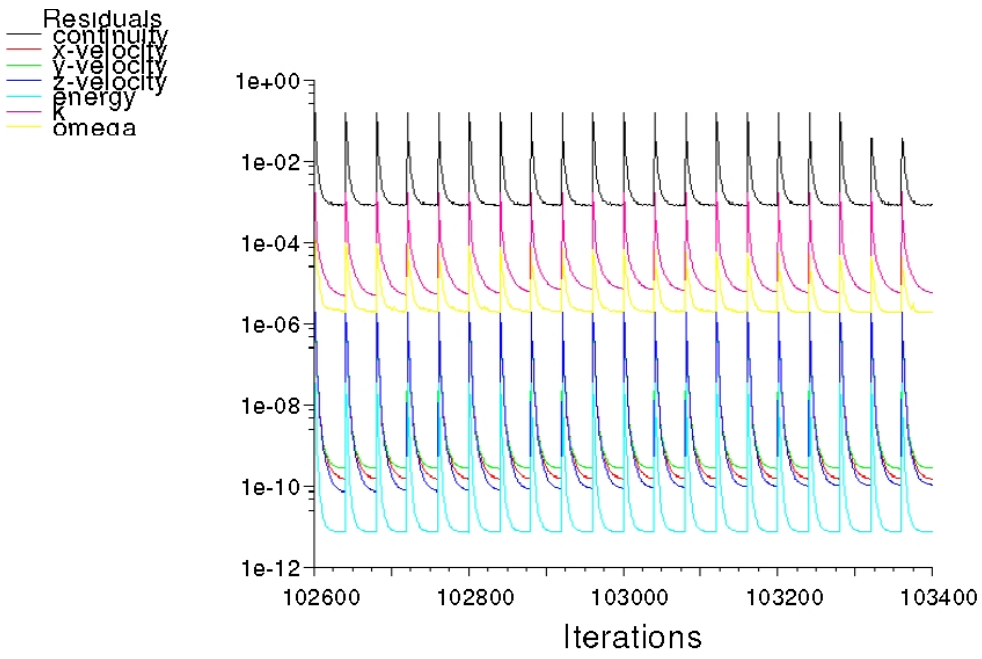

(b) Simulation of the square duct with the full blade propeller.

Figure 4.22: Residuals convergence history for two simulations with installed components. Figure (a) corresponds to the convergence history for the simulation of the circular duct with the actuator disk, and Figure (b) corresponds to the convergence history for the simulation of the square duct with the propeller. The operating condition of the respective propulsor, in each case, corresponds to a high thrust setting: 0.7 advance ratio.

III

RESULTS

5

ISOLATED DUCTS CHARACTERISATION

In this chapter, the results obtained for the isolated ducts are presented and discussed. Firstly, the results from the 2D axisymmetric simulation of the ring wing are presented, in section 5.1. Secondly, the results from the 3D simulation of the isolated circular wing are shown, in section 5.2. Thirdly, the results from the simulation of the square shroud are presented, in section 5.3. The chapter includes results from the grid convergence studies of the several cases. Furthermore, the results from the isolated circular duct simulation are compared against results from other authors, for validation.

It is important to introduce several parameters used to evaluate the aerodynamic performance of the different test cases. The pressure coefficient was defined as:

$$c_p = \frac{p - p_\infty}{q_\infty}, \tag{5.1}$$

where p is the static pressure, p_∞ is the free-stream static pressure, and q_∞ is the free-stream dynamic pressure. Similarly, the total pressure coefficient was defined as:

$$c_{p_t} = \frac{p_t - p_\infty}{q_\infty}, \tag{5.2}$$

where p_t is the total pressure. The skin friction coefficient was defined as:

$$c_f = \frac{\tau_w}{q_\infty}, \tag{5.3}$$

where τ_w is the wall friction. The three-dimensional drag coefficient of the shrouds was defined as:

$$C_D = \frac{D}{q_\infty S_p}, \tag{5.4}$$

where D is the drag of the duct, and S_p is the propeller disk area. A second drag coefficient definition used was:

$$C'_D = \frac{D}{q_\infty S_{duct}}, \tag{5.5}$$

where S_{duct} is the reference area of each duct:

$$S_{duct} = P_{duct} c_{duct}, \tag{5.6}$$

where P_{duct} is the perimeter of the duct, measured at the leading edge. Since both ducts used have the same chord, the reference area of the quadrangular duct, S_{qduct}, is larger than the reference area of the circular duct by approximately 25%:

$$S_{qduct} \approx 1.25 \times S_{cduct}. \tag{5.7}$$

5.1. 2D AXISYMMETRIC CIRCULAR DUCT

The present section shows and discusses results for the 2D simulation of the circular duct. From the isolated simulation of the circular duct, it is important to evaluate the force components of the body's aerodynamic drag. Furthermore, it should be understood how the duct influences the velocity of the flow at the propeller location, since this velocity will influence the performance of the propeller. As an example, the angle of attack (α) of each blade section will directly depend on the income flow's axial velocity (see Figure 2.2, relative to BEM theory).

The results presented in this section correspond to the simulation with the mesh with medium refinement, for consistency with the overall report. The results have a higher discretization error than the results obtained with the most refined mesh, but have the advantage of being more comparable to the results of the installed configurations, since the grids are more similar. In sub-section 5.1.1, the results for the medium mesh used for the 2D simulation are compared against results from grids with different refinements. In this way, the discretization error in the simulations is evaluated.

In order to achieve a deeper understanding of the flowfield around the circular duct, the pressure coefficient and the axial velocity (divided by the free-stream velocity) of the flow in the vicinity of the duct section can be seen in Figures 5.1 and 5.2. From Figure 5.1, it can be understood that there is a lower pressure inside the duct than near the outer surface of the duct, even though the airfoil is symmetric. This is due to the higher contraction of the flow that has to occur inside the duct. Correspondingly, the axial velocity of the flow is also higher inside the duct (Figure 5.2). A greater axial velocity of the flow inside the duct is expected to influence the performance of a propeller located in this region. This is due to the fact that the effective velocity vector at each blade section is modified, with an increase in the axial component of the flow velocity. This effect is expected to decrease the effective angle of attack of each blade section, and therefore its loading, as it can be understood from Figure 2.2 (relative to blade element theory).

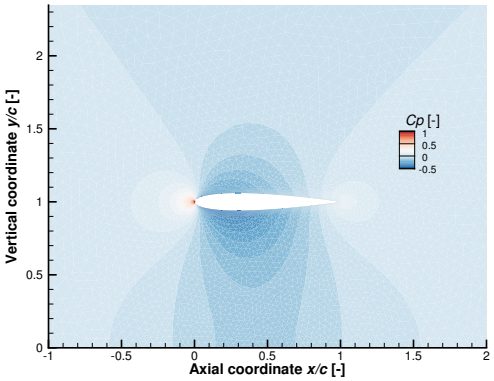

Figure 5.1: Pressure coefficient (C_p) distribution in the vicinity of the ring wing section. Results obtained from the 2D axisymmetric simulation with the medium mesh.

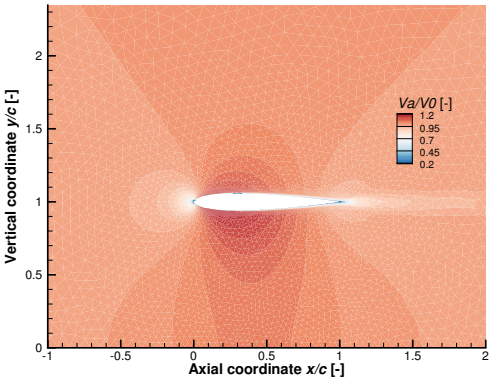

Figure 5.2: Axial velocity (V_a) distribution, normalised with the free-stream velocity, V_0, in the vicinity of the ring wing section. Results obtained from the 2D axisymmetric simulation with the medium mesh.

In Figure 5.3, it can be seen the C_p distribution across the ring wing section, versus x position divided by the duct's chord, x/c. It this plot it is also clear that the pressure coefficient is lower inside the duct than in the outer surface. Moreover, it is interesting to notice that C_p does not increase to 1 at the trailing edge of the duct section. This is due to a viscous effect, i.e. there is flow separation at the trailing edge of the duct. Flow separation at the trailing edge is a cause for the isolated duct's pressure drag, since there is a stagnation point at the leading edge of the duct, where C_p is 1.

In Figure 5.4, it can be seen the axial skin friction coefficient, C_{f_x}, distribution versus x/c. This distribution helps understanding the causes for friction drag generated along the duct. Near the leading edge of the duct, C_{f_x} is maximum due to the low height of the boundary layer in that region. As the BL grows, C_{f_x} also decreases towards the trailing edge. However, around 10% chord ($x/c = 0.1$) there is a sudden increase in skin friction, due to transition of the boundary layer from laminar to turbulent.

In Figure 5.3, it is shown how the boundary layer height (δ) grows on both surfaces of the duct. For a better understanding, the result is compared against Blasius' solution for the boundary layer height of a turbulent flat plate without a pressure gradient ($\Delta p = 0$). It is interesting to notice that, on both duct surfaces, the boundary layer of the duct first grows slower than the BL of the flat plate. However, at $x/c = 1$, i.e. at the trailing edge of the duct, δ is similar to the BL height of the flat plate. The main reason for these differences is the pressure gradient created in the flowfield due to the presence of duct. Indeed, boundary layers grow slower in the presence of a favourable pressure gradient (when $dp/dx < 0$), and grows faster under unfavourable pressure gradients ($dp/dx > 0$). The differences between the BL of the ring wing and the BL of a turbulent flat plate can also be understood from Figure 5.6. Here, it is plotted the height of the boundary layer of the duct obtained from the 2D simulation divided by the height of a turbulent flat plate at an equivalent chordwise position. It is interesting to noticed that the shape of this plot (Figure 5.6) resembles the shape of the C_p distribution plot, in Figure 5.3. The correspondence between the two plots further demonstrates the effect of a pressure gradient on a BL growth.

The evaluation of the duct's boundary layer height is also important to understand the propeller's performance inside the duct. The propulsive system was designed so that the blade tip clearance would be small, 0.3% of the blade radius. In this way, the gap between blade and duct is only approximately 0.28% of the duct's chord, which is less than half of the isolated duct's BL height at the propeller location (Figure 5.5). In this way, it could be expected that the duct's boundary layer would increase the loading at the blade tip sections, which would be under an inflow with a lower axial velocity, associated with a lower total pressure. However, it is difficult to predict exactly how the duct's boundary layer would influence the propeller's efficiency just from the isolated duct's simulation. The results from the ducted propeller simulation are shown and discussed in the next chapter (Chapter 7), which is dedicated to the installed configurations. Before analysing the installed configurations, it is also relevant to compare the results from the 2D axisymmetric simulation of the ring wing with the results from the 3D simulation (section 5.2), and it is important to analyse the results obtained for the isolated square duct (section 5.3) and propeller (sections 6.1 and 6.2).

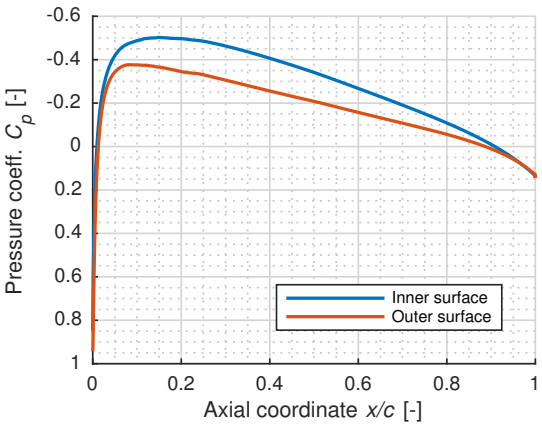

Figure 5.3: Pressure coefficient distribution at the ring wing section, versus chordwise position, x/c. Results obtained from the 2D axisymmetric simulation with the medium mesh.

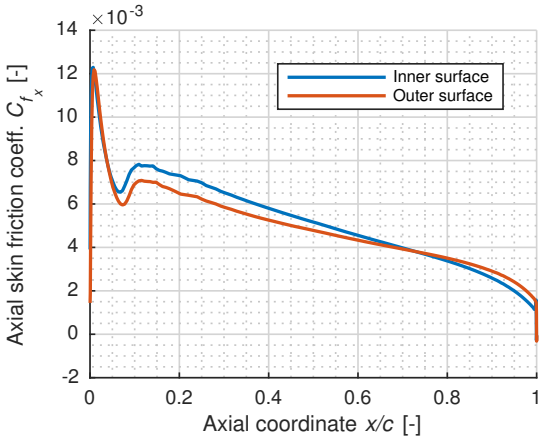

Figure 5.4: Axial skin friction coefficient distribution at the ring wing section, versus chordwise position, x/c. Results obtained from the 2D axisymmetric simulation with the medium mesh.

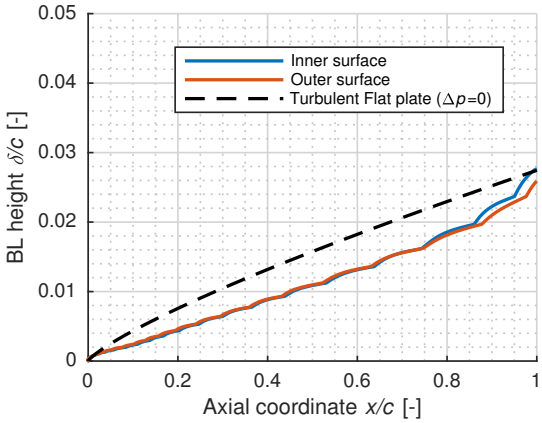

Figure 5.5: Ring wing boundary layer height, versus chordwise position. The results obtained from the 2D axisymmetric simulation with the medium mesh are compared against Blasius' solution for the turbulent BL height over a flat plate, with zero pressure gradient.

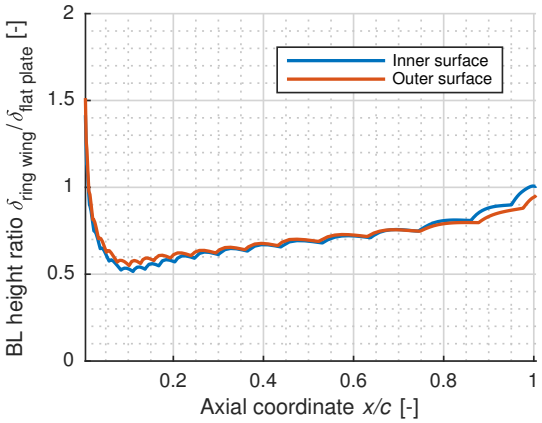

Figure 5.6: Ring wing boundary layer height divided by the height of a flat plate turbulent BL, $\delta_{ring\,wing}/\delta_{flat\,plate}$, versus chordwise position. Results obtained from the 2D axisymmetric simulation with the medium mesh.

5.1.1. MESH CONVERGENCE STUDY

Since the computations were done with 2 spatial dimensions instead of 3, the grids used were orders of magnitude smaller (in total number of elements), and the computational costs were considerably lower. Thus, the 2D problem was the case in which it was possible to test grids with a higher refinement, for the convergence study. The basis used for the estimation of the discretization uncertainty was the Grid Convergence Index (GCI), according to which [33]:

$$U = F_s|\delta_{RE}|\,, \tag{5.8}$$

where U is the uncertainty, F_s is a safety factor and δ_{RE} is the estimated error.

In Table 5.1, the values for the drag coefficients obtained with the different grids are specified. Grid 4, with a medium refinement, is the grid generated with settings most similar to the meshing settings used to mesh the ducts in the installed configurations. Furthermore, in Table 5.1 it is also shown an estimated exact value (ϕ_0), which would correspond to an equivalent simulation with a mesh (mesh 0) with infinite number of elements. The exact value was estimated based on Richardson extrapolation. In this way, it were calculated the values of ϕ_0, of the constant α and of the observed order of accuracy, p, which would minimize the function [33]:

$$S(\phi_0,\alpha,p) = \sqrt{\sum_{i=1}^{n_g}\left(\phi_i - (\phi_0 + \alpha h_i^p)\right)^2}\,, \tag{5.9}$$

using a least squares root approach. In equation 5.9, n_g is the number of meshes used in the convergence study, ϕ_i is the value of the variable obtained with mesh i, and h_i is a value representative of the cell size in mesh i.

In Figure 5.7, it is shown the convergence of the drag coefficients C_{D_p}, C_{D_f} and C_{D_t}, with respect to grid size. The values are shown in terms of relative difference, in percentage, to the grid with a medium refinement (grid 4). It is also shown a line with the values which can be obtained from extrapolation. The line was calculated using:

$$\phi_i' = \phi_0 + \alpha h_i^p\,, \tag{5.10}$$

where ϕ_i' is the extrapolated value of a given quantity, for a mesh with element size h_i.

2D Ring wing - grid converge study

Mesh	Refinement	# of elements	h_i/h_1 [-]	C_{D_p} [-]	C_{D_f} [-]	$C_{D_{total}}$ [-]
6	very coarse	7917	2.886	0.007279	0.022420	0.029699
5	coarse	14177	2.157	0.007167	0.022949	0.030116
4	medium	19856	1.822	0.006991	0.023220	0.030211
3	fine	28460	1.522	0.006991	0.023376	0.030367
2	very fine	42881	1.24	0.007012	0.023385	0.030397
1	super fine	65949	1	0.006992	0.023452	0.030443
0	-	∞	0	0.006964	0.023543	0.030509

Table 5.1: Grids used for the 2D convergence study and drag coefficients on the circular duct from the 2D axisymmetric simulations.

In Table 5.2, it is shown the apparent order of convergence for each quantity, the standard deviation of each fit, the error of the medium grid, $\delta_{RE,4}$, and, also for the medium grid, the discretization uncertainty $U_{\phi,4}$. The standard deviation, U_s, of each fit was calculated from:

$$U_s = \sqrt{\frac{\sum_{i=1}^{n_g} \left(\phi_i - (\phi_0 + \alpha h_i^p)\right)^2}{n_g - 3}}. \tag{5.11}$$

The error was estimated from [33]:

$$\delta_{RE} = \phi_i - \phi_0 \,, \tag{5.12}$$

and the discretization uncertainty, U_ϕ, was calculated from:

$$U_\phi = 1.25|\delta_{RE}| + U_s \,, \tag{5.13}$$

for the cases shown in Figure 5.7, where monotonic convergence of the solutions was identified.

2D Ring wing - grid converge study

Quantity	C_{D_p} [-]	C_{D_f}	C_{D_t}
p	2.87	2.55	2.41
U_s [%]	0.770471	0.219784	0.086193
$\delta_{RE,4}$ [%]	-0.385130	1.390088	0.986422
$U_{\phi,4}$ [%]	1.251884	1.957394	1.319221

Table 5.2: Grid convergence study used for the 2D axisymmetric simulation of the ring wing, considering the pressure, friction and total drag coefficients of the duct.

Furthermore, it were also checked the convergence of the C_p and C_{f_x} chordwise distributions at the ring wing. These plots can be seen in Figs. 5.8 and 5.9, respectively. The Figures show the results obtained with the 2D mesh with medium refinement (4), and with the grids which are most different from the medium grid: 1 and 6. From Fig. 5.8, it can be understood that the C_p distributions are similar for the 3 grids. The larger differences are found around half duct chord, even though the pressure gradients in this region are lower. The region with higher discretization error of the C_p is, therefore, the region where the meshes are coarser. In Figure 5.9, it can be seen that the discretization error of skin friction at the duct is higher near the transition location (around $x/c = 0.1$). This indicates that the refinement of the mesh has as an influence on the specific

location where the solver predicts transition.

In Figure 5.10, it can be seen the axial velocity distributions inside the isolated circular duct, at the propeller location (30% duct chord). The axial velocity was normalised with the free stream velocity (V_a/V_0), and it is shown versus radial position r/R_p, where R_p is the propeller radius. Since it is a 2D simulation, $r = y$. The distributions shown were obtained with the finest, medium and coarsest meshes, respectively, 1, 4 and 6. It can be understood that the result is very similar for the three grids. The axial velocity shown is higher than the free-stream velocity, due to flow contraction. Only at the location of the blade tips, the axial velocity drops to values lower than free-stream, due to the presence of the duct's boundary layer, until V reaches 0 m/s at the duct's surface. Indeed, a no-slip boundary conditions was implemented at the duct's surfaces (as it was referred in section 4.4).

Despite the small differences found, it was concluded that both C_p, C_{f_x} and V_a/V_0 distributions calculated by grid 1 and 4 are relatively similar. Therefore, it was considered that the mesh settings used for meshing the 2D grid 4 would be appropriate to mesh the duct in the installed configurations. Naturally, the threshold for the acceptable duct's mesh spanwise refinement was not accessed with the 2D convergence study. This could only be done with 3D simulations of the circular duct, which are presented in the next section.

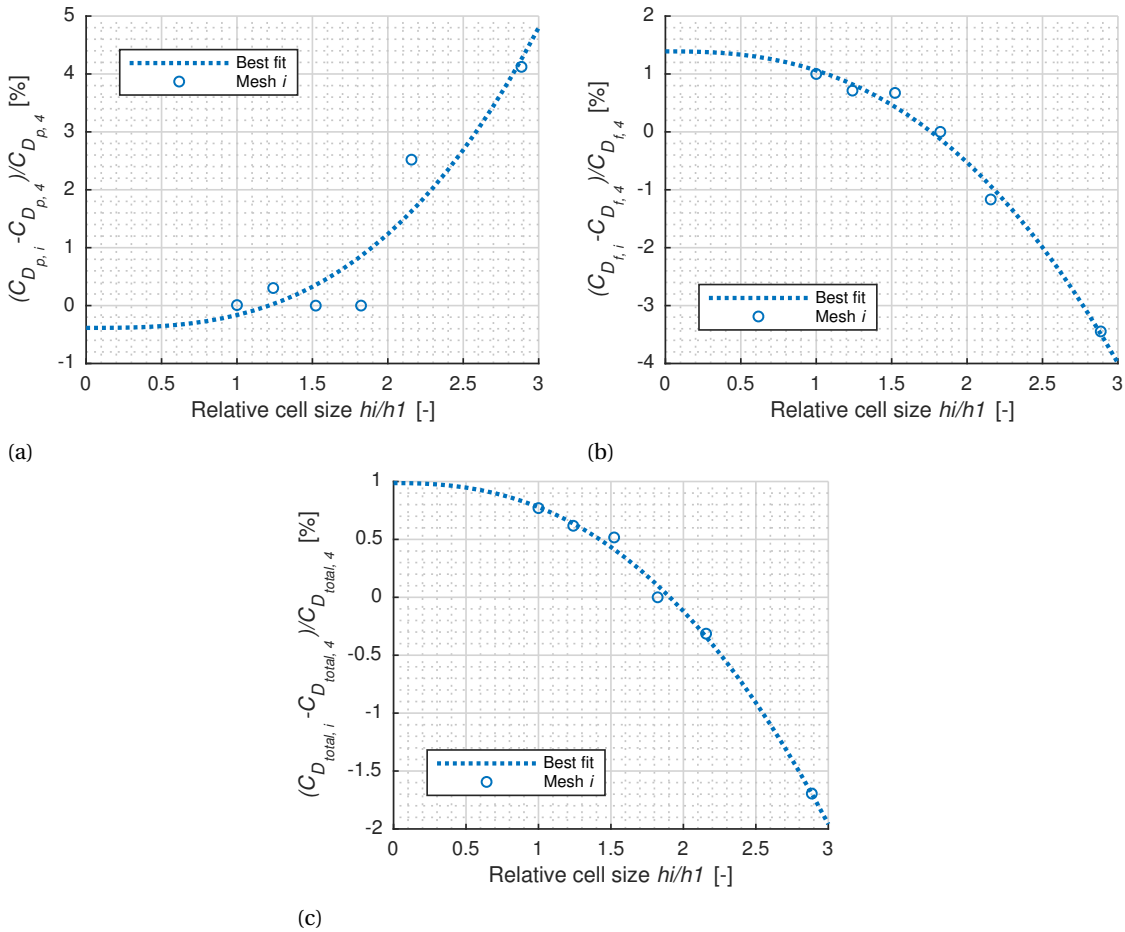

Figure 5.7: Convergence study of the isolated circular wing's pressure drag coefficient (top-left), friction drag coefficient (top-right) and total drag coefficient (bottom), with respect to grid element size. Results obtained with 2D axisymmetric simulations. It is shown the relative difference to the value calculated with mesh 4 (medium refinement), C_{D_4}.

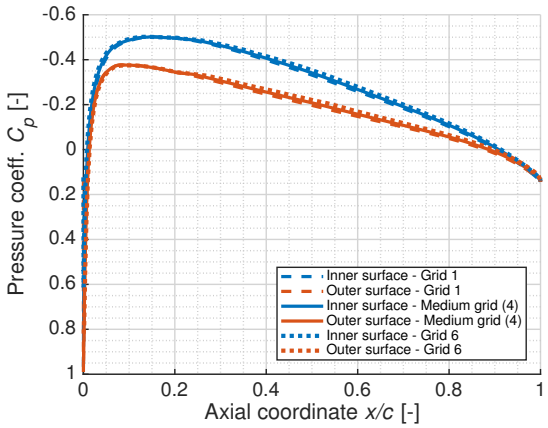

Figure 5.8: Convergence study of the isolated circular wing's pressure coefficient chordwise distribution, with respect to grid element size. Results obtained with 2D axisymmetric simulations.

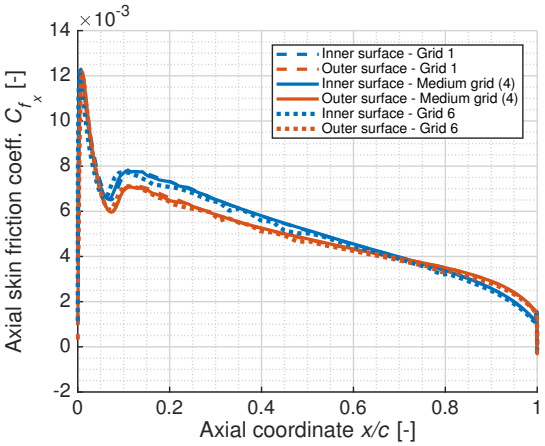

Figure 5.9: Convergence study of the isolated circular wing's skin friction coefficient (in the x direction) chordwise distribution, with respect to grid element size. Results obtained with 2D axisymmetric simulations.

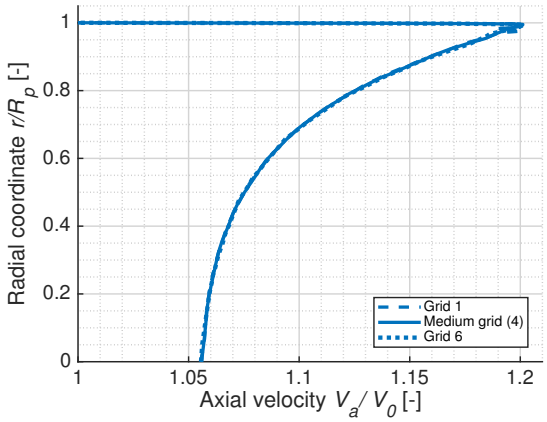

Figure 5.10: Convergence study of the axial velocity distribution at the propeller location ($x/c = 0.3$), inside the isolated circular duct, with respect to grid element size. The results were obtained with 2D axisymmetric simulations, with grids 1 (super fine), 4 (medium refinement), and 6 (very coarse).

5.2. 3D CIRCULAR DUCT - ISOLATED

The present section shows and discusses the results obtained from the 3D simulation of the circular duct, with a computational mesh with medium refinement. The results obtained with grids with different refinements are shown in sub-section 5.2.1, which is relative to the grid convergence study.

Figures 5.11 and 5.12 show, respectively, the pressure coefficient contour and the axial velocity contour around the duct. The C_p and V_a/V_0 contours are very similar to the ones obtained from the 2D simulation (Figs. 5.1 and 5.1). It can also be identified, from the 3D computation, that inside the duct the C_p is lower than the free-stream and the axial velocity is higher. As it was discussed in section 5.1, this has an effect in the performance of a propeller placed inside the duct. For this reason, the axial velocity contour at $x/c_{duct} = 0.3$ (at the propeller location) is also shown, in Fig. 5.13. It can be understood that, as expected, the axial velocity contour is uniform in the tangential direction. The V_a/V_0 contour is uniform due to the fact that the circular duct, or ring wing, is axisymmetric and the inflow is uniform. Only for the square duct, which is not axisymmetric, it was expected that the axial velocity contour would be non-uniform at the propeller location, in the tangential direction. The results for the isolated square duct are shown and discussed in the next section (Sect. 5.3).

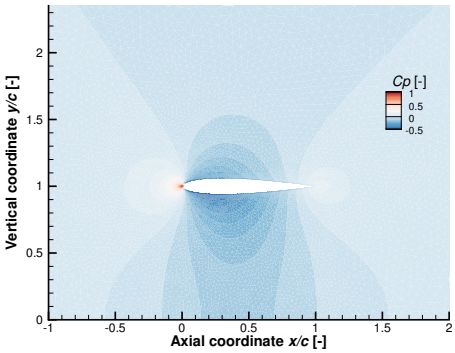

Figure 5.11: Pressure coefficient (C_p) distribution in the vicinity of the ring wing section. Results obtained from the 3D axisymmetric simulation with the medium mesh.

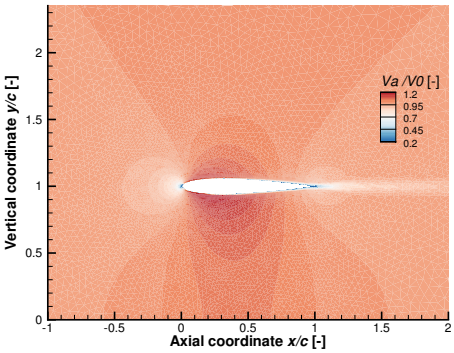

Figure 5.12: Axial velocity (V_a) distribution, normalised with the free-stream velocity, V_0, in the vicinity of the ring wing section. Results obtained from the 3D simulation with the medium mesh.

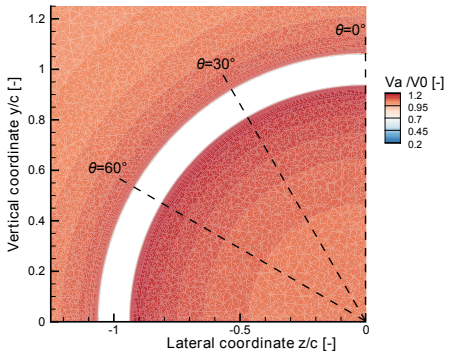

Figure 5.13: Axial velocity distribution, normalised with the free-stream velocity, in a plane perpendicular to the duct, at the propeller location ($x/c = 0.3$). Results obtained from the 3D simulation of the isolated ring wing, with the medium mesh. Moreover, it is also shown locations where it were made slices to evaluate the results ($\theta = 0°$, $\theta = 30°$ and $\theta = 60°$), in relation to the following plots of this report.

In Figs. 5.14 and 5.15, it is shown, respectively, the pressure coefficient and the skin friction coefficient (in the axial direction) at the duct's surface. The results correspond to three slices made at the duct, at $\theta = 0°$, $\theta = 30°$ and $\theta = 60°$ (represented in Fig. 5.13), so that it can be understood if there is a spanwise variation in pressure and axial skin friction distributions. Since the duct is axisymmetric, it was not expected a spanwise variation of these quantities. For the pressure coefficient distribution (Fig. 5.14), it is hardly noticeable any difference between the three slices. Moreover, the result matches well with the pressure coefficient distribution obtained from the 2D circular duct simulation (Fig. 5.3). For the axial skin friction coefficient, however, Fig. 5.15 shows that there are small differences in the distributions over the three slices. This is assumed to be due to noise associated with a numerical error in the calculations. In appendix A, the same distributions are plotted for the six grids with different refinements (Fig. A.2). It was found that the spanwise variations of axial skin friction decrease for higher cell refinements, and are excessively large for the coarsest grids used. Besides the small differences in spanwise skin friction, it was also found that the axial skin friction distribution estimated from the 3D calculation is very similar to the distribution obtained from the 2D circular wing simulation 5.4, as expected.

The boundary layer height is plotted in Fig. 5.16, for same the three duct locations referred earlier ($\theta = 0°$, $\theta = 30°$ and $\theta = 60°$). The height of the boundary layer of a turbulent flat plate in a flowfield without pressure gradients is also plotted, for comparison. The results are also very similar to the results of the 2D simulation (Fig. 5.5), considering the duct's boundary layer height. Similarly to the axial skin friction distribution on the

duct (Fig. A.2), there is also a relatively small spanwise variation of the boundary layer height in the results from the 3D simulation. It is also assumed that this variation is due to the fact that a finite number of elements was used for the calculations, resulting in a numerical error. The numerical discretization error in the isolated circular duct simulations is analysed in more detail in the following sub-section (5.2.1).

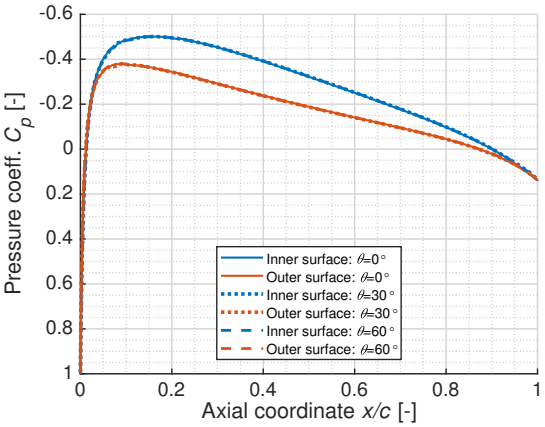

Figure 5.14: Pressure coefficient distribution at three circular duct sections, versus chordwise position, x/c. Results obtained from the 3D isolated circular duct simulation with the medium mesh. The three sections correspond to cuts of the duct at three different planes: at $\theta = 0°$, $\theta = 30°$ and $\theta = 60°$.

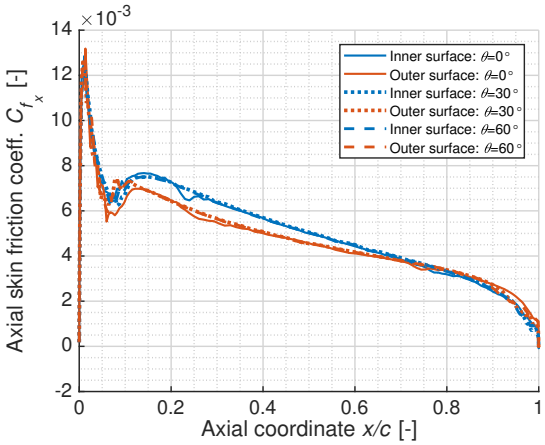

Figure 5.15: Axial skin friction coefficient distribution at three circular duct sections, versus chordwise position, x/c. Results obtained from the 3D isolated circular duct simulation with the medium mesh. The three sections correspond to cuts of the duct at three different planes: at $\theta = 0°$, $\theta = 30°$ and $\theta = 60°$.

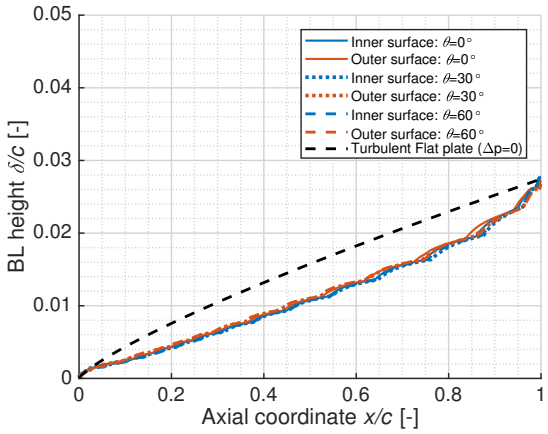

Figure 5.16: Ring wing boundary layer height, versus chordwise position. The results obtained from the 3D simulation with the medium mesh are compared against Blasius' solution for the turbulent BL height over a flat plate, with zero pressure gradient. The results correspond to three cuts of the flowfield at three different planes: at $\theta = 0°$, $\theta = 30°$ and $\theta = 60°$.

5.2.1. MESH CONVERGENCE STUDY

This section presents the results obtained from the grid convergence study performed for the isolated circular duct 3D simulation, in order to evaluate the discretization error in each grid. In table 5.3, it is specified which grids were used for the convergence study. The mesh with a medium refinement (3) is the most similar to the meshes used for the installed configurations, and to the medium mesh used for the 2D convergence study (mesh 4 in table 5.1). Moreover, the drag coefficients of the ring wing obtained with each mesh are also shown in Table 5.3. The estimated exact values are also shown. The exact values correspond to the values that would be obtained with a mesh with an infinite number of elements (mesh 0), i.e. from an equivalent simulation without a discretization error. The estimated exact values (for mesh 0) were calculated for each quantity from two different fits: the best fit and a similar fit where the observed order of convergence was kept constant at $p^* = 3$. The best fit was calculated in the same way as it was done for the 2D convergence

study (Sec. 5.1.1). However, the observed order of convergence estimated with the best fit was, for the three variables, considerably larger than the theoretical order of convergence. In these simulations, the theoretical order of convergence is 3, as this is the order of the discretization schemes used. The fits with $p^* = 3$ were calculated for each variable due to the excessively high order of convergence estimated from the best fits, following the recommendations in [33].

With respect to the two fits calculated for the convergence of each drag coefficient (best fit and fit with $p^* = 3$), Table 5.4 shows values of the apparent order of convergence, p, the standard deviation of the fit, U_s, and the error of the medium mesh with respect to the estimated exact value, $\delta_{RE,3}$. The uncertainty of the value obtained with the medium mesh $U_{\phi,3}$ is shown as well. The uncertainty was calculated from:

$$U_\phi = 1.25|\delta^*_{RE}| + U^*_s \,, \tag{5.14}$$

where the asterisk means that the value is relative to the fit with $p^* = 3$.

3D Ring wing - grid converge study

Mesh	Refinement	# of elements	h_i/h_1 [-]	C_{D_p} [-]	C_{D_f} [-]	$C_{D_{total}}$ [-]
6	super coarse	2.322×10^6	1.762	0.008461	0.021649	0.030109
5	very coarse	2.596×10^6	1.698	0.007804	0.022252	0.030057
4	coarse	3.295×10^6	1.568	0.007703	0.022660	0.030363
3	medium	4.610×10^6	1.402	0.007380	0.023077	0.030457
2	fine	7.002×10^6	1.220	0.007164	0.023205	0.030369
1	very fine	12.713×10^6	1	0.007013	0.023413	0.030426
0 (Best fit)	-	∞	0	0.007040	0.023363	0.030432
0* (Fit with $p = 3$)	-	∞	0	0.006649	0.023915	0.030564

Table 5.3: Grids used for the 3D convergence study with the circular duct, and the drag coefficients on the duct.

3D Ring wing - grid converge study

Quantity	C_{D_p} [-]	C_{D_f}	C_{D_t}
p	6.724325	7.835668	9.853318
U_s [%]	2.315794	0.434015	0.302908
$\delta_{RE,3}$ [%]	-4.606396	1.240129	-0.084285
$p*$	3	3	3
$U*_s$ [%]	2.846	1.002	0.398
$\delta*_{RE,3}$ [%]	-9.903	3.630	0.350
$U_{\phi,3}$ [%]	24.522390	9.556741	1.644229

Table 5.4: Grid convergence study performed for the 3D simulation of study with the circular duct, considering the pressure, friction and total drag coefficients on the duct.

In Figs. 5.17, 5.18 and 5.19 it is shown the plots relative to the convergence studies for the pressure, friction and total drag coefficients at the duct, respectively. The values for each mesh are shown in terms of relative difference to the value obtained with the medium mesh (3). Moreover, the lines relative to the best fit for each quantity are plotted, along with the fits obtained considering $p = 3$. From these plots, it is clear that the highest relative difference in the drag coefficient of mesh 3 with respect to finer meshes is found for C_{D_p}. Correspondingly, the pressure drag coefficient is also the quantity for which a higher uncertainty was calculated for mesh 3 (see Table 5.4).

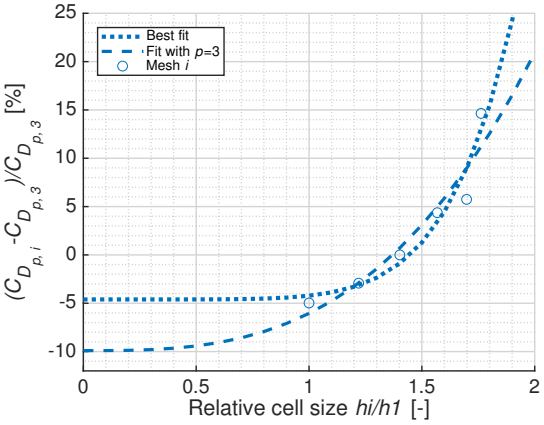

Figure 5.17: Convergence study of the isolated circular wing's pressure drag coefficient, with respect to grid element size. Results obtained with 3D axisymmetric simulations. It is shown the relative difference to the value calculated with mesh 3 (medium refinement), $C_{D_{p,3}}$. The circles correspond to the values relative to each simulation, and the dotted line corresponds to the best fit.

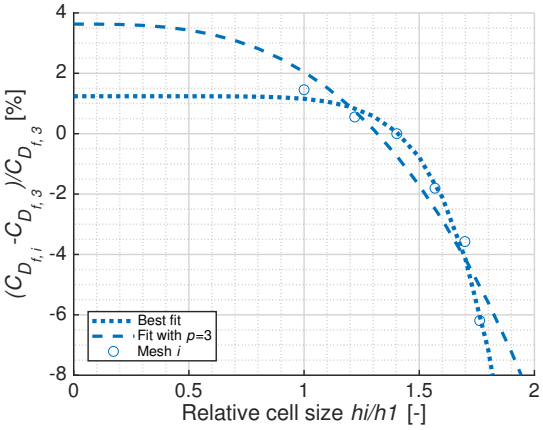

Figure 5.18: Convergence study of the isolated circular wing's friction drag coefficient, with respect to grid element size. Results obtained with 3D axisymmetric simulations. It is shown the relative difference to the value calculated with mesh 3 (medium refinement), $C_{D_{f,3}}$. The circles correspond to the values relative to each simulation, and the dotted line corresponds to the best fit.

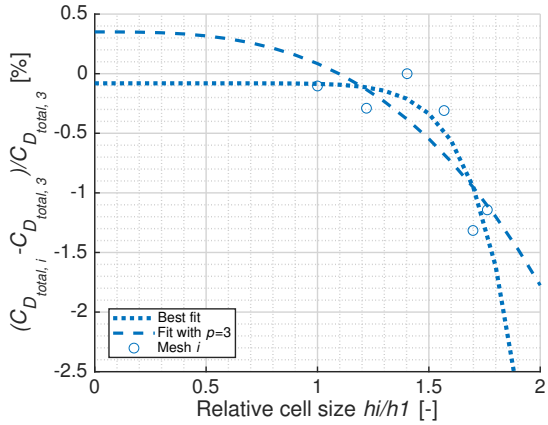

Figure 5.19: Convergence study of the isolated circular wing's total drag coefficient, with respect to grid element size. Results obtained with 3D axisymmetric simulations. It is shown the relative difference to the value calculated with mesh 3 (medium refinement), $C_{D_{total,3}}$. The circles correspond to the values relative to each simulation, and the dotted line corresponds to the best fit.

Besides analysing the convergence of the drag coefficients with respect to grid element size, it were also analysed the convergence of pressure and axial skin friction coefficient chordwise distributions. Figures 5.20 and 5.21 show the C_{D_p} and $C_{D_{f_x}}$ distributions at the duct's surface for three different grids. The convergence of the axial velocity profile at the propeller location, at $x/c = 0.3$ inside the duct, was also analysed for the same three grids (Fig. 5.22). These grids are the medium mesh (3), and the meshes with extreme levels of refinement in this convergence study: mesh 1 and mesh 6. From Fig. 5.20, it can be noticed that the difference in C_{D_p} distributions for the three meshes is very small. However, in Fig. 5.20 it can be clearly noticed a difference in the $C_{D_{f_x}}$ distributions for the different grids. These results are specially interesting, considering the fact that the relative difference in drag coefficient obtained with the different meshes is higher for C_{D_p} than for $C_{D_{f_x}}$, as it was shown in Figs. 5.17 and 5.18. Relatively to the convergence of the axial velocity profile at the propeller location, it is seen in Fig. 5.22 that the three grids result in the estimation of identical V_a

distributions. This indicates that even the coarsest grid used (grid 6) has a refinement which is acceptable for the calculation of the axial velocity profile at the propeller location, for the case of the isolated circular duct.

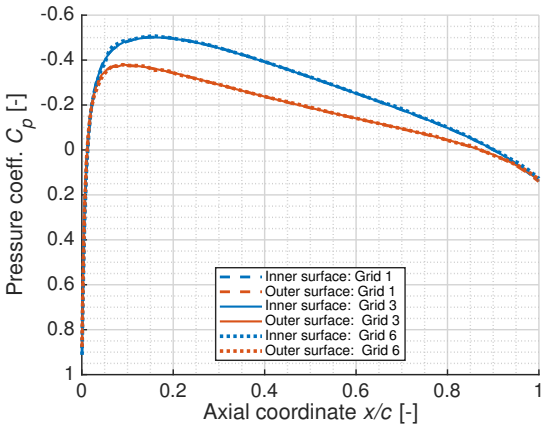

Figure 5.20: Convergence study of the isolated circular wing's pressure coefficient chordwise distribution, with respect to grid element size. Results obtained with 3D simulations.

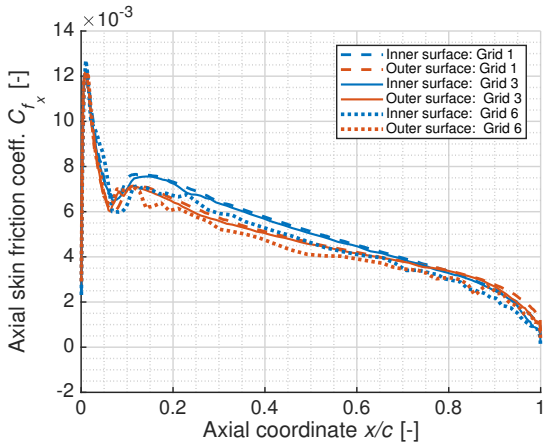

Figure 5.21: Convergence study of the isolated circular wing's skin friction coefficient (in the x direction) chordwise distribution, with respect to grid element size. Results obtained with 3D simulations.

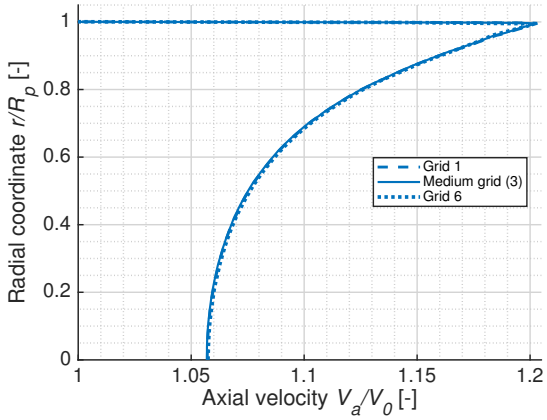

Figure 5.22: Convergence study of the axial velocity distribution at the propeller location ($x/c = 0.3$), inside the isolated circular duct, with respect to grid element size. Results obtained with 3D simulations. The x axis shows the axial velocity divided by the free-stream velocity (V_a/V_0), and the y axis shows the radial position inside the duct divided by the Xprop's radius (r/R_p).

5.2.2. VALIDATION

On the previous sections, the isolated circular duct (or ring wing) flowfields calculated from CFD were verified, and the main sources of numerical error were evaluated. This section addresses the validation of the computed results. In order to validate the simulations, the estimated values of the isolated NACA0012 ring wing's total drag coefficient were compared against results found in literature regarding similar geometries. The results from this research are compared against results from three other studies:

- wind tunnel simulation of a NACA0012 profile [10]. There are several differences between this study and this thesis' research. The most important differences are:
  - the aim of the experiments was to study a NACA 0012 (2D) profile. The NACA 0012 is in fact a different geometry from the ring wing investigated in this thesis, even though the airfoil section is the same. The ring wing would be expected to result in a higher pressure drag on each section, due to a blockage effect.
  - the ratio of inertial forces to viscous forces (Reynolds number) is different in the two cases. In this research, the Reynolds number based on the ducts' chord length was $Re = 0.45 \times 10^6$ (Re definition was shown in equation 4.7). NACA's report [10] includes results for the C_d of the NACA0012 profile at $Re = 0.17 \times 10^6$, $Re = 0.33 \times 10^6$ and $Re = 0.66 \times 10^6$ (amongst others). However, the difference between the values shown for $Re = 0.33 \times 10^6$ and $Re = 0.66 \times 10^6$ appears to be very small (at $\alpha = 0°$) relatively to the accuracy with which it is possible to read the values shown in the report. Being conservative, it can be considered that the uncertainty in reading the C_d from the report is ± 0.002.
  - in the CFD calculation, the effect of turbulence is modelled by the $k-\omega$ SST turbulence model. On the other hand, in NACA's wind tunnel experiments all range of turbulent structures (for each Re) are present and affect the solution.
- wind tunnel simulation of a wing ring with the same airfoil, NACA0012, and aspect ratio, $AR = 2$ [55]. There are also differences between this research and this thesis' simulations. One should highlight:
  - the Reynolds number is also different in the two cases. The Reynolds number in the experiments was lower: $Re = 0.17 \times 10^6$ [55]. This difference is expected to result in a higher C_D of the experiments, since NACA's report shows a considerable decrease in the 2D drag coefficient of the NACA0012 airfoil as the Reynolds number increases from $Re = 0.17 \times 10^6$ to $Re = 0.33 \times 10^6$.
  - the ring wing used in the experiments is supported by a structure which can cause a blockage effect at the ring wing's trailing edge. This difference is also expected to increase the drag of the ring wing obtained from the experiments. According to Traub, the only corrections made to the measured values were wind tunnel wall corrections [55].
- CFD computations with a NACA0012 ring wing with the same aspect ratio as studied in this thesis, $AR = 2$ [25]. This study is the most similar to the investigation carried out during this thesis. However, there are still several differences regarding how the flowfield was modelled in CFD:
  - Kanoria and Damodaran's study was done based on unsteady incompressible RANS equations. On the other hand, the simulation of the isolated ducts in this thesis was done using steady compressible conditions, as it was previously referred. However, the unsteady effects present on the RANS flowfield of a NACA 0012 profile at $\alpha = 0°$ are expected to be very small. The only unsteady aerodynamic phenomenon expected is the separation at the trailing edge, which can originate trailing edge vortex shedding (phenomenon studied e.g. by [1]). Furthermore, the effect of compressibility in these simulations is also small, since the free-stream Mach numbers are $M_\infty = 0.09$, for this thesis computations, and would be $M_\infty = 0.12$ for the literature's computational study, assuming sea-level conditions.
  - the Reynolds number on Kanoria and Damodaran's simulations was $Re = 0.26 \times 10^6$ [25]. This lower Re could in fact lead to a higher drag of the duct, as discussed before.
  - the turbulence model used by Kanoria and Damodaran is also different: the one-equation Spalart and Allmaras' turbulence model. The difference in turbulence models is also expected to cause differences in the drag coefficient results.

– the domains used are also different. Whereas in this thesis it was simulated one quarter of the duct geometry (in the 3D simulation), the simulations shown in literature were made with one half of the duct model, so that it would be possible to study the effect of changing α. Furthermore, in Kanoria and Damodaran's study the inlet and far field boundaries were place 5 duct chords away from the geometry, whereas the outlet was placed 10 duct chords downstream. In this thesis, the distances used to the boundaries of the domain were double, which is expected to result in a lower influence of the conditions imposed at the boundaries on the flowfield in the vicinity of the ring wing.

Based on the information taken from the studies described above, Figure 5.23 was generated in order to compare the drag estimated from the different sources. The values shown in Fig. 5.23 refer to the drag coefficient of the NACA 0012 airfoil at two Reynolds number, and to the values of average section drag coefficient, C_d, from the estimations with the NACA 0012 ring wing. From the results of this thesis, C_d is simply equal to C'_D, since the reference area used to calculate C'_D is the perimeter of the duct times the chord, which is constant (see equation 5.5).

Figure 5.23 clarifies that there is indeed a that there is a considerable decrease in C_d of the NACA 0012 from $Re = 0.17 \times 10^6$ towards $Re = 0.33 \times 10^6$. However, the airfoil's drag almost doesn't change from $Re = 0.33 \times 10^6$ towards $Re = 0.66 \times 10^6$. The drag of the ring wing tested by Traub appears to be considerably larger than the drag of all the other cases shown. For this, it has contributed the relatively low Reynolds and the blockage caused by the support structure, as previously discussed. The C_d calculated from Kanoria and Damodaran's appears to be the same as the sectional drag coefficient estimated by NACA for the airfoil at a higher Reynolds. This result is considered to be strange, since the NACA 0012 ring wing should have a higher drag, due to blockage. Still, a relatively high numerical error in the computation could explain this result. The results shown from this thesis, relative to the 2D and 3D simulations, appear to be in agreement with each other. However, this thesis' results do not perfectly match any of the other results. Still, it is understandable that the C_d estimated in this thesis for the ring wing is higher than the airfoils' C_d, at the same Reynolds. The fact that the C_d calculated in this research is lower than the value calculated by Traub also makes sense, due to the higher Reynolds (in this research) and to the higher blockage in Traub's experiment. Concluding, it is impossible to be perfectly sure that the simulations carried during this thesis are in agreement with the results from literature. However, the differences can be considered acceptable, taking into account that the estimation methods used in each case are very different, as previously discussed.

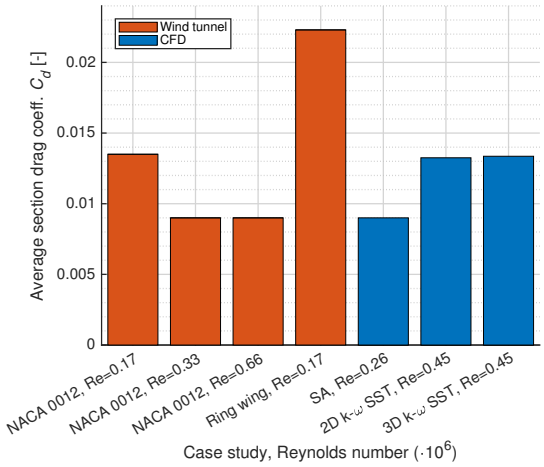

Figure 5.23: Validation of the isolated circular duct (or ring wing) simulations. The Figure compares values of average section drag coefficient from different sources.

5.3. SQUARE DUCT

In the present section, the results obtained from the simulation of the isolated square duct are shown and discussed. Firstly, the results obtained with the grid with a medium refinement are presented. Afterwards, in sub-section 5.3.1, it is discussed the effect of modifying the grid element size on the results. In Figs. 5.24 and 5.25 it is shown, respectively, the pressure coefficient and normalised axial velocity contours around the duct,

at the symmetry plane (at the plane where $\theta = 0°$). It can be understood that the two contours are similar to the equivalent contours for the circular duct (Figs. 5.11 and 5.12). In this way, there is a higher decrease of C_p inside the duct than outside, associated with higher axial velocities inside the duct. As it was previously discussed, the change in axial velocity at the propeller location was expected to impact its performance. In Fig. 5.24, it is also shown the location where it were made two other planes to analyse the flowfield: at $x/c = 0.3$ (propeller location), and at $x/c = 0.99$ (duct's trailing edge). In Fig. 5.25, it can also be seen the edge of the square duct's boundary layer, since it is shown the location where the total pressure coefficient is 0.98, thus 98% of the free-stream C_{p_t}.

Figures 5.26 and 5.27 correspond to contours at a plane that passes through the centre and the corner of the square duct (the plane where $\theta = 45°$). Figures 5.26 and 5.27 show, respectively, C_p and V_a/V_0 contours. Comparing Figs. 5.24 and 5.26, it can be understood that the pressure fields are different for $\theta = 0°$ and $\theta = 45°$. At the corner of the duct, the pressure coefficient reduces more than at the plane of symmetry, inside the duct. Outside the duct, however, C_p is lower at the plane of symmetry. This is due to the fact that there is a higher contraction of the flow at the duct's corner inside the duct, and a lower contraction outside. This difference in the pressure field also leads to a slight movement of the stagnation point (where $C_p = 1$) from the leading edge, at $\theta = 0°$, to the inside of the duct, at $\theta = 45°$. Comparing Figs. 5.25 and 5.27, it can be understood that the lower C_p values inside the duct, near its corner, is also associated with an increase of the axial velocity. However, this increase in V_a at the corner was not expected to directly impact the performance of the propeller, since it occurs outside of the propeller disk. It was expected, however, that this phenomenon could have an impact on the overall performance of the square ducted propeller system. Moreover, in Fig. 5.27 it is also shown the edge of the duct's boundary layer. By comparing with Fig. 5.25, it can be understood that the duct's boundary layer is significantly larger inside the duct at its corner (where $\theta = 45°$) than at the symmetry plane (where $\theta = 0°$). This is consistent with the literature that can be found regarding corner flow. As it was discussed in section 2.2.5, the boundary layer is expected to be higher at a corner between two surfaces.

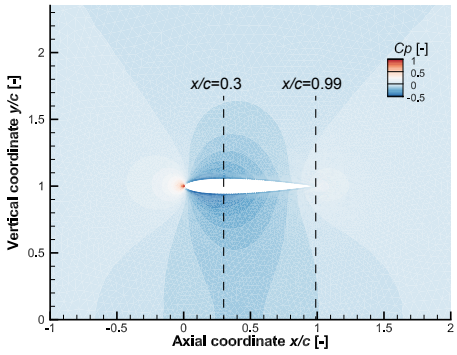

Figure 5.24: Pressure coefficient (C_p) distribution in the vicinity of a square duct section. The contour is located at the symmetry plane ($\theta = 0°$). Results obtained with the medium mesh. It is also represented the location where two other planes used to analyse the flowfield are located: at $x/c = 0.3$ and at $x/c = 0.99$.

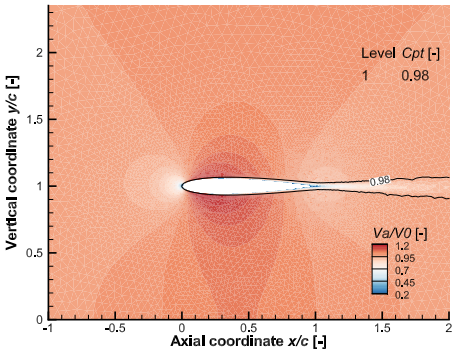

Figure 5.25: Axial velocity (V_a) distribution, normalised with the free-stream velocity, V_0, in the vicinity of a square duct section. It is also shown the location where the total pressure coefficient is 98% of its free-stream value, i.e. where $C_{p_t} = 0.98$. C_{p_t} is 0.98 at the edge of the boundary layer. The contour is located at the symmetry plane ($\theta = 0°$). Results obtained with the medium mesh.

Figures 5.28 and 5.29 show normalised axial velocity contours at two planes, $x/c = 0.3$ and $x/c = 0.99$, respectively. The lines of constant total pressure coefficient, where $C_{p_t} = 0.98$, are shown as well. Moreover, from Fig. 5.28 it can be understood how the azimuthal position θ was defined. It is shown the locations where $\theta = 0°$ and where $\theta = 45°$. In Fig. 5.29, it is also shown different locations where it were made slices to evaluate the flowfield near the duct's surface. These slices were made based on the non dimensional spanwise position at the square duct, ϕ, which was defined as:

$$\phi \equiv l_p/(p_{qduct}/4)\,, \tag{5.15}$$

where l_p is the distance along the perimeter of the duct from $(y,z) = (c_{duct}, 0)$, and p_{qduct} is the perimeter of

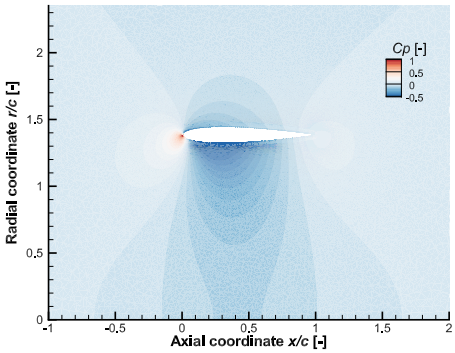

Figure 5.26: Pressure coefficient (C_p) distribution in the vicinity of the square duct corner section. The contour is located at the plane that passes through the centre of the duct and through its corner ($\theta = 45°$). Results obtained with the medium mesh.

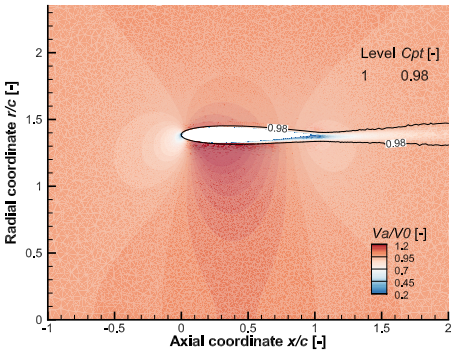

Figure 5.27: Axial velocity (V_a) distribution, normalised with the free-stream velocity, V_0, in the vicinity of the square duct corner section. It is also shown the location where the total pressure coefficient is 98% of its free-stream value, i.e. where $C_{p_t} = 0.98$. C_{p_t} is 0.98 at the edge of the boundary layer. The contour is located at the plane where $\theta = 45°$. Results obtained with the medium mesh.

the square duct. It should be noticed that, for the square duct, the spanwise locations $\phi = 0$, $\phi = 0.5$, $\phi = 1$ are, respectively, at the azimuthal positions $\theta = 0°$, $\theta = 45°$ and $\theta = 90°$. However, slices made at the duct at different ϕ (e.g. $\phi = 0.25$) do not have all points at a constant θ. On the other hand, for the circular duct, any spanwise location for a slice at $0 \leq \phi \leq 1$ corresponds to a constant azimuthal location at $0° \leq \phi \leq 90°$, with $\theta = \phi \times 90°$.

From Fig. 5.28 it can be understood that, at the propeller location, the axial velocity profile (versus radial position) is not uniform, i.e. it is not constant for varying θ. Even though V_a is highest at the corner of the duct, it can be seen in Fig. 5.28 that the axial velocities at the propeller disk decrease from $\theta = 0°$ or $\theta = 90°$ towards $\theta = 45°$. From this consideration, it could be expected that the propeller blade loading would be highest when the blade would be at $\theta = 45°$. However, there are other phenomena that can affect the loading of the blades differently. For example, the tip clearance effect was expected to be highest when the blade is at $\theta = 0°$ or $90°$. As it was discussed in 2.2.3, the loading at the blade's high radial locations can increase when the gap between the blade tip and its duct is small.

At $x/c = 0.3$ the duct's BL is too thin to be properly noticed in the contour of Fig. 5.28. In Fig. 5.28, however, it can be seen that the boundary layer thickness varies for different spanwise locations. More specifically, it can be noticed that the boundary layer inside the duct is larger at the corner than at the centre of the duct.

In Figs. 5.30 and 5.31, it is shown, respectively, the pressure coefficient and axial skin friction coefficient chordwise distributions. These distributions are shown for 3 duct spanwise locations (which were shown in Fig.5.29): at $\phi = 0$ (at the symmetry plane), at $\phi = 0.25$ and at $\phi = 0.5$ (at the corner). Figure 5.30 shows that the C_p chordwise distributions are very similar for $\phi = 0$ and $\phi = 0.25$. However, the C_p distribution at the corner location ($\phi = 0.5$) is very different from the duct's C_p distribution away from the corner. At the corner's inner surface, the suction peak is considerably larger, and it is located more downstream. At the corner's inner surface, the lowest C_p is reached at $x/c = 0.2$. At the corner's outer surface, however, the suction peak moves closer to the leading edge. The change in axial location of the suction peaks at the corner is associated with the movement of the stagnation point, which also moved slightly, along the leading edge of the corner's inner surface. In this way, the conclusions made from Fig. 5.30 are in agreement with what can be seen in the C_p contours of Figs. 5.24 and 5.26.

When analysing Fig. 5.31, it easy to notice the large "noise" in the results for the slice made at the corner of the square duct ($\phi = 0.5$), more specifically at its inner surface. This region of large "noise" in the C_{f_x} distribution corresponds with the region where it was used an unstructured mesh at the duct's surface (shown previously in Fig. 4.14). As it was discussed in section 4.5, it was not expected that using an unstructured mesh at the duct's corner would be ideal. Still, this type of mesh was used in regions where the computational

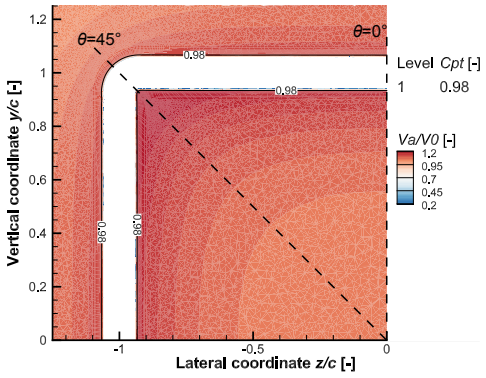

Figure 5.28: Axial velocity distribution, normalised with the free-stream velocity, in a plane perpendicular to the square duct, at the propeller location ($x/c = 0.3$). It is shown the location where $C_{p_t} = 0.98$. Results obtained with the medium mesh. Moreover, it is also represented locations where it were made planes to evaluate the results ($\theta = 0°$, and $\theta = 45°$).

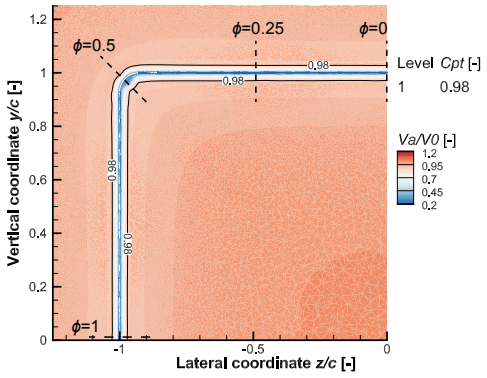

Figure 5.29: Axial velocity distribution, normalised with the free-stream velocity, in a plane perpendicular to the square duct, at the trailing edge location ($x/c = 0.99$). It is shown the location where $C_{p_t} = 0.98$. Results obtained with the medium mesh. Moreover, the figure shows locations where it were made slices to evaluate the results at the duct ($\phi = 0$, $\phi = 0.25$, $\phi = 0.5$ and $\phi = 1$).

geometry had a high degree of complexity, such as the corner of the square duct. Despite of the "noise" found in the C_{f_x} chordwise distributions, it can also be noticed that the skin friction distribution is similar for the slices at $\phi = 0$ and $\phi = 0.25$. However, the corner slice ($\phi = 0.5$) shows a different trend. At the inner surface of the corner, skin friction drops more rapidly, which is normal since the corner's boundary layer grows faster, at its inner surface. Moreover, it can also be seen that the skin friction coefficient drops to negative values near the trailing edge. This indicates that there is flow separation at the inner surface of the duct's corner. The occurrence of flow separation can be justified by the higher suction peak at this location, which leads to a higher adverse pressure gradient, and also by the higher thickness of the boundary layer at this location, which makes the BL more prone to separation. Flow separation at the corner can have adverse effects on the aerodynamic performance of the square duct. Indeed, this effect can lead to a higher pressure drag of the component, increasing its overall drag.

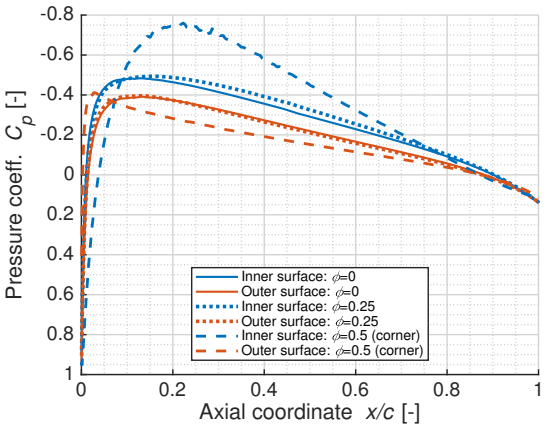

Figure 5.30: Pressure coefficient distribution at three sections of the square duct, versus chordwise position, x/c. Results obtained with the medium mesh. The three sections correspond to cuts of the duct at three different planes: at $\phi = 0$, $\phi = 0.25$ and $\phi = 0.5$.

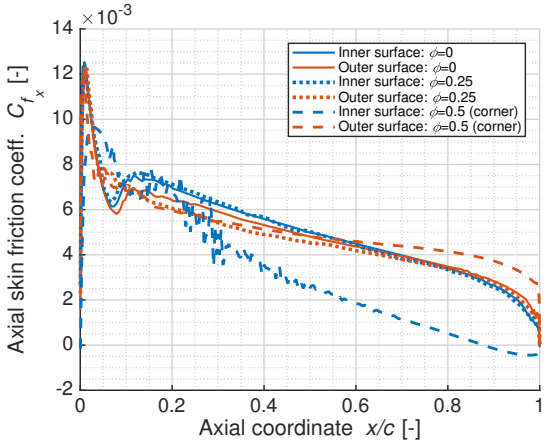

Figure 5.31: Axial skin friction coefficient distribution at three sections of the square duct, versus chordwise position, x/c. Results obtained with the medium mesh. The three sections correspond to cuts of the duct at three different planes: at $\phi = 0$, $\phi = 0.25$ and $\phi = 0.5$.

Figures 5.32 and 5.33 show the thickness of the boundary layer over the square duct, at three spanwise locations: at $\phi = 0$, $\phi = 0.25$ and $\phi = 0.5$. Figure 5.32 relates to the inner surface of the duct, and Fig. 5.33 relates to its outer surface. For comparison, the average BL thickness over each surface of the isolated circular duct is also plotted, as well as the thickness of the turbulent boundary layer over a flat plate with zero pressure

gradient. From Fig. 5.32, it is interesting to notice that the boundary layer thickness at $\phi = 0$ and $\phi = 0.25$ is very similar to the BL thickness over the inner surface of the circular duct. However, at the inner surface of the square duct's corner, the BL thickness grows considerably larger. The faster growth of the corner layer can be noticed from $x/c = 0.2$. At the trailing edge ($x/c = 1$), the BL at the corner's inner surface is approximately 74% larger than the thickness of the turbulent BL of a flat plate. The corner's large BL is one of the reasons why separation occurs at the duct's corner, as it was previously discussed. In Fig. 5.33, it can be noticed that the outer BL at $\phi = 0$ and $\phi = 0.25$ is also similar to the circular duct's outer BL, despite being slightly thinner. At the corner, however, there is a more noticeable difference regarding the height of the outer surface's BL thickness. Due to the corner's curvature, the BL grows less than for other spanwise locations. This is the opposite phenomenon of what happens at the BL of the corner's inner surface, where the proximity of different surfaces leads to a thicker BL.

Figure 5.32 shows axial velocity profiles versus radial position, for the flow inside the duct, at the propeller's chordwise location ($x/c = 0.3$). The results are shown for different azimuthal locations: $\theta = 0°$, $\theta = 30°$ and $\theta = 45°$. The average axial velocity profile at the propeller disk is also shown, as well as the average V_a profile at an equivalent location inside the isolated circular duct, for comparison. Firstly, it is interesting to notice that the axial velocity decreases, at the propeller disk, towards the corner's azimuthal position ($\theta = 45°$). This phenomenon is expected to cause variations in the blade loading, during its rotation. However, the highest axial velocities are found for $\theta = 45°$ at high radial positions, outside of the propeller disk ($r/R_p > 1$). These findings are in agreement with what was discussed with respect to the V_a/V_0 and C_p contours shown earlier in this section. By comparing with the V_a profile inside the circular duct, it can be understood that the average axial velocity is lower at the propeller disk in the square duct. This was expected to contribute to a higher loading of the propeller when placed inside the square duct, assuming that the same blade pitch and rotational speed would be used in both installed cases.

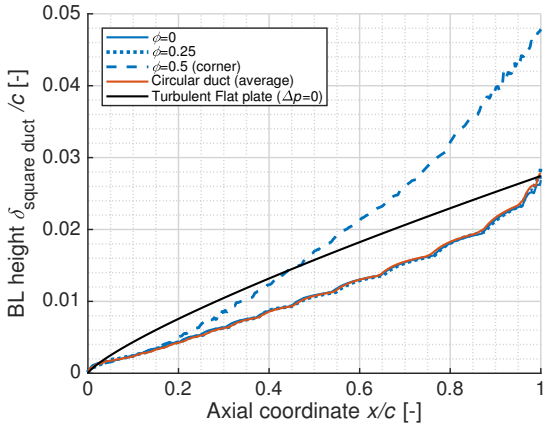

Figure 5.32: Square duct inner boundary layer height, at three different spanwise locations, versus chordwise position. The results obtained with the medium mesh are compared against Blasius' solution for the turbulent BL height over a flat plate, with zero pressure gradient. The results correspond to cuts of the flowfield at three different locations: at $\phi = 0$, $\phi = 0.25$ and $\phi = 0.5$.

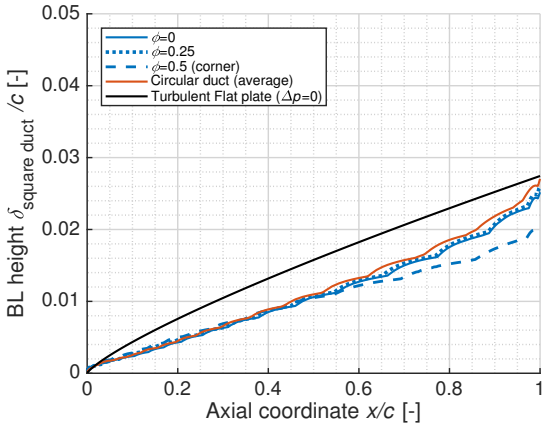

Figure 5.33: Square duct outer boundary layer height, at three different spanwise locations, versus chordwise position. The results obtained with the medium mesh are compared against Blasius' solution for the turbulent BL height over a flat plate, with zero pressure gradient. The results correspond to cuts of the flowfield at three different planes: at $\phi = 0$, $\phi = 0.25$ and $\phi = 0.5$.

5.3.1. MESH CONVERGENCE STUDY

In this section, it is discussed the grid convergence study of the square duct. For this convergence study, 4 different grids were used. The convergence study for the square duct has the particularity of having the grid with a medium refinement as the finest grid used (grid 1). Similar mesh settings were used to mesh the isolated square and circular ducts with their own medium grids. However, the square duct's medium mesh has considerably more elements, almost as many elements as the finest mesh used in the circular duct's grid convergence study (around 12 million). This is due to the fact that a very large number of cells was required to properly mesh the square duct's corner. The larger number of elements results in an increase in computational cost of the simulations. In Table 5.5, it can be seen several characteristics of the different meshes used: the level of refinement, the number of elements, and their relative cell size with respect to the cell size of the

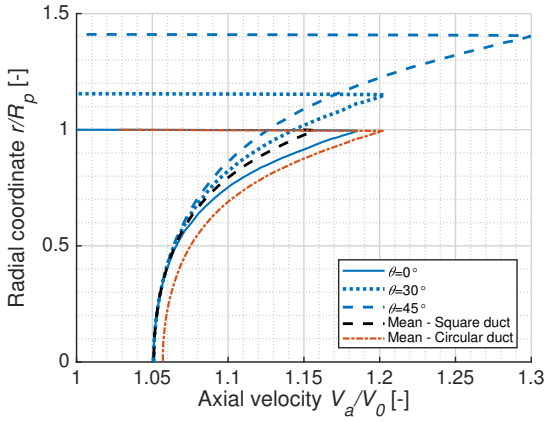

Figure 5.34: Axial velocity profile, normalised with the free-stream velocity, inside the square duct, at the propeller location. Results obtained with the medium mesh. The results correspond to three cuts of the flowfield at three different locations: at $\theta = 0°$, $\theta = 30°$ and $\theta = 60°$. The average velocity profile at the propeller disk location is also shown. The average velocity profile at an equivalent location inside the circular duct is plotted as well, for comparison.

finest grid, h_i/h_1. The pressure, friction and total drag coefficients calculated with each grid are shown as well. Moreover, their extrapolated exact values are also shown. The estimated exact values shown are relative to 2 different fits: one is the best fit, with an unconstrained observed order of convergence, p, and the second fit was obtained assuming p to be equal to the theoretical order of convergence. The theoretical order of convergence is 3, since the discretization schemes used in the simulations were 3^{rd} order schemes. It should be noticed that the exact value estimated for $C_{D_{total}}$ with the best fit is very unrealistic, since the observed order of convergence for this fit is extremely low.

The observed order of convergence of each fit, along with its standard deviation, U_s, are shown in Table 5.6. The relative difference between each estimated exact drag coefficient and the value obtained for the medium grid, $\delta_{RE,1}$, is also shown. It should be noticed that the observed order of convergence for the best fits of C_{D_p} and C_{D_f} are considerably higher than the theoretical order of convergence, which leads to an underestimation of $\delta_{RE,1}$. This motivated the calculation of fits with $p = 3$, which lead to more conservative error estimations. Moreover, Table 5.6 also shows the relative uncertainty of the calculation of each drag coefficient with the medium mesh, $U_{\phi,1}$. The uncertainty was not estimated equally for the three cases. For C_{D_p} and C_{D_f}, the uncertainty was calculated from equation 5.14. For $C_{D_{total}}$, the uncertainty was calculated from:

$$U_\phi = min(\delta_{RE} + U_s, 1.25\Delta_M)\,, \tag{5.16}$$

where Δ_M is the maximum difference between all solutions available. This was done in agreement with the recommendations found in [33], for the cases when the observed order of convergence is positive, but bellow 0.95. In this specific case:

$$\Delta_M = 1.25|C_{D_{total,1}} - C_{D_{total,3}}|\,. \tag{5.17}$$

Square duct - grid converge study

Mesh	Refinement	# of elements	h_i/h_1 [-]	C_{D_p} [-]	C_{D_f} [-]	$C_{D_{total}}$ [-]
4	Super coarse	5.232×10^6	1.331	0.011537	0.027450	0.038987
3	Very coarse	7.082×10^6	1.203	0.010516	0.028762	0.039279
2	Coarse	9.260×10^6	1.100	0.010286	0.028637	0.038924
1	Medium	12.342×10^6	1	0.009870	0.029042	0.038912
0 (Best fit)	-	∞	0	0.009672	0.028879	-0.000107
0* (Fit with $p = 3$)	-	∞	0	0.008638	0.030227	0.038866

Table 5.5: Grids used for the convergence study with the isolated square duct, and the drag coefficients on the duct. Two different extrapolated values are shown for each drag coefficient. The first one (on the second last row) corresponds to an extrapolation with the best fit, and the second (last row) corresponds to a fit where p was constrained to 3, the theoretical order of convergence.

Square duct - grid converge study

Fit	Quantity	C_{D_p}	C_{D_f}	C_{D_t}
Best fit (Unconstrained p)	p	6.926	21.017	0.0148
	U_s [%]	1.548	0.956	0.697
	$\delta_{RE,1}$ [%]	-2.011	-0.561	-100.276
Fit with the theoretical order of convergence ($p = 3$)	p^*	3	3	3
	U_s^* [%]	2.319	1.754	0.721
	$\delta^*_{RE,1}$ [%]	-12.480	4.081	-0.120
Overall Uncertainty	$U_{\phi,1}$ [%]	21.108	6.855	1.177

Table 5.6: Grid convergence study performed for the simulation with the square duct, considering the pressure, friction and total drag coefficients on the duct. For the best fit, and for the fit with $p = 3$, it is shown the standard deviation of the fit, U_s, and the error of the medium mesh with respect to the extrapolated value, $\delta_{RE,1}$, both in percentage of the drag coefficient obtained for the medium mesh. The overall uncertainty of the drag coefficient obtained with the medium mesh, $U_{\phi,1}$, is shown in the last row. The equation used to calculate $U_{\phi,1}$ for each drag coefficient is specified in the text.

In Figs. 5.35, 5.36 and 5.37, it is shown the plots relative to the convergence study of C_{D_p}, C_{D_f} and $C_{D_{total}}$, with respect to grid element size. In this way, the lines relative to the best fit and to the fit with $p = 3$ are plotted as well. For the C_{D_p} and C_{D_f} plots, it is clear that the best fit curve leads to under predictions of the discretization error of the grids, since it shows very small variations for $0 < h_i/h_1 < 1$. It is also interesting to notice that, for the grids used, $C_{D_{total}}$ shows a very small variation with respect grid element size. This is mainly due to the fact that decreasing the element size led to reductions of C_{D_p}, at the same time as it led to an increase in C_{D_f}. Since $C_{D_{total}} = C_{D_p} + C_{D_f}$, the variation of $C_{D_{total}}$ is less noticeable, in this case. This also led to an calculation of a very low uncertainty of the estimation of $C_{D_{total}}$ with mesh 1, in comparison with the uncertainty in the estimation of the pressure and friction drag coefficients.

In Figs. 5.38 and 5.39, it is shown,respectively, the convergence of the pressure and axial skin friction chordwise distributions, with respect to grid refinement. The distributions shown are the average of the distributions for the spanwise locations $\phi = 0$, $\phi = 0.25$ and $\phi = 0.5$. From Fig. 5.38, it can be understood that the difference in C_p chordwise distribution between different grids is very small, even for the coarsest grid used. With Fig. 5.38, it is possible to understand that the usage of grids 1 and 2 lead to similar C_{f_x} distributions, despite of the "noise" that is found in these distributions, specially at the inner surface of the duct. The grid element size was also found to have an influence in the "noise" seen in the C_p and C_{f_x} distributions, since it was found that coarser grids would lead to stronger peaks, in the "noise". This can be seen in section A.2 of

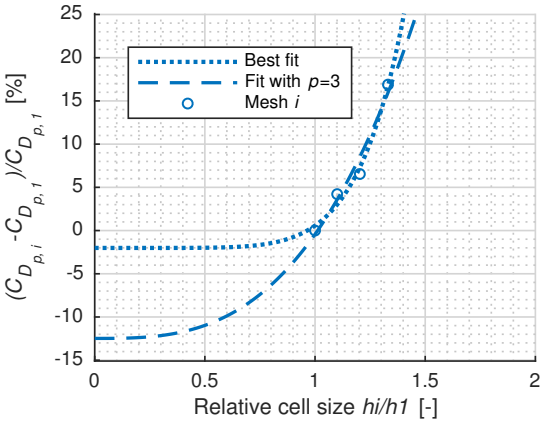

Figure 5.35: Convergence study of the isolated square duct's pressure drag coefficient, with respect to grid element size. It is shown the relative difference to the value calculated with mesh 1 (medium refinement), $C_{D_{p,1}}$.

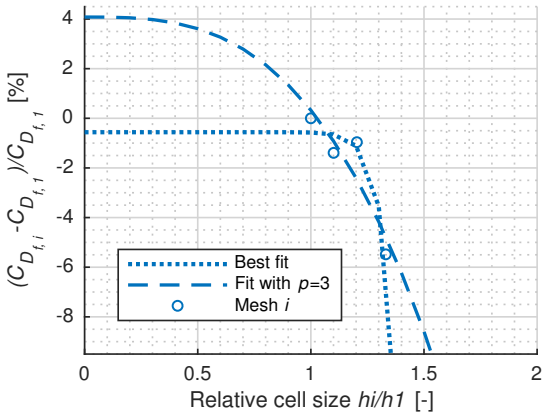

Figure 5.36: Convergence study of the isolated square duct's friction drag coefficient, with respect to grid element size. It is shown the relative difference to the value calculated with mesh 1 (medium refinement), $C_{D_{f,1}}$.

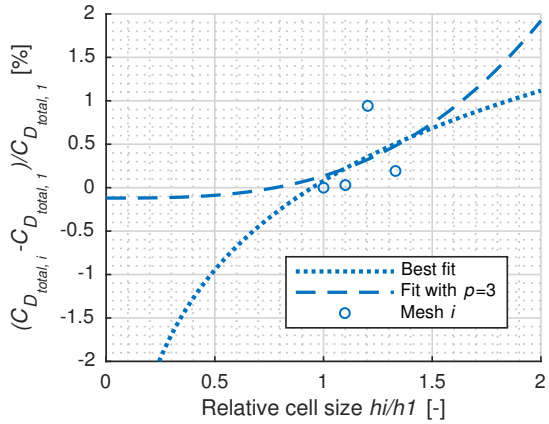

Figure 5.37: Convergence study of the isolated square duct's total drag coefficient, with respect to grid element size. It is shown the relative difference to the value calculated with mesh 1 (medium refinement), $C_{D_{total,1}}$.

the appendix, where there are presented additional plots showing the C_p and C_{f_x} distributions obtained with each of the four grids, for each of the three slices ($\phi = 0$, $\phi = 0.25$ and $\phi = 0.5$).

In Fig. 5.40, it is presented the mean axial velocity profile at the propeller disk, for three different grids: grid 1 (medium refinement), grid 2 (coarse) and grid 4 (super coarse). It can be understood that the refinement of the mesh does not have a strong influence in the calculation of V_a at the propeller location, since it is difficult to notice differences in the results from the three grids. However, the same can not be said with respect to the estimation of the duct's BL thickness with these grids. With Fig. 5.41, it is possible to compare the BL thickness over the inner and outer surfaces of the square duct, for the medium, coarse and super coarse grids. The results shown in Fig. 5.41 are an average of the results obtained at the spanwise locations $\phi = 0$, $\phi = 0.25$ and $\phi = 0.5$. Firstly, it is clear that the usage of the super coarse grid leads to very different estimations than the other two grids. Grids 1 and 2 also lead to slightly different predictions of the BL thickness, for both the inner and outer surfaces of the duct. However, this discretization error had to be accepted. Since Grid 1 already had a considerably large number of elements, further increasing the refinement of the mesh would lead to excessive computational costs.

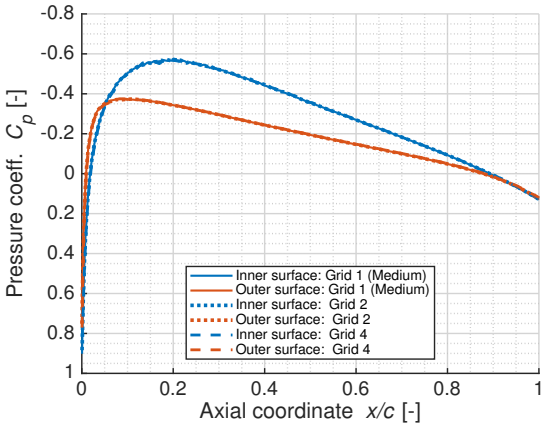

Figure 5.38: Convergence study of the isolated square duct's pressure coefficient chordwise distribution, with respect to grid element size. The distributions are an average between the distributions obtained at three different duct spanwise locations: at $\phi = 0$, at $\phi = 0.25$ and at $\phi = 0.5$ (locations illustrated previously if Fig. 5.29).

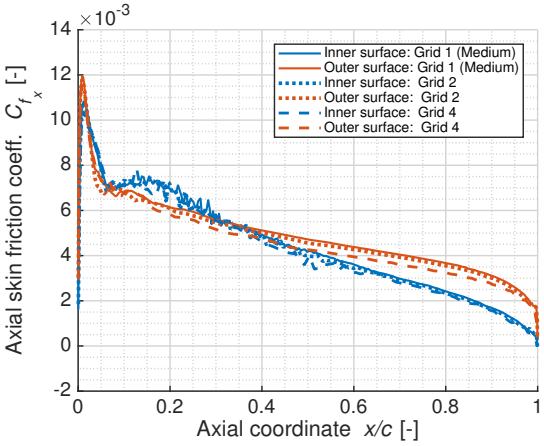

Figure 5.39: Convergence study of the isolated square duct's axial skin friction coefficient chordwise distribution, with respect to grid element size. The distributions are an average between the distributions obtained at three different duct spanwise locations: at $\phi = 0$, at $\phi = 0.25$ and at $\phi = 0.5$.

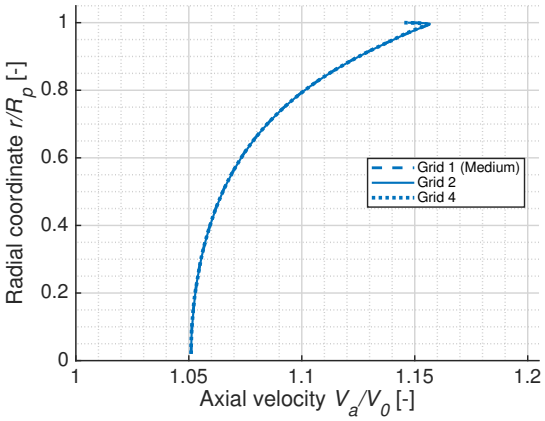

Figure 5.40: Convergence study of the average axial velocity profile inside the square duct, at the propeller location, with respect to grid element size.

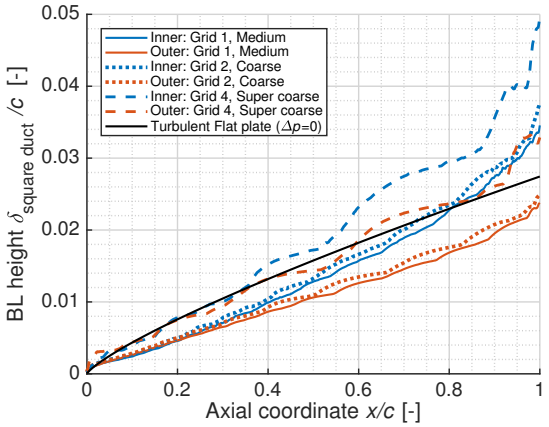

Figure 5.41: Convergence study of the square duct's boundary layer height, with respect to grid element size. The BL heights shown are an average between the BL heights obtained at three different duct spanwise locations: at $\phi = 0$, at $\phi = 0.25$ and at $\phi = 0.5$.

6

ISOLATED PROPELLER PERFORMANCE

After having discussed the aerodynamic behaviour of the two isolated ducts, circular and square, it is relevant to present and discuss the aerodynamic performance of the isolated propeller. Firstly, the results from the simulation of the isolated propeller with the conventional domain are shown in section 6.1. The results obtained with the conventional domain are also compared against results from two other methods, wind tunnel experiments and XROTOR, for validation. Afterwards, the results from the Xprop's simulation with the radially small propeller domain are discussed in section 6.2.

6.1. ISOLATED XPROP - CONVENTIONAL PROPELLER DOMAIN

As it was previously discussed, the Xprop was first simulated with a conventional propeller domain, i.e. with a domain with a radius considerably larger than the propeller radius (shown in Figs. 4.7a and 4.7b). Afterwards, the Xprop was also simulated in an isolated case with a radially smaller propeller domain, which was then used for the installed propeller simulations. The results obtained with the small propeller domain, for the uninstalled case, are shown in the next section (6.2).

For understanding and verifying the flowfield around the Xprop, it is first looked at the total pressure coefficient, static pressure coefficient, and normalised axial and tangential velocity contours around the simulated blade, from the steady simulation. The contours were therefore recorded at the blade's azimuthal location, $\theta = 45°$. Since the vorticity generated by the propeller has a strong influence in its flowfield, the isolines of constant total vorticity coefficient, $C_{\omega_t} = 0.5$ and $C_{\omega_t} = 1$, are also plotted. The total vorticity coefficient was defined as:

$$C_{\omega_t} = \frac{\omega_t}{2\Omega}, \tag{6.1}$$

where ω_t stands for magnitude of vorticity, and Ω is the angular velocity of the propeller, in rad/s. $2\vec{\Omega}$ is the vorticity of a rigid body, e.g. a propeller, rotating with an angular velocity $\vec{\Omega}$.

The C_{p_t}, C_p, V_a/V_0 and V_t/V_0 contours around the propeller are shown, respectively, in Figs. 6.1, 6.2, 6.3 and 6.4. Firstly, it can be understood from the C_{p_t} contours that there is a total pressure jump at the propeller location. This matches what can be found in literature regarding propeller aerodynamics (shown in Fig. 2.3). As referred in section 2.1.3, the jump in total pressure at the propeller's axial location is associated with a jump in static pressure (seen in Fig. 6.2), whereas there is no jump in axial velocity at the propeller disk, which matches with the contours of Fig. 6.3. Moreover, it is also shown that the C_p decreases upstream of the propeller, towards its disk, and also downstream of the propeller, after the pressure jump, until C_p reaches its free-stream value, $C_p = 0$. The decrease in static pressure, both upstream and downstream of the propeller, is associated with an increase in axial velocity, seen in Fig. 6.3. These trends in C_p and V_a also match what could be predicted from aerodynamic theory, according to Fig. 2.3. Moreover, Fig. 6.4 shows an increase in tangential velocity (in module) at the propeller disk, in the propeller's direction of rotation. Furthermore, it can also be noticed the influence of the blade tip vortices in the propeller's slipstream. In Fig. 6.2, it can be

noticed a lower static pressure in the core of the vortices generated at the blades' tip. It can also be seen (in Fig. 6.3) an influence of these vortices in the axial velocity, increasing V_a at lower radial positions of each vortex and decreasing V_a at higher radial positions of the vortex. This effect of the tip vortices in V_a indicates the direction of the vorticity vector component perpendicular to the plane of study, and matches with what would be expected from a vortex caused by the movement of the flow from a blade tip pressure surface to its suction surface.

However, there is one characteristic of the flowfield which does not appear to match what is described in theory as clearly. More specifically, it can be seen in Fig. 6.1 that the total pressure is decreasing upstream of the propeller, towards its disk. On the other hand, total pressure was described in section 2.1.3 to be constant and equal to the free-stream P_t until the static pressure jump occurs at the propeller disk (see Fig. 2.3). To further investigate this phenomenon, the C_{p_t} contours at a plane 10% duct chord upstream of the propeller blades ($x/c = -0.1$) are shown in Fig. 6.1. It can be understood that, at this axial location, C_{p_t} varies between values considerably higher and lower than the free-stream ($C_{p_{t\infty}} = 1$). Knowing that the blade, in this steady simulation, is located at $\theta = 45°$, it is possible to understand that the region in Fig. 6.1 with a total pressure deficit matches with the region of lower static pressure, under the influence of the blade's suction surface. At azimuthal locations further away from the blade, however, it can be seen that C_{p_t} is higher than its free-stream value. In order to further understand this phenomenon, it were made 180 slices at different azimuthal locations, spaced by $\Delta\theta = 0.5°$, at the plane characterized by $x/c = -0.1$. At each slice, it was recorded the C_{p_t} profile, which can be seen in Fig. 6.6. With this image, it is more clear that the total pressure of the flow at $x/c = -0.1$ reaches values lower than the free-stream total pressure by a difference larger than $2q_\infty$, where q_∞ is the free-stream dynamic pressure, since C_{p_t} reaches values lower than -1. On the other hand, there are also azimuthal locations where the total pressure reaches values higher than $P_{t\infty}$ by a factor of $0.5q_\infty$, when $C_{p_t} > 1.5$. These differences in total pressure with respect to $P_{t\infty}$ are too large to be considered negligible, or even to be simply attributed to a numerical discretization or iterative error. In this way, it was plotted in figure 6.6 the average of the C_{p_t} profile at $x/c = -0.1$. Since the mean C_{p_t} profile is constant and equal to the free-stream total pressure coefficient, for all radial positions evaluated, it can be concluded that the results from this steady CFD simulation of the propeller are in fact in agreement with aerodynamic theory described in section 2.1.3.

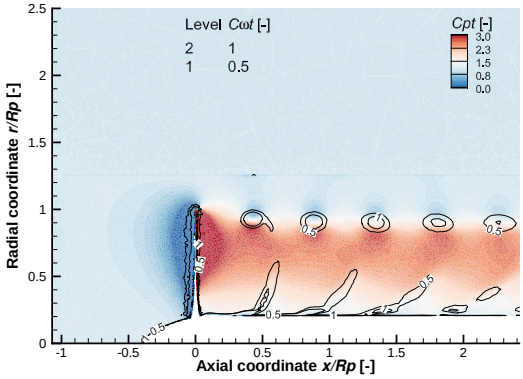

Figure 6.1: Total pressure coefficient, C_{p_t}, distribution in the vicinity of the isolated propeller. The lines of constant vorticity coefficient, for $C_{\omega_t} = 0.5$ and $C_{\omega_t} = 1$, are also shown. The contour is located at the azimuthal position of the blade, $\theta = 45°$. Results obtained using the medium mesh, for the conventional propeller domain.

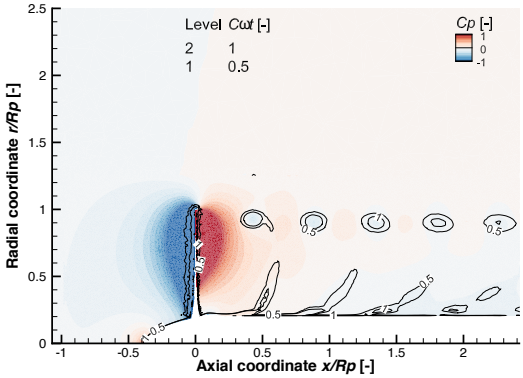

Figure 6.2: Pressure coefficient, C_p, distribution in the vicinity of the isolated propeller. The lines of constant vorticity coefficient, for $C_{\omega_t} = 0.5$ and $C_{\omega_t} = 1$, are also shown. The contour is located at the azimuthal position of the blade, $\theta = 45°$. Results obtained using the medium mesh, for the conventional propeller domain.

In order to understand why total pressure can not be constant and equal to $P_{t\infty}$ everywhere upstream of the blades, it should be noted that the propeller is moving with respect to the referential used to analyse the simulations, due to its rotation (even though the solver Fluent considered a different referential to calculate the flowfield with a steady computation). As an example, the inviscid flowfield around an isolated flying wing has a constant total pressure, if it is analysed with a referential that moves with the wing, as it is commonly

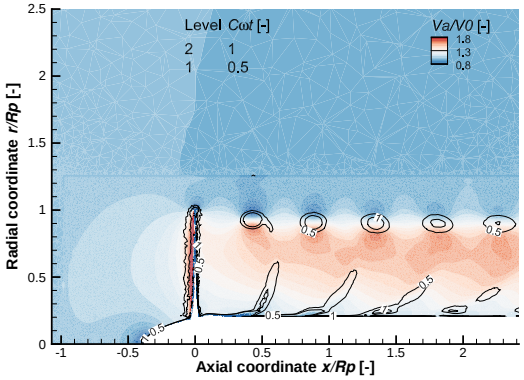

Figure 6.3: Axial velocity, V_a, distribution, normalised with the free-stream velocity, V_0, in the vicinity of the isolated propeller. The lines of constant vorticity coefficient, for $C_{\omega_t} = 0.5$ and $C_{\omega_t} = 1$, are also shown. The contour is located at the azimuthal position of the blade, $\theta = 45°$. Results obtained using the medium mesh, for the conventional propeller domain.

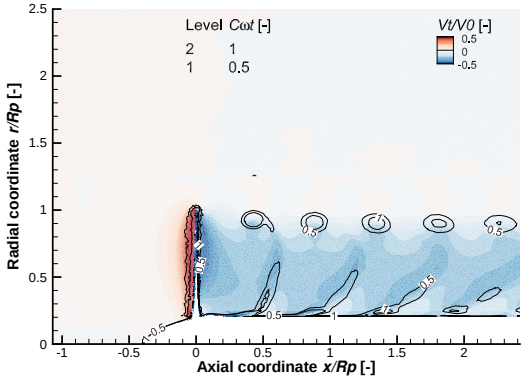

Figure 6.4: Tangential velocity, V_t, distribution, normalised with the free-stream velocity, V_0, in the vicinity of the isolated propeller. The lines of constant vorticity coefficient, for $C_{\omega_t} = 0.5$ and $C_{\omega_t} = 1$, are also shown. The contour is located at the azimuthal position of the blade, $\theta = 45°$. Results obtained using the medium mesh, for the conventional propeller domain.

done. However, if the same flowfield is analysed with a referential which is not moving with respect to the free-stream air, the flow's total pressure will vary along the flowfield. In the later case, the flow's free-stream total pressure will be equal to the free-stream static pressure, since ($v_\infty = 0m/s$). However, the flow's static pressure at the wing's leading edge "stagnation point" would be higher than the free-stream P_s, meaning that the flow's total pressure would have to be higher as well. On the other hand, at the wing's suction surface, where the static pressure is lower than the free-stream P_s, the flow's total pressure would be lower than the free-stream total pressure, despite the increase in dynamic pressure in this region.

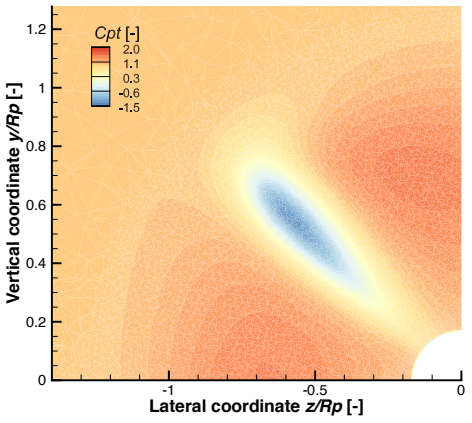

Figure 6.5: Total pressure coefficient, C_{p_t}, distribution upstream of the isolated propeller. The contour is located 10% duct cord ($0.1c_{duct} = 0.107R_p$) upstream of the blades. Results obtained using the medium mesh, for the conventional propeller domain.

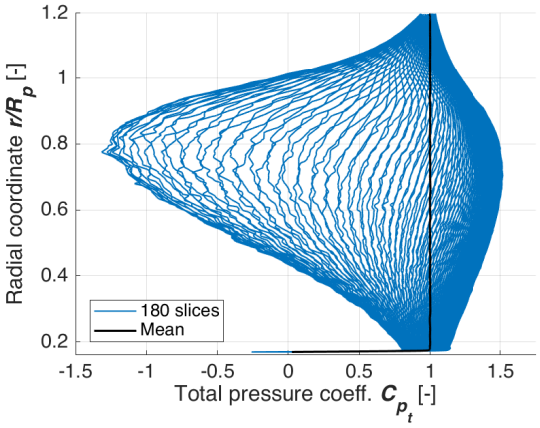

Figure 6.6: Total pressure coefficient, C_{p_t}, distribution upstream of the isolated propeller, for 180 slices at different azimuthal positions. The slices are located 10% duct cord ($0.1c_{duct} = 0.107R_p$) upstream of the blades, and are spaced by $\Delta\theta = 0.5°$. The blue lines correspond to the distributions over each of the 180 slices, and the black line corresponds to the average. Results obtained using the medium mesh, for the conventional propeller domain.

6.1.1. MESH CONVERGENCE STUDY

Before this section, it were analysed the flowfield results from the Xprop's steady simulation, in order to verify that the results match with what could be expected from propellers' aerodynamic theory, previously dis-

cussed in section 2.1, based on findings from literature. In this section, it is proceeded for the evaluation of the discretization error in the simulations. Firstly, it were analysed the variation of thrust and torque coefficients over the propeller, as well as the spinner's thrust, with respect to grid element size. Secondly, it were analysed the influence of the mesh size in the thrust and torque radial distributions over the simulated propeller blade. Finally, it were analysed the changes, due to mesh size, in the C_{p_t}, C_p, V_a/V_0 and V_t/V_0 profiles at different axial positions.

In Table 6.1, it can be seen the characteristics of the 3 grids used: their level of refinement, the number of elements and their cell refinement ratio, with respect to the finest grid (grid 1), h_i/h_1. For each of the three grids, it is also shown the thrust and torque coefficients of the propeller, as well as the thrust coefficient of the spinner. The thrust coefficient of the propeller, T_c, was separated into its pressure and friction components:

$$T_c = T_{c_p} + T_{c_f} = \frac{-F_{p_x}}{q_\infty S_p} + \frac{-F_{f_x}}{q_\infty S_p}\,, \tag{6.2}$$

where T_{c_p} and T_{c_f} are the pressure and friction thrust coefficients, and F_{p_x} and F_{f_x} are the pressure and friction forces in the axial direction, respectively. It should be understood that the friction force of the flow over the propeller in the axial direction actually points downstream (positive $\vec{e}_x$ in the coordinate system considered in this report). Therefore, the friction force over the Xprop is a contribution to the drag of the propulsor, and T_{c_f} was calculated to be negative.

Moreover, Table 6.1 also shows estimated exact values for the quantities referred. As it was discussed in a previous section (5.1.1), the exact value ϕ_0 is found along with the constant α and the observed order of accuracy, p, by minimizing the function $S(\phi_0, \alpha, p)$ which was described in equation 5.9. For the convergence study of the Xprop's steady simulation, since it were used only three grids, it was possible to find an analytical solution to minimize $S(\phi_0, \alpha, p)$, instead of a least squares root solution. For this reason, it is shown in Table 6.1 a row corresponding to the estimated exact value of each quantity, obtained with an analytical fit. For the propeller's torque coefficient, Q_c, however, it was not possible to find an analytical fit. In this way, ϕ_0, α and p were found with a least squares root approach, by finding a local minimum for $S(\phi_0, \alpha, p)$. The estimated exact value for Q_c can also be seen in Table 6.1, in the row relative to the best fit. Moreover, it were also found least square root solutions of $S(\phi_0, \alpha, p)$ for $p = 3$, being 3 the theoretical order of convergence of the simulations, which were performed with 3^{rd} order discretization schemes. The estimated exact values of each quantity, considering $p = 3$, are also shown in Table 6.1, in the last row.

Table 6.2 shows the characteristics of the several fits obtained during this mesh convergence study. The table incles the observed order of convergence of each fit, the uncertainty, U_s, (which is zero for the analytical fits), and the estimated relative error of the value obtained for the medium mesh, with respect to the estimated exact value, $\delta_{RE,2}$. Moreover, it is also shown the convergence ratio, R, whcih was calculated from [33]:

$$R = \frac{\phi_2 - \phi_1}{\phi_3 - \phi_2}\,. \tag{6.3}$$

According to Eça and Hoekstra [33], R is useful in a convergence study with set of three grids where $h_2/h_1 = h_3/h_2$, which is approximately the case in the Xprop's mesh convergence study. In this way, R was used to classify the apparent convergence condition [33]:

$$
\begin{aligned}
0 < R < 1 &\Rightarrow \text{Monotonic convergence}\,, \\
-1 < R < 0 &\Rightarrow \text{Oscilatory convergence}\,, \\
R > 1 &\Rightarrow \text{Monotonic divergence}\,, \\
R < -1 &\Rightarrow \text{Oscilatory divergence}\,.
\end{aligned}
\tag{6.4}
$$

In this way, according to Table 6.2, the convergence of the propeller quantities T_{c_p}, T_{c_f} and T_c was classified as monotonic divergence, whereas the convergence of the Xprop's Q_c was classified as oscillatory convergence, and the convergence of the spinner's T_c was classified as monotonic convergence. These classifications influenced the way that the uncertainty, U_ϕ, was calculated for each quantity. For the propeller quantities T_{c_p}, T_{c_f}, T_c and Q_c, since it was not observed a monotonic convergence, uncertainty was calculated for all grids from:

$$U_\phi = 3\Delta_M\,, \tag{6.5}$$

according to [33]. Δ_M is the maximum difference between all solutions available. However, it should be noted that this method for estimating uncertainty (when monotonic convergence is not observed) does not appear to be perfect, since it would have led to a higher uncertainty estimation if more grids had been used. For the spinner's T_c, since the converged was classified as monotonic and $0 < p < 0.95$, uncertainty was calculated with equation 5.16.

Isolated Xprop - grid convergence study

				Propeller				Spinner
Mesh	Refinement	# of elements	h_i/h_1 [-]	T_{c_p} [-]	T_{c_f} [-]	T_c [-]	Q_c [-]	T_c [-]
3	Coarse	4.01×10^6	1.59	1.1321	-0.00499	1.1271	0.378511	0.009735
2	Medium	7.96×10^6	1.27	1.1332	-0.00506	1.1282	0.378154	0.009728
1	Fine	16.18×10^6	1	1.1347	-0.00514	1.1296	0.378176	0.009722
0 (Analytical fit)	-	∞	0	1.1268	-0.00958	1.1225	-	0.009689
0 (Best fit)	-	∞	0	-	-	-	0.378161	-
0* (Fit with $p = 3$)	-	∞	0	1.135324	-0.00518	1.1301	0.377998	0.009719

Table 6.1: Grid convergence study performed for the simulation with the isolated propeller, considering the pressure, friction and total thrust coefficients on the propeller, the propeller's torque coefficient and the spinner's thrust coefficient. Two different extrapolated values are shown for each drag coefficient. The first one (on the second last row) corresponds to an extrapolation with the best fit, and the second (last row) corresponds to a fit where p was constrained to 3, the theoretical order of convergence.

Isolated Xprop - grid convergence study

Fit	Quantity	$T_{c_{p,prop}}$	$T_{c_{f,prop}}$	$T_{c,prop}$	$Q_{c,prop}$	$T_{c,spinner}$
Analytical fit (Unconstrained p)	p	-0.884	0.0733	-0.942	-	0.662
	U_s [%]	0	0	0	-	0
	$\delta_{RE,2}$ [%]	-0.567	89.115	-0.504	-	-0.408
Best fit (Unconstrained p)	p	-	-	-	14.955	-
	U_s [%]	-	-	-	0.00644	-
	$\delta_{RE,2}$ [%]	-	-	-	0.00185	-
Fit with the theoretical order of convergence ($p = 3$)	p^*	3	3	3	3	3
	U_s^* [%]	0.0415	-0.400	0.0399	0.0289	0.0131
	$\delta_{RE,2}^*$ [%]	0.184	2.286	0.175	-0.0412	-
Convergence ratio	R [-]	1.27	1.02	1.29	-0.062	0.89
Overall Uncertainty	$U_{\phi,2}$ [%]	0.707	9.108	0.700	0.0950	0.00875

Table 6.2: Grid convergence study performed for the simulation with the isolated propeller, considering the pressure, friction and total thrust coefficients on the propeller, the propeller's torque coefficient and the spinner's thrust coefficient. For each fit, it is shown the standard deviation of the fit, U_s, and the error of the medium mesh with respect to the extrapolated value, $\delta_{RE,2}$, both in percentage of the drag coefficient obtained for the medium mesh. It is also shown the convergence ratio, R, for each quantity. The overall uncertainty of the drag coefficient obtained with the medium mesh, $U_{\phi,2}$, is shown in the last row. The equation used to calculate $U_{\phi,2}$ for each drag coefficient is specified in the text.

From this convergence study, it is interesting to notice that the estimated uncertainties are considerably low for most of the quantities considered. Only for the propeller's friction thrust coefficient the uncertainty is larger than 1% of the value obtained with the medium grid (grid 2). Indeed, the uncertainty of the propeller's T_{c_f} ($U_{\phi,2} \approx 9\%$) appears to be significantly high. However, it can be understood from table 6.1 that the friction force represents a relatively small contribution to the propeller's total thrust. For grid 1:

$$\frac{T_{c,1}}{T_{c_{f,1}}} \times 100\% = 0.46\% \,. \tag{6.6}$$

In this way, it can be concluded that the thrust and torque of the Xprop, as well as the spinner's thrust, are well captured with the grid with a medium refinement, with a relatively low discretization error. The plots relative to the Xprop's steady simulation grid converge study are shown in the following Figure. Fig. 6.7 is relative to the convergence of $T_{c_{p,prop}}$, $T_{c_{f,prop}}$, $T_{c,prop}$ and $T_{c_{p,spinner}}$. Each plot, besides showing the relative difference of the value obtained with each grid with respect to grid 2 (medium refinement grid), also shows either the analytical fit or the best fit with an unconstrained p, and the best fit with $p = 3$. It is interesting to notice that, in Figs. 6.7a, 6.7b and 6.7c the fit with $p = 3$ appears to be more adequate to estimate the exact value for each quantity, whereas the analytical fit appears to diverge to values very different that the values obtained with the three grids. This matches with the classification of the convergence of the propeller's T_{c_p}, T_{c_f} and T_c as monotonic divergence. In Fig. 6.7d, the fit with $p = 3$ also appears to be more adequate to estimate the exact value of Q_c. This is due to the fact that the apparent order of accuracy, p, for the convergence of Q_c was calculated to be too high (considerably larger than the theoretical order of the method). In this way, the best fit for Q_c is too optimistic, in the sense that it leads to an estimation of an exact value which is too close to the values obtained with the three grids. For the convergence of the spinner's T_c, which was the only case where monotonic convergence was identified, it can be seen in Fig. 6.7e that the analytical fit also leads to an acceptable estimation of the exact value, in this case also more conservative than the fit with $p = 3$.

After analysing the grid convergence of thrust and torque integrated over entire components, it is also relevant to analyse the radial distributions of these quantities over the simulated propeller blade. Figure 6.8 shows, precisely, the thrust and torque distributions over a propeller blade for the three grids used in the Xprop's steady simulation. It can be understood that the distributions obtained from the three grids are very

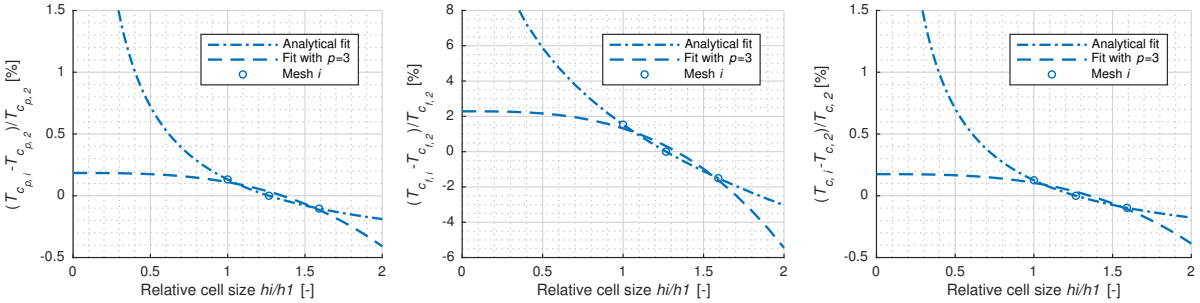

(a) Blade's T_{c_p} (b) Blade's T_{c_f} (c) Blade's T_c

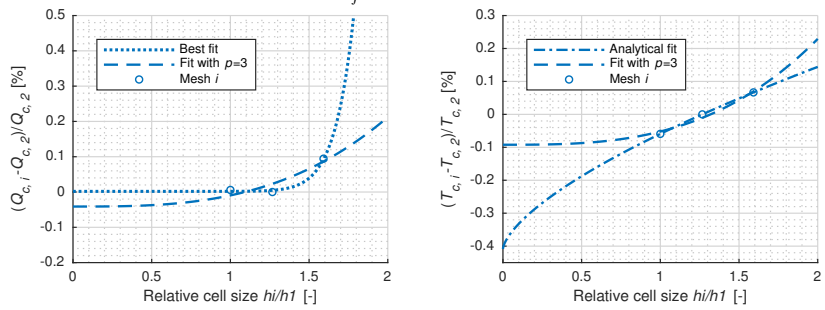

(d) Blade's Q_c (e) Spinner's T_c

Figure 6.7: Convergence study of the isolated propeller's blade pressure thrust coefficient (top-left), blade friction thrust coefficient (top-middle), blade total thrust coefficient (top-right), blade torque coefficient (bottom-left) and spinner total thrust coefficient (bottom-right), with respect to grid element size. It is shown the relative difference to the value calculated with mesh 2 (medium refinement).

similar, which indicates a small discretization error. This conclusion is in agreement with the small uncertainties previously estimated for the propeller's overall T_c and Q_c. In Fig. 6.8 it is also interesting to notice the sudden increase in loading at the propeller tip. This phenomenon was found to be caused by the blade tip vortex, which impinges on the blades' suction surface at the tip, locally increasing the loading. The pressure at the blade tip suction surface is reduced when in contact with the vortex, since the blade tip vortex core is characterized by a lower pressure (seen e.g. in Fig. 6.4). The lower pressure at the blade tip suction surface, caused by the tip vortex, can be seen in Fig. 6.9. It is clear that there is a sudden low pressure peak at the blade tip, downstream of the leading edge's suction peak. In Fig. 6.12, it is shown the blade tip vortex, with an isosurface of constant tangential vorticity coefficient, $C_{\omega_{tangential}}$. $C_{\omega_{tangential}}$ was defined similarly to the total vorticity coefficient, simply substituting total vorticity by tangential vorticity in equation 6.1. In this way, from Fig. 6.12 it is possible to verify that the blade tip vortex indeed impinges on the blade's tip suction surface, in the region where it occurs a peak of low pressure.

Besides analysing the grid convergence of the forces and moments over the propeller, it is also relevant to understand how the cell size influences the flowfield in the propeller's stream-tube. For this reason, the flowfields calculated with the three grids were compared at different axial locations. These location were, with respect to the propeller blades's axial position: $x/c_{duct} = -0.1$, $x/c_{duct} = 0.2$ and $x/c_{duct} = 1$. The locations were defined with respect to the duct's chord, instead of the propeller radius, for easier comparison with the installed configurations. As it was previously referred, in the installed configurations, the propeller is located at 30% duct chord. In this way, Figs. 6.11, 6.12, 6.13 and 6.14 show, respectively, the c_{p_t}, C_p, V_a and V_t radial profiles for the three referred axial locations. Overall, it can be seen that in all plots it was found a good agreement between the distributions calculated with the three grids. The most clear exception appears to be found on the C_p profiles downstream of the blades, at the blade tip vortex region. Indeed, in Fig. 6.12 it can be noticed that the pressure deficit in the core of the vortex increases with cell refinement.

In the plot relative to C_{p_t} (Fig. 6.11), it is also interesting to notice that the region of increased total pressure moves towards lower radial positions from $x/c = 0.2$ to $x/c = 1$. This phenomenon is caused by the slipstream contraction that occurs while static pressure reduces downstream towards P_{s_∞} (Fig. 6.12), and

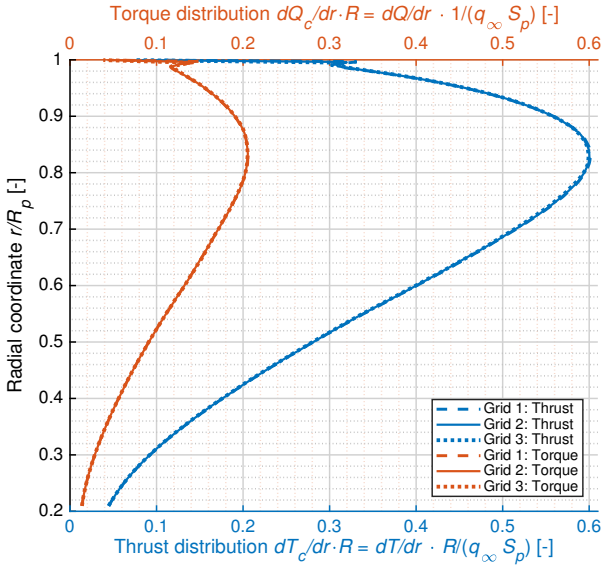

Figure 6.8: Thrust and torque coefficient (T_c and Q_c) radial distributions over a blade of the isolated propeller, for the three different grid refinements tested. The dashed lines correspond to the fine grid (grid 1), the continuous lines correspond to the grid with a medium refinement (grid 2) and the dotted lines correspond to the coarse grid (grid 3). The thrust distributions are represented with blue lines and the torque distributions are represented with the red lines. Results obtained with the conventional propeller domain.

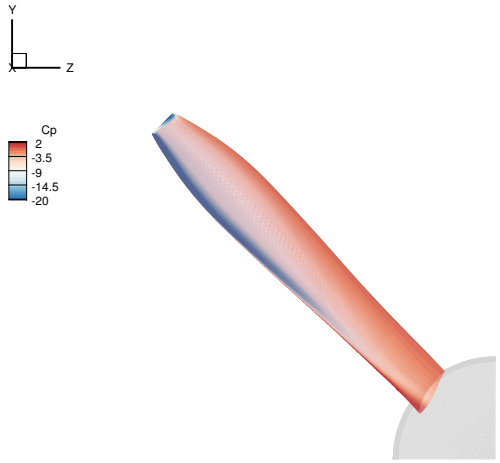

Figure 6.9: Pressure coefficient, C_p, contours over the Xprop's blade suction surface. Results obtained using the conventional propeller domain, with the medium mesh.

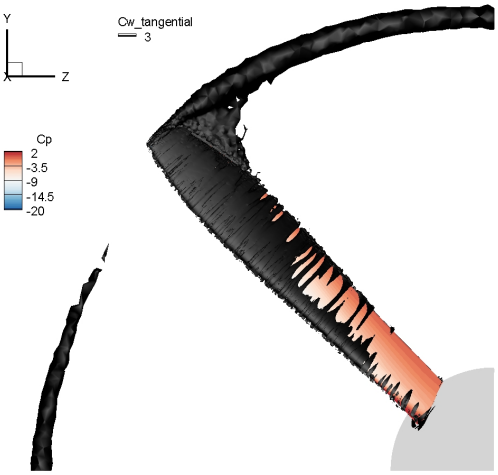

Figure 6.10: Blade tip vortex shown by an isosurface of constant tangential vorticity coefficient, $C_{\omega_{tangential}} = 3$. The pressure coefficient, C_p, contours over the Xprop's blade are also plotted. Results obtained using the conventional propeller domain, with the medium mesh.

flow velocity increases in the slipstream (6.13). From Fig. 6.14, it is also possible to understand that the tangential velocity peak increases, in module, from $x/c = 0.2$ towards $x/c = 1$. The very large negative peak in V_t at $x/c = 0.2$ and for very low radial positions (near $r/R_p = 0.2$) is due to the rotation of the spinner, which was modelled as a no-slip boundary.

6.1.2. VARYING ADVANCE RATIO

After studying the effect of mesh size on the simulation results, it was also important to analyse the effect of changing the operating condition of the propeller. The Xprop's operating condition was varied by changing the advance ratio, J. Since all simulations were performed with $V_\infty = 30 m/s$, J was varied by changing the rotational velocity of the propeller. The advance ratio was varied, for the Xprop's steady simulation, for two

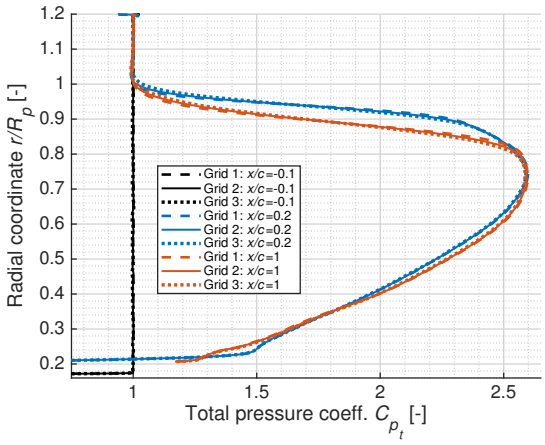

Figure 6.11: Total pressure coefficient, C_{p_t}, average radial distributions in the vicinity of the propeller, at three axial locations, for the three different grid refinements tested. The axial position is indicated in terms of distance to the propeller disk. $x/c > 0$ downstream of the propeller. $x/c_{duct} = 1 \Leftrightarrow x/R_p \approx 1.07$. Results obtained with the conventional propeller domain.

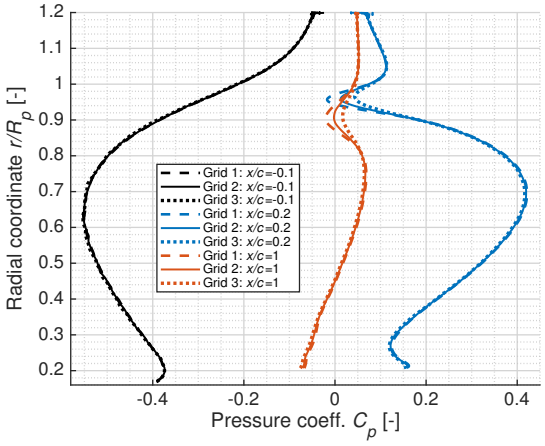

Figure 6.12: Pressure coefficient, C_p, average radial distributions in the vicinity of the propeller, at three axial locations, for the three different grid refinements tested. Results obtained with the conventional propeller domain.

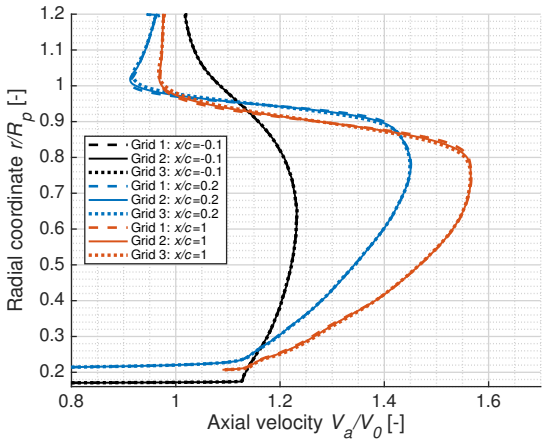

Figure 6.13: Axial velocity (V_a) average radial distribution, normalised with the free-stream velocity, V_0, in the vicinity of the propeller, at three axial locations, for the three different grid refinements tested. Results obtained with the conventional propeller domain.

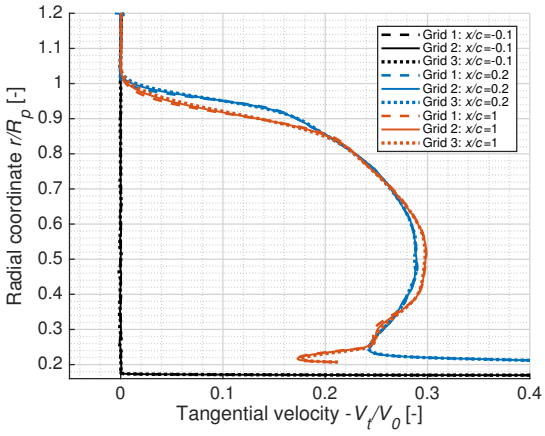

Figure 6.14: Tangential velocity (V_t) average radial distribution, normalised with the free-stream velocity, V_0, in the vicinity of the propeller, at three axial locations, for the three different grid refinements tested. Results obtained with the conventional propeller domain.

main reason's. Firstly, it was intended to validate the simulations against experimental results, which were available for a wide range of advance ratios, for the same free-stream flow velocity. Secondly, it was intended to obtain thrust and torque distributions at different advance ratios, which would serve as an input to the installed configurations with an AD. The steady simulations of the Xprop at different advance ratios were performed with the grid with a medium refinement. The medium grid led to low discretization errors with respect to the propeller's T_c and Q_c at $J = 0.7$, as discussed in the previous section.

In Table 6.3, the operating conditions relative to each advance ratio tested are specified, as well as the overall values for thrust coefficient, torque coefficient, power coefficient and efficiency at each J. It is clear that the loading on the propeller decreases for higher advance ratios, within the range tested, as T_c and Q_c reduce. From the P_c column, it can be understood that the power added to the flow sees large variations for the apparently small range of advance ratios tested, considering that $P_{c_{J=0.7}} = 2.5 P_{c_{J=0.9}}$. In this way, it was considered that this range of operating conditions could already provide a good indicative of how the CFD results compare with the experimental results. It was also considered that this range of J would be enough to understand how the performance of each ducted system is influenced by the change in power setting, in

the installed configurations with an AD. Adding more power settings, or advance ratios, would contribute to improve the reliability of the conclusions taken from the research, but would also greatly increase the test matrix. In terms of efficiency of the propeller, it can also be understood that it declines with increasing advance ratio. Efficiency was estimated since it is an important parameter to compare the performance of the different propulsion systems. Thus efficiency was found to be relevant to help answering the thesis research questions.

Isolated Xprop steady simulation - varying advance ratio

J	Ω [rad/s]	T_c [-]	Q_c [-]	P_c [-]	η [-]
0.7	662.60	1.128	0.378	1.697	0.665
0.8	579.77	0.763	0.272	1.069	0.714
0.9	515.35	0.519	0.197	0.689	0.754

Table 6.3: Thrust, torque and power coefficients, as well as efficiency of the Xprop at different advance ratios. The advance ratio was modified by changing the propeller's angular velocity, in the steady simulations.

The thrust and torque distributions over the propeller blade are the main inputs for the installed simulations with an AD. These distributions a plotted in Fig. 6.15, for the three advance ratios tested. The distributions indicate that the reduction of loading for higher J is uniform along the blade. This could happen differently if, for example, one of the advance ratios tested would lead to flow separation at the blade. Moreover, the flowfields obtained for each advance ratio were also verified, in order to confirm that the difference in T_c and Q_c for the different J would lead to corresponding variations of C_{p_t}, C_p, V_a and V_t in the streamtube. These plots can be consulted in Appendix A.3.

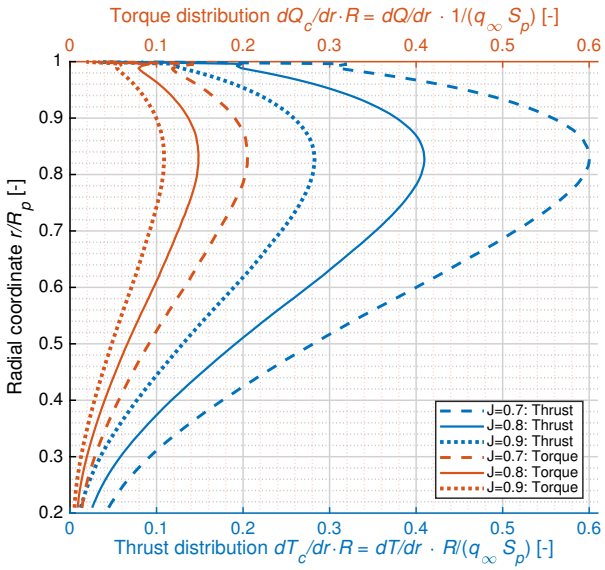

Figure 6.15: Thrust and torque coefficient (T_c and Q_c) radial distributions over a blade of the isolated propeller, for the three advance ratios tested. The dashed lines correspond to the highest advance ratio, $J = 0.7$, the continuous lines correspond to $J = 0.8$ and the dotted lines correspond to the lowest advance ratio tested, $J = 0.9$. The thrust distributions are represented with blue lines and the torque distributions are represented with red lines. Results obtained with the conventional propeller domain.

6.1.3. UNSTEADY SIMULATION

The final and most computationally expensive simulations of the thesis were decided to be performed with transient calculations. For this reason, it was found relevant to first perform equivalent unsteady calculations of the isolated Xprop, so that these could be verified and validated. However, it was not performed a new grid convergence study for the unsteady simulation of the Xprop, since it would lead to too large computational

costs. It would have also been interesting to analyse the influence of the selected time step on the temporal discretization error of the simulation, but this was not performed to lower computational costs and to keep the size of the test matrix at check. The unsteady results presented in this section were performed using the steady propeller flowfield as an initial solution. Moreover, the results were obtained with a time step, Δt, equivalent to 1° of propeller rotation. The results were recorded with an interval of 5 time steps, during a period corresponding to 180° of propeller rotation. In this way, the results presented in this section correspond to 36 time steps, which reflect the evolution of the flowfield during half a propeller rotation. It is also important to refer that the results were calculated with grid 1. This choice was based on the practical consideration that the grid with a medium refinement, grid 2, did not lead to a converged unsteady solution in terms of residuals or even forces on the propeller blade. Thus, this section compares the results of the Xprop's unsteady simulation at $J = 0.7$, obtained with the fine grid, with the results from the equivalent steady simulation.

In Fig. 6.16, it is shown the radial T_c and Q_c distributions obtained from the recorded time steps of the unsteady simulation, which are compared against the distributions obtained from the steady simulation, with the same grid (fine grid) and with the same advance ratio ($J = 0.7$). Firstly, it interesting to notice that there is a good agreement between the steady and the unsteady results, since it is difficult to find differences in the radial distributions shown. Secondly, it can also be understood that the results from the unsteady calculation exhibit a small scatter. The small scatter is an indicative that the simulation was well converged, and also that there were no strong unsteady aerodynamic effects occurring (in the propeller's rotating reference frame). For example, Stokkermans [51] found a relatively large scatter in the thrust and torque distributions at the lower radial positions of the propeller simulated in CFD, which demonstrated the presence of flow separation in those blade sections.

Furthermore, it was also found relevant to compare the total values of thrust and torque coefficient from the Xprop's unsteady simulation with the equivalent results from the steady simulation. This is shown in Fig. 6.17, considering the propeller's T_{c_p}, T_c and Q_c. In the first time step recorded, the azimuthal position of the blade was considered to be at $\theta_{blade} = 50°$. From this figure, it is clear that both steady and unsteady simulations of the Xprop, with this grid and boundary conditions, lead to the calculation of similar values of thrust and torque coefficients. Furthermore, it is also possible to understand that there is a relatively small variation of the thrust and torque in the unsteady simulation, which appears to be periodic. This oscillating result could be due to different reasons. Firstly, the Xprop's blade trailing edge is expected to shed a vortex which would cause oscillations the blade loading. The effect of blunt trailing edge's vortex shedding, causing loading fluctuations, was studied for example by Zobeiri et al. [1]. However, in the Xprop's unsteady simulation results, the oscillation of the given quantities could also be due to a non fully converged solution, and also due to the influence of the boundary conditions, since periodic boundaries were used to reduce the domain to one quarter (90° domain instead of a 360° domain). In this case, the iterative error, combined with the error caused by the usage of a sliding mesh approach and periodic BC, appears to be the main cause of the fluctuations on the T_c and Q_c time-accurate results. Firstly, it is seen in Fig. 6.17 that the fluctuations in thrust and torque coefficients have a periodicity of 90°, which most likely is not a coincidence with the fact that a 90° domain was used. The propeller domain and mesh return to the same azimuthal position with respect to the outer domain with a periodicity of 90° as well, with the sliding mesh approach in a 90° domain. Secondly, the small difference between consecutive higher or lower peaks in the quantities seen in Fig. 6.17 indicates that the solution was not yet completely converged. However, the shown fluctuations were considered to be sufficiently small to be accepted, this way avoiding additional computational costs.

6.1.4. VALIDATION

The validation of the isolated Xprop's CFD calculations was based on the comparison of the computed CFD values with experimental results, as well as calculations performed with a lower fidelity method. In this section, it is first discussed the uncertainties relative to the comparison of results obtained with different methods. Afterwards, the several results are shown and discussed.

UNCERTAINTIES IN THE VALIDATION PROCESS

The main data available for validation of the propeller CFD results consists of experimental data obtained in TU Delft's open jet facility (OJF). The wind tunnel (WT) data was provided by T. Sinnige, via internal communication. The equivalent data consists of thrust and torque values obtained at the same free-stream velocity

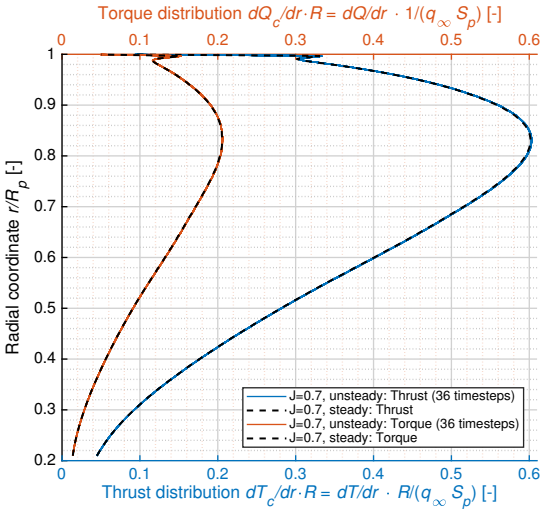

Figure 6.16: Thrust and torque coefficient radial distributions over a blade of the isolated propeller. Results obtained with the fine grid of the conventional propeller domain, from both steady and unsteady calculations, at $J = 0.7$.

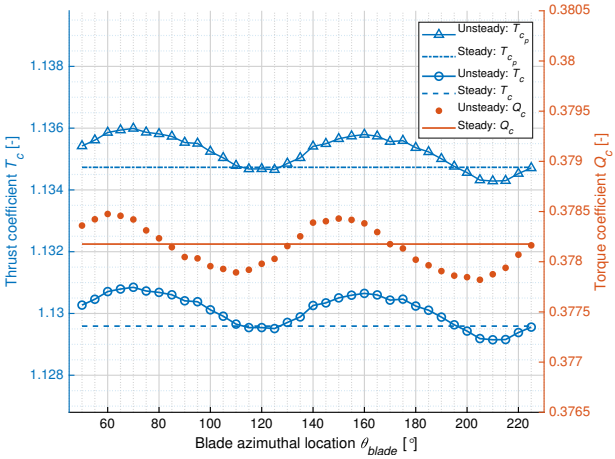

Figure 6.17: Pressure thrust, total thrust, and torque coefficients of the isolated propeller. Results obtained with the fine grid of the conventional propeller domain, from both steady and unsteady calculations, at $J = 0.7$.

and advance ratio. However, the Xprop used in OJF has the main difference of having 6 blades, whereas the Xprop used in this thesis' computations had its number of blades reduced to 4. Besides the number of blades, there are more differences which were expected to cause discrepancies between the wind tunnel and CFD results, e.g.:

- Boundary conditions:
  - the wind tunnel facility is an open jet, which means that shear stresses occur between the jet and the flow outside of the jet. In the CFD simulations it were imposed pressure far-field conditions, which also cause a blockage effect by imposing an axial velocity to the flow in the far field.
  - the turbulence intensity, I, is different at the two inlets. At the OJF, turbulence intensity is kept lower than 0.24% [49]. However, in the CFD calculations the free-stream turbulence is considerably lower: $I_\infty = \sqrt{2k_\infty/3}/V_\infty = 0.08\%$.
  - the Xprop's nacelle was modelled as a free-slip boundary in CFD, to simplify the simulations. In the wind tunnel, the no-slip condition applies at the nacelle surface.
- In the wind tunnel, the force acting on the spinner is included in the balance measurements of thrust and torque of the propeller. However, the forces on the spinner were not considered when calculating the total forces and moments on the propeller from the CFD simulations. This was due to the fact that the spinner was modelled in CFD as open surface (it is connected to the nacelle without a gap). Pressure forces should ideally be calculated from integrating pressure over closed surfaces.
- Turbulence modelling: in the CFD results the effect of turbulence in the flowfield was estimated based on a turbulence model, $k-\omega$ SST.
- The Xprop geometry was simplified for the CFD computations. The simplification with an expected largest influence in the flowfield was the extension of the nacelle until the outlet. In the wind tunnel, however, there is a jet of air flow starting from the trailing edge of he nacelle, which acts as an exhaust of air, increasing the mass flow in the wind tunnel.

Since the different number of blades between the CFD and wind tunnel geometries was expected to cause strong discrepancies in the results, it was decided to perform equivalent calculations with a lower order method (less expensive than CFD). In this way, the program XROTOR was selected to analyse the performance of the Xprop with both 4 and 6 blades, in order to compare the difference in performance in both cases. XROTOR is a program based on lifting line theory. In this way, XROTOR iteratively calculates the circulation distribution over a rotor, along with the induced velocities at its lifting line [56]. In order to perform

the calculations, XROTOR receives airfoil properties as an input. During this thesis, XROTOR was run using a MATLAB tool developed by Sinnige, *m*ROTOR, which works as described in [49]. The tool was developed to be able to provide to XROTOR the airfoil characteristics of the Xprop blade at different radial sections, taking into account the change in Reynolds number. Even though *m*ROTOR uses airfoil polars obtained with XFOIL, XROTOR only accepts as input the necessary information to rebuild the polars, e.g. section maximum lift coefficient, zero-lift angle of attack and lift curve slope. For this reason, *m*Rotor optimises the XROTOR inputs so that there is a lower discrepancy between the polar estimated by XROTOR and the actual polar obtained from XFOIL. The tool also allows for the specification of more basic characteristics, such as the flow free-stream velocity, rotational velocity of the propeller and number of blades. Overall, the tool used has the advantage of being able to obtain fast results, but it also leads to differences with respect to the CFD and experimental results, such as:

- Only considering axial and tangential flow over the blades. Radial flow is neglected.
- Using a wake semi-rigid model, which means that the direction of the trailing vortex sheet is iteratively calculated, but wake contraction is not taken into account [56].
- As XROTOR only accepts a limited number of airfoil characteristics as input, the airfoil polars loose accuracy.
- The spinner is not modelled in XROTOR. This means that the force on the spinner is not calculated, and the influence of the spinner on the inflow velocities at the propeller disk is not taken into account.
- Turbulence is only modelled in the sense that the airfoil polars considered by *m*ROTOR were obtained from XFOIL considering a fully turbulent flow over the airfoil, i.e. the transition location was set to $x/c = 0$.

COMPARISON OF CFD, WIND TUNNEL AND XROTOR RESULTS

Having discussed the differences between each method used in the validation process, it is then possible to proceed for the comparison of the results from CFD, wind tunnel and Xrotor. Figures 6.18 and 6.19 show the thrust coefficients obtained from both CFD, wind tunnel, and XROTOR for a single XPROP blade at $V_\infty = 30 m/s$ and three different advance ratios: $J = 0.7$, $J = 0.8$ and $J = 0.9$. As it was previously referred, the CFD results correspond to the 4 bladed Xprop steady simulation with the large propeller domain. The wind tunnel results were obtained with the 6 bladed Xprop, and the XROTOR calculations were performed for both the 4 and 6 bladed versions of the propeller. From Fig. 6.18, it is clear that the blade T_c obtained from CFD is higher than the values obtained experimentally. Even though there are multiple differences between the two methods, the number of blades was found to be the main cause for this discrepancy. Having a higher number of blades results in a higher total thrust of the propeller, which means that the axial induced velocities at the propeller disk will be higher as well. With higher induced velocities, the effective angle of attack of each blade section reduces (see Fig. 2.2), and the total thrust produced by each blade reduces as well. The same trend can be noticed on the XROTOR calculations of thrust with the two versions of the Xprop, confirming that decreasing the number of blades would indeed cause an increase in each blade's T_c. However, it can also be understood that the XROTOR results do not match either the CFD or the WT T_c values, for the corresponding number of blades. It was found that XROTOR leads to an over prediction of thrust with respect to the two higher fidelity methods. There are multiple differences between the XROTOR and the other two methods, which were previously discussed. Still, it is suggested that the non-inclusion of the spinner could lead to a these large increases in terms of blade T_c. The spinner forces a contraction of the flow in the vicinity of the blades' location, which therefore also causes an increase in axial flow velocity at the propeller disk. As it was referred, higher V_a at the propeller disk usually leads to a lower loading of the blades.

With respect to the torque coefficients obtained from each method, it can be understood that the trends seen in Fig. 6.19 are similar to the T_c trends. The CFD simulations lead to an estimation of a higher torque per blade than the wind tunnel experiments. This observation can also be mainly attributed to the different number of blades used in the two cases, since the XROTOR calculations with the Xprop with 4 and 6 blades show the same relation. Moreover, it can also be understood that XROTOR estimates a higher torque than both CFD and wind tunnel experiments, for the same number of propeller blades. This is similar to what had been observed in Fig. 6.18, regarding the thrust coefficient of the blades.

In order to understand if the differences between CFD and wind tunnel results can in fact be predominantly attributed to the difference in number of blades, the ratios of blade T_c and Q_c between estimations with the 4 and 6 bladed versions of the Xprop are shown in Fig. 6.20. In this way, for each coefficient, C, it is shown the ratio between CFD and wind tunnel results ($C_{CFD(4Bl.)}/C_{WT(6Bl.)}$), and the ratio between XROTOR estimations with the 4 and 6 bladed propeller ($C_{XROTOR(4Bl.)}/C_{XROTOR(6Bl.)}$). Regarding blade thrust, it can be understood that the relation between CFD and WT results is very close to the ratio calculated from the XROTOR results, at $J = 0.7$. However, the ratio between CFD and WT estimations decreases with increasing advance ratio, whereas the ratio between calculations with 4 and 6 blades from XROTOR appears to increase with advance ratio. These trends lead to a higher disparity of the two ratios at the highest J considered, 0.9. For the torque ratios, a similar relation can be observed, with the difference that there is a higher disparity between the two ratios at $J = 0.7$, leading to an even larger difference at higher J. It was not identified a dominant factor which could explain the differences between the two ratios. Still, it was acknowledged that the differences between the three estimation methods, which were highlighted in the previous sub-section, are relatively large. In this way, the disparities seen in the results were accepted. Possible next steps to improve the validation of the CFD simulations would have been performing computations with the 6 bladed version of the Xprop, or making the CFD computational domain and set-up more similar to the experimental set-up. Due to time constraints, it was instead proceeded for the next planned steps of the research.

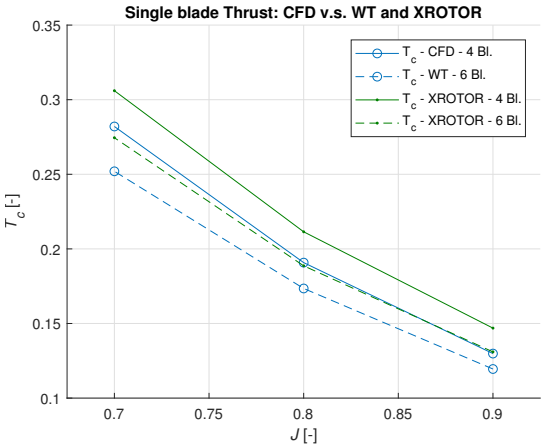

Figure 6.18: Thrust coefficients of a single Xprop blade, versus advance ratio. Results obtained with CFD steady simulations of the 4 bladed Xprop, with wind tunnel experiments using the 6 bladed Xprop, and with XROTOR calculations for both the 4 and 6 bladed versions of the propulsor.

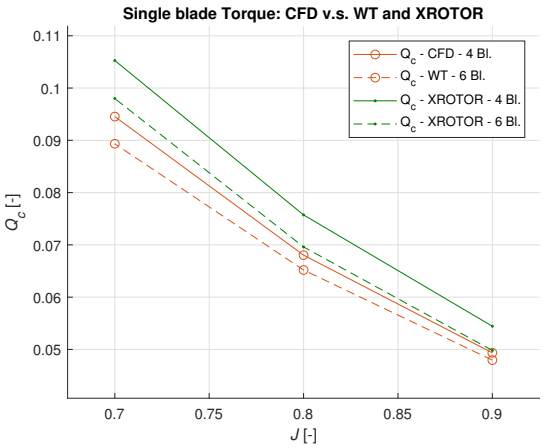

Figure 6.19: Torque coefficients of a single Xprop blade, versus advance ratio. Results obtained with CFD steady simulations of the 4 bladed Xprop, with wind tunnel experiments using the 6 bladed Xprop, and with XROTOR calculations for both the 4 and 6 bladed versions of the propulsor.

6.2. ISOLATED XPROP - SMALL PROPELLER DOMAIN

After having verified and validated the CFD results obtained with the large propeller domain (LPD), it was proceeded for the simulation of the propeller flowfield with the radially small propeller domain (sPD). The Xprop computations with the sPD were performed for $J = 0.7$, which is the same advance ratio that was used in the ducted propeller CFD simulations. As it was previously discussed, the ducted Xprop simulations had to be performed with the sPD instead of the more conventional LPD, since the propeller domain had to "fit" inside the duct. In this way, this section tackles the verification of the steady simulation of the Xprop with the sPD (sub-section 6.2.1), as well as the verification of the equivalent unsteady simulation, in sub-section 6.2.2. During the verification process, the results obtained with the sPD are compared against the results obtained with the fine mesh for the LPD, since this was the mesh used for the unsteady simulation with the large propeller domain.

6.2.1. STEADY SIMULATION

This section aims at understanding if the steady simulation of the Xprop with the sPD leads to reliable results. It is considered that the isolated propeller simulation should lead to an acceptable prediction of the forces on the blades, as well as an accurate estimation of the influence of the propeller in the flowfield. In

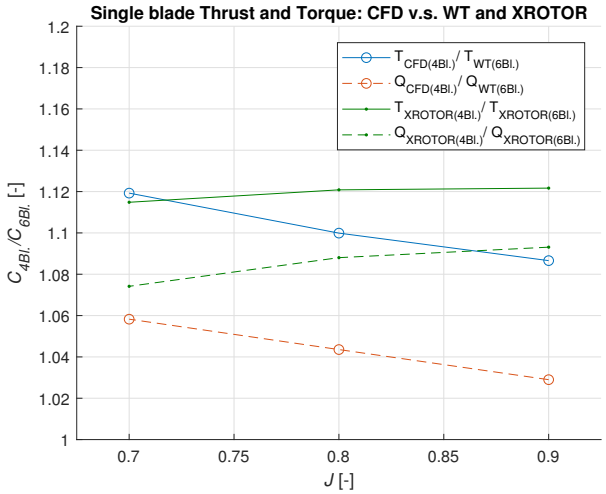

Figure 6.20: Ratios of thrust and torque coefficients of a single Xprop blade between the two Xprop versions, versus advance ratio. It is shown the ratio between the CFD (4 bladed Xprop) and the wind tunnel (6 bladed) results, and the ratio between the results obtained with the 4 and 6 bladed versions of the Xprop from XROTOR.

this way, the thrust and torque coefficients obtained from the steady computation with the sPD are first compared with the equivalent results from the steady simulation of the Xprop with the fine mesh. Table 6.4 shows the number of elements of each mesh, the estimated T_c and Q_c, and the relative difference of T_c and Q_c to the value computed with the large propeller domain (with the fine grid). It can be concluded that there is a relatively large difference between the values calculated with the two domains, for both T_c and Q_c. The difference can be considered specially large, since it is one order of magnitude larger than the differences reported previously in section 6.1.1, during the grid convergence study of the same quantities. Even though the mesh generated for the sPD is not geometrically similar to the grids generated for the LPD, it was considered that the discretization error due to a short number of elements should not be the dominant factor to justify the different results obtained with the unconventional propeller domain. In fact, the number of elements of the grid generated for the sPD lies between the number of elements of the LPD's fine and medium grids.

In order to show how the change in the propeller computational domain affected the radial distribution of forces along the Xprop blades, the blade radial distributions of thrust and torque coefficients are plotted in Fig. 6.4. The distributions shown in Fig. 6.4 are relative to both steady simulations, using the sPD and the LPD with the fine grid (grid 1). It is interesting to notice that the radial distributions of T_c and Q_c estimated with the two domains match well for low radial positions ($0.2 < r/R_p < 0.6$). However, for higher radial locations the two distributions see a divergence of the section thrust and torque coefficients. In this way, the results indicate that the usage of a smaller propeller leads to an under estimation of blade loading at high radial positions. Confirming that this trend would indeed be an inaccuracy caused by the usage of the sPD, it should then be concluded that using such an unconventional propeller domain is not appropriate for ducted propeller's research. In fact, one of the advantages of ducting a propeller is the possibility of increasing its loading at high radial positions (discussed previously in section 2.2.3). In this way, it was considered important to perform CFD computations which lead to an accurate prediction of the forces on the ducted blades, certainly without disregarding high radial locations.

Isolated Xprop, steady, at $J = 0.7$ - different propeller domains

Propeller domain	# of elements	T_c [-]	$\frac{(T_c - T_{c,LPD})}{T_{c,LPD}}$ [%]	Q_c [-]	$\frac{(Q_c - Q_{c,LPD})}{Q_{c,LPD}}$ [%]
Large (Grid 1)	16.18×10^6	1.129590	0	0.378176	0
Small - unconventional	10.49×10^6	1.052670	-6.8096	0.356924	-5.6197

Table 6.4: Thrust and torque coefficients obtained from the Xprop steady simulations with the LPD (grid 1) and with the sPD. It is also shown the relative difference of T_c and Q_c with respect to the value obtained with the LPD´s fine grid, as well as the number of mesh elements used in each simulation.

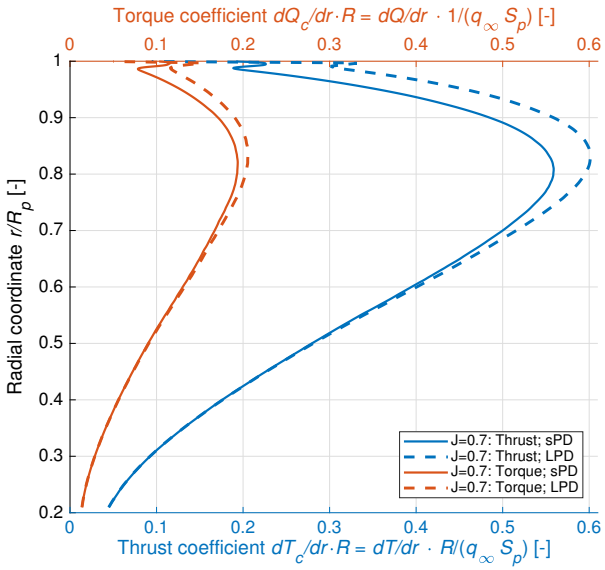

Figure 6.21: Thrust and torque coefficient radial distributions over a blade of the isolated propeller, for the two propeller domains tested (sPD and LPD). The results relative to the large propeller domain were obtained with the fine mesh. Both results were obtained for $J = 0.7$.

In order to understand the cause of the differences in estimated propeller trust and torque coefficients for each domain, the flowfield computed with the sPD was investigated. In Figs. 6.22 and 6.23 it is shown, respectively, the axial velocity and total pressure coefficient contours in the vicinity of the propeller, for a plane at the simulated blade's azimuthal position. Furthermore, the lines of constant vorticity coefficient, $C_{\omega_t} = 0.5$ and $C_{\omega_t} = 1$, are also shown. These contours can be compared against the previously shown equivalent contours for the LDP (in Figs. 6.1 and 6.3). It is clear that using the small propeller domain leads to strange strange patterns in the V_a/V_0 and C_{p_t}. Moreover, the isolines of constant C_{ω_t} relative to the tip vortices also show unphysical trends. Besides, in Figs. 6.24 and 6.25 it is shown the V_a/V_0 contours at $x/c = 0.2$ (downstream of the blades), obtained from the sPD and LPD simulations. The isolines of $C_{\omega_t} = 0.5$ and $C_{\omega_t} = 1$ are also shown for Figs. 6.24 and 6.25. These Figures show that, for the simulation with the sPD, there are clear discontinuities in the V_a contours at the interface between the propeller domain and the outer domain. The discontinuities in the C_{ω_t} isolines are also clear in Fig. 6.24.

In this way, it was understood that the steady simulation of the Xprop with the sPD leads to unphysical flowfield characteristics around the propeller, and to incorrect loading distributions over the propeller at high radial positions, which led to inaccurate predictions of thrust and torque at $J = 0.7$. It was understood that having an outer domain too close to the propeller blade tip leads to unphysical results, when using the multiple reference frame (MRF) approach. This is due to the fact that, with the MRF approach used, the flow in the propeller domain rotates with an angular velocity equal to the propeller's Ω, but with the opposite sign. The propeller and the flow in the outer domain do not rotate, with the approach taken. In this way, the blade tip vortices and the flow which enters the propeller small domain from the outer domain rapidly change their

rotational velocity. This can lead to discontinuities, when flow is "dragged" towards a different azimuthal location whereas its previously adjacent flow with the same characteristics (e.g. same V_a) continues at the same azimuthal position.

Summarizing, it was concluded that this unconventional propeller domain, the sPD, is not appropriate to perform steady simulations of a propeller with the multiple reference frame approach. Steady simulations with the sPD were still used, however, to initialise the flowfield before performing unsteady simulations with the same domain. In the next section, the results from the isolated Xprop unsteady simulation with the sPD are verified and discussed.

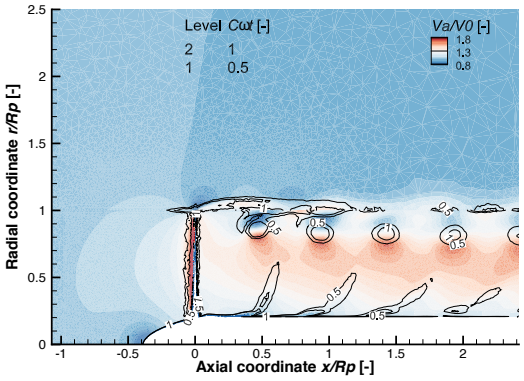

Figure 6.22: Axial velocity, V_a, distribution, normalised with the free-stream velocity, V_0, in the vicinity of the isolated propeller. The lines of constant vorticity coefficient, for $C_{\omega_t} = 0.5$ and $C_{\omega_t} = 1$, are also shown. The contour is located at the azimuthal position of the blade, $\theta = 45°$. Results obtained using the radially small propeller domain.

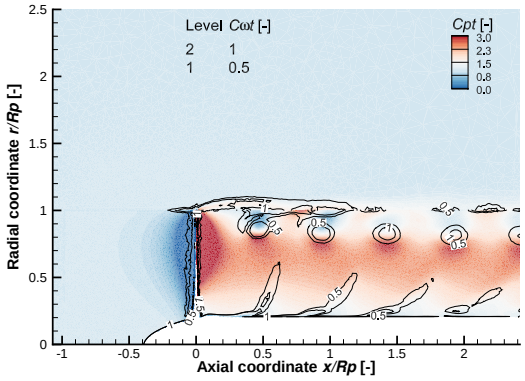

Figure 6.23: Total pressure coefficient, C_{p_t}, distribution in the vicinity of the isolated propeller. The lines of constant vorticity coefficient, for $C_{\omega_t} = 0.5$ and $C_{\omega_t} = 1$, are also shown. The contour is located at the azimuthal position of the blade, $\theta = 45°$. Results obtained using the radially small propeller domain.

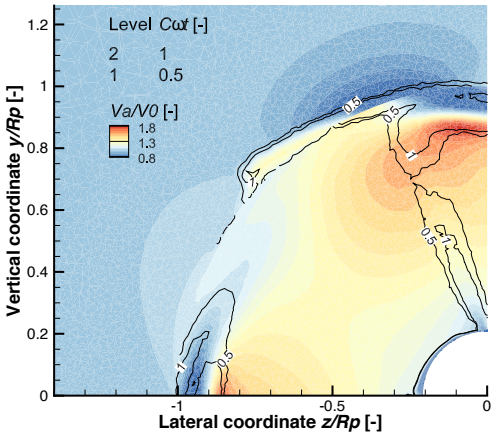

Figure 6.24: Axial velocity, V_a, distribution, normalised with the free-stream velocity, V_0, in the vicinity of the isolated propeller. The lines of constant vorticity coefficient, for $C_{\omega_t} = 0.5$ and $C_{\omega_t} = 1$, are also shown. The contour is located 20% duct cord ($0.2c_{duct} = 0.214R_p$) downstream of the blades. Results obtained using the radially small propeller domain.

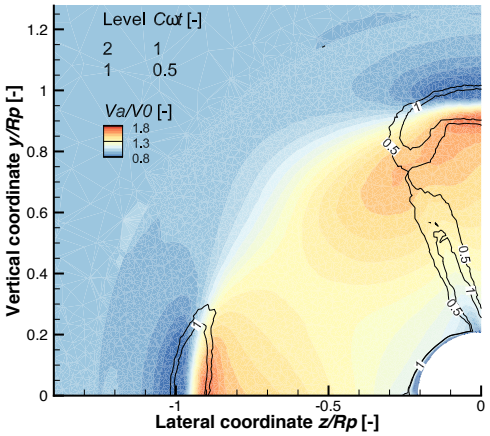

Figure 6.25: Axial velocity, V_a, distribution, normalised with the free-stream velocity, V_0, in the vicinity of the isolated propeller. The lines of constant vorticity coefficient, for $C_{\omega_t} = 0.5$ and $C_{\omega_t} = 1$, are also shown. The contour is located 20% duct cord ($0.2c_{duct} = 0.214R_p$) downstream of the blades. Results obtained using the fine mesh, for the conventional propeller domain.

6.2.2. UNSTEADY SIMULATION

After having discussed the problems associated with the steady simulation of a propeller with a too small propeller domain (radially), it is important to understand if the unsteady simulation of the Xprop, with the same sPD, leads to more reliable results. In this way, the unsteady results obtained with the sPD are first compared with the unsteady results obtained with the LPD. In Figure 6.26, it is shown the normalised radial distributions of thrust and torque along a propeller blade. The distributions are shown for the unsteady simulation with the LPD (time average), for the steady simulation with the sPD and for the unsteady simulation with the sPD (both time accurate and average results). Firstly, it is clear that the unsteady results obtained with the LPD are different from the distributions obtained in the steady case, for high radial positions. This was expected, since high radial locations are the locations where the steady distributions from the sPD were found to be inaccurate (as discussed in the previous section). Moreover, it is also possible to understand, from Fig. 6.26, that the average distribution calculated from the unsteady results with the sPD matches with the equivalent result from the LPD. This also indicates that the unsteady simulation of the Xprop with the sPD and with a sliding mesh approach can lead to accurate results. Analysing the spread of the time accurate results shown in Fig. 6.26, for the unsteady simulation with the sPD, it can be understood that the radial distribution of loading sees very small variations, for the recorded time steps. This is in agreement with what had been found previously for the unsteady simulation of the Xprop with the LPD.

Besides comparing radial distributions of thrust and torque, it was also found relevant to compare the time-accurate total values of thrust and torque coefficients on the Xprop, for the two different domains. Thus, it is shown in Fig. 6.27 the temporal evolution of T_{c_p}, T_c and Q_c for the 36 recorded time steps, with each domain. The 36 recorded time steps have intervals of 5° of propeller rotation between each other. Therefore, these time steps correspond to a 180° rotation of the Xprop. It had already been discussed in section 6.1.3 that the unsteady results obtained with the large propeller domain match well with the equivalent steady results, despite of small oscillations of T_c and Q_c throughout the propeller rotation. Looking at Fig. 6.27, it can be understood that similar oscillations are found for the sPD. However, the plotted coefficients seem to oscillate less in this simulation for the initial time steps recorded, with the blade's azimuthal position $50° < \theta_{<blade} < 100°$. It is also relevant to mention that the calculated thrust and torque coefficients are very close for the two simulations, considering the 36 recorded time steps. This is a specially interesting result considering that the two simulations where initialised with steady calculations, which means that their initial flowfields were very different, as discussed in the previous section. Therefore, the results indicate not only that the sPD is adequate to perform unsteady simulations, but also performing a steady simulation with the sPD can be useful to initialise the flowfield for a corresponding unsteady simulation. Based on these findings, it was decided to use the sPD on the ducted installed simulations, using a steady MRF approach to initialise the flowfield before the unsteady calculation. The results obtained from the simulation of the installed configurations are presented and discussed in the next chapter.

As a final comparison of the simulations performed for the isolated Xprop at $J = 0.7$, it is shown in Figs. 6.28a and 6.28b their estimated T_c and Q_c, respectively. The values are shown in terms of relative difference to the value calculated with the Xprop steady simulation with the LPD's large grid. It is also shown a fit to the values obtained with the three grids used in the LPD's grid convergence study. This is the fit with p equal to the theoretical order of convergence of the method (3). As it was discussed in section 6.1.1, this fit provides an indication of the possible convergence of each quantity for more refined grids. Besides showing the steady results calculated with the LPD, Figs. 6.28a and 6.28b also show the unsteady values of T_c and Q_c obtained with both the small and the large propeller domains. It should be mentioned that the grid refinement ratio h_i/h_1 was also calculated for the sPD's mesh, and used in the two plots, even though this grid is not geometrically similar to the three grids generated for the large propeller domain. From the figures, it can be understood that the results of the unsteady simulation with the sPD appear to be slightly further away from the grid convergence study results than the unsteady estimations with the LPD. Still, this difference is very short, and the reliability of the unsteady results obtained with the sPD is also sustained by Figures 6.28a and 6.28b.

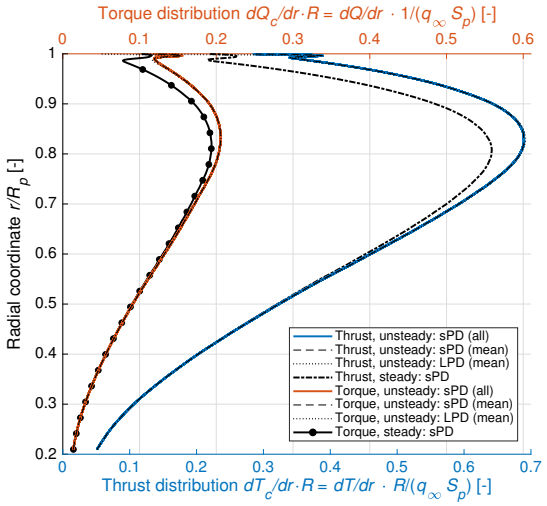

Figure 6.26: Thrust and torque coefficient radial distributions over a blade of the isolated propeller, for the two different propeller domains tested. It is shown the mean of the unsteady results obtained with the conventional propeller domain (LPD, fine grid), the steady results from the sPD, the time accurate unsteady results obtained from the sPD and the mean of the sPD unsteady results.

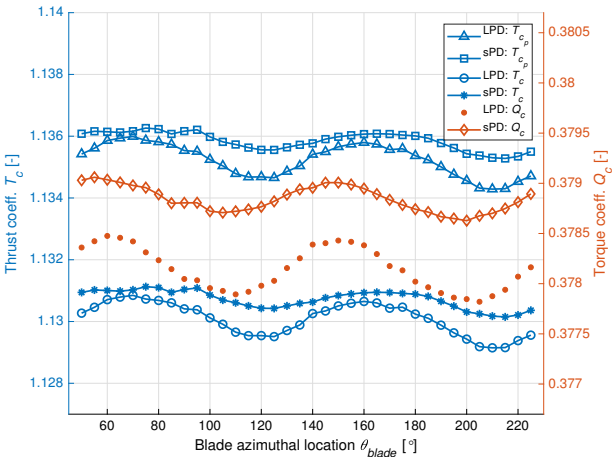

Figure 6.27: Comparison of time accurate thrust pressure coefficient T_{c_p}, thrust coefficient, T_c, and torque coefficient, Q_c, over the isolated propeller, for the unsteady simulations with the two different propeller domains tested, LPD (with the fine grid) and sPD. Simulations performed for $J = 0.7$.

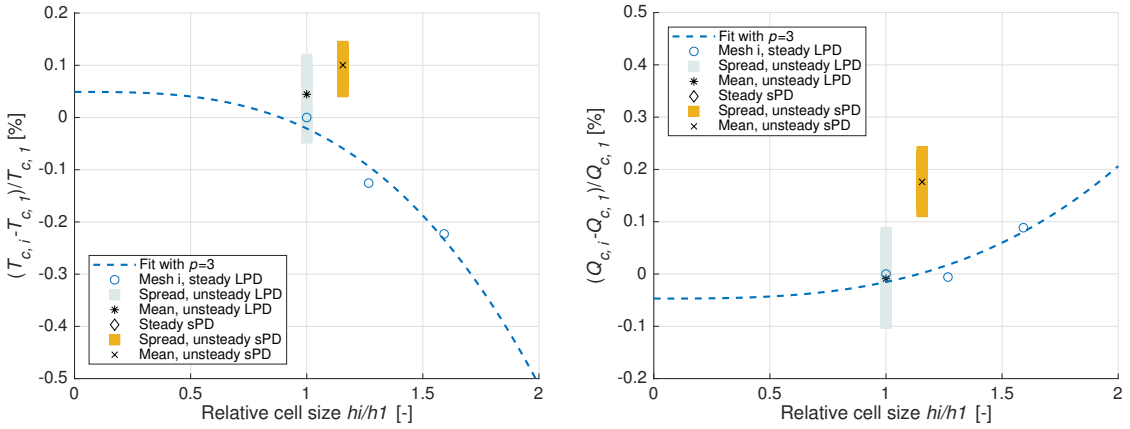

(a) Thrust coefficient

(b) Torque coefficient

Figure 6.28: Comparison of the thrust coefficient (left-image) and torque coefficient (right-image) estimated at $J = 0.7$ from several isolated propeller CFD simulations. From the LPD, it is shown the steady results obtained with the three grids, as well as the unsteady result obtained with the fine grid. From the small propeller domain, it is shown the unsteady results. For each result, it is shown the relative difference to the coefficient calculated with the LPD's fine grid.

7

INSTALLED DUCTED SYSTEMS PERFORMANCE

In the previous chapters, the CFD simulations of the isolated components were discussed. The verification and validation of the simulations was addressed, and it were understood the main characteristics of the flowfield generated by each component. From the isolated ducts simulation, it should be highlighted that there is a higher axial velocity inside the circular duct, than inside the square (or quadrangular) duct, at the propeller disk location inside the shrouds (at 30% duct chord). This was predicted to result in a negative effect in the propeller's performance, since propellers can operate at a higher thrust to power ratio when the flow's axial velocity is lower. Besides, it was also found that the flow's axial velocity profile varies for different azimuthal positions inside the square duct. This was expected to lead to loading variations at the propeller blades. Moreover, it was also found that the boundary layer at the corner of the square duct grows considerably larger than the turbulent boundary layer over a flat plate of the same length (at the same Reynolds number). This result matches with the literature discussed in section 2.2.5, regarding corner flow. As it was discussed, the thicker BL at the duct's corner is more prone to separation. Separation can result in a performance decrease of the propulsion system, contributing to an increase in drag at the duct's corner. In fact, it was found that separation occurs at the corner of the square duct in the isolated case.

From the isolated propeller simulations, it should be highlighted that using a radially small propeller domain (sPD), which fits inside the ducts, leads to an unphysical solution when a steady simulation is performed. Still, the unsteady Xprop simulation with the sPD led to accurate results, when compared against the equivalent results obtained with the radially larger propeller domain. In this way, it was concluded that the sPD could be used in the ducted Xprop simulations only with the aim of calculating unsteady solutions, with the sliding mesh approach. From the results shown in the previous chapter, it is also relevant to highlight that the variation of radial loading distribution at the Xprop is very low for during the range of timesteps recorded, at $J = 0.7$. This indicates that severe separation does not occur on the blades at this operating condition, and that any strong oscillations in blade loading found in the unsteady ducted simulations can be attributed to the interaction between the propeller and the duct.

After the flowfields calculated for the isolated components were well understood, verified and validated, it was possible to proceed to the analyse of the flowfields of the installed configurations. Firstly, this chapter discusses the results obtained from the simulation of both ducts with an actuator disk and with the propeller's nacelle (section 7.1). Afterwards, in section 7.2, it is proceeded for the analyse of the flowfields generated by the complete installed systems, the circular ducted Xprop (Cduct system) and the square ducted Xprop (Qduct system). In this way, it was possible to evaluate the performance of each propulsive system.

7.1. DUCTS WITH NACELLE AND AD

In this section, it is studied the effect of installing each duct on its performance. Firstly, the aerodynamic performance of the two ducts with the propeller's nacelle, in a power-off condition, is compared against the

performance of each duct in the isolated case, in sub-section 7.1.1. Afterwards, it is studied the effect of turning on the actuator disk inside the duct with nacelle system, in sub-section 7.1.2. The AD was tested with inputs from the isolated propeller steady simulations, at three different advance ratios: $J = 0.9$, $J = 0.8$ and $J = 0.7$. When analysing the results shown in section 7.1.2, it is important to keep in mind that only the performance of the duct is being investigated, since the performance of the AD is set by the thrust and torque inputs obtained from isolated propeller calculations. The power considered when calculating the overall efficiency of the AD propulsion systems is also the shaft power calculated from the isolated Xprop simulations, with equation 2.4.

7.1.1. POWER-OFF

As it was referred, it is first analysed the power-off performance of the ducts installed with the propeller nacelle, in comparison with the aerodynamic performance of the isolated ducts. In this way, it were compared the chordwise pressure and skin friction distributions, the axial velocity inside the ducts (at the propeller location) and the drag forces integrated over the duct surfaces.

PRESSURE AND SKIN FRICTION AT THE DUCTS

In Figures 7.1 and 7.2, it is shown the chordwise C_p distributions on the isolated and installed power-off configurations, for the circular and square ducts, respectively. In Figs. 7.3 and 7.4, equivalent chordwise distributions are shown for the axial skin friction coefficient. On each of the four Figures, the chordwise distributions are shown at two spanwise locations: $\theta = 30°$ and $\theta = 60°$ for the circular duct (which correspond to $\phi_{cduct} = 1/3$ and $\phi_{cduct} = 2/3$), and $\phi_{qduct} = 0$ and $\phi_{qduct} = 0.5$ for the square duct plots.

Analysing Fig. 7.1, it can be understood that for both the circular duct isolated and installed cases there is a low variation of C_p distributions for different spanwise locations. This had already been noticed for the isolated circular duct simulation, when Fig. 5.20 was analysed. In Fig. 7.1, it is also interesting to notice that the low pressure peaks on the duct change when the duct is installed. On the inner surface, the pressure peak moves downstream and decreases, whereas on the outer surface the opposite occurs: the pressure peak moves towards the leading edge and increases. This indicates that the stagnation point at the leading edge moves towards the lower surface, due to the blockage caused by the Xprop's nacelle. An equivalent trend is found for the suction peak at the square duct surfaces, for both spanwise positions analysed in Fig. 7.2.

From Fig. 7.3, it is difficult to spot major differences between the C_{f_x} distributions of the circular duct's isolated and installed cases. The differences between the several lines plotted for each duct surface appear to be of the order of the noise deviations on the distributions due to numerical error. In Fig. 7.4, relative to the square duct, it can also be seen that the noise in the C_{f_x} distributions is large. The numerical noise is specially large at the corner of the square duct, where an unstructured mesh had to be used. Still, Fig. 7.4 indicates that at $\phi_{qduct} = 0.5$, at the trailing edge, separation on the inner surface of the duct is slightly less severe for the installed case. Still, it was expected an overall larger pressure drag for both ducts in the installed case, due to the blockage effect caused by the nacelle. The blockage effect makes the recovery of static pressure at the trailing edge of the ducts more difficult, increasing the difference in static pressure between the leading edge and the trailing edge of the duct.

FLOW AT THE PROPELLER AXIAL LOCATION

From the power-off duct simulations, it is also relevant to analyse how the axial velocity at the propeller location changes with the addition of the nacelle. This is due to the fact that the axial velocity at the propeller disk has a strong influence in the propeller performance. In Fig. 7.5, it is shown the average V_a/V_0 profile inside each duct on the isolated and power-off installed configurations, at $x/c = 0.3$. The two curves relative to the installed configurations start at $r/R_p \approx 0.2$, since this is the radius of the spinner at $x/c = 0.3$. V_a/V_0 does not go to 0 at this location, since the entire nacelle was modelled as a free-slip surface for the installed configurations without the full propeller blade model (simulations with an AD or power-off). In Fig. 7.5, it is interesting to notice that there is an increase in axial velocity at low radial positions (approximately for $0.2 < r/R_p < 0.6$) due to the installation of the nacelle, in both ducts. This is due to the fact that the presence of the nacelle forces a contraction of the flow. However, for high radial positions the axial velocity is higher

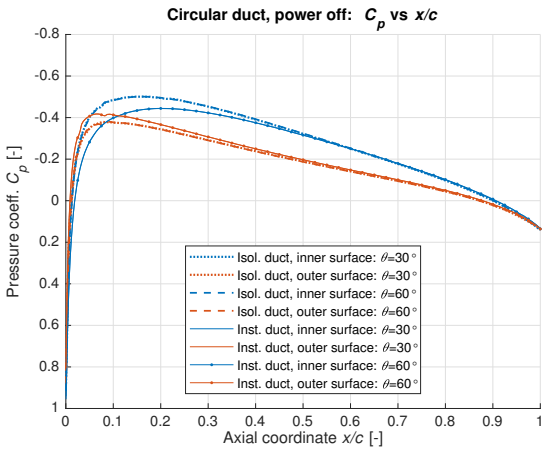

Figure 7.1: Pressure coefficient distribution at two sections of the circular duct: $\theta = 30°$ and $\theta = 60°$. The result obtained from the isolated simulation (medium refinement grid) is compared against the (power-off) installed case, including the duct and the propeller's nacelle.

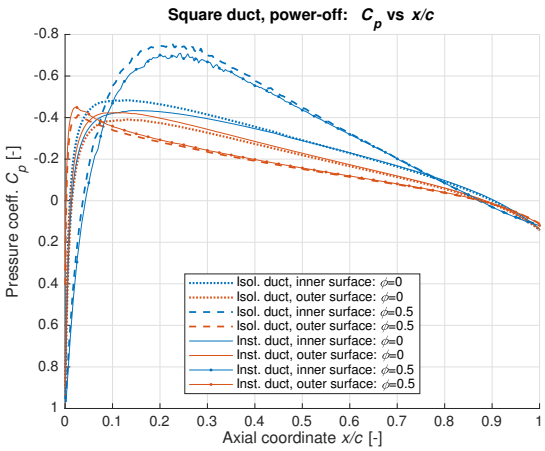

Figure 7.2: Pressure coefficient distribution at two sections of the square duct: $\phi = 0$ and $\phi = 0$. The result obtained from the isolated simulation (medium refinement grid) is compared against the (power-off) installed case, including the duct and the propeller's nacelle.

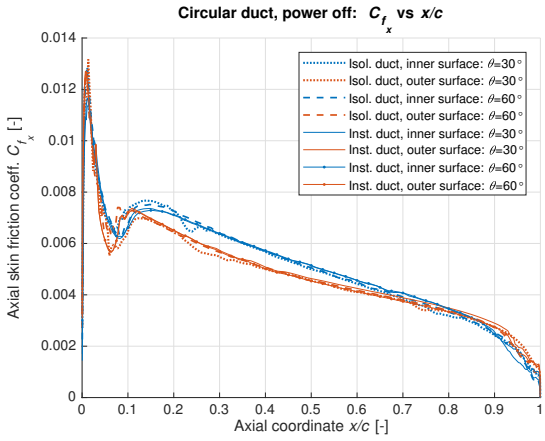

Figure 7.3: Axial skin friction coefficient distribution at two sections of the circular duct: $\theta = 30°$ and $\theta = 60°$. The result obtained from the isolated simulation (medium refinement grid) is compared against the (power-off) installed case, including the duct and the propeller's nacelle.

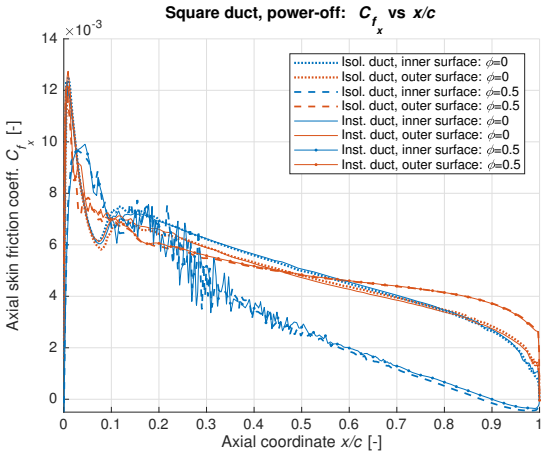

Figure 7.4: Axial skin friction coefficient distribution at two sections of the square duct: $\theta = 30°$ and $\theta = 60°$. The result obtained from the isolated simulation (medium refinement grid) is compared against the (power-off) installed case, including the duct and the propeller's nacelle.

in the isolated case, for both ducts. This observation is consistent with the lower low pressure peaks in the installed C_p distributions at the inner surface of each duct, which were identified in Figs. 7.1 and 7.2. It is also important to note that, for the installed case, the V_a inside the circular duct is also larger than the V_a in the installed square duct. Moreover, this difference in V_a increases for higher radius, indicating that the Xprop should be able to produce more thrust inside the square duct than inside the circular duct, specially at high radius. However, inside the square duct the blade tip clearance is larger than inside the circular duct for most blade azimuthal locations. This could have the opposite affect, decreasing blade loading at high radius for the square ducted system. In this way, it can again be defended that full blade model simulations are required to fully understand the aerodynamic interaction differences between the two ducted systems.

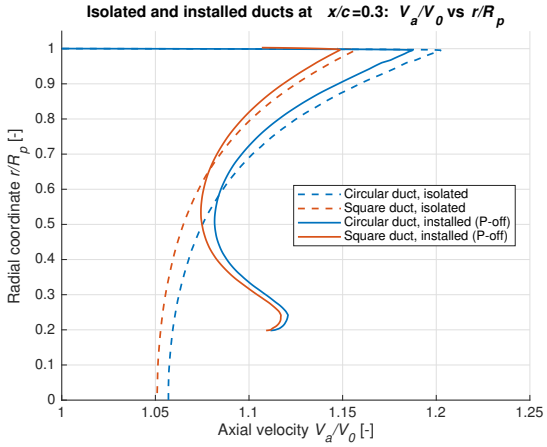

Figure 7.5: Average axial velocity profile, normalised with the free-stream velocity, inside both circular and square ducts, at the propeller or AD location: $x/c = 0.3$. The results are shown for both the isolated cases (medium refinement grid) and the power-off installed configurations, which include a duct and the propeller's nacelle.

FORCES ON THE DUCTS

So far, it has been understood that there are aerodynamic differences in the flowfields generated by the two ducts, between the isolated and installed cases. It is also relevant to understand how these differences influence the drag of the ducts, in the power-off configurations. In Figs. 7.6 and 7.7 it is shown the friction and pressure drag coefficient of the ducts obtained from the different power-off cases: isolated circular duct (2D simulation), isolated circular duct (3D simulation), isolated square duct, installed circular duct (3D) and installed square duct. The values obtained from the 2D circular duct simulation were included for verification purposes, since it simulates the same case as the 3D isolated circular duct simulation. For each of the isolated cases, it is shown the values calculated with the meshes with a medium refinement, which are the grids more similar to the grids used in the installed configurations. In Fig. 7.6, the drag coefficients were calculated using the propeller disk area as the reference area, according to equation 5.4. On the other hand, in Fig. 7.6 each ducts' reference area (S_{duct} as defined in equation 5.6) was used to calculate the drag coefficients, according to equation 5.5. In this way, Fig. 7.6 provides a good comparison of the total drag forces on the different cases, and Fig. 7.6 helps understanding which cases result in more drag per unit span, i.e. in the second drag coefficient definition, C'_D, it is corrected for the fact that the area of the square duct is larger than the area of the circular duct, due to its larger span (or perimeter).

From Fig. 7.6, it can be firstly understood that the C_D estimated for the isolated circular duct from the 2D and 3D simulations match well. Still, it can be noticed a slightly higher pressure drag from the 3D calculation. From the isolated cases, it can also be concluded that the square duct produces more friction and pressure drag than the isolated circular duct. This was expected, due to the larger size of the square duct. When installing each duct, it can be understood that the friction drag of each duct stays at the same level. However, the pressure drag increases for both cases due to the presence of the nacelle. As it was previously referred, the nacelle causes a blockage effect which makes it more difficult for the static pressure to recover towards the trailing edge of each duct. Thus, the blockage effect leads to a higher difference in static pressure between the leading edge and the trailing edge of the duct, this way increasing the ducts drag.

Analysing Fig. 7.7, it can be understood that both C'_{D_f} and C'_{D_p} are similar for the isolated circular and square ducts. Nevertheless, it can be seen that the square duct results in a higher C'_{D_p}. This can be explained based on the separated region which was found at the inner surface of the square duct's corner (see Fig. 7.4). Figure 7.7 also shows that the pressure drag coefficient of the circular duct increases more, per unit span, due to the installation of the nacelle than the square duct. This is due to the fact that the cross-sectional area inside the circular duct is smaller than the equivalent area inside the square duct. In this way, the nacelle occupies a larger percentage of this area inside the circular duct, resulting in a stronger blockage.

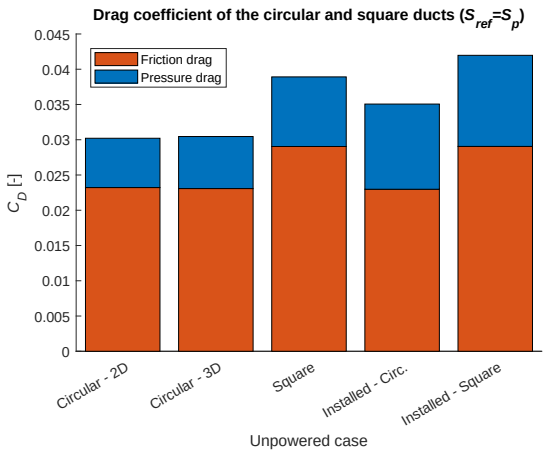

Figure 7.6: Comparison of the drag coefficients calculated for the different duct power-off cases. The drag coefficient (definition 1) was defined using the propeller's disk area as reference.

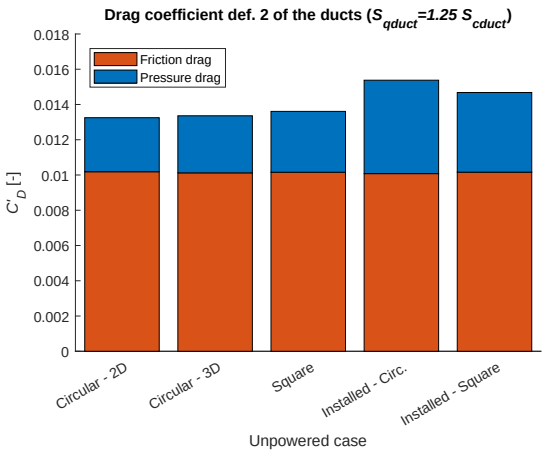

Figure 7.7: Comparison of the drag coefficients calculated for the different duct power-off cases. The drag coefficient (definition 2) was defined using each ducts' area (perimeter at the leading edge × chord) as reference.

7.1.2. POWER-ON (AD)

After having analysed the aerodynamic performance of the circular and square ducts in the power-off installed configurations, it is possible to proceed for the investigation of the performance of the ducted propulsion systems with an AD. Firstly, it is important to characterize the flowfields generated by the ducted systems. Secondly, it is relevant to understand how turning on the AD influences the pressure and skin friction chordwise distributions at the duct surfaces. It is also important to understand how the axial velocity varies at the propeller disk location, for the two ducts and at the different advance ratios tested. Moreover, the spanwise distributions of forces at the ducts are also analysed, for the different J. Finally, it is made a comparison between the performance of the ducted propulsion systems with an AD and the performance of the isolated propeller.

FLOWFIELD CHARACTERISATION

From the literature relative to corner flow discussed in section 2.2.5, it was found that the corner between two flat plates can generate a swirling flow. However, closed vortical patterns are not expected to be created in such case, according to the calculations presented in [44]. In this sub-section, in order to characterise the power-on flowfields, it is also investigated whether the installation of the AD in the square duct results in the generation of vortices. In this way, it is shown in Fig. 7.8 the isosurfaces of constant axial vorticity or axial vorticity coefficient, C_{ω_x}, obtained from four simulations. On the top-left image, it is shown the isosurfaces of constant axial vorticity $\omega_x = -257.7$ and $\omega_x = 257.7$, for the square duct installed configuration in the power-off case. Since it is a power-off case, it is not possible to show C_{ω_x} isosurfaces. The vorticity coefficient, as defined in equation 6.1, requires an assumed propeller angular velocity to be calculated. On the top-right and bottom images, it is seen the isosurfaces of constant vorticity coefficient $C_{\omega_x} = -0.25$ and $C_{\omega_x} = 0.25$. The top-right image refers to the circular ducted AD simulation at $J = 0.7$, and the bottom-left and bottom-right images refer to the square ducted AD computations at $J = 0.9$ and $J = 0.7$, respectively. At $J = 0.9$, when $\Omega_{prop} = 515.4$ rad/s, $C_{\omega_x} = 0.25 \Leftrightarrow \omega_x = 257.7$.

The top images of Fig. 7.8 indicate that, in these installed cases, there are no strong vortices being generated. On the other hand, from the bottom images it is clear that two counter rotating vortices form at the corner of the square duct in the AD simulations. These symmetric vortices are formed due to the static pressure jump that occurs at the AD location. The pressure jump causes a static pressure gradient between the spanwise locations of the duct far away from the corners ($\phi_{qduct} = 0$ and $\phi_{qduct} = 1$, in the image) and the flow's static pressure at the corner ($\phi_{qduct} = 0.5$). In this way, these vortices were expected to have a strong influence in the performance of the system. Firstly, the vortices were expected to influence the C_p and C_{f_x} distributions on the duct surfaces. In strong association with the impact on the C_p distributions around the duct, the corner vortices were also expected to contribute towards an increase in the induced drag of the system. In this way, the corner vortices were expected to influence the spanwise distribution of forces on the

square duct as well. These matters are further discussed in the following sub-sections.

Besides the two corner vortices, it can also be noticed a weaker vortex in the two bottom images of Fig. 7.8, inside the square duct and near the spanwise location $\phi_{qduct} = 1$ (bottom right of each image). An equivalent vortex does not occur in the "symmetric" spanwise location (at $\phi_{qduct} = 0$). Thus, it can be concluded that this vortex is generated due to the rotation of the flow inside the duct, which is caused by the AD. It should be stated that the AD is simulating a propeller which rotates with a negative angular velocity in the axial direction: $\vec{\Omega}_{prop,J=0.7} = -662.59\vec{e}_x$. Thus, seen from downstream, as in Fig. 7.8, the propeller rotates in the clockwise direction. Nevertheless, Fig. 7.8 indicates that the counter rotating vortex pair at the corner of the duct is considerably stronger than the vortex seen near $\phi_{qduct} = 1$, and should have a larger influence in the performance of the system.

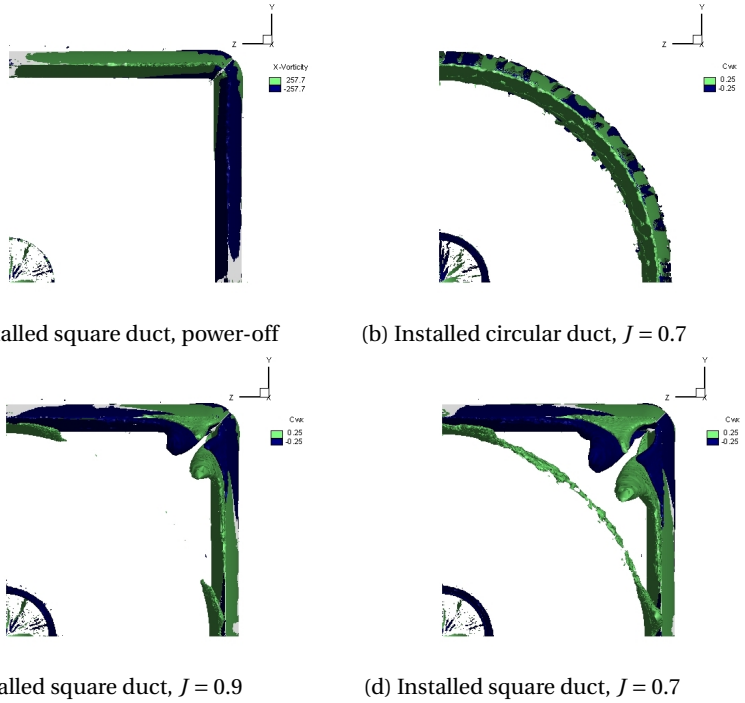

(a) Installed square duct, power-off

(b) Installed circular duct, $J = 0.7$

(c) Installed square duct, $J = 0.9$

(d) Installed square duct, $J = 0.7$

Figure 7.8: Axial vorticity isosurfaces from several installed configurations, with a duct, the Xprop's nacelle and the AD. In the four images, the isosurfaces are seen from downstream. The top-left image shows the result from the installed square duct simulation in the power-off case. It is shown the isosurfaces of constant axial vorticity: $\omega_x = -257.7$ and $\omega_x = 257.7$. The top-right image shows the result from the installed circular duct simulation with the AD operating at $J = 0.7$. The bottom left and right images show the results from the installed square duct simulations with the AD operating at $J = 0.9$ and $J = 0.7$, respectively. The top right and bottom images show isosurfaces of constant axial vorticity coefficient: $C_{\omega_x} = -0.25$ and $C_{\omega_x} = 0.25$.

In order to gain a better understanding of how the corner vortices are generated, the flow velocities at the corner of the square duct were evaluated. Figure 7.9 shows the contours of axial velocity at the duct's corner y and z location at four axial planes: $x/c = 0.3$, $x/c = 0.5$, $x/c = 1$ and $x/c = 1.5$. The Figure also shows vectors indicative of the flow velocity in each plane of study. Figures 7.9a, 7.9b and 7.9c show that there is an axial reversed flow region at the duct's corner, which is indicative of separation. This indicates a drawback of square ducted propellers, since separation can adversely affect performance by contributing towards pressure drag. The velocity vectors of Figs. 7.9a and 7.9b show that the flow is moving from the corner towards the centre of the duct. This phenomenon can be associated with the slipstream contraction caused by the AD. Due to mass flow conservation, this phenomenon is only possible due to the reverse flow at the corner. Indeed, Fig. 7.9a suggests that there is a source at the corner, which would be difficult to explain without considering separation and the corner's recirculating flow. Figure 7.9c indicates that the spanwise movement of the flow along the duct's surface towards the corner indeed occurs at the trailing edge, due to the spanwise pressure

gradient, which is favourable if the flow is moving towards the corner. The velocity vectors in Fig. 7.9c also suggest that the vortices are already present, or forming, in this axial location. Half duct chord downstream of the duct, the corner vortices are more clearly noticeable, as shown in Figure 7.9d.

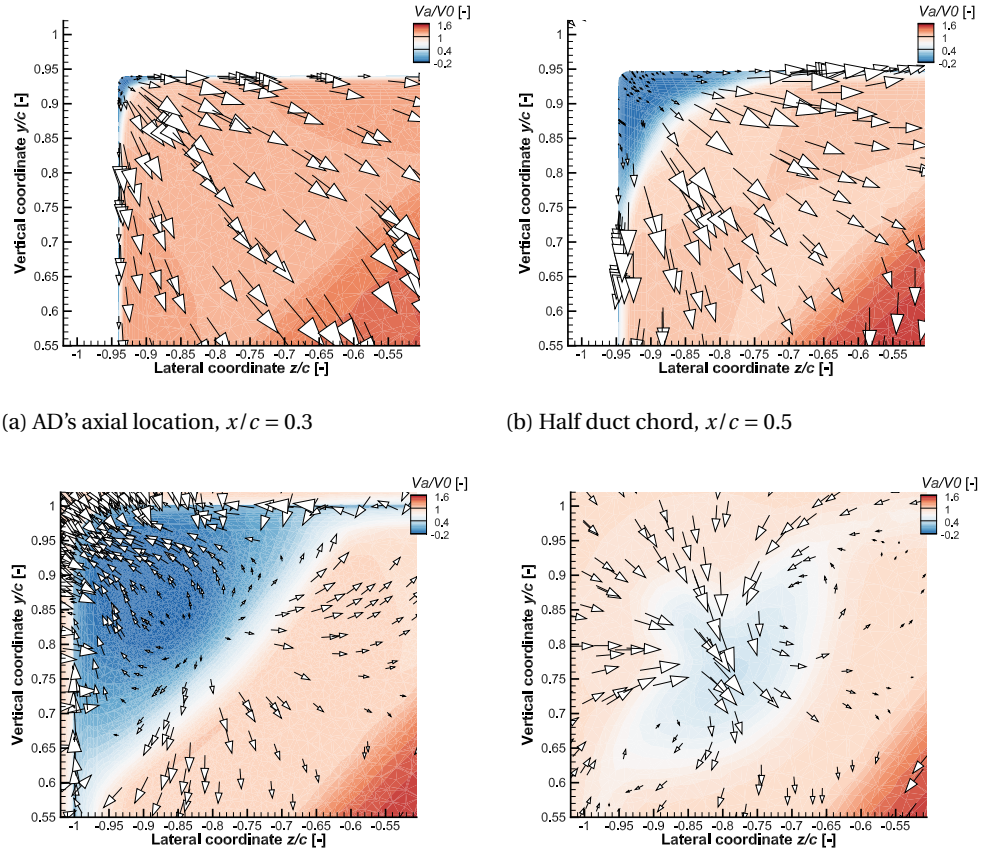

(a) AD's axial location, $x/c = 0.3$

(b) Half duct chord, $x/c = 0.5$

(c) Duct's trailing edge, $x/c = 1$

(d) Downstream of the duct, $x/c = 1.5$

Figure 7.9: Axial velocity contours and transversal velocity vectors at the corner of the square duct, at four axial planes: $x/c = 0.3$ (top-left), $x/c = 0.5$ (top-right), $x/c = 1$ (bottom-left) and $x/c = 1.5$ (bottom-right). The length of the vectors shown, λ, was calculated from $\lambda/c = 0.3\sqrt{V_y^2 + V_z^2}/V_0$.

In order to access if the adverse effects caused by separation are indeed affecting the square duct's flowfield, Fig. 7.10 shows the C_{p_t} contours in the viccinity of the duct, at a plane defined by the azimuthal location 7.10. Thus, the Figure includes the increase in total pressure in the AD's slipstream. The phenomenon of slipstream contraction can also be noticed, inside the duct. This contrasts with what would have been expected for a circular duct, for which slipstream contraction is only expected to occur outside the duct, assuming that mass is conserved inside the duct. Figure 7.10 also indicates that there is a large loss of total pressure at the duct's corner, which is associated with losses due to dissipation. Therefore, the large region of low C_{p_t} also suggests that separation occurs at the corner.

Figure 7.11 summarises the understanding of the formation of corner vortices which was obtained from the results presented in this section. The Figure shows a sketch representative of the flowfield at a plane at the duct's trailing edge. The regions of higher static pressure in the slipstream of the propeller are represented, as well as the region of lower C_p at the corner. The region of low total pressure at the corner, due to separation, is also represented. Moreover, the direction of movement of the flow is also represented: in the tangential direction in the AD's slipstream, along the duct's surface due to the pressure gradient and at the corner, representing the vortices.

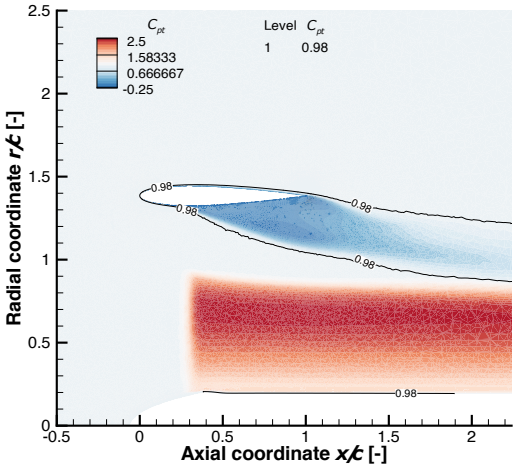

Figure 7.10: Total pressure coefficient, C_{p_t}, distribution in the vicinity of the square duct, installed with the nacelle and with the AD. The lines of constant $C_{p_t} = 0.98$ are highlighted. The contour is located at $\theta = 45°$. Results obtained from the simulation with the AD operating at $J = 0.7$.

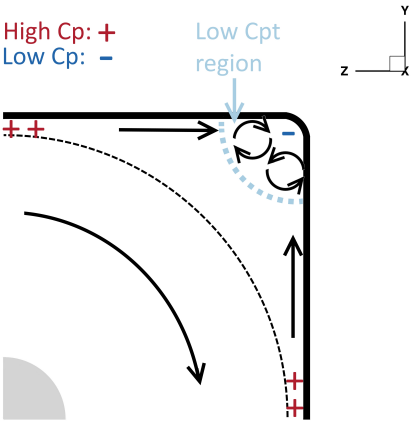

Figure 7.11: Sketch representative of the formation of corner vortices in the powered square duct simulations, at the duct's trailing edge. The black arrows indicate the direction of flow velocity in the plane considered, either due to the slipstream rotation, due to the vortices, or due to the pressure gradient towards the corner.

PRESSURE AND SKIN FRICTION AT THE DUCTS

In Figs. 7.12 and 7.13, it is shown the chordwise C_p distributions at the installed circular and square ducts, respectively. The distributions are shown for the power-off case, and for the case with the AD operating at $J = 0.7$. C_p was evaluated for the circular duct at the spanwise locations $\theta = 30°$ and $\theta = 60°$, and for the square duct at $\phi = 0$ and $\phi = 0.5$. In Figs. 7.14 and 7.15, it is shown equivalent distributions for the axial skin friction coefficient.

In Fig. 7.12, it can be noticed that the C_p distributions match well for different spanwise locations at the circular duct. This occurs due to the fact that the two cases considered in Fig. 7.12 are axisymmetric problems. Indeed, the increase in momentum and energy done by the AD is uniform for all azimuthal positions. Figure 7.12 also shows the strong low pressure peak that occurs at the leading edge of the circular duct, with the AD operating at $J = 0.7$. The C_p chordwise distribution at the circular duct in the power on case resembles the C_p distribution of an airfoil at an angle of attack. This is due to the fact that the slipstream contraction which occurs upstream of the duct indeed causes a change in effective angle of attack of the duct sections.

In Fig. 7.13, the suction peaks at the square ducts inner surface for the power-on condition are also noticeable. However, it is clear that the C_p distributions vary with spanwise position, for the installed square ducts case. At $J = 0.7$, it is also clear that the low pressure suction peak is stronger at $\phi = 0$ than at $\phi = 0.5$. This result is specially interesting considering that, as it had been referred previously, for the power-off case the suction peak is larger at the corner of the square duct. At $J = 0.7$, the suction peak is stronger at $\phi = 0$ than at the corner of the duct because the ducts' corner is further away from the AD. In this way, the effect of slipstream contraction in changing the duct sections' effective angle of attack is less felt at the square duct corner than at $\phi = 0$. Moreover, it is also interesting to notice that the suction peak at the location $\phi = 0$ of the square duct is lower than the suction peak at the circular duct's inner surface, for the same operating condition. There are two reasons which justify the difference. Firstly, it is more difficult to have a localised very high suction peak at the square duct, at $\phi = 0$, since the low pressure peak would be force to spread in the spanwise direction. On the other hand, at the circular duct (shrouding an uniform AD), the low pressure peak occurs at all spanwise locations. Secondly, the cross sectional area inside the square duct is larger than inside the circular duct. This means that the slipstream contraction upstream of the AD is less constrained by the square duct than by the circular duct. In this way, the effective angle of attack of the circular duct sections is higher than the effective α at the square duct's spanwise location $\phi = 0$. Even though the difference is small, it can be noticed from Figs. 7.12 and 7.13 that the axial position of the stagnation point at the circular duct's outer surface is further downstream than the stagnation point of the square duct at $\phi_{=}0$, for the power-on condition.

This difference in stagnation point location also indicates that the circular duct section experiences a higher effective α. Moreover, from 7.13 it can also be noticed that the static pressure coefficient at the corner of the square duct does not recover to values higher than the free-stream ($C_{p_\infty} = 0$), towards the trailing edge. One of the causes for this trend are vortices which are formed at the corner of the square duct, in the power-on simulations. The vortices are characterized by a lower static pressure at its core (as seen e.g. in Fig. 6.2). In this way, the impingement of the vortices in the duct results in a lower pressure felt at the surface. The lower static pressure at the trailing edge of the square duct corner sections results in a higher drag of the system (or lower thrust production).

In Fig. 7.14, it can be seen that there is also an agreement between the skin friction distributions over the circular duct, for different spanwise locations. The differences found for the C_{f_x} distributions between $\theta = 30°$ and $\theta = 60°$ (for the same operating condition) can be attributed to a numerical error. It had already been noticed in Figs. 5.20 and 5.21 (relative to the circular duct's convergence study) that the numerical discretization error is more noticeable on the C_{f_x} chordwise distributions than on the C_p distributions. Despite of the influence of the numerical error, it can be understood from Fig. 7.14 that the transition location moves upstream at the inner surface of the duct, for the power-on condition. Besides, it can also be understood that there is a strong decrease in skin friction at the AD location ($x/c = 0.3$). This is due to the fact that the static pressure jump at the AD causes vorticity in the positive tangential direction at high radial locations (at $r/R_p \approx 1$). The flow at $r/R_p \approx 1$ is "pushed" from the higher static pressure region towards the low pressure region. This phenomenon indicates that a higher static pressure jump could cause local separation of the duct's boundary layer, since it could cause the flow to have a negative axial velocity at the vicinity of the duct's surface.

In Fig. 7.15, it can be noticed that there is also a sudden decrease of skin friction at the AD location (at $J = 0.7$), at the square duct's spanwise location $\phi = 0$. This matches with what was identified in the circular duct relative to the corresponding power-on configuration. At the corner location ($\phi = 0.5$), it can be understood that strong separation occurs for the powered case, at the inner surface. Indeed, it can be seen that C_{f_x} turns negative around $x/c = 0.2$, at this spanwise location. It had already been noticed from the unpowered simulations that the square duct's corner BL was prone to separation, due to the BL's high thickness. However, separation appears to be considerably more severe at $J = 0.7$ than at the power-off case, when separation only occurs very close to the trailing edge (as shown in Fig. 7.15). Boundary layer separation is also expected to influence the performance of the system, resulting in an increase in pressure drag of the duct.

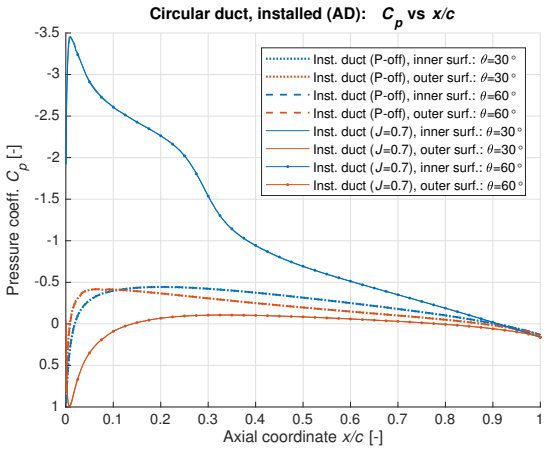

Figure 7.12: Pressure coefficient distribution at two sections of the circular duct: $\theta = 30°$ and $\theta = 60°$. The result obtained from the (power-off) installed case is compared against the result obtained for the power-on AD case, at $J = 0.7$.

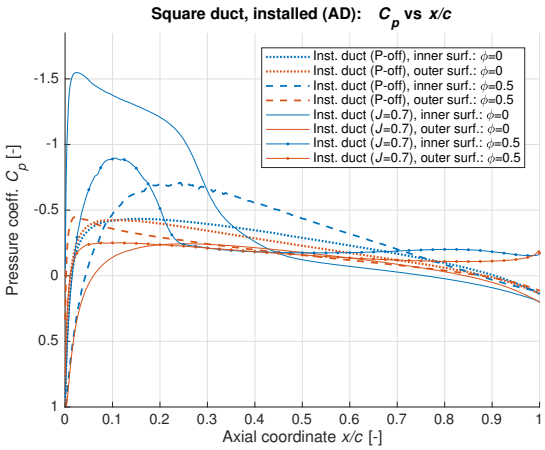

Figure 7.13: Pressure coefficient distribution at two sections of the square duct: $\phi = 0°$ and $\phi = 0.5°$. The result obtained from the (power-off) installed case is compared against the result obtained for the power-on AD case, at $J = 0.7$.

Besides comparing the C_p and C_{f_x} chordwise distributions of the square duct in the power-on condition versus the unpowered case for specific spanwise locations, it was also found relevant to analyse the C_p and C_{f_x} contours over the entire inner surface of the square duct, for the powered case. In fact, it was found relevant to understand how the corner vortices may influence the pressure over the duct's surface, and also to

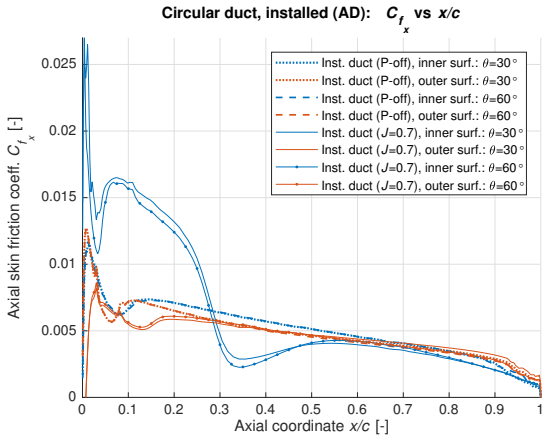

Figure 7.14: Axial skin friction coefficient distribution at two sections of the circular duct: $\theta = 30°$ and $\theta = 60°$. The result obtained from the (power-off) installed case is compared against the result obtained for the power-on AD case, at $J = 0.7$.

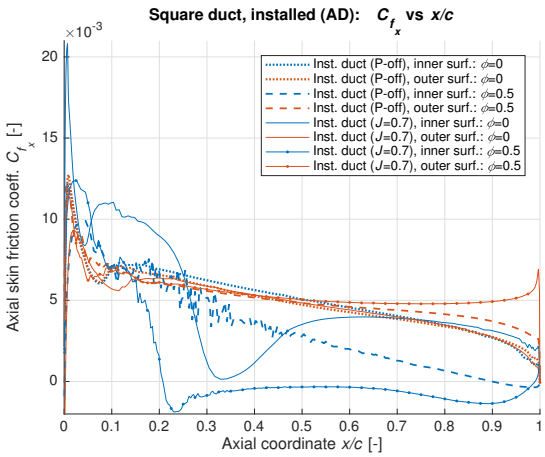

Figure 7.15: Axial skin friction coefficient distribution at two sections of the square duct: $\phi = 0°$ and $\phi = 0.5°$. The result obtained from the (power-off) installed case is compared against the result obtained for the power-on AD case, at $J = 0.7$.

analyse the extent of the reverse flow region at the duct's corner indicated by Fig. 7.15. In this way, Figs. 7.16a and 7.16b show precisely the C_p and C_{f_x} contours over the inner surface of the duct, from the simulation with the AD operating at $J = 0.7$. The contours are seen from a point of view inside the duct. From the C_p contour, it is interesting to clarify that the suction peak near the duct's leading edge indeed lowers gradually from the duct spanwise locations near the AD disk, $\phi_{qduct} = 0$ and $\phi_{qduct} = 1$, towards the corner location. Furthermore, in Fig. 7.16a it can also be noticed that there are two relatively small regions of lower static pressure at the trailing edge, located symmetrically in the spanwise direction with respect to the corner. These two regions of low static pressure can be attributed to the corner vortices, as vortices are characterized by a low static pressure in its core.

In Fig. 7.16b, the C_{f_x} contours shown are constrained between $-0.003 < C_{f_x} < 0.003$, even though the axial skin friction coefficient at the duct's inner surface reaches values considerably higher, as shown e.g. in Fig. 7.15. This constraint was set so that the region of reversed flow at the duct's surface could be more easily identified. In fact, from Fig. 7.16b it can be understood that the region of reversed axial flow at the duct's surface is relatively large, covering a considerable spanwise portion at near the trailing edge. Moreover, it is also interesting to notice that the flow separates in the axial direction firstly at the corner location, slightly upstream of the AD. However, from the C_{f_x} contour alone it can not be concluded if BL separation actually occurs, since the flow may still be moving in the spanwise direction when $C_{f_x} = 0$.

In order to gain a more complete understanding of the movement of the flow along the square duct's surface, Fig. 7.16c shows the tangential skin friction contours at the duct. Moreover, oil flow visualisation lines are also shown at the duct's surface, in Fig. 7.16c. Since the velocity at the duct's (no-slip) surface is 0, the oil flow lines are calculated by the solver considering the skin friction direction at the wall. Figure 7.16c is in agreement with the results discussed previously, e.g. shown in Fig. 7.9), regarding the velocity of the flow in the vicinity of the duct's corner. Indeed, Fig. 7.16c also indicates a movement of the flow away from the corner at the AD's axial location, $x/c = 0.3$, associated with the slipstream contraction caused by the AD. Near the duct's trailing edge, Fig. 7.16c also indicates a movement of the flow towards the duct's corner, which is consistent with what had been previously discussed regarding the effect the spanwise pressure gradient in the movement of flow at the duct's trailing edge. Furthermore, Fig. 7.16c also suggests that the corner vortices may originate at the duct's surface. Near the trailing edge, the oil flow lines indicate two vortical flow regions (symmetric with respect to the corner), which are consistent with the regions of lower C_p shown in Fig. 7.16a. The vortical flows appear to be caused by the combined effects of separation in the axial direction (which leads to reversed axial flow) and of the spanwise movement of the flow towards the corner due to a spanwise pressure gradient.

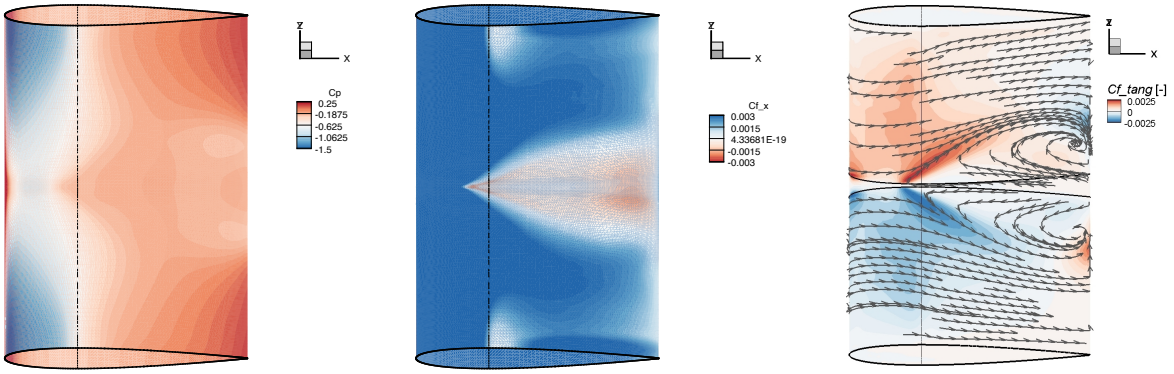

(a) Pressure coefficient

(b) Axial skin friction coefficient

(c) Tangential skin friction coefficient

Figure 7.16: Contours of pressure coefficient (left image), axial skin friction coefficient (center image) and tangential skin friction coefficient (right image) on the square duct's inner surface. The right image also shows oil flow lines over the duct's surface. Results obtained with the AD operating at $J = 0.7$. It is also shown a slice at the AD axial location: $x/c = 0.3$.

PROPELLER INFLOW AXIAL VELOCITY

As it was previously referred, the performance of the propulsor is fixed in the AD simulations, from the inputs given to the model. Still, it is possible to make predictions regarding the performance of the propeller inside each duct from the flowfields calculated with the ducted AD computations. In Fig. 7.17, it is shown the average axial velocity (normalised with free-stream velocity) at the propeller location versus radial position, from the results of each installed simulation with the AD. The results obtained from the installed power-off calculations are also shown. From Fig. 7.17, it can be understood that at every AD operating condition tested V_a is higher inside the circular duct than inside the square duct. Moreover, this difference also appears to increase with higher AD thrust settings (lower J). For the unpowered cases, the difference in V_a profiles between the two ducts has been attributed to the higher contraction of the cross sectional area inside the circular duct from the leading edge towards $x/c = 0.3$. For the power-on cases, the thrust produced by each duct also has an effect in the axial velocity inside the duct. As it was seen in Figs. 7.12 and 7.13, the leading suction peaks are stronger for the circular duct than for the square duct, with the operating AD. The lower C_p in the vicinity of the circular duct's leading edge, which is associated with the production of thrust by the duct, is also associated with a higher flow velocity in this region. Indeed, total pressure is constant upstream of the AD, in the installed simulations. As it was previously referred, a higher V_a profile at the propeller disk leads to a lower thrust production by the propeller, considering a constant rotational velocity.

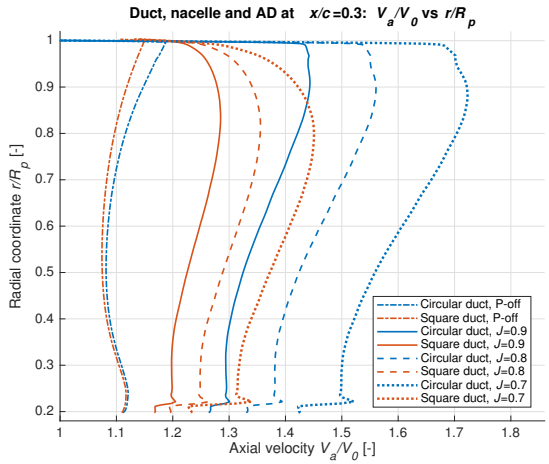

Figure 7.17: Average axial velocity profile, normalised with the free-stream velocity, inside both circular and square ducts, at the AD location: $x/c = 0.3$. The results are shown for the installed cases, with a duct, the propeller's nacelle and the AD.

FORCES ON THE COMPONENTS

In order to understand how the aerodynamic performance of each duct is affected by the operating condition of the AD, it is also relevant to analyse the spanwise distribution of forces at the two ducts, for each thrust setting. Figures 7.18 and 7.19 show the spanwise distribution of pressure and friction thrust forces on the circular and square ducts, respectively. For each component, it is shown the thrust coefficient per unit span. The friction thrust coefficient, T_{c_f}, is negative for both ducts in all spanwise locations, since the friction force always acts in the downstream direction. From Fig. 7.18, it can be understood that, for all operating conditions, the T_{c_p} and T_{c_f} distributions do not vary in the spanwise direction. This result is consistent with what what been discussed previously regarding the C_p and C_{f_x} chordwise distributions at the circular duct surface. Indeed, the C_p and C_{f_x} distributions were also found to be constant in the circular duct surface, along the spanwise direction. Another interesting result seen from Fig. 7.18 is that the friction "thrust" does not appear to vary much for the different AD settings.

In Fig. 7.19, it can be seen that the square duct's T_{c_p} experiences noticeable variations in the spanwise direction, for all operating conditions considered. This variation contrasts with what is shown in Fig. 7.18 for the circular duct. Still, the result for the square duct could have been predicted based on what was discussed regarding the square duct's C_p and C_{f_x} chordwise distributions. As it was referred, there is a higher suction peak at the inner surface of the square duct for the sections closer to the AD (an further away from the corner), in the powered calculations. Furthermore, the flow at the duct's corner inner surface was found to experience strong separation, at $J = 0.7$. The vortices at the duct's corner were also found to contribute to a higher pressure drag in this region. In this way, it is understandable that T_{c_p} is higher for square duct section further away from the corner (which is located at $\phi = 0.5$), whereas the sections near the corner actually produce a pressure drag, or a negative T_{c_p}. Comparing Figs. 7.18 and 7.19, it can also be noticed that the pressure thrust produced at the square duct is lower than the pressure thrust produced by the circular duct, at the same J, for all spanwise positions. This result is also consistent with what had been referred regarding the C_p distributions of both ducts, since the circular duct experiences stronger low pressure peaks at the leading edge.

From Fig. 7.19, it is also interesting to notice that T_{c_f} is higher (closer to 0) for the square duct sections near the corner. This phenomenon is caused by the BL separation which occurs at the corner of the duct, and which gets more severe for higher AD thrust settings. Since BL separation has a strong effect on increasing the duct's pressure drag, the small increase in T_{c_f} at the corner should not be seen as an improvement in propulsive performance of the system.

Figure 7.20 makes a final comparison between the thrust forces present on all the power-on and installed configurations discussed so far. In this way, the T_c of the Xprop obtained from the isolated simulations can be compared with the thrust coefficient of each duct and of each ducted system (duct + AD), for the three advance ratios considered. It has been referred before that the thrust of the AD in each installed configuration corresponds to the thrust of the isolated Xprop at the same J. Moreover, in Fig. 7.20 it is also plotted, for comparison, the thrust of the installed ducts in the power-off case, which is therefore negative (it is a drag force). It is also plotted the thrust of each Xprop blade, which is 1/4 of the Xprop's isolated thrust, as the forces on the spinner and nacelle were neglected. The thrust of each blade was plotted for comparison with the thrust generated by each duct in the AD powered simulations.

From Fig. 7.20 it is first very clear that the circular duct is capable of producing more thrust than the square duct, independently of the advance ratio. Moreover, it is also interesting to notice that, at $J = 0.7$, the circular duct produces almost as much thrust as one isolated Xprop blade. From the total thrust of each system, it can be seen that the square ducted AD produces a similar thrust as the isolated Xprop, due to the fact that the square duct's thrust is small compared to the isolated Xprop's thrust. It can also be understood that, at the lowest J tested, the square duct produces a negative thrust (drag), since the effect of slipstream contraction is too small. The thrust produced by the circular ducted AD system is higher than the thrust produced by the isolated Xprop for all operating conditions tested, even though it is noticeable that this difference is shortening fast as the advance ratio is increased. It is also expected that the circular duct would produce drag instead of thrust for a sufficiently low AD thrust setting.

Furthermore, Fig. 7.20 also shows the efficiency of the three propulsive systems considered: isolated

Xprop, circular ducted AD and square ducted AD. However, it should be kept in mind that this efficiency comparison is quite unfair, in the sense that for the three cases it was considered the same power supplied by the system: the shaft power of the isolated Xprop (at each J). This is due to the fact that the isolated Xprop torque distributions were used as an input for the AD, and the rotational velocity Ω associated with the AD simulations was the same as the Ω_{prop} at which the input for the AD was obtained. However, this angular velocity has no direct influence in the ducted AD results, as the AD model does not require Ω as an input.

Despite the fact that this efficiency comparison between the three propulsion systems can be considered unfair, it is still interesting to notice that the efficiency curve of the isolated propeller system seems to be the curve which is further away from the maximum efficiency values. On the other hand, for the ducted AD systems, the gradient of each efficiency curve appears to be closer to 0 at the highest advance ratio tested, $J = 0.9$. This indicates that, for ducted propeller propulsion systems, maximum efficiency should be reached at a lower J than the maximum efficiency of the corresponding isolated propeller.

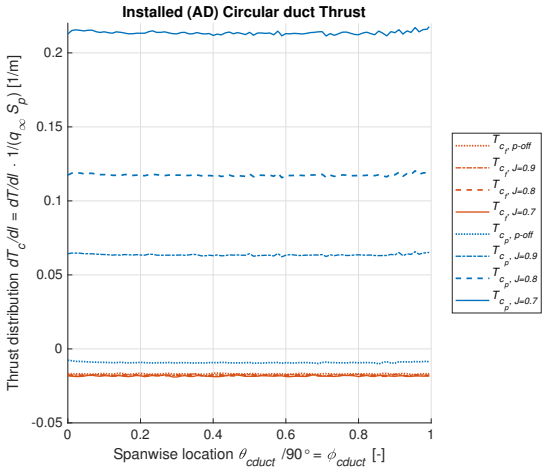

Figure 7.18: Spanwise thrust coefficient distribution at the circular duct from the installed simulations with an AD. It is shown the pressure and friction thrust coefficient curves for the power-off case and for the AD operating conditions: $J = 0.9$, $J = 0.8$ and $J = 0.7$.

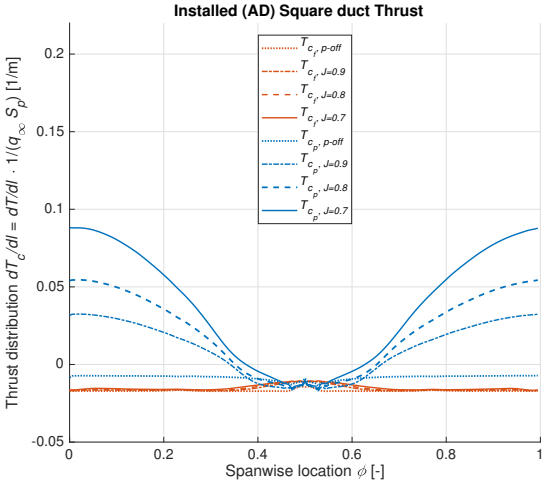

Figure 7.19: Spanwise thrust coefficient distribution at the square duct from the installed simulations with an AD. It is shown the pressure and friction thrust coefficient curves for the power-off case and for the AD operating conditions: $J = 0.9$, $J = 0.8$ and $J = 0.7$.

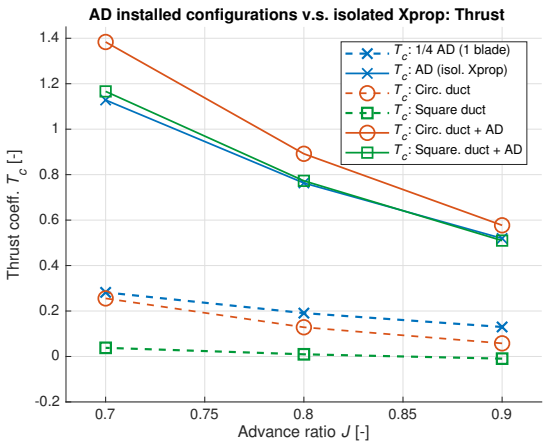

(a) Thrust coefficient

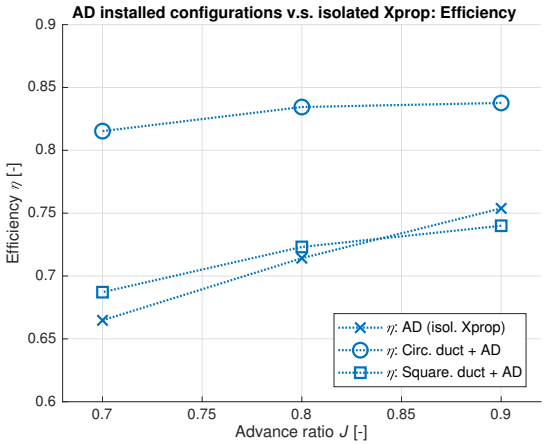

(b) Efficiency

Figure 7.20: Thrust coefficient (left-image) and efficiency (right-image) estimated from different simulations, versus advance ratio. It is shown the thrust coefficient of the circular and square ducts from the installed AD-on simulations, as well as the thrust provided from the actuator disk at each J. For the power-on cases, it is also shown the systems' thrust (duct + AD). The efficiency shown for each power-on case corresponds to the efficiency of the system.

7.2. DUCTED XPROP

In the previous section it was investigated how the aerodynamic performances of the circular and square ducts were affected by installation. It were considered both unpowered and power-on AD cases. However, since powered results shown in the previous section were obtained with an AD (with fixed T and Q distributions), it was not yet discussed the effect of installation on the Xprop. Since it was expected that this effect would be different for the two ducts, it was considered essential to investigate how each duct would affect the performance of the propeller. In this way, this section analyses the results obtained from the two unsteady ducted propeller simulations. Firstly, it is analysed the vortices generated at each ducted system (section 7.2.1). Secondly, it is evaluated the pressure coefficient and skin friction coefficient distributions at each duct, in section 7.2.2. Thirdly, it were analysed the radial distributions of thrust and torque at the propeller (section 7.2.3). Afterwards, it is investigated the effect of the full blade propeller model on the spanwise thrust distributions on each duct (section 7.2.4). Finally, it is then possible to make final comparisons over the overall performance of the three full blade model propulsion systems (section 7.2.5): isolated Xprop, circular ducted Xprop and square ducted Xprop.

7.2.1. FLOWFIELD CHARACTERISATION

In the previous section (7.1), it were identified vortices generated by the square ducted AD system, and their influence on the performance of the propulsion system. The present section aims at understanding if corresponding vortices are also generated in the installed systems with the full blade propeller model. In this way, it is shown in Fig. 7.21 isosurfaces of constant axial vorticity coefficient $C_{\omega_x} = -0.25$ and $C_{\omega_x} = 0.25$, for three installed systems operating at $J = 0.7$: square ducted AD, in Fig. 7.21a, square ducted Xprop, in Fig. 7.21b, and circular ducted Xprop, in Fig. 7.21c. The isosurfaces are seen from downstream, but the point of view is not aligned with the x-axis. This axonometric projection was found to show the corner vortices on the ducted propeller system more clearly. In fact, there is more "noise" shown at the figures with C_{ω_x} isosurfaces relative to the propeller ducted systems, since the propeller's blade also generates vorticity.

By comparing Figs. 7.21a and 7.21b, it can be understood that the corner vortices are also generated on the propeller system. However, the figures indicate that the corner vortices are stronger at the AD system, since these vortices dissipate further downstream in this simulation. However, the dissipation of the vortices is also associated with the numerical error in the simulations, which could happen differently in the two cases, e.g. because the two grids are different. Furthermore, the vortices generated in the AD system also appear to be more uniform. As it was previously discussed, the corner vortices are caused by the spanwise pressure gradient from the middle of the duct ($\phi_{qduct} = 0$ and $\phi_{qduct} = 1$) towards the corner ($\phi_{qduct} = 0.5$), which is due to the static pressure jump caused by the propulsor (AD or propeller). In the AD's steady simulation, the pressure gradient towards the corner is constant. However, in the unsteady square ducted propeller simulation, the pressure gradient towards the corner is only present when the blade's azimuthal position is near the middle sections of the duct (θ_{blade} close to 0° or 90°). This difference can explain why the vortices are more uniform at the corner of the ducted AD system. The difference also indicates that the decrease in performance of the system caused by the corner vortices is more prominent in the AD system. Moreover, Fig. 7.21b also indicates that the vortex created at $\phi_{qduct} = 1$ due to the rotation in the slipstream induced by the propulsor is also present in the square ducted propeller simulation. However, comparing Figs. 7.21a and 7.21b it can also be understood that this vortex is more uniform in the AD simulation. In the full blade simulation, the vortex is only formed when the blade passes near the duct surface (at $\phi_{qduct} = 1$).

Comparing Figs. 7.21b and 7.21c, it can be understood that there is less axial vorticity generated in the circular ducted propeller system, with respect to the square ducted system. This indicates an advantage of the circular ducted system in terms of performance, since the circular duct does not generate as strong vortices as the corner vortices at the square ducted system. In both Figs. 7.21b and 7.21c it is also possible to identify vorticity generated by the propeller. At low radial positions, the rotation in the flow caused by the propeller results in negative axial vorticity. On the other hand, the blade tip generates a positive axial vorticity, as the blade tip vortex is created. The isosurfaces of positive C_{ω_x} at high radial positions ($r/R_p \approx 1$) in Figs. 7.21b and 7.21c indicate that the blade tip vortices are stronger on the square ducted system. It was already expected that the blade tip vortices would be stronger on the square ducted system, for two main reasons. Firstly, the blade tip clearance is lower, on average, for the circular ducted system. It was already discussed in section 2.2.3 that a lower tip clearance between the blade and the duct results in a lower tip loss, as it is generated a lower tip vortex at the tip. Secondly, from the results of the AD simulations it was concluded that there is a

considerably lower axial velocity at the propeller location inside the square duct than inside the circular duct, for the same AD thrust. In the full blade simulations, a lower flow axial velocity at the propeller disk results in a higher blade thrust, for the same Ω_{prop}, and consequently in stronger blade tip vortices.

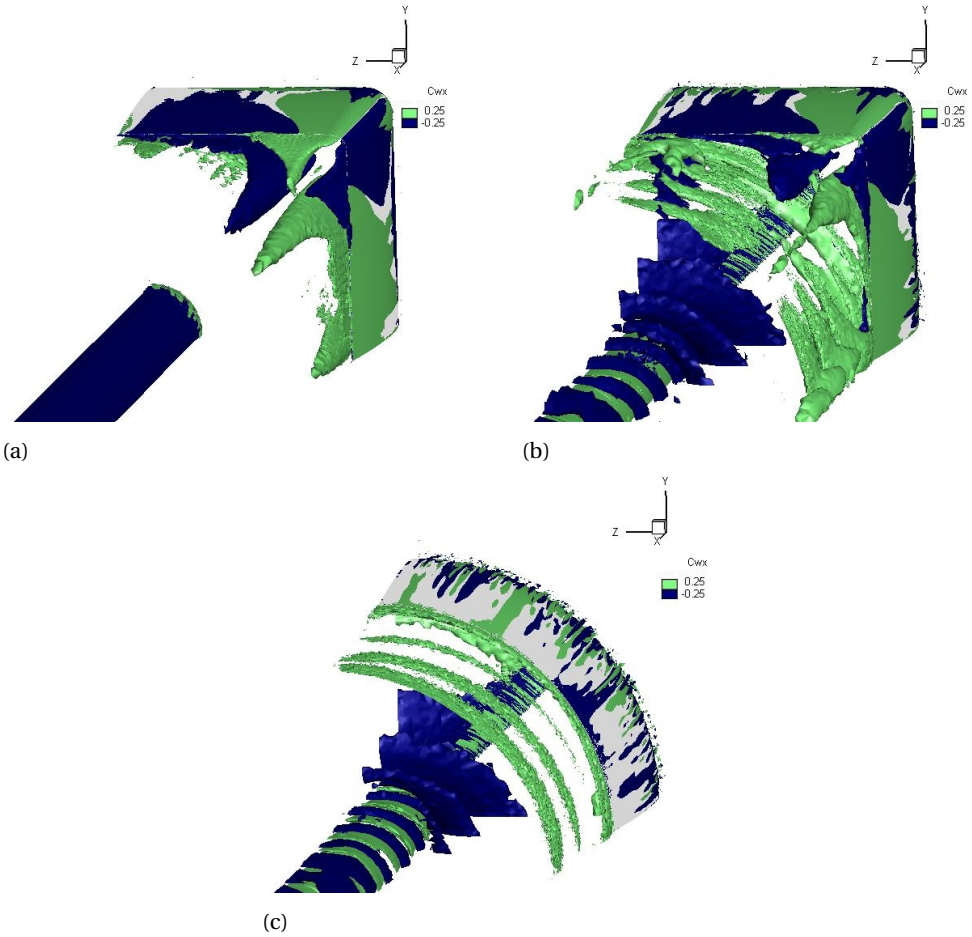

Figure 7.21: Axial vorticity coefficient isosurfaces from three installed configurations: square duct with the AD (top-left), square duct with the Xprop (top-right), and circular duct with the Xprop (bottom). The operating condition corresponds to $J = 0.7$, for the three cases. The images show isosurfaces of constant axial vorticity coefficient: $C_{\omega_x} = -0.25$ and $C_{\omega_x} = 0.25$. The isosurfaces are seen from downstream in an axonometric projection.

Time-accurate axial vorticity coefficient isosurfaces from the unsteady simulation of the square duct with the Xprop. The Figure shows isosurfaces of constant axial vorticity coefficient $C_{\omega_x} = -0.25$ and $C_{\omega_x} = 0.25$, for radial positions $1.05 < r/R_p$. The azimuthal position of the blade at the recorded timestep was $\theta_{blade} = 45°$. It is also shown a slice at the duct's surface, at the propeller's axial location: $x/c = 0.3$. View from inside the duct.

7.2.2. PRESSURE AND SKIN FRICTION AT THE DUCTS

In this section, it is analysed the pressure and axial skin friction coefficient distributions over each duct's inner surface from the ducted propeller simulations. In the previous sections of the report, is has been noticed that the C_p and C_{f_x} chordwise distributions on the circular duct's surface are constant for different spanwise (or azimuthal) locations. However, for the full blade simulations, the flowfield was not expected to be axisymmetric, due to the presence of the blade. Therefore, for the full blade simulations, it was decided to analyse the contours of C_p and C_{f_x} over the duct surfaces. In Fig. 7.22, it is shown precisely the time-accurate C_p and C_{f_x} contours over the inner surface of the circular duct. In the recorded timestep, the azimuthal position of the blade was $\theta_{blade} = 45°$. In Fig. 7.22a, it can be seen the influence of the blade position on the C_p contour. Near the duct's leading edge, it can be understood that the suction caused by the blade is more heavily felt on the azimuthal positions near the blade. At a higher blade tip Mach number, it could be expected that the

region of higher suction at the leading edge would move further behind the blade (in the azimuthal direction). This is due to the fact that in a compressible simulation the pressure perturbations propagate at the speed of sound (which is also a pressure perturbation). The fact that there is a lower C_p at the duct's leading edge for azimuthal locations near the blade indicates that, at this time step, the duct spanwise locations in the vicinity of $\theta_{cduct} = 45°$ should be able to produce more thrust than the spanwise locations further away from the blade.

Figure 7.22a also shows that there is a line of low pressure propagating downstream from the blade's location. Comparing Fig. 7.22a with Fig. 7.22b, it can be understood that the line of lower C_p which starts at the blade location corresponds to a region of reversed flow in the axial direction, where C_{f_x} is negative. The reverse axial flow appears to start at the propeller blade tip location. This can be explained due to the high adverse pressure gradient felt at the duct surface near the blade tip, due to the influence of the blade's suction and pressure sides on the flowfield. In order to understand how the reverse flow region propagates downstream, it is shown in Fig. 7.23 a zoom at the C_{f_x} contour over the duct's inner surface near the blade tip location. In Fig. 7.23, it is also shown the isosurfaces of constant tangential vorticity coefficient: $C_{\omega_\theta} = -1$ and $C_{\omega_\theta} = 15$. In this way, it is possible to understand from Fig. 7.23 that the blade tip vortex, shown by the isosurface $C_{\omega_\theta} = 15$, causes the reverse flow at the duct surface. Immediately downstream of the vortex, C_{f_x} turns again positive. For this reason, it is expected a low influence of the blade tip vortex on the drag (or thrust) of the circular duct. Immediately upstream of the blade tip vortex, it can be noticed a relatively short region of high axial skin friction. In this region, it can also be understood that there is a secondary vortex (seen from the isosurface $C_{\omega_\theta} = -1$), counter rotating with respect to the main blade tip vortex. Therefore, the secondary vortex explains the region of high axial skin friction upstream of the main vortex. Figure 7.24 illustrates the influence of the blade tip vortex in the axial skin friction felt at the circular duct's surface.

Figure 7.25 shows the C_p and C_{f_x} contours on the inner surface of the square ducted system, for a timestep where the blade was located at $\theta_{blade} = 45°$. In Fig. 7.25a, it can be understood from the C_p contours that the duct's leading edge suction peak is higher for spanwise locations further away from the corner. Since the blade is at $\theta_{blade} = 45°$, this observation contrasts with what was seen in Fig. 7.22a, relative to the circular duct, where it was observed that the strongest leading edge suction on the duct happens for azimuthal locations in the vicinity of the blade. Furthermore, form Fig. 7.25a, it can also be understood that the square ducts' corner vortices lead to lower pressure near the ducts' trailing edge. From Fig. 7.25a, it is also interesting to notice that the C_p distribution at the inner surface of the square duct is highly asymmetric with respect to the corner's spanwise location ($\phi_{qduct} = 0.5$). This asymmetry is due to the unsteadiness caused by the blade rotation, as it contrasts with the relatively small asymmetries seen for the equivalent contour in the square ducted AD system (Fig. 7.16a).

From Fig. 7.25b, it is important to notice that there is a relatively large region of reversed axial flow in the vicinity of the ducts' corner. This phenomenon negatively affects the performance of the duct, as it prevents the static pressure from recovering towards the trailing edge. For fully unseparated flows, the axial velocity of the flow is expected to lower towards the trailing edge of a component, e.g. a wing or duct, enabling a static pressure recovery, considering a constant total pressure outside the BL. However, this phenomenon is not possible if the axial velocity of the flow is reversed for a large region over a duct's surface, as seen in Fig. 7.25b. From the C_{f_x} contour, it can also be seen a small region of negative axial skin friction in a spanwise position far from the corner, near $\phi_{qduct} = 0$. This short region of reversed flow can be caused by the blade tip vortex, similarly to the phenomenon observed in Fig. 7.23 for the circular duct.

7.2.3. INSTALLED PROPELLER PERFORMANCE

In order to understand how the performance of the propulsion system changes by modifying the duct shape, it is also important to analyse the influence of the modification in the performance of the propeller. In this way, Figs. 7.26 and 7.27 were used to compare the thrust and torque coefficient distributions of the propeller for the different cases in which a full blade model was used in the computations. Figure 7.26 shows the average radial distributions of thrust and torque at one Xprop blade from the unsteady simulations at $J = 0.7$ of the isolated propeller (with the small propeller domain), of the circular ducted propeller, and of the square ducted propeller. Furthermore, Fig. 7.26 also shows the time-accurate blade distributions from the circular ducted case at 60 different timesteps, which were spaced by the time equivalent to a 3° blade rotation. In this way, the 60 distributions shown for the circular ducted system indicate the spread of the thrust and torque

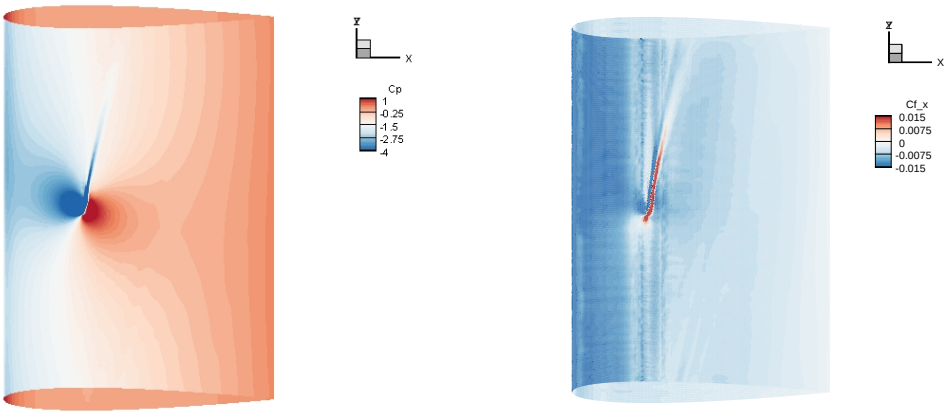

(a) (b)

Figure 7.22: Time-accurate pressure coefficient and axial skin friction coefficient contours at the circular duct's inner surface, from the ducted propeller unsteady simulation. The azimuthal position of the blade at the recorded timestep was $\theta_{blade} = 45°$. View from inside the duct.

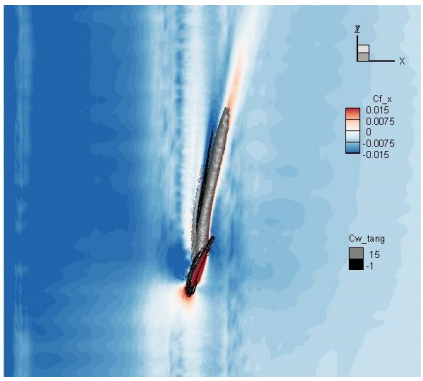

Figure 7.23: Time-accurate axial skin friction coefficient contour at the circular duct's inner surface, from the ducted propeller unsteady simulation. It is also shown isosurfaces of constant tangential vorticity coefficient, $C_{\omega\theta=-1}$ and $C_{\omega\theta=15}$, at radial locations $0.95 < r/R_p < 1$. The azimuthal position of the blade at the recorded timestep was $\theta_{blade} = 45°$. View from inside the duct, zoom at the blade tip location.

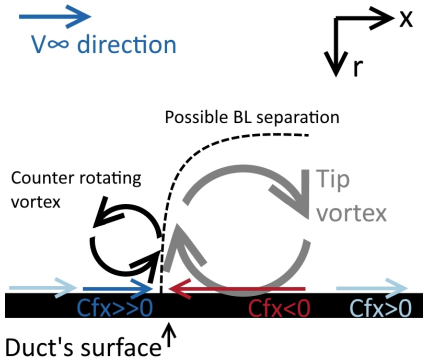

Figure 7.24: Sketch representative of the interaction between the blade tip vortex (and its counter rotating weaker vortex) and the circular duct's boundary layer. The direction of skin friction felt at the duct is indicated, as well as the location where BL separation may occur, in case the tangential skin friction is also 0 at this location.

coefficient radial distributions over a 180° blade rotation. In Fig. 7.26, it is also shown the distributions of T_c and Q_c for the square ducted case at 90 different blade azimuthal positions, spaced by 1°. The distribution at each blade location was calculated from the average over three timesteps at which the blade was located at the same θ_{blade}. The distributions for the square ducted system were calculated from a 270° blade rotation. In this way, the distributions at 90 blade locations indicate the spread of the T_c and Q_c radial distributions for a blade ducted by a square duct.

Analysing Fig. 7.26, it is possible to understand from the mean distributions of T_c and Q_c that the average loading is highest at the isolated propeller's blade for almost all radial locations. The circular ducted case appears to result in the lowest average blade loading for most radial positions, considering the three systems. This can be explained assuming that the presence of each duct causes an increase in V_a at the propeller disk, in comparison with the isolated propeller case. In the previous section, it was also concluded from the ducted AD simulations that the flow's axial velocity at the propeller disk is higher for the circular ducted case than for the square duct (see Fig. 7.17).

However, at high radial locations, near the tip, it is possible to understand that the average loading of the circular ducted propeller is higher than for the isolated propeller case. This happens due to the fact that, in-

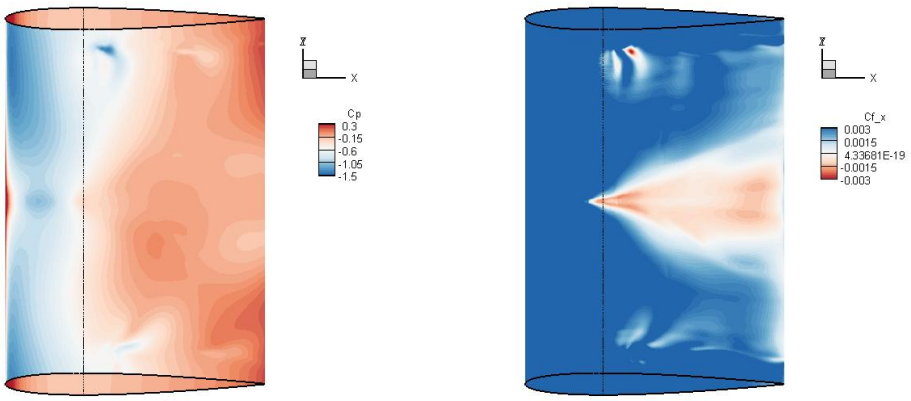

(a) (b)

Figure 7.25: Time-accurate pressure coefficient and axial skin friction coefficient contours at the circular duct's inner surface, from the ducted propeller unsteady simulation. The azimuthal position of the blade at the recorded timestep was $\theta_{blade} = 45°$. View from inside the duct.

side the circular duct, there is a reduction of the blade tip vortex, and consequently a reduction of the blade loss of loading near the tip. As discussed in section 2.2.3, the reduction of the tip loss is possible due to the small gap (or tip clearance) existing between the propeller tip and the duct surface. For the square ducted system, however, the tip clearance varies according to the blade position. Only for the positions $\theta_{blade} = 0°$ and $\theta_{blade} = 90°$ the tip clearance of the blade inside the square duct is as low as the clearance inside the circular duct. For this reason, on average the blade loading tip loss is higher for the propeller shrouded by the square duct than for the circular ducted case.

Furthermore, from Fig. 7.26, it is also possible to understand that the spread in the distributions is considerably higher for the square ducted case than for the circular ducted case. This was expected, since the propeller experiences a constant inflow when ducted by the circular duct, whereas the for the square ducted case the flow velocities at the propeller disk are expected to vary with the azimuthal position. Indeed, the non-axisymmetric shape of the square duct was found to result in a non-axisymmetric flowfield at the propeller disk. This was shown previously in Fig. 5.28, relative to the isolated square duct simulation. Furthermore, the varying tip clearance at the square ducted propeller is also understood to cause variations in the propeller's blade loading.

As there is a large spread in the blade loading distributions for the square ducted case, it was decided to analyse the blade T_c and Q_c distributions for specific blade azimuthal locations. In this way, it was decided to analyse the blade loading for $\theta_{blade} = 0°$ and $\theta_{blade} = 45°$, which are the positions of minimum and maximum tip clearance, respectively. Moreover, it was also decided to analyse the blade azimuthal positions $\theta_{blade} = 4°$ and $\theta_{blade} = 73°$, which are the positions where the blade loading is highest and minimum, respectively. Moreover, the position $\theta_{blade} = -4°$ was also analysed (which is the same as $\theta_{blade} = 86°$ for a 4 bladed propeller), since the tip clearance is the same in this case as for the position of maximum blade tip loading. The distributions of thrust and torque for these specific locations is shown in Fig. 7.27. Firstly, it can be concluded that the location $\theta_{blade} = 0°$, of lower tip clearance, indeed leads to the highest thrust and torque at the tip, indicating that it is indeed the location where the loading tip loss is lowest. However, at $\theta_{blade} = 4°$ the blade is able to produce more thrust and torque than at $\theta_{blade} = 0°$, for the radial location of maximum loading ($r/R_p \approx 0.85$). Moreover, for high radial location, the blade also produces more thrust at $\theta_{blade} = 4°$ than at $\theta_{blade} = -4°$ despite of the similar tip clearance. Taking into account that the blade is rotating in the direction of increasing θ_{blade}, the trend seen in the blade distributions indicates that there is a time response associated with the increase in loading at high radial locations due to the decrease in tip clearance. In this way, the results indicate that the blade loading keeps increasing from $\theta_{blade} = 0°$ towards $\theta_{blade} = 4°$, as the tip clearance is still relatively short for $0° < \theta_{blade} < 4°$. However, there can also be differences in the blade's inflow velocity for $-4° < \theta_{blade} < 4°$ which may also cause differences in the blade loading for these azimuthal positions. Furthermore, it should also be mentioned that there is an uncertainty related to the temporal dis-

cretization error of the simulation, which was not estimated. The unsteady simulation of the square ducted propeller was made using a time step interval correspondent to 0.5° of blade rotation. By performing more simulations of the square ducted system with different time intervals between the time steps, it would have been possible to study the influence of the temporal discretization error in the results. Thus it would have been possible to analyse the influence of the temporal discretization error in the time response required for the blade loading to increase due to the decrease in tip clearance. However, the temporal discretization error was not accessed in this research due to time constraints.

Furthermore, Fig. 7.27 also allows the comparison of the blade distributions at $\theta_{blade} = 45°$ and $\theta_{blade} = 73°$. It is possible to understand that, for both cases, the thrust and torque (and therefore loading) is low for radial position near the tip. This indicates that, in these two cases, the tip loss due to the high tip clearance indeed causes a decrease in blade loading. For $\theta_{blade} = 45°$, however, the loading at the radial positions in the vicinity of $r/R_p = 0.85$ is considerably larger than for $\theta_{blade} = 73°$. From the analyse of the isolated square duct, it was understood that $\theta = 45°$ was the azimuthal location where the V_a profile (versus radius) at the propeller disk position showed lower axial velocities. Indeed, a lower axial inflow velocity at $\theta_{blade} = 45°$ can explain the higher blade loading in this location, with respect to blade positions where the tip loss effect has a similar influence on the loading.

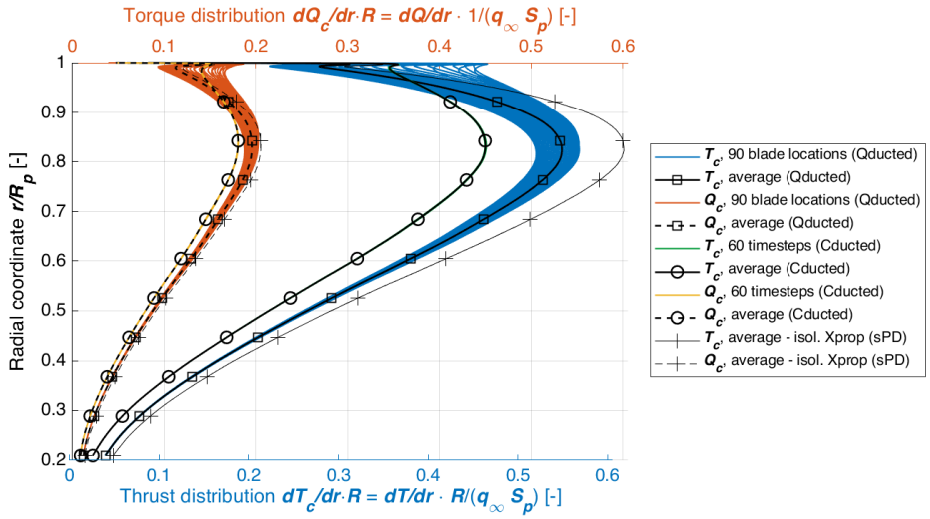

Figure 7.26: Radial thrust coefficient distribution at the Xprop's blade in the isolated (sPD) and installed configurations. For the isolated case, it is shown the average distribution. For the circular ducted case (Cducted), it is shown both the average distribution and the distributions for the 60 recorded timesteps. For the square ducted case (Qducted), it is shown both the average distribution and the distributions for the 90 recorded blade locations.

7.2.4. DUCT THRUST

Besides studying the effect of modifying the duct shape on the propeller performance, it is also important to analyse the differences in duct performance between the AD and the full blade simulations. Figure 7.28 shows the thrust coefficient of each duct from the installed power-off configurations, from the installed simulations with the AD operating at $J = 0.7$, and from the installed configurations with the Xprop, also operating at $J = 0.7$. For the installed cases with the Xprop, it is shown the average of the thrust produced by each duct from the recorded timesteps. The values from the power-off cases are represented for comparison. These values are negative, as the unpowered systems produce drag instead of thrust. It can be noticed that the definition of thrust coefficient used in this report is simply the inverse of the drag coefficient defined with the propeller disk area as the reference area: $T_c = -C_D$.

From Fig. 7.28, it is clear that the circular duct is capable of producing considerably more thrust than the square duct, for the operating conditions tested. Furthermore, it is also interesting to notice that the thrust produced by the circular duct is higher for the AD case. On the other hand, the square duct produces more thrust when ducting the propeller than the AD. In the previous section, it has been shown that the propeller produces more thrust in the isolated configuration than on the two ducted cases. Comparing the ducted

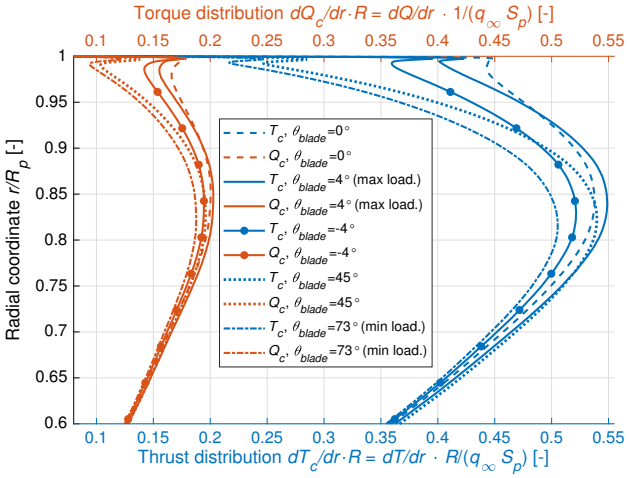

Figure 7.27: Radial thrust coefficient distribution at the Xprop's blade in the isolated (sPD) and installed configurations. For the isolated and circular ducted case, it is shown the average distribution. For the square ducted case, it is shown both the average distribution and the distributions for specific blade locations.

cases it has also been understood that the propeller produces less thrust when ducted by the circular duct. Since the AD was modelled with inputs obtained from the isolated propeller simulations, it should be considered that the the thrust produced by the AD inside each duct was higher than the thrust produced by the propeller in the corresponding simulation. For the circular duct simulation, a higher thrust of the AD can be understood to cause a stronger slipstream contraction upstream of the duct, therefore causing a higher thrust production by the duct. The effect of slipstream contraction on the pressure forces over the duct was previously explained in section 2.2.4.

For the square duct, a higher thrust of the AD with respect to the Xprop could also be expected to cause a greater generation of thrust by the duct. However, Fig. 7.28 indicates the opposite, as it shows that the square duct produces more thrust when ducting the Xprop. In section 7.2.1, it has been discussed that the square duct corner vortices appear to be stronger on the AD simulation than on the Xprop simulation. Stronger vortices at the corner would indeed explain a higher pressure drag at the square duct's corner, this way decreasing its thrust. In order to gain further understanding of the differences in duct thrust production from each case, it is proceeded for the analyse of the spanwise distributions of thrust on the ducts.

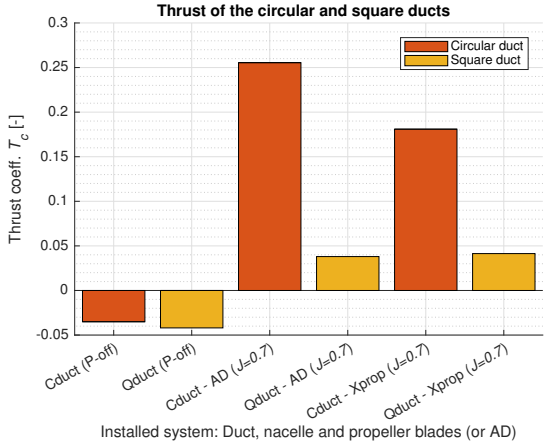

Figure 7.28: Comparison of the duct thrust coefficient calculated for several installed cases. The results relate to the power-off simulations of both ducts with the Xprop's nacelle, and to the ducted simulations with an AD or with the Xprop at $J = 0.7$.

In Figure 7.29 it is shown the spanwise variation of thrust at the circular duct obtained from the AD and full blade model simulations, at $J = 0.7$. The plotted lines represent the friction, pressure and total thrust coefficients per spanwise unit length. For the full blade case, the spanwise location is defined as the azimuthal

distance, in degrees, to the blade's azimuthal location, θ'. Negative θ' relates to spanwise locations behind the nearest blade, and positive θ' relates to azimuthal locations in front of the blade, considering the blade's direction of rotation. For the AD simulation, θ' was defined to be zero at the azimuthal location $\theta = 45°$. For the full blade case, it is shown the spanwise distribution for the 60 recorded timesteps, which as it was previously referred represent a 180° blade rotation. From Fig. 7.29, it can be understood that the distributions from the unsteady simulation show a relatively small spread, considering the different timesteps. This is due to the fact that the problem which is being simulated can in fact be considered a steady problem, if it is studied in a reference frame which is rotating with the blade.

Analysing the friction thrust coefficient distributions shown in Fig. 7.29, it can be noticed that the T_{c_f} distributions match well for the AD and full blade model simulations. As expected, T_{c_f} is in fact negative for all spanwise locations. However, the T_{c_p} distributions are shown to be quite different for the AD and full blade case. Whereas for the AD simulation T_{c_p} is constant along the duct's span (or perimeter), for the full blade computation T_{c_p} sees large variations depending on the azimuthal distance of each spanwise location to the blade. Indeed, it can be seen that in the vicinity of the blade there is a peak of high pressure thrust. This is due to the fact that the suction caused by the blade is more heavily felt in its vicinity. This phenomenon has been previously discussed in section 7.2.2, when the C_p contours over the circular ducted propeller where analysed. The total thrust coefficient, T_c, is the sum of the pressure and skin friction components.Thus, it is possible to understand that the differences in the T_c spanwise distributions between AD and full blade model are similar to the differences between the T_{c_p} distributions.

In Fig. 7.30, it is shown the spanwise thrust coefficient distributions over the square duct for the unsteady simulation with the full blade model. In order to show the spread, it were plotted the distributions on the duct relative to each of the 90 blade locations for which the results were recorded. Moreover, the average distributions are also shown. From the Figure, it is possible to understand that the friction thrust also sees small variations for each spanwise location, during the propeller's rotation. The pressure thrust, however, sees large variations between the time steps recorded. Moreover, it is also interesting to notice that the local T_{c_p} sees a larger variation with time for spanwise locations further away from the corner (near $\phi = 0$ or $\phi = 1$). This is due to the fact that these locations are closer to the propeller disk, and therefore experience a higher change in effective angle of attack when the blade passes. From the average distributions, it is also interesting to notice that the locations far from the corner are able to contribute towards the generation of thrust by the system, whereas the corner sections produce drag (T_c is negative). The low T_{c_p} at the corner is due to several reasons. Firstly, the corner sections are far from the propeller disk, and therefore experience a low change in effective α due to slipstream contraction. Secondly, the vortices generated at the corner can locally reduce the static pressure at the duct's trailing edge, as seen in Fig 7.25a. Moreover, the reverse axial flow region at the corner seen in Fig. 7.25b also makes it more difficult for the static pressure to recover towards the trailing edge, as it was previously discussed.

Comparing Figs. 7.29 and 7.30, it can again be verified the higher capability of the circular duct to produce thrust. This observation is specially interesting considering the fact that the Xprop produces more thrust inside the square duct than inside the circular duct. For the square duct, the maximum local thrust production is seen for spanwise locations in the vicinity of $\phi = 0$. However, the maximum dT_{c_p}/dl seen for the square duct is considerably lower than the maximum dT_{c_p}/dl for the circular duct. This result is interesting since the minimum blade tip clearance at the square ducted system is the same as the constant tip clearance in the circular ducted case. In this way, the change in effective α at $\phi_{qduct} = 0$ when the blade passes might be similar to the change in effective α for the circular duct section at $\theta' = 0$. However, for the square duct the change in α for the remaining duct sections is smaller. In this way, the high suction which may be generated at $\phi_{qduct} = 0$ has to spread in the spanwise direction.

Figure 7.31 compares the spanwise thrust distributions on the square duct between the AD simulation and the full blade simulation (average distributions). From the T_{c_f} distributions, it can be noticed that there is a good agreement for most of the spanwise locations. However, for the full blade case, there appears to be a sudden decrease in T_{c_f} at $\phi_{qduct} \approx 0.05$ and $\phi_{qduct} \approx 0.95$. This pattern appears to be associated with a sudden decrease in T_{c_p} at the same locations. Since this is only seen for the full blade simulation, it is presumed that this sudden variation should be related to the vortex created when the blade passes in these locations. Indeed, when reaching the trailing edge of the duct, a vortex generated by the blade would locally reduce the

static pressure (as vortices have a low pressure in its' core), and in this way locally reduce T_{c_p}. For the static pressure at the duct's outer surface to match the static pressure of the inner surface at the trailing edge, the flow at the outer surface would have to accelerate towards the trailing edge. The acceleration of the flow at the outer surface could in this way explain the sudden decrease in T_{c_f}.

Analysing in more detail the T_{c_p} distributions from Fig. 7.31, it can be understood that for spanwise locations near the duct's corner, $0.25 < \phi_{qduct} < 0.75$, it was estimated a higher T_{c_p} from the full blade simulation than from the AD computation. This result is consistent with the observation made in section 7.2.1, that the corner vortices appear to be stronger for the AD case. The vortices are generated due to the pressure gradient between the duct sections at $\phi_{qduct} = 0$ and $\phi_{qduct} = 1$ towards the corner of the duct, which causes a spanwise movement of the flow towards the corner of the duct. In this way, the pressure gradient that generates the vortices also contributes towards a pressure induced drag, similarly to the induced drag which occurs on finite wings (when generating lift) due to their pressure gradient between the pressure and suction surfaces.

Furthermore, Fig. 7.31 also suggests that the square duct is capable of producing more thrust at the spanwise locations far from the corner when ducting the AD. This effect can be attributed to the fact that the thrust produced by the AD is higher than the propeller's thrust when installed. Furthermore, the locations near $\phi_{qduct} = 0$ and $\phi_{qduct} = 1$ experience a constant favourable effect of the propulsor in changing the duct sections' effective α in the AD simulation. The propeller only induces a strong change in the angle of attack of each duct section when the blade passes near that spanwise location. On the other hand, the loading of the AD at each azimuthal location is lower than the loading of the propeller blade in the full blade model simulation. Therefore, when the blade is located at $\theta_{blade} = 0°$, the square duct sections near $\phi_{qduct} = 0$ and $\phi_{qduct} = 1$ are able to produce more thrust than in the AD simulation. This phenomenon can be understood more clearly by analysing Fig. 7.32.

In Fig. 7.32, it is shown the spanwise friction and pressure thrust distributions on the square duct from the full blade model simulation, for specific blade azimuthal locations. The blade locations considered were $\theta_{blade} = 0°$, $\theta_{blade} = 8°$, $\theta_{blade} = 45°$ and $\theta_{blade} = 56°$. $\theta_{blade} = 0°$ and $\theta_{blade} = 45°$ correspond to minimum and maximum blade tip clearances, respectively. $\theta_{blade} = 8°$ and $\theta_{blade} = 56°$ correspond to the blade positions where the duct produces maximum and minimum thrust, respectively. Analysing the Figure, it can be understood that the T_{c_p} distributions are relatively similar between for the blade positions $\theta_{blade} = 0°$ and $\theta_{blade} = 8°$, as is it noticeable a large thrust production far from the duct corner, and a relatively high pressure drag at the corner. For these two cases, the spanwise position of maximum trust at the duct varies depending on the duct section which is closer to the blade at each point. Since it had already been discussed in section 7.2.3 that the blade location of maximum blade thrust is $\theta_{blade} = 4°$ instead of the location of minimum tip clearance, it is also understandable that the duct thrust is highest for an azimuthal location of the blade slightly higher than $\theta_{blade} = 0°$. Firstly, an increase in blade loading also causes a greater change in effective α at the duct, this way increasing the duct's thrust. Secondly, the duct is also found to have a response time associated with the increase in thrust due to the influence of each blade in the flowfield.

Analysing the distributions of T_{c_p} at the duct for $\theta_{blade} = 45°$ and $\theta_{blade} = 56°$, it is understandable that the duct locations far from the corner suffer a large decrease in thrust production when the blade reaches these azimuthal positions. However, this trend is slightly compensated by an increase in T_{c_p} at the corner locations. It is also interesting to notice that the duct thrust is higher for $\theta_{blade} = 45°$ than $\theta_{blade} = 56°$ even though the blade is closer to the duct surface at 56°. This difference can be attributed to the fact that the blade is producing more thrust at $\theta_{blade} = 45°$. It was referred in section 7.2.3 that the blade thrust keeps reducing from $\theta_{blade} = 45°$ towards $\theta_{blade} = 73°$.

7.2.5. OVERALL PERFORMANCE OF THE PROPULSION SYSTEMS

In the previous sections, it were analysed the most relevant aerodynamic phenomena which influence the performance of the ducted full blade model propulsion systems. In this way, it were discussed the vortices generated by the square ducted system (section 7.2.1), it were analysed the pressure and skin friction contours on both ducts (section 7.2.2), it were analysed the radial distributions of thrust and torque at the propeller blades (section 7.2.3), and it were investigated the spanwise distributions of thrust at each duct, in section 7.2.4. In this way, it is now possible to make final comparisons over the overall performance of the ducted systems.

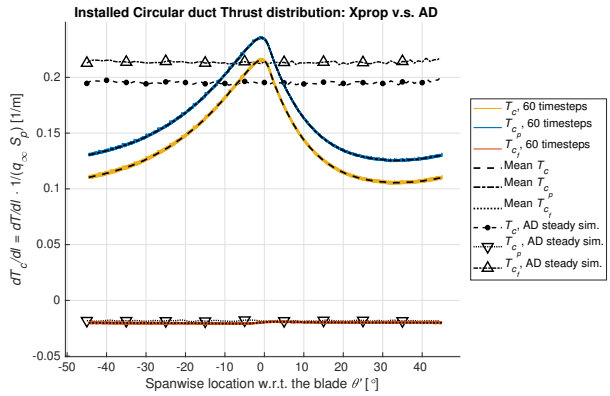

Figure 7.29: Spanwise thrust coefficient distributions at the circular duct. Comparison of the results obtained from the installed simulations with the AD and with the Xprop, at $J = 0.7$. The spanwise location is shown in terms of azimuthal distance (in degrees) to the Xprop Blade location, θ'. Positive and negative values of θ' refer to azimuthal positions in front and behind the blade, respectively.

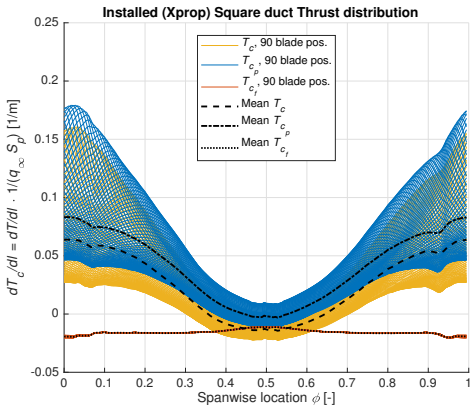

Figure 7.30: Spanwise thrust coefficient distributions at the square duct. Results obtained from the square ducted Xprop simulation, at $J = 0.7$. It is shown the spanwise distributions at the duct for 90 different blade locations, spaced by $\Delta\theta_{blade} = 0.5°$. For each blade position, the distributions were averaged between 3 different timesteps, since the results were recorded during a 270° blade rotation. The mean distributions (between all blade positions) are also shown.

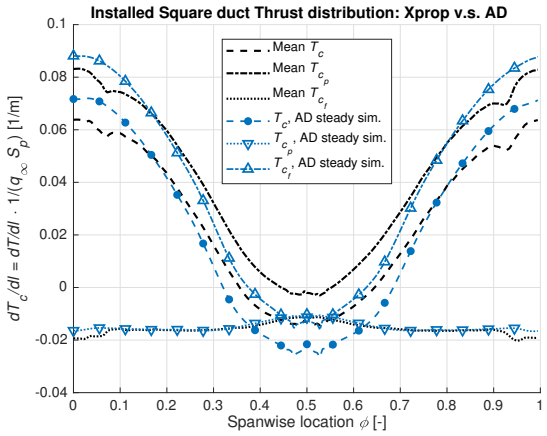

Figure 7.31: Spanwise thrust coefficient distributions at the square duct. Comparison of the results obtained from the installed simulations with the AD and with the Xprop, at $J = 0.7$. The distributions from the full blade model unsteady simulations were averaged between all the recorded timesteps.

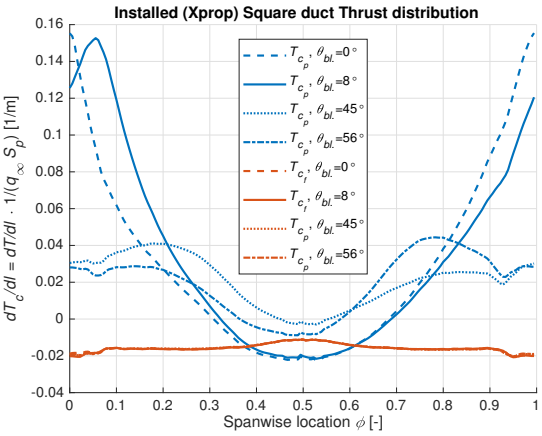

Figure 7.32: Spanwise thrust coefficient distributions at the square duct. Results obtained from the square ducted Xprop simulation, at $J = 0.7$. The distributions were obtained with the blade at specific azimuthal locations: $\theta_{blade} = 0°$ (equivalent to $\theta_{blade} = 90°$), $\theta_{blade} = 8°$ (maximum duct thrust), $\theta_{blade} = 45°$ and $\theta_{blade} = 56°$ (minimum duct thrust). For each blade position, the distributions were averaged between 3 different timesteps, since the results were recorded during a 270° blade rotation.

In Figure 7.33, it is compared the performance of the three propulsion systems for which a full blade simulation was made: the isolated Xprop, the circular ducted Xprop and the square ducted Xprop. From each simulation, Fig. 7.33 shows time-accurate values of thrust and torque coefficients from the different components, over a period corresponding to a 180° blade rotation at the advance ratio considered ($J = 0.7$). From the isolated propeller simulation with the small propeller domain (sPD), it is shown the T_c and Q_c of the propeller at each recorded time step during the recorded 180° blade rotation. For the each ducted system it is shown the T_c and Q_c of the propeller, the duct's T_c and the propulsion system's total thrust coefficient ($T_{c_{system}} = T_{c_{prop}} + T_{c_{duct}}$). Regarding the thrust produced by each installed duct, Fig. 7.33 further clarifies that the circular duct is capable of producing more thrust than the square duct, for the same operating conditions.

It is also understandable that the T_c of the square duct sees larger variations with time, with respect to the circular duct. This is in agreement with what was discussed in the previous section, as it was shown that the square duct's spanwise thrust distribution is greatly dependent on the blade's azimuthal position inside the duct.

Analysing the the thrust produced by the Xprop from each configuration, it is possible to understand from Fig. 7.33 that, for any of the time steps considered, the propeller produces more thrust in the isolated configuration, followed by the square ducted configuration. This result is also in agreement with what was discussed in section 7.2.3, where the blade thrust and torque radial distributions were evaluated, for the three systems. As it was referred, the thrust on the propeller is highest when the axial velocities on the propeller disk are lower, for the same Ω_{prop} (and assuming that separation does not occur on the blades). In this way, it was understood that V_a at the propeller disk is lowest for the isolated configuration, and highest for the circular ducted case. Moreover, the inflow velocities experienced by the propeller blade were also found to vary with the blade's azimuthal location, when shrouded by the square duct. This observation helps explaining the large variations of T_c and Q_c seen in Fig. 7.2.3 for the Xprop installed with the square duct. Furthermore, Fig. 7.2.3 also shows that the system which produces the most thrust is the isolated propeller, followed by the square ducted Xprop system. However, the torque coefficients of the Xprop in the three systems was also found to vary in the same order, with the isolated Xprop producing the most torque, followed by the Xprop shrouded by the square duct.

In this way, it was found necessary to compare the efficiencies of the three propulsion systems, in order to show which one has the best performance in these operating conditions. Figure 7.34 shows precisely the time-accurate efficiency of the isolated propeller, circular ducted propeller and square ducted propeller over a 180° blade rotation period. From the Figure, it is possible to understand that, under these operating conditions, the circular ducted propeller is the most efficient configuration, followed by the isolated Xprop. For the better performance of the circular ducted propeller, it has contributed the fact that the strong slipstream contraction caused by the relatively high thrust setting resulted in a large thrust force at the circular duct itself. The square ducted system was estimated to have the lowest η of the three systems, being 4.5% less efficient than the circular ducted system, on average. It is relevant to highlight that the thrust produced by the square ducted system is higher than the thrust of the circular ducted propeller (on average), but the difference is relatively small (only 0.4%). The vortices formed at the corner of the square duct were found to have a strong influence deteriorating the systems' performance. Indeed, part of the power added to the flow by the propeller is "lost" due to the formation of the corner vortices, in the sense that the energy present in these vortices could have been otherwise added kinetic energy to the flow in the streamwise direction.

However, the result shown in Fig. 7.34 should not be directly extrapolated to other ducted propellers designs, as it is only being compared the efficiency of the three systems at one operating condition. As an example, circular ducted propellers have been concluded to be more efficient for high slipstream contractions caused by the propeller. In this way, it is expected that at a higher free-stream velocity or at a lower J the isolated propeller would instead be the most efficient system. In this way, it should be kept in mind that the aim of this research was to study the fundamental aerodynamic effects which can explain differences in performance between the tested systems, rather than making exact conclusions regarding how much is gained or lost in performance by opting for one of the configurations.

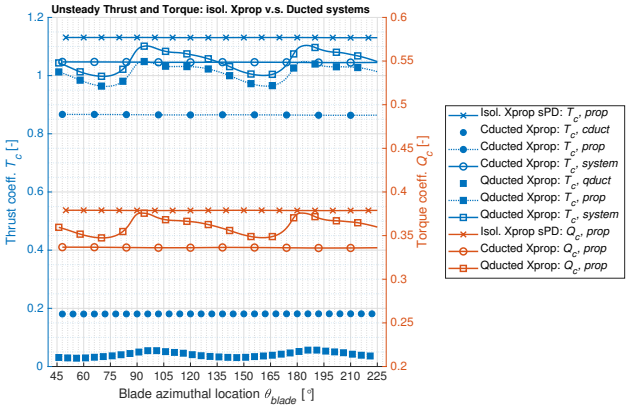

Figure 7.33: Comparison of time-accurate thrust and torque coefficients estimated at $J = 0.7$ for the three full blade model propulsion systems considered: isolated propeller, circular ducted propeller and square ducted propeller. The results are shown for the ducts (thrust), for the propeller (thrust and torque), and for the complete system (thrust), which includes both the thrust at the duct and at the propeller blades.

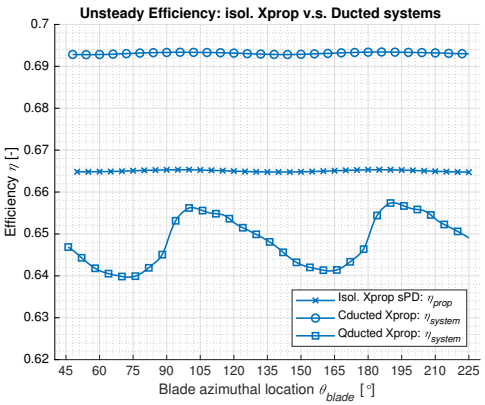

Figure 7.34: Comparison of the time-accurate efficiencies estimated at $J = 0.7$ for the three full blade model propulsion systems considered: isolated propeller, circular ducted propeller and square ducted propeller.

IV

CONCLUSION AND RECOMMENDATIONS

8

CONCLUSION

This thesis is devoted to the study of the aerodynamic interaction effects present in an unconventional ducted propeller design, featuring a square duct. The aerodynamic phenomena present in square ducted propellers was compared against the interaction effects present in a more conventional circular ducted propulsion system. In the previous chapters, the main results obtained from the CFD simulations were presented and discussed. This chapter intends to highlight the main conclusions of the research, by answering the research questions defined in Section 1.2. Section 8.1 discusses the main conclusions obtained from the simulation of the isolated ducts. Afterwards, Section 8.2 answers the research questions relative to the installed configurations. Finally, Section 8.3 evaluates the capability of the numerical methods used to model the studied flowfields.

8.1. ISOLATED CONFIGURATIONS

The CFD simulations of the isolated circular and square ducts were performed with the intention of studying the differences in drag of the two designs, along with the characterization of the flowfield at the propeller disk location (at 30% duct chord). Therefore, the following research questions were considered:

- **How does the aerodynamic performance of an isolated square duct compare to the performance of a conventional circular duct?**
  - *How can the main differences in the drag of both designs be justified?*
    The isolated square duct was found to result in more drag than the circular duct. This was found to be mainly due to the higher wetted area of the square duct, which has a larger frontal perimeter. However, the square duct was also found to be more prone to boundary layer separation, at the inner corner, due to the larger BL thickness at this location. Indeed, in the results of the isolated square duct simulation indicate that separation occurs near the square duct's trailing edge, at the corner. This effect can also explain the slightly higher pressure drag coefficient of the isolated square duct in comparison with the circular ducts C'_D, when the reference area considered for the calculation of the drag coefficient took into account the different perimeters of each duct (C'_D as defined in 5.5).
  - *How does each duct affect the flowfield at the propeller location, inside the shroud?*
    There are two main differences between the flow characteristics inside the two ducts, at the propeller location. Firstly, the flow's average axial velocity is higher inside the circular duct. This was expected to lower the propeller's performance. Secondly, the axial velocity of the flow was found to vary with the azimuthal position inside the square duct. Indeed, the results of the isolated square duct simulation indicate that the propeller blades would feel a higher axial inflow velocity at azimuthal locations far from the corner (e.g. $\theta_{blade} = 0°$) and a lower axial inflow velocity near $\theta_{blade} = 45°$. Therefore, the results indicate that blade loading would vary along the rotation, when the propeller is placed inside the square duct. For the circular duct, the axial velocity profile

was found to be independent of the azimuthal location.

8.2. INSTALLED CONFIGURATIONS

After analysing the isolated geometries, it was proceeded to the simulation of the installed configurations. The study of these more complex configurations was based on the following research questions:

- **How does the performance of a propeller in a square duct compare with a circular duct system?**
  - *Which steady aerodynamic effects affect the performance of the quadrangular ducted propeller system?*
    The steady simulation of the square duct with an AD model was important to understand how the unconventional duct's performance can be affected by the presence of the propulsor. It was interesting to notice that the square duct is able to produce thrust when the slipstream contraction caused by the AD is large. However, the thrust produced by the circular duct was always considerably larger, taking into account the range of J tested. The lower thrust production of the square duct was attributed to several factors. Firstly, the effect of slipstream contraction was found to be less felt on the spanwise locations far from the AD (closer to the corner). In this way, the change in effective angle of attack, responsible for the production of thrust by the duct, is less noticeable at the duct's corner. Secondly, the results indicate that axial separation occurs at the square duct's corner. This was found to be due to the higher BL thickness at the corner (seen in the isolated duct computations), and due to the higher suction peak of the corner sections in the powered case, which leads to a higher adverse pressure gradient downstream of the peak. Moreover, the results also indicate that slipstream contraction occurs inside the square duct due to the AD. This effect could also contribute towards separation at the duct's corner. Finally, it was found that the square ducted AD system leads to the production of two counter rotating vortices at the corner of the square duct. These vortices also lower the thrust of the system. Due to these vortices, the kinetic energy of the flow associated with the flow velocity in the axial direction decreases, which means that the momentum of the flow in axial direction is also lower.

  - *Which aerodynamic interference effects are dominant between the propeller and the quadrangular duct, considering the unsteady effects caused by the rotation of the blades?*
    Whereas the circular ducted propeller can be studied as a steady problem (in a rotating reference frame), the square ducted propeller with the full blade model is an unsteady problem. Indeed, both the thrust of the propeller and duct were found to vary depending on blade's azimuthal location. Moreover, the torque of the propeller and the time-accurate efficiency were also found to be dependent on the blade location.
    The forces on the blade were found to be dependent on the tip clearance at each time step and on the inflow velocities at each azimuthal location. Even though blade tip loss is lowest when the blade is at $\theta_{blade} = 0°$ (position equivalent to $\theta_{blade} = 90°$), the results suggest that blade loading is highest at $\theta_{blade} = 4°$, at the operating conditions tested. Therefore, the results indicate that there is a time-response associated with the rise of blade loading due to decreasing tip clearance. However, the temporal discretization uncertainty was not estimated for the unsteady simulations. Therefore, the blade location for maximum loading might be different than $\theta_{blade} = 4°$ if the unsteady simulation of the square ducted propeller is repeated with a lower transient time step or with a higher temporal discretization scheme. Furthermore, even though tip clearance is highest when the blade is at $\theta_{blade} = 45°$, the blade loading was found to be lowest when the blade is located at $\theta_{blade} = 73°$. Besides the time response required for blade loading to decrease, the results also suggest that blade loading is higher at $\theta_{blade} = 45°$ than at $\theta_{blade} = 73°$ due to the lower axial inflow velocity felt by the blade at $\theta_{blade} = 45°$.
    The thrust produced by the square duct was also found to vary with depending on the blade location. For blade locations near $\theta_{blade} = 0°$, duct thrust was found to increase. This is due to the shorter distance between the blade and the closest duct sections (when compared to blade locations near $\theta_{blade} = 45°$) and also due to the higher thrust of the blade near $\theta_{blade} = 0°$. The blade location correspondent to maximum duct thrust was found to be at $\theta_{blade} = 8°$, after the point of maximum blade thrust, which also indicates a time response required for the duct thrust to in-

crease. Axial flow separation was also found to be present at the square duct's corner in the transient full blade model simulation. As it was previously referred, this phenomenon is important to explain the lower production of thrust at the square duct's corner, in the installed configurations.

- *How does the overall performance of the different propulsive systems compare at the specific operating conditions tested, considering the isolated propeller, the circular ducted propeller and the square ducted propeller?*
  The unsteady full blade model simulations of the three different propulsion systems were performed at constant propeller angular velocity, in order to keep the advance ratio constant at $J = 0.7$. Therefore, the axial velocity at the propeller disk had a dominant effect in the thrust and shaft power (obtained from equation 2.4) of each propulsive system. With the lowest V_a at the propeller disk, the isolated propeller case resulted in the highest thrust production, which was also associated with a higher torque on the blades and, therefore, with a higher shaft power (see equation 2.4). The simulation with a square duct shrouding the propeller resulted in a higher thrust and shaft power than the equivalent simulation with circular duct, also due to the difference in V_a at the disk. Nevertheless, the thrust produced by the circular ducted system was estimated to be only 0.4% lower than the thrust produced by the square ducted system, on average and at these operating conditions. Since higher thrust production indicates a better propulsive performance of a system and higher shaft power indicates a worst performance, propulsive efficiency (defined in equation 2.5) was used to compare the performance of the three systems. The results indicate that the circular ducted propeller is the system with the highest efficiency, followed by the isolated propeller. The square ducted propeller was found to be the least efficient system, with an efficiency 4.5% lower than the circular ducted system at the operating conditions tested. If the comparison had been made for constant shaft power, it would have been expected that the efficiency of the square ducted propeller would be more similar to the efficiency of the circular ducted propeller. However, the results of this research indicate that the circular ducted system produces more thrust in a scenario where shaft power is kept constant.

8.3. CFD MODELLING

The thesis was based on CFD simulations, which were used to compute the flowfields of the different test cases. The results were analysed with criticism, therefore conclusions can be made with respect to the applicability of the methods used to simulate each configuration. The analyse of the methods was also based on several research questions:

- **How well do the numerical methods used perform in terms of accurately predicting the aerodynamic characteristics of the different flowfields?**
  - *How well does the turbulence model used represent the aerodynamic characteristics of the flowfield?*
    In this research, turbulence was modelled in the CFD simulations using the two equation turbulence model $k-\omega$ SST. This model was chosen since literature suggests that it is an accurate model considering a wide range of aerodynamic problems [26], and in comparison with models which are similarly expensive (computationally). However, literature also suggests that the $k-\omega$ SST model experiences difficulties in estimating flowfields where separation occurs [5]. This drawback of the turbulence model indicates that the estimation of the square duct's performance may have been less accurately estimated than the performance of the remaining configurations, since the results indicate that separation is a major contributor to the drag force calculated at the duct's corner. Furthermore, the turbulence model was also built and calibrated to be used with flowfields around isolated components. Therefore, it is uncertain if the $k-\omega$ SST model can accurately predict, for example, the blade tip vortices which were identified to be interacting with the circular duct's boundary layer, in the unsteady full blade model simulation.

  - *How well do the results from the two different domains used to model the isolated full blade propeller model compare, considering both steady and unsteady simulations?*
    The isolated propeller was simulated using two different propeller domains, which were described in Section 4.4.2. The conventional domain, LPD, was used in the validation process, with steady

simulations, which led to an acceptable agreement with experimental results, as discussed in Section 6.1.4. The unsteady simulation of the propeller with the LPD was also found to give similar results to the steady simulation with the same domain. The second domain used was a radially smaller propeller domain, sPD, which was found to lead to an unphysical estimation of the flowfield characteristics when the steady MRF approach was used in the computation. As an example, the steady results with the sPD indicate that the blade tip vortices move between the propeller and the outer domains, which leads to an inaccurate calculation since the solver considers different reference frames in each domain. In the propeller domain, the propeller is considered to be stationary, as the reference frame is considered to be rotating. Due to the incorrect estimation of the flowfield, the steady simulation of the propeller with the sPD also led to inaccurate estimations of the propeller thrust and torque. Nevertheless, the steady solution obtained with the sPD was used as an initial guess for the equivalent unsteady propeller simulation. The unsteady simulations of the propeller were performed with the sliding mesh approach instead of the MRF technique, and it was found good agreement between the isolated propeller unsteady simulations with the two domains. Therefore, the isolated propeller results indicate that the sPD could indeed be used to model the propeller inside each duct, for the unsteady ducted propeller calculations. However, these simulations had to be run for more iterations due to the fact that the initial solution was calculated with the steady MRF approach, which was found to result in an inaccurate calculation of the flowfield.

– *How does the estimated performance of each installed system modelled with an actuator disk compare to the performance estimated with a complete propeller model?*
The installed configurations were first modelled with an AD instead of the full blade propeller model. The inputs used for the AD were the radial thrust and torque distributions obtained from the isolated propeller simulations. Therefore, the increase in momentum and energy of the flow caused by the propulsor, AD or full blade model, is different for the two cases, considering the conclusions made in the previous Section (8.2). Furthermore, the resulting flowfields were also found to have differences. As an example, the vortices generated at the corner of the square duct from the AD simulation at $J = 0.7$ appear to be stronger than the corner vortices in the full blade model simulation. Another important difference is that the momentum increase provided by the AD is constant in the azimuthal direction. This was also found to result in differences in the forces felt by the duct from the AD and full blade model simulations. In the AD simulation of the circular ducted system, the spanwise distribution of thrust at the duct was found to be constant. However, the full blade model simulation indicates that the duct produces more thrust at the spanwise locations in the vicinity of the blade. Furthermore, the AD simulation results in a higher thrust production at the circular duct than the full blade model case. This was found to be mainly due to the higher thrust of the AD, which results in a higher average change in effective angle of attack of the duct sections.
For the square ducted simulation, the full blade model was also found to result in lower thrust production than the AD. However, the results of the AD simulation indicate a slightly lower thrust production by the duct, in this case. This result can be explained by comparing the corner vortices generated in each configuration (AD or full blade model), considering that these vortices are indeed stronger in the AD simulation. The spanwise distributions of thrust obtained from the two cases (considering the time-average for the unsteady simulation) also indicate that the pressure thrust produced at the duct's corner is considerably lower for the AD case (more negative). This result is also indicative that the corner vortices are stronger in the AD simulation. On the other hand, the results indicate that the square duct is able to produce more thrust at the locations further away from the corner when shrouding the AD. This result is consistent with the fact that the AD produces more thrust than the full blade model, in these square duct simulations.
The efficiency of each system was also estimated from the AD simulations. However, the shaft power considered in the AD cases was the shaft power of the isolated propeller, for each advance ratio. This can be be considered a very strong assumption, specially since the full blade model ducted simulations indicate a large change in thrust and power of the propeller in comparison with the isolated case. Indeed, efficiencies of the systems calculated at $J = 0.7$ from the AD simulations are considerably over predicted, in comparison to the more accurate predictions obtained with the full blade model simulations. Nevertheless, the efficiency (vs. J) curves estimated from

the AD computations provide an interesting indication that the highest efficiency point of the ducted systems occurs for a lower J than for the case of the isolated propeller. This result is consistent with what can be found in literature on ducted propellers, which often demonstrates that using ducted propellers is most advantageous when the slipstream contraction caused by the propeller is larger (e.g. by [7]).

Based on the analyse of the results presented in this thesis, it can be concluded that the use of unconventional ducted propeller propulsion systems (such as square ducted propellers) still deserves further study. The next chapter provides recommendations for future work, considering the findings of this research.

9

RECOMMENDATIONS FOR FUTURE WORK

As discussed in the previous chapter, the research results provide valuable improvement towards a better understanding of the aerodynamic characteristics of square ducted propeller systems. These results were compared against computational tests with a conventional circular duct design, which behaved in agreement with what is described in literature regarding ducted propellers. Besides the conclusions made from the discussion of the CFD results, the thesis work can also be used for gaining insight into what can be done on future studies. This chapter first gives recommendations regarding numerical methods which were tested in this research (Section 9.1). Afterwards, Section 9.2 gives suggestions on how square ducted propellers can be studied in future research. Section 9.3 gives suggestions of alternative duct designs related to square ducts which can be studied with the aim of improving the propulsive efficiency, despite the fact that the present research indicates several aerodynamic disadvantages of square ducts.

9.1. NUMERICAL METHODS

This section discusses the numerical methods used, and how these can be valuable for future research. The meshing of the different domains was found to be a challenging part of the research, and therefore it is also relevant to give recommendations regarding the meshing procedure. As discussed in chapter 4.5, the meshes generated during the research were mainly composed of unstructured elements. Nevertheless, most of the boundary layer regions were modelled with elements which resemble a structure mesh, even though the solver (ANSYS Fluent) always reads the mesh as unstructured. Generating an unstructured mesh was found to be easier, specially for difficult areas such as the square duct corner or the gap between the blade tip and the ducts. However, the results also show that more noise is found in the regions where an unstructured mesh was used, e.g. Fig 5.31 shows that the C_{f_x} distribution obtained at the square duct's corner is more noisy than for other spanwise locations. This higher noise in the results was partly attributed to interpolation errors of the post-processing software (Tecplot), which interpolates the flow quantities outside cell centres, presumably without considering the discretization schemes used in the simulations. Nevertheless, using an unstructured mesh may also cause a lower convergence of the residuals, leading to higher imbalances in regions with unstructured elements. Literature indicates that CFD solvers perform better when calculating flowfields where the cells are well oriented with the flow direction [25], which may be difficult when the mesh is unstructured. Therefore, it is also recommended from this research that, when possible, the domains are meshed with a structured mesh.

The previous chapter also presented conclusions regarding the applicability of the domains tested, to model the propeller flowfields. The isolated propeller was first simulated with an conventional domain and afterwards with a domain which was radially smaller, so that it could fit inside the ducts tested. From the verification and validation of the results, it was concluded that a radially small domain (with a radius close to the propeller radius) should only be used for unsteady simulations, with the sliding mesh technique. Using the sPD led to unphysical flowfields when the steady MRF approach was used. Still the steady results proved to be valuable to provide an initial flowfield initialization before running the (computationally) more expensive unsteady simulation. Still, the results of this research indicate that, if a similar radially small propeller domain is used in future studies, the unsteady simulation should be expected to require more iterations in

order to reach a converged and physical solution.

This research also gave insight into the applicability of actuator disk models to estimate the performance of a ducted propeller system. Using an AD instead of a full blade model leads to great savings in terms of computational costs, and therefore it is a very attractive approach. The results from this research show that the AD simulations were indeed very valuable to understand how the performance of the ducts' is influenced with installation, and to characterize the respective. However, the inputs provided to the AD were obtained from the isolated propeller simulations, and proved to be considerably different from the thrust and torque distributions calculated for the full blade propeller model in each installed simulation. For this reason, the thrust of each duct was also different in the AD and in the respective full blade simulation. The efficiency of each system was largely over predicted by the usage of an AD model. The difference in axial inflow velocities of the flow was found to be a main contributor to the difference in loading of the propeller in the isolated and in the installed configurations. Therefore, the results of this research suggest that future studies which intend to predict the performance of a ducted propeller systems using an AD model could benefit from incorporating a blade element model with the AD. An example of an AD model incorporated with a blade element method can be found in [3].

9.2. FUTURE STUDY OF SQUARE DUCTS

The results of this thesis indicate that there are several aerodynamic disadvantages associated with square ducts. These geometries were found to be more prone to boundary layer separation than circular ducts, an the duct corners were found to be prone to the generation of vortices. Furthermore, the corner sections also showed to be less effective in the production of thrust due to the larger distance between these sections and the propeller disk. At the operating conditions tested, the square duct's efficiency was calculated to be 4.5% lower than the circular duct's efficiency, for a very similar thrust setting (only 0.4% higher for the square duct, on average). However, the present research was only able to provide an estimation of efficiency of the two systems with the full blade model for one operating condition. Therefore, future research is required in order to quantify more precisely the loss in efficiency due to the usage of a square duct. Wind tunnel experiments can be used in order to estimate the performance of a circular and square duct propeller systems at different operating conditions. One of the advantages of wind tunnel testing with respect to CFD is that it is easier to study experimentally a wider test matrix in terms of operating conditions (e.g. varying advance ratio and free-stream velocity), provided that the geometries are available and that the wind tunnel facility fulfils the test requirements. The high computational costs of unsteady CFD simulations with full blade propeller models difficult the growth of the test matrix. Moreover, a future wind tunnel testing of square ducts would most likely benefit from the findings obtained with the present thesis, since the square duct flowfields were characterised in detail. Besides varying advance ratio and free-stream velocity of the systems, it would also be interesting to vary the duct and propeller geometries (e.g. by changing the airfoil sections), as well as their relative location, in order to find if the adverse aerodynamic phenomena occurring in square ducts can be mitigated.

The computational results showed in this report should also be evaluated critically, due to uncertainties associated with the numerical error in the simulations and with the applicability of the turbulence model used, for example. The separation found at the square duct corner's in the installed configurations was found to be a major contributor to the loss in performance of the system. However, separated flows are one of the points where the turbulence model $k-\omega$ SST shows more difficulties. Therefore, future studies on square ducted propellers would also benefit from the usage of more expensive computational methods. As an example, Mannini et al. [5] studied different turbulence models and concluded that the Reynolds Stress model tested performs better in predicting separated flows than the $k-\omega$ SST model. One of the main differences between the two models, which helps explaining differences in the results, is relative to the fact that the $k-\omega$ SST model assumes turbulence to be isotropic, i.e. assumes that the turbulent fluctuations are uniform in all directions, on average. The isotropic assumption can result in an inaccurate calculation of flowfields where separation occurs, or other flowfields where strong streamline curvature occurs [5].

Furthermore, if in the future square ducted propellers are found to be suitable for a given aircraft configuration, the differences between noise production of the square ducted system and the noise of a simi-

lar circular ducted system should be studied. Even though propeller ducts are often praised for their noise shielding capabilities, the noise produced by square ducted propellers may still be higher than the noise of an equivalent isolated propeller system. The results of this research indicate that the loading of the blades sees strong variations depending on their azimuthal location. Therefore, the results indicate that the pressure perturbation caused by the blades on the flowfield varies in time, which can result in an increased noise generation.

9.3. ALTERNATIVE UNCONVENTIONAL DUCT DESIGNS

The square ducted propeller system studied in the thesis was found to be less efficient than the corresponding circular ducted system. However, there can still be aircraft configurations where using a square ducts may be a better option, relative to circular ducts. As an example, there are aircraft configurations using distributed propeller concepts where each propeller is shielded by a duct, as discussed in Section 1.1. For such a configuration, there are operating conditions (e.g. during cruise) where the duct may be producing drag instead of thrust, if the slipstream contraction caused by the propeller is relatively small. In such a scenario, reducing the wetted area of the ducts may be beneficial to improve the performance of the system, while possibly keeping the noise shielding capabilities of the system.

The sketches in Figures 9.1a and 9.1b show over the wing distributed propulsion systems featuring, respectively, circular and square ducts around each propeller. Figure 9.1b shows that the square ducts share surfaces with each other (as well as with the wing), and therefore the frontal perimeter of the square ducted system is considerably lower than for the circular ducts array (Fig. 9.1a). The results of this research obtained from the isolated ducts simulation indicate that, in unpowered cases, the difference in drag of the circular and square ducts can mainly be attributed to the difference in their wetted area. Therefore, for operating conditions where the influence of the propeller in the flowfield is smaller (e.g. when slipstream contraction is low), the drag of the two ducts is expected to become closer to being proportional to their wetted area. Thus, studying the propulsive performance of distributed propulsion systems with circular and square duct can still be considered very relevant, in spite of the disadvantages of square ducts which were highlighted by the results obtained in this thesis. These distributed propulsion systems can also be studied with CFD. In order to prevent the computational costs from scaling drastically, preliminary calculations can be made with AD or actuator line models (e.g. as studied by [51]). The usage of symmetry and periodic boundary conditions should also be studied, in order to reduce the computational costs of preliminary calculations over distributed propulsion systems.

Finally, Fig. 9.1c shows a propeller distributed propulsion system where the propellers are shielded by a large rectangular duct. This concept can also help reducing wetted area, while keeping the duct's eventual noise shielding capabilities. Studying such a configuration, however, can also become more difficult due to the expected interaction between adjacent propellers. Moreover, investigating possible modifications to the corners of the rectangular shroud can also lead to significant improvements. For example, research can be made in order to access how much do the rectangular duct corners need to be rounded in order to mitigate the adverse aerodynamic effects associated with corner flow.

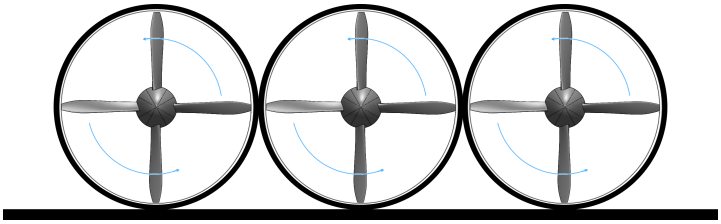

(a) Distributed circular ducted propellers

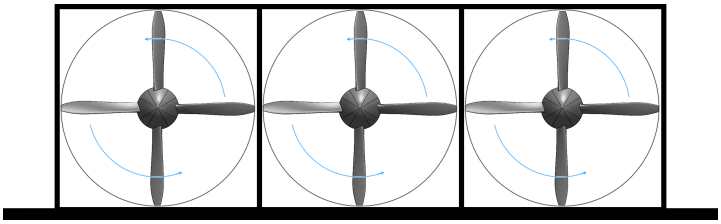

(b) Distributed square ducted propellers

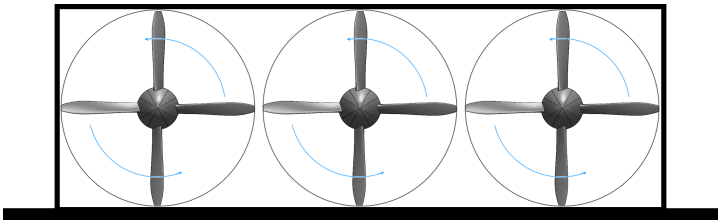

(c) Distributed propellers shielded by a single rectangular duct

Figure 9.1: Representation of three different over the wing distributed propulsion ducted propeller concepts. The top image shows a distributed circular ducted propellers system. The image at the centre shows a distributed ducted propeller system with a square duct around each propeller. Finally, the bottom image shows a distributed propeller system with a single large rectangular duct around the propellers.

BIBLIOGRAPHY

[1] F. Avellan A. Zobeiri, P. Ausoni and M. Farhat. Vortex shedding from blunt and oblique trailing edge hydrofoils. In *3rd IAHR International Meeting of the Workgroup on Cavitation and Dynamic Problems in Hydraulic Machinery and Systems*, 2009.

[2] B. Ernesto. Significance of blade element theory in performance prediction of marine propellers. *Ocean Engineering*, 31:957–974, 2004. doi: 10.1016/j.oceaneng.2003.12.001.

[3] B. Li, H. Lu and S. Deng. Validation of an actuator disk model for numerical simulation of propeller. *Proceedings of the Institution of Mechanical Engineers, Part G: Journal of Aerospace Engineering*, 229(8): 1454–1463, 2015.

[4] B. Ortun, R. Boisard, I. Gonzalez-Martino. In-plane airloads of a propeller with inflow angle: prediction vs. experiment. In *30th AIAA Applied Aerodynamics Conference*, 2012. doi: 10.2514/6.2012-2778.

[5] C. Mannini, A. Soda, and G. Schewe. Unsteady rans modelling of flow past a rectangular cylinder: Investigation of reynolds number effects. *Computers & fluids*, 39(9), 2010. doi: 10.1016/j.compfluid.2010.05.014.

[6] D. Küchemann and J. Weber. *Aerodynamics of Propulsion*. McGraw-Hill, 1953.

[7] D. M. Black, H. S. Wainauski, and C. Rohrbach. Shrouded propellers - a comprehensive performance study. *AIAA 5th Annual Meeting and Technical Display*, 1968. doi: 10.2514/6.1968-994.

[8] R. de Vries. Unsteady pylon loading for pylon-mounted tractor propellers. Msc thesis, Delft University of Technology, Delft, The Netherlands, December 2016.

[9] E. J. Hall, R. A. Delaney, and J. L. Bettner. Investigation of advanced counterrotation blade configuration concepts for high speed turboprop systems, task 1 - ducted propfan analysis. Technical report, NASA, 1990.

[10] E. N. Jacobs and A. Sherman. Airfoil section characteristics as affected by variations of the reynolds number. Technical report, NASA, 1937.

[11] Editor: J. M. Ramsden. Bell-x22a: Analysis of a vtol research vehicle. *Flight International*, pages 445–449, 23 March 1967.

[12] Editor: R. J. Brown. Propeller ring raises plane's speed. *Popular Science*, 122(4):15, April 1933.

[13] F. E. Hitchens. *Propeller Aerodynamics*. Andrews UK Limited, 2015.

[14] F. Falissard, R. Boisard, and G. Delattre. Aeroacoustic computation of a contra rotating open rotor model with test rig installation effects. In *18th AIAA/CEAS Aeroacoustics Conference (33rd AIAA Aeroacoustics Conference)*, 2012. doi: 10.2514/6.2012-2218.

[15] F. M. de Piolenc, and G. E. Wright Jr. *Ducted Fan Design*, volume 1. 1997.

[16] F. R. Menter. Two-equation eddy-viscosity turbulence models for engineering applications. *AIAA Journal*, 32(8):1598–1605, 1994.

[17] ANSYS Fluent. 12.0 user's guide, 2009. Ansys Inc.

[18] ANSYS Fluent. 12.0 theory guide, 2009. Ansys Inc.

[19] H. S. Fletcher. Experimental investigation of lift, drag, and pitching moment of five annular airfoils. Technical report, National Advisory Committee for Aeronautics, 1957.

[20] H. S. Ribner. The ring airfoil in nonaxial flow. *Journal of Aeronautical Sciences*, 14(9):529–530, September 1947. doi: 10.2514/8.1437.

[21] K. J. M. Hameeteman. Unconventional propulsive empennage - future or fiction? Msc thesis, Delft University of Technology, Delft, The Netherlands, September 2017.

[22] V. N. Harinarain. Aerodynamic performance study on a ducted propeller system for propulsion and control and stability applications. Msc thesis, Delft University of Technology, Delft, The Netherlands, May 2017.

[23] I. B. Celik, U. Ghia, P. J. Roache, C. J. Freitas, H. Coleman and P. E. Raad. Procedure for estimation and reporting of uncertainty due to discretization in cfd applications. *Journal of fluids Engineering*, 130(7), 2008. doi: 10.1115/1.2960953.

[24] I. Masters, J. C. Chapman, M. R. Willis and J. A. C. Orme. A robust blade element momentum theory model for tidal stream turbines including tip and hub loss corrections. *Journal of Marine Engineering & Technology*, 10(1):25–35, 2011. doi: 10.1080/20464177.2011.11020241.

[25] J. Andresen, G. Degrez, J. Degroote et al. *Computational Fluid Dynamics, An Introduction*. Springer-Verlag, Berlin Heidelberg, 3rd ed. edition, 2009.

[26] T.J. Coakley J. E. Bardina, P.G. Huang. Turbulence modeling validation. In *In 28th Fluid dynamics conference*, 1997. doi: 10.2514/6.1997-2121.

[27] K. Bogdański, et al. Design and optimization of low speed ducted fan for a new generation of joined wing aircraft. In *Proceedings of the 29th Congress of International Council of the Aeronautical Sciences*, Saint Petersburg, 2014.

[28] A. A. Kanoria and M. Damodaran. Computational prediction of annular wing aerodynamic characteristics. *Journal of Aircraft*, 2016. doi: 10.2514/1.C033876.

[29] A. A. Kanoria and M. Damodaran. Computational prediction of annular wing aerodynamic characteristics. *Journal of Aircraft*, 52(2):815–824, 2017. doi: 10.2514/1.C033876.

[30] Siddappaji Kiran and Mark G. Turner. Counter rotating propeller design using blade element momentum theory. 2015. doi: 10.13140/RG.2.1.5089.9925.

[31] S. Krajnović and L. Davidson. Flow around a simplified car, part 1: Large eddy simulation. *Journal of Fluids Engineering*, 127(5):907–918, 2005.

[32] D. Ejmocki Krzysztof Szafran, O. Shcherbonos. Effects of duct shape on ducted propeller thrust performance. In *Prace Instytutu Lotnictwa*, 2014.

[33] L. Eça and M. Hoekstra. Discretization uncertainty estimation based on a least squares version of the grid convergence index. In *Proceedings of the Second Workshop on CFD Uncertainty Analysis, Instituto Superior Técnico, Lisbon, Oct.*, 2006.

[34] L. P., Ruiz-Calavera, and D. Perdones-Diaz. Cfd computation of in-plane propeller shaft loads. In *AIAA/ASME/SAE/ASEE Joint Propulsion Conference*, 2013. doi: DOI:10.2514/6.2013-3798.

[35] L. W. Traub. Experimental investigation of annular wing aerodynamics. *Journal of Aircraft*, 46(3):988–997, 2009. doi: 10.2514/1.39822.

[36] M. H. Williams, J. Cho, and W. N. Dalton. Unsteady aerodynamic analysis of ducted fans. *Journal of Propulsion and Power*, 7(5):800–804, 1991. doi: 10.2514/3.23394.

[37] M. J. Werle. Aerodynamic loads and moments on axisymmetric ring-wing ducts. *AIAA Journal*, 52(10): 2359–2363, October 2014. doi: 10.2514/1.J053116.

[38] D. McLean. *Understanding aerodynamics: arguing from the real physics*. John Wiley & Sons, 2012.

[39] M. Méheut. Thrust and torque far-field analysis of propeller and counter rotating open rotor configurations. In *31st AIAA Applied Aerodynamics Conference*, 2013. doi: 10.2514/6.2013-2803.

[40] M.W.C. Oosterveld. *Wake adapted Ducted Propellers*. PhD thesis, Delft University of Technology, Delft, The Netherlands, June 1970.

[41] P. R. Spalart and C. L. Rumsey. Effective inflow conditions for turbulence models in aerodynamic calculations. *AIAA Journal*, 45(10):2544–2553, 2007. doi: 10.2514/1.29373.

[42] Jason L. Pereira. *Hover and wind-tunnel testing of shrouded rotors for improved micro-air vehicle design*. PhD thesis, University of Maryland, College Park, 2008.

[43] S. Rubin. Incompressible flow along a corner. *Journal of Fluid Mechanics*, 26(1):97–110, 1966.

[44] S. Rubin and B. Grossman. Viscous flow along a corner: numerical solution of the corner layer equations. *Quarterly of applied mathematics*, 1971.

[45] M.K. Rwigema. Propeller blade element momentum theory with vortex deflection. In *Proceedings of the 27th Congress of the International Council of the Aeronautical Sciences*, Nice, France, September 2010.

[46] S. Gaggero, et al. EFD and CFD design and analysis of a propeller in decelerating duct. *International Journal of Rotating Machinery*, 2012. doi: 10.1155/2012/823831.

[47] S. I. Joseph. Vertical take-off flying platform, September 1960. US Patent 2,953,321.

[48] S. M. El-Behery, et al. CFD prediction of air–solid flow in 180 ° curved duct. *Powder Technology*, 191(1): 130–142, 2009. doi: 10.1016/j.powtec.2008.09.018.

[49] T. Sinnige. The effects of pylon blowing on pusher propeller performance and noise emissions. Master's thesis.

[50] T. C. A. Stokkermans. Design and analysis of swirl recovery vanes for an isolated and a wing mounted tractor propeller. Msc thesis, Delft University of Technology, Delft, The Netherlands, August 2015.

[51] T. Stokkermans, N. van Arnhem, T. Sinnige and L. Veldhuis. Validation and comparison of rans propeller modeling methods for tip-mounted applications. *AIAA Aerospace Sciences Meeting*, 2018. doi: 10.2514/6.2018-0542.

[52] T. Watanabe, et al. Simulation of steady and unsteady cavitation on a marine propeller using a rans cfd code. In *Proceedings of the Fifth International Symposium on Cavitation*, Osaka, Japan, 2003.

[53] Jane's All the World's Aircraft. Kuznetsov nk-93. http://janes.ihs.com/Janes/Display/1306105, August 2016. [Online; 21-09-2017].

[54] Jane's All the World's Aircraft. Lilium jet. http://janes.ihs.com/JAWADevelopmentProduction/Display/1774324, September 2017. [Online; 12-09-2017].

[55] Lance W. Traub. Preliminary investigation of the effects of stagger on an annular wing. *Journal of Aircraft*, pages 1–7, September 2017. doi: 10.2514/1.C034310.

[56] N. van Arnhem. Design and analysis of an installed pusher propeller with boundary layer inflow. Master's thesis, Delft University of Technology, September 2015.

[57] Nando van Arnhem. Duuc aircraft with the innovative 'propulsive empennage' concept, 2016. URL https://www.youtube.com/watch?v=VDbJBkcQBPI. [YouTube video; 21-09-2017].

[58] N.H.M. van den Dungen. Synthesis of an aircraft featuring a ducted-fan propulsive empennage. Msc thesis, Delft University of Technology, Delft, The Netherlands, April 2017.

[59] L.L.M. Veldhuis. *Propeller Wing Aerodynamic Interference*. PhD thesis, Delft University of Technology, Delft, The Netherlands, June 2005.

[60] Q.R. Wald. Aerodynamics of propellers. *Progress in Aerospace Sciences*, (42:85-128), 2006.

[61] T. Wan and H. Saravia. Aerodynamic calculation of an elliptic ring wing. *29th Aerospace Sciences Meeting, Aerospace Sciences Meetings*, 1991. doi: 10.2514/6.1991-68.

A

APPENDIX - ADDITIONAL RESULTS

A.1. CIRCULAR DUCT - 3D SIMULATION, MESH CONVERGENCE STUDY

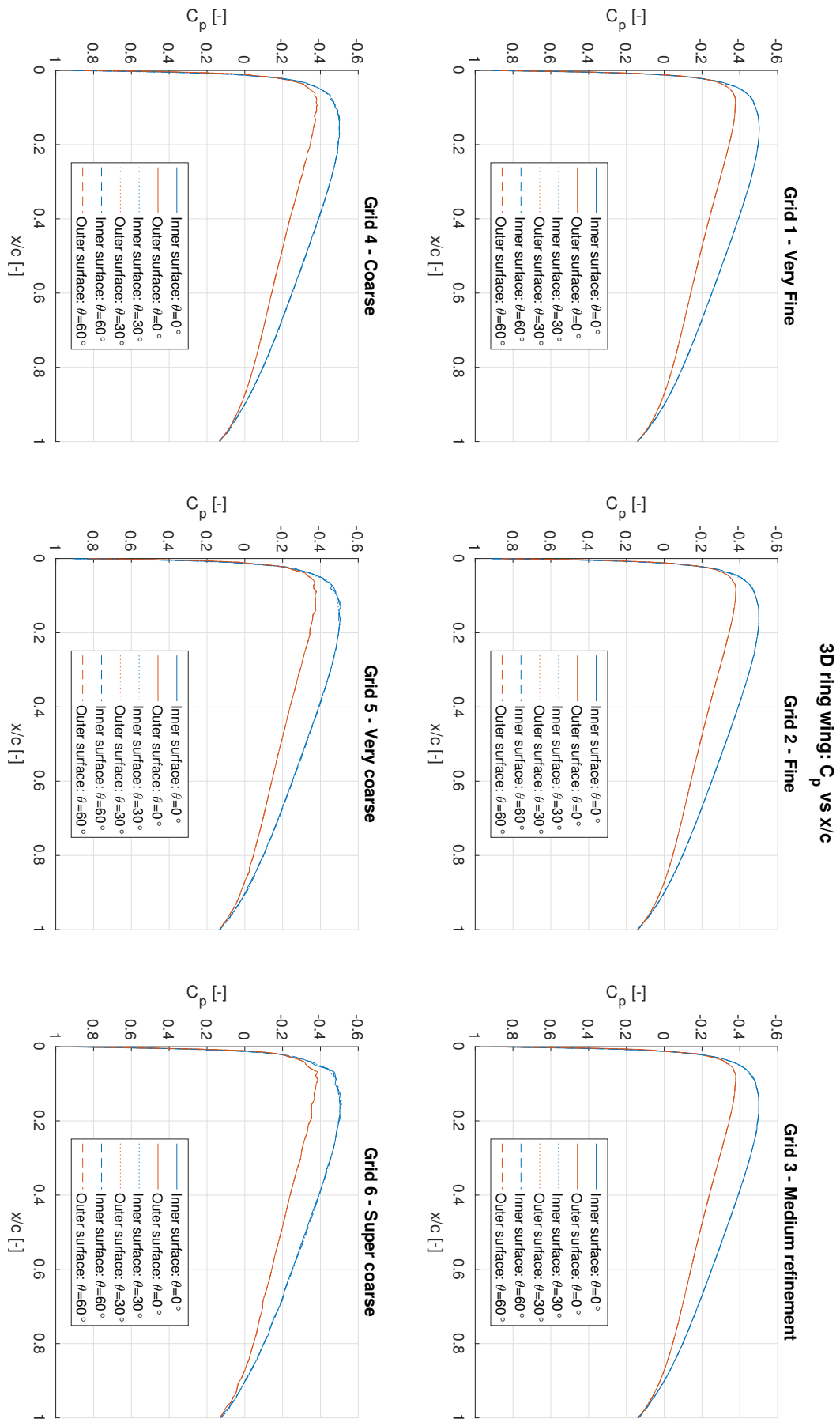

Figure A.1: Convergence of the pressure coefficient distributions over the circular duct, with respect to grid element size

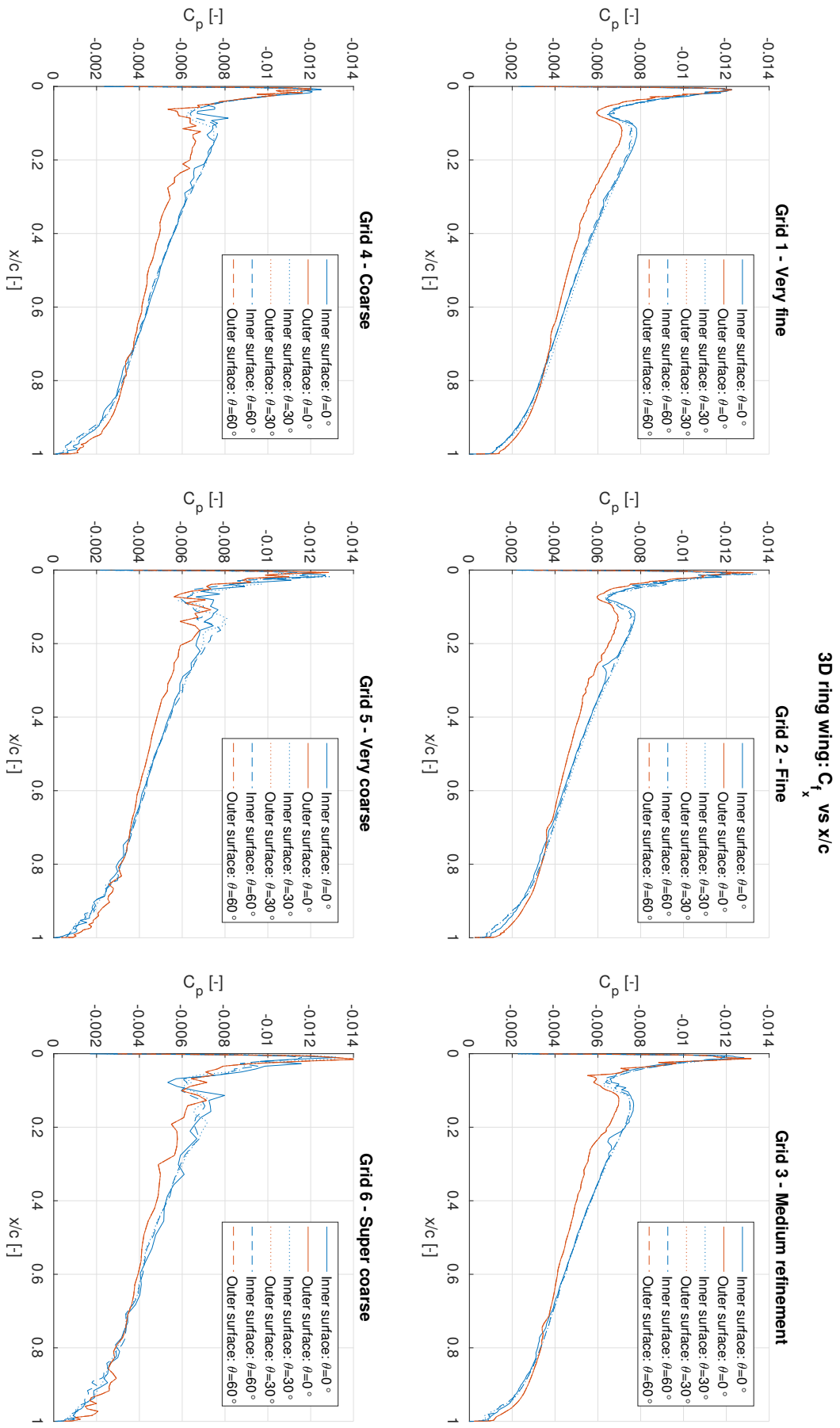

Figure A.2: Convergence of the skin friction coefficient distributions over the circular duct, with respect to grid element size

A.2. SQUARE DUCT - MESH CONVERGENCE STUDY

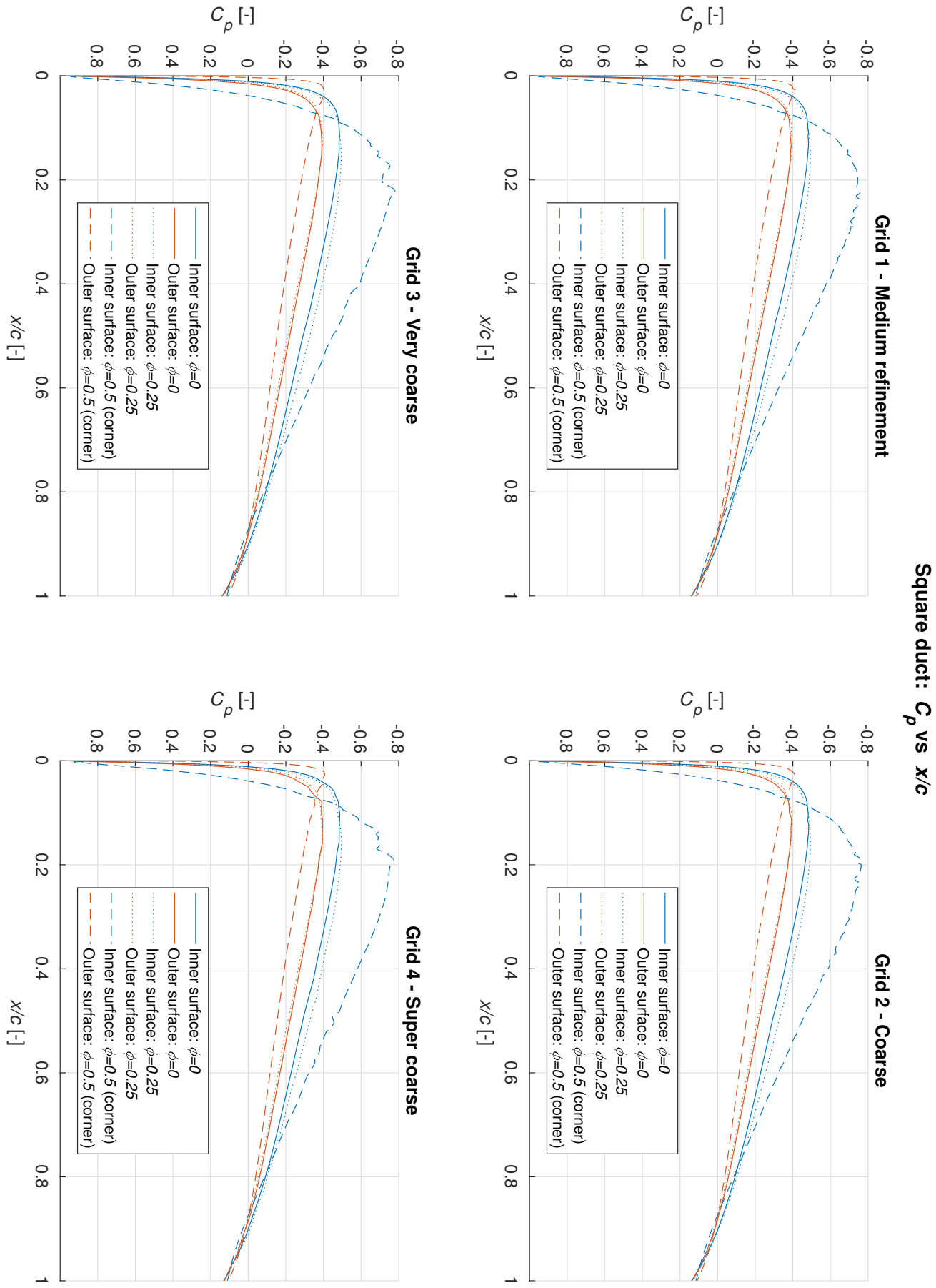

Figure A.3: Convergence of the pressure coefficient distributions over the square duct, with respect to grid element size

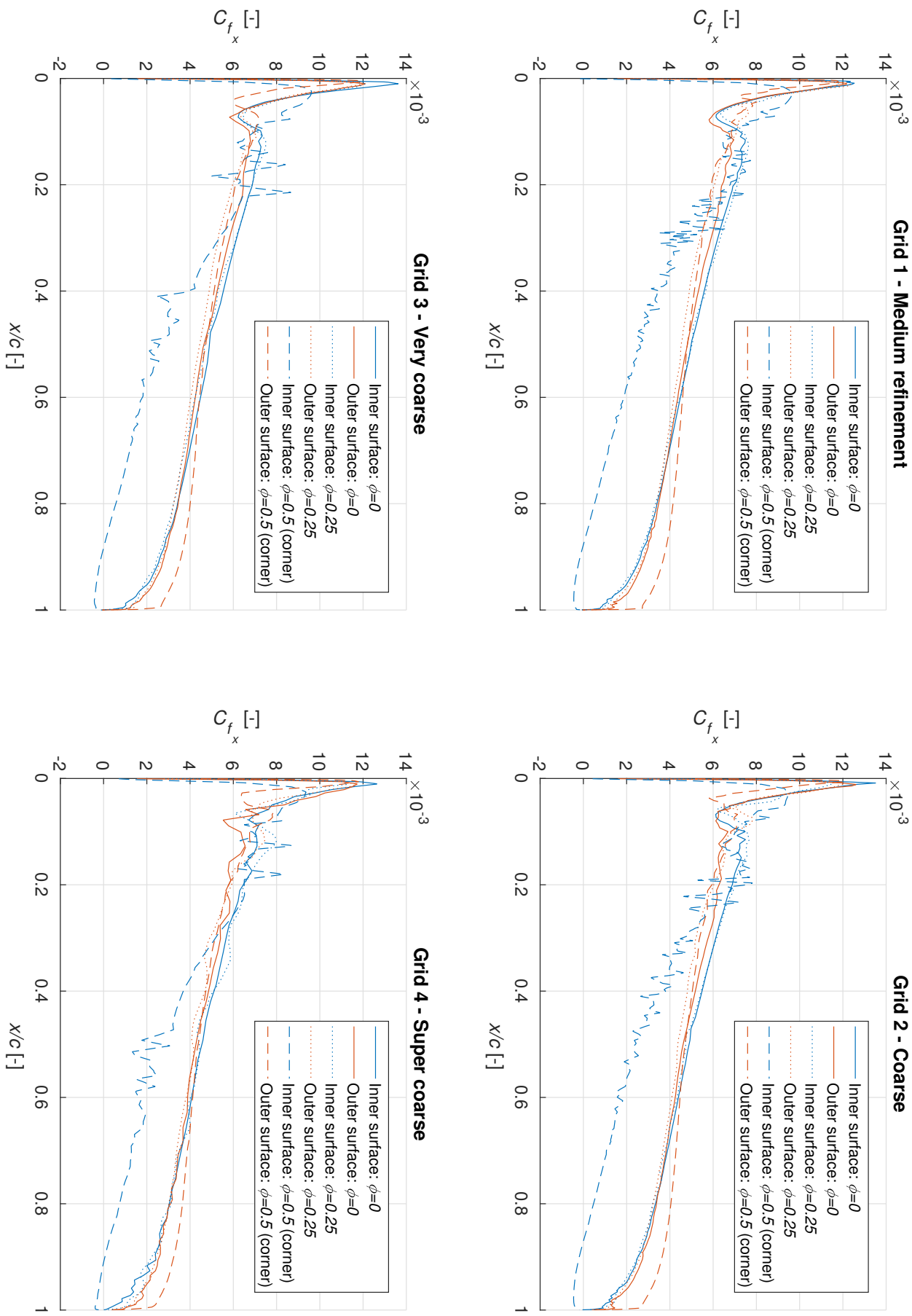

Figure A.4: Convergence of the skin friction coefficient distributions over the square duct, with respect to grid element size

A.3. PROPELLER - VARYING ADVANCE RATIO

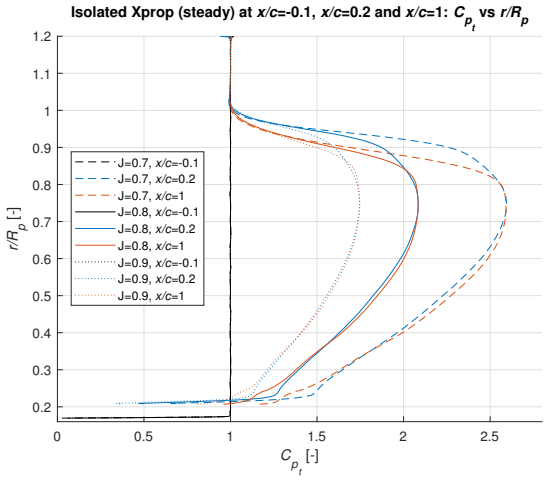

Figure A.5: Total pressure coefficient, C_{pt}, average radial distributions in the vicinity of the propeller, at three axial locations, for the three advance ratios tested. The dashed lines correspond to the highest advance ratio, $J = 0.7$, the continuous lines correspond to $J = 0.8$ and the dotted lines correspond to the lowest advance ratio tested, $J = 0.9$. The black lines correspond to the axial position 10% duct chord upstream of the blades, $x/c_{duct} = -0.1 \Leftrightarrow x/R_p \approx -0.107$, the blue lines correspond to the axial position 20% duct chord downstream of the blades, $x/c_{duct} = 0.2 \Leftrightarrow x/R_p \approx$, and the red lines correspond to the axial position 100% duct chord downstream of the blades, $x/c_{duct} = 1 \Leftrightarrow x/R_p \approx 1.07$. Results obtained with the conventional propeller domain.

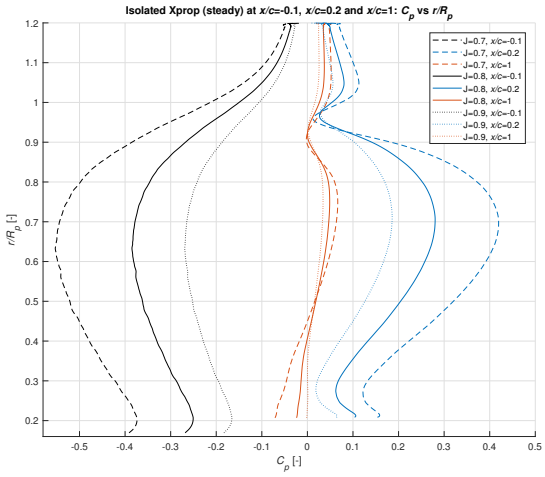

Figure A.6: Pressure coefficient, C_p, average radial distributions in the vicinity of the propeller, at three axial locations, for the three advance ratios tested. Results obtained with the conventional propeller domain. The lines represent the same as for Fig. 6.11.

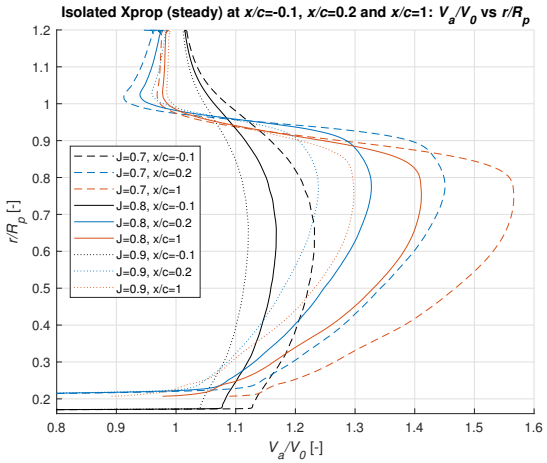

Figure A.7: Axial velocity (V_a) average radial distributions, normalised with the free-stream velocity, V_0, at three axial locations in the vicinity of the propeller, for the three advance ratios tested. Results obtained with the conventional propeller domain. The lines represent the same as for Fig. 6.11.

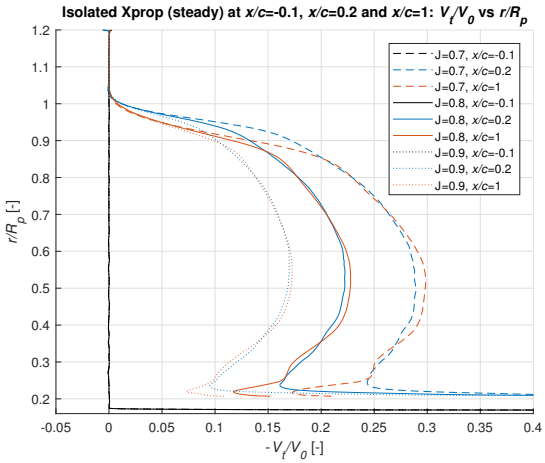

Figure A.8: Tangential velocity (V_t) average radial distributions, normalised with the free-stream velocity, V_0, at three axial locations in the vicinity of the propeller, for the three advance ratios tested. Results obtained with the conventional propeller domain. The lines represent the same as for Fig. 6.11.